The Identification and Generation of Meteotsunamis on the Southern North Sea

Masters of Science Thesis

Joep Huijbregts

Delft University of Technology

TU Delft

The Identification and Generation of Meteotsunamis on the Southern North Sea

by

Joep Huijbregts
4798988

Chair:	M.F.S. Tissier
Committee:	A.J.H.M. Reniers, S.P. Porchetta, M. Messmer
Faculty:	Faculty of Civil Engineering, Delft

Cover: Water Waves in Gray Scale in Greece Silivanova (2021)

TU Delft

Preface

To finalize my Master's Degree in Civil Engineering at Delft University of Technology, I was given the opportunity to write my thesis about the identification and generation of meteotsunamis on the Southern North Sea. These wave types are difficult to identify but can form significant threats via rip currents or floods in general. Over the past 9 months, I applied a known identification method for meteotsunamis and proposed a new method using continuous wavelet analysis. I used the results of those methods to perform six case studies, where I characterized the events and checked for Proudman resonance for each event. I hope my work will have contributed to the general subject of meteotsunamis and will have laid a foundation for meteotsunami research in relation to the Dutch coast.

In this thesis, I applied the knowledge of waves that I had obtained in the Master's program on a specialized topic. I extended this knowledge during the project and learned much about other wave analysis methods. Moreover, this thesis allowed me to dive into a field that was relatively unknown to me, namely geosciences. I started this project with only basic knowledge of this field, but throughout the thesis, I learned more and more.

I would first like to thank Marion Tissier for being my primary supervisor during this research. I very much enjoyed the weekly meetings where we would combine good discussions and critical questions with a relaxed working environment. These discussions and critical questions helped me to keep reaching for the best possible result. Secondly, I would like to thank my second supervisor from the Fluid Mechanics department, Ad Reniers. I valued the feedback during the progress meetings, which was always well put and useful.

Finally, I would like to thank my supervisors from the geosciences department, Sara Porchetta and Martina Messmer. Their enthusiasm for the subject and my curiosity about their field formed a very productive climate in which I was free to ask questions and also elaborate on the wave side of the tsunami process.

Altogether, I am very grateful that I got to research a topic that allowed me to extend my knowledge of known subjects, whilst also researching a completely new subject. This would not have been possible without the help of my supervisors.

Joep Huijbregts
Delft, October 2024

Abstract

In this thesis, the identification and generation of meteotsunamis on the Southern North Sea are investigated. Although meteotsunamis are well known in other areas, hardly any research has been done on them near the Dutch Coast. Here, nine years of sea level elevation data are evaluated using the classic approach and a subsequent wavelet analysis to identify a list of potential meteotsunamis. Six of those events have been selected, for which the atmospheric conditions were simulated by WRF. To definitively classify them as meteotsunamis, a pressure jump and atmospheric front responsible for the generation are identified. The six events are characterized by computation of their angle of incidence, wave period, and wave height, and are checked for the probability of Proudman resonance. The six selected events were all linked to a pressure jump and an atmospheric front, and thus classified as meteotsunamis. Two events propagated from the North-West and the other four from the South through the English Channel. The wave periods varied between 10 and 25 minutes, and the wave heights varied around 0.20 meters, with a maximum wave height of 0.63 meters. Three events were linked to a front propagating overseas, all of which had a high probability that Proudman resonance contributed to their amplification. These results form a foundation for future research on meteotsunamis on the Southern North Sea.

Contents

1

Introduction

On the 29th of May 2017, some unusually high waves approached the Dutch coast (Figure 1.1). Fortunately, they arrived before the first tourists, resulting in no casualties and only property damage. However, a later arrival time of these waves might have led to much greater consequences (or even casualties), as the waves struck at a known popular tourist spot (Sibley et al., 2020). The phenomenon that caused these unusually high waves is known as a meteotsunami. A first understanding of this mechanism can be obtained by separating the term into meteo- and -tsunami.

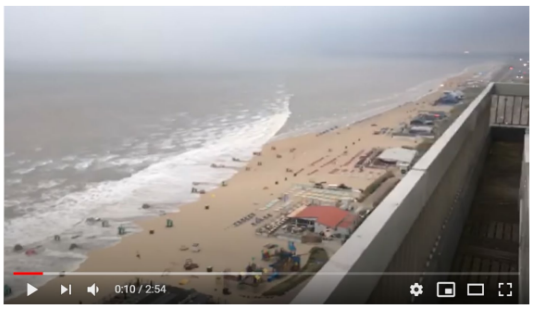

Figure 1.1: The tsunami wave of the 29th of May 2017, a video by Jan Koning

When referring to tsunamis, often 'seismic tsunamis' are meant, as these tsunamis are the tsunamis that make it into the news due to their size, severe damages, and loss of human life. This assumption is incorrect, as the word tsunami does not imply anything about its source. The word tsunami originates from Japan, where "tsunami" means "a big wave in a harbor" (Monserrat et al., 2006). Tsunamis are predominantly a result of earthquakes, but subsidiary sources include subaerial and submarine landslides, volcanic collapse and eruption, or even extraterrestrial impacts. The correct description of a tsunami is a shallow water wave, whose wavelengths are at least 20 times the water depth (Tappin et al., 2013), with a wave period between several minutes to several hours (Sibley et al., 2020).

Unlike the term -tsunami, the term meteo- elaborates on the source of the tsunami wave. The word originates from Greece, where meteoros means "high above the ground". In modern language, meteorology is known as the study of the atmosphere and weather. Combining the two terms, a first explanation of the meteotsunami is found: a tsunami wave, caused by an atmospheric component.

The term is relatively new, but the phenomenon itself is not. In the Adriatic Sea (Denamiel et al., 2019), the Gulf of Mexico (Olabarrieta et al., 2017), and the Yellow Sea (Ha et al., 2018) meteotsunamis occur much more often than in the Southern North Sea, and have caused much bigger damages and even loss of life. Consequently, research into meteotsunami is further advanced in these regions, with some even implementing early warning systems. Examples are the Balearic RIssaga Forecasting System (BRIFS) for the Balearic Islands (Mourre et al., 2020) and the Adriatic Sea and Coastal model (AdriSC) (Denamiel et al., 2019) for the Adriatic coast. Even within these systems, the actual prediction of a meteotsunami is difficult.

Though meteotsunamis occur near the Dutch coast, barely any research has been done to investigate them, as their consequences have not been significant yet. In literature, only two events have been recorded, namely the event on the 29th of May 2017 (Sibley et al., 2020) and the 3rd of January 2012 (Verhagen et al., 2014). Because of this lack of research, very little is known about their frequency or properties. To increase awareness and knowledge on meteotsunamis near the Dutch coast, this research investigates "The Identification and Generation of Meteotsunamis on the Southern North Sea".

First, the state of the art on meteotsunamis is presented via a literature review in chapter 2. Based on this literature review, four research questions have been formulated to investigate the topic of this thesis. The methods to answer these questions are presented in chapter 3. The four research questions will be presented and shortly elaborated in the next few paragraphs.

Research Question 1) How frequently do meteotsunamis occur on the Southern North Sea?

The first part of the thesis will focus on the frequency of meteotsunamis near the Dutch coast, by identifying meteotsunamis that have passed the Dutch coast in recent years. This identification will consist of an oceanic part, presented in chapter 4, and an atmospheric part, presented in chapter 5.

Research Question 2) What are the atmospheric conditions generating meteotsunamis on the Southern North Sea?

The atmospheric component is not only relevant for identification purposes. An important part of gaining knowledge on Dutch meteotsunamis is an understanding of their atmospheric component. To answer this question, two parameters will be researched: the shape of the front and the height of the pressure jump generating the meteosunami. This will be presented in chapter 5.

Research Question 3) What are the characteristics of meteotsunamis on the Southern North Sea?

To gain further knowledge on the oceanic component of meteotsunamis on the Southern North Sea, the identified events are characterized. In this characterization, the angle of incidence, the wave period, and the wave height of a list of selected events will be computed. This characterization is performed in chapter 6. After the events have been characterized, the final part of the thesis, chapter 7, focuses on the propagation of meteotsunamis by investigating the most important amplification mechanism for meteotsunamis for the identified events, namely Proudman resonance. This led to the formulation of the last research question.

Research Question 4) What role does Proudman resonance play in meteotsunami amplification on the Southern North Sea?

Proudman resonance is one of the most important amplification mechanisms for meteotsunamis (Monserrat et al., 2006). Therefore, the influence of this mechanism near the Dutch coast is investigated in question 4. The results of this research are presented in Appendix I.

After all the results have been presented, they are interpreted and discussed in chapter 8. Then to finalize the thesis, in chapter 9 and chapter 10 the answers to the research questions will be summarized and the recommendations for future work will be presented.

2

Literature review

2.1. Acquisition of Elevation Data for Meteotsunami Identification

Data from tide gauges is most commonly used when classifying waves. These measure sea-level elevation over varying time scales, depending on the country that is maintaining them. Fortunately, many tide gauges are deployed in the Southern North Sea near harbors, popular beaches, and places of interest for oceanographic studies (Williams, 2019). In areas where in situ measurements are scarce or difficult to access, remote sensing options, like Coastal High-Frequency (HF) radars, can be a solution. These are land-based remote sensing instruments that provide data at both high spatial and temporal resolutions. They use the principle of backscattering of electromagnetic signals by the sea surface (Rossi et al., 2021). These Coastal HF radars have been used to identify meteotsunamis and were even part of the first discovered meteotsunami in the West-African region (Dzvonkovskaya et al., 2019).

As stated in the introduction, meteotsunami research has already developed much further in regions more prone to their hazards, such as the Mediterranean (Šepić et al., 2012), the Australian west coast (Pattiaratchi and Wijeratne, 2014), the eastern Yellow Sea (Kim et al., 2021b), the Gulf of Mexico (Olabarrieta et al., 2017), and even the United Kingdom (Ozsoy et al., 2016). In these areas, the sea level elevation data from tide gauges is used to detect meteotsunamis. The sampling intervals at these tide gauges differ per research, varying from 1 minute (Pattiaratchi and Wijeratne, 2014) to 15 minutes Williams et al. (2019). Previous research on the Southern North Sea also used sampling intervals from 1 minute near the French coast (Tappin et al., 2013) to 15 minutes near the English coast (Williams et al., 2019). These 1-minute sampling intervals were achieved by measurements every 15 seconds that were integrated (SHOM DOPS/HOM/MAC, 2018). The English tide gauges present mean values over these 15-minute windows (Holgate et al., 2012). However, all research that uses sampling intervals of 15 minutes states that shorter sampling intervals would benefit their results (Ozsoy et al., 2016).

2.2. Classification of Ocean Waves

The measured sea-level fluctuations are caused by a broad spectrum of wave types, including tsunamis. A general understanding of these wavetypes is necessary to separate meteotsunamis from the others. In Figure 2.1 an overview of the most commonly occurring waves in coastal waters is given. In this overview, the tsunami waves are shown with periods between 2 minutes and 2 hours (Williams, 2019).

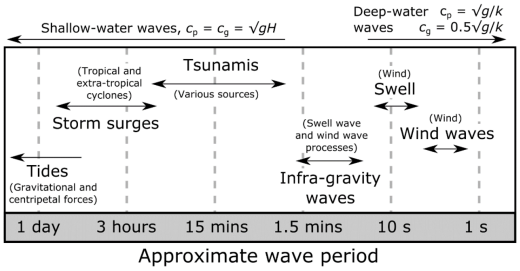

Figure 2.1: An overview of the full spectrum of wave classes and their periods. The top of the figure shows the distinction between shallow- and deep-water waves. The source mechanisms for each wave class are added in brackets (Williams, 2019).

2.2.1. Deep- and Shallow-Water Waves

The top of the figure shows an important distinction in wave classification: the distinction between deep-water waves and shallow-water waves. If a wave is classified as either a deep- or shallow-water wave, the governing equations to calculate parameters such as phase speed (c) and group speed (c_g) simplify. If a wave falls within the deep-water regime, the wave speed is independent of the depth, whereas, in the shallow-water regime, the wave speed is fully dependent on the depth and independent of the wave properties. To determine whether a wave is a shallow- or deep-water wave, the limits are defined as follow:

$$kd << 1 \qquad \text{Shallow water} \tag{2.1}$$

$$kd = O(1) \qquad \text{Intermediate water} \tag{2.2}$$

$$kd >> 1 \qquad \text{Deep water} \tag{2.3}$$

In these limits, k represents the wave number (equal to $2\pi/L$), and d the water depth. Via the phase velocity, k and T can be related (Equation 2.4).

$$c = \frac{L}{T} = \frac{\omega}{k} \tag{2.4}$$

Here, c is the phase velocity, L the wavelength, T the wave period, ω the angular frequency (equal to $2\pi/T$), and k the wave number. As shown, k is proportional to T. Therefore the waves with a longer period are in general shallow water waves, whereas the short-period waves are in general deep water waves.

2.2.2. Wave Classes

Waves can be classified even further, based on their source mechanisms. The shortest waves in Figure 2.1 are wind and swell waves, both of which are ocean surface gravity waves. The main difference between wind and swell waves is that wind sea waves are generated by local winds, while swell waves can propagate over entire ocean basins (Semedo et al., 2014). Both have periods between one and thirty seconds, significantly smaller than tsunami periods (Sorensen, 2006).

Wind and swell waves travel in packets. The oscillations of these packets can form groups, known as wave groups. These wave groups can generate waves with longer periods than the wind and swell waves themselves, called infra-gravity waves (IG waves). IG waves are long-period surface gravity waves, ranging from 0.005 Hz to 0.05 Hz. These correspond to wave periods between 20 and 200 seconds. In general, IG waves only become significant in shallow water due to (near) resonant nonlinear interactions with the sea-swell waves. They contribute to various nearshore processes, such as sediment transport and beach erosion. Due to their long periods, IG waves can also trigger harbor seiching (Rijnsdorp et al., 2021), an amplification mechanism also found in meteotsunami amplification. Apart from their mutual relation to seiching, IG waves and meteotsunamis can also overlap in period. The shortest tsunami waves have periods of 120 seconds, while the longest IG waves have periods of 200 seconds. This shows that classification based purely on the wave spectrum is difficult, necessitating the use of other classification methods based on the source mechanisms.

The other waves that overlap in period with tsunami waves are storm surges. Similar to meteotsunamis, storm surges are meteorologically forced long wave motions. The source of a storm surge is either a mid-latitude storm or a tropical cyclone. The waves are formed as a result of extreme wind stress, accompanied by a change in atmospheric pressure. Specifically, the wind stress results in a wave period that is generally longer than tsunami waves, with periods of up to several hours (Bode and Hardy, 1997). Differentiation between meteotsunamis and storm surges is done via their main source mechanism. For storm surges, this is extreme wind stress (Bode and Hardy, 1997). For meteotsunami, this is a change in atmospheric pressure (Monserrat et al., 2006).

The wave class with the longest period in Figure 2.1 is the tide. Due to the gravitational attraction of the moon and sun, most places on earth have two high and low tides, causing a lower and higher sea level near the coast. If these high and low tides are approximately the same height every time, the tide is classified as a semidiurnal tide (Sumich, 1992). The Southern North Sea experiences such a semidiurnal lunar tide, with a period of 12.4 hours, half a lunar day (Howarth, 2001).

2.3. Generation of Meteotsunamis

Tsunamis can be caused by several source mechanisms, such as seismic events, volcanic eruptions, or even extraterrestrial impacts (Tappin et al., 2013). The source mechanism for a meteotsunami specifically is a sudden change in atmospheric pressure (Monserrat et al., 2006). The atmosphere and ocean surface interact via the "inverted barometer effect" (Jeffreys, 1916). This mechanism represents a direct proportionality between the sea-level elevation and the negative gradient in air pressure. As a result, a 1 hPa drop in air pressure leads to a 1 cm sea-level elevation increase and to a 1 cm sea-level elevation decrease for a 1 hPa jump in air pressure (Gravalon et al., 2021). This principle is visualised in Figure 2.2.

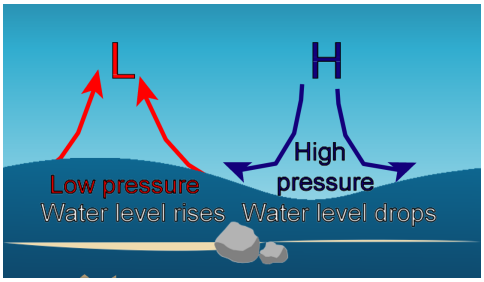

Figure 2.2: Inverted barometer effect explained (Gravalon et al., 2021). On the left, a decrease in air pressure shows an increase in water level, and on the right the inverse occurs.

These pressure changes are responsible for the generation of meteotsunami, though they are no bigger than a few hPa (Monserrat et al., 2006). There have been meteotsunami events registered with pressure jumps between 1-2 hPa in Japan (Asano et al., 2012), between 1-3 hPa in the Adriatic sea (Horvath et al., 2019), and between 1-3 hPa in the area of interest; the Southern North Sea (Gusiakov, 2020). Based solely on the inverted barometer effect, no significant wave will be generated. However, over its trajectory, the tsunami wave grows via several amplification mechanisms. This thesis focuses on the most important mechanism, Proudman Resonance. The other potential amplification mechanisms are shortly explained in Appendix A.

2.3.1. Proudman Resonance

The foremost mechanism in the growth of meteotsunamis is Proudman resonance. Proudman resonance occurs when the atmospheric forcing speed equals the shallow-water wave speed. This atmospheric forcing speed represents the speed at which the pressure disturbance, responsible for the meteotsunami generation, travels. Since this disturbance occurs at sea level (Piecuch and Ponte, 2015), the atmospheric forcing speed is also measured at sea level. The equality between the atmospheric forcing speed and the shallow water wave speed is best described by the Froude number (Equation 2.5) (Proudman, 1929):

$$Fr = \frac{U}{\sqrt{gh}} \tag{2.5}$$

Here, Fr represents the Froude number, U is the atmospheric forcing speed, g is the gravitational constant, and h is the water depth. the term in the square roots represents the shallow-water wave speed. If these speeds are close, the Froude number becomes near one, causing a linear growth of the tsunami wave, known as Proudman resonance. This linear growth continues until the assumption of negligible wave height is broken. In the definition of Proudman resonance, several assumptions are made. These assumptions can be subdivided into oceanographic and atmospheric assumptions. The oceanographic assumptions contain the stillness of the water and the flat-bottom assumption, whereas the atmospheric assumptions contain a constant forcing speed, a constant forcing amplitude, and a few one-dimensional assumptions (Proudman, 1929). In practice, these assumptions rarely hold. Extensive research has been done on the influence of these assumptions not being met and their effect on the occurrence of resonance.

For the stillness of water, the biggest disturbance is the tide. Tides induce fluctuations in the shallow water speed, causing the overall wave speed to deviate from the atmospheric forcing speed, reducing resonance. The same generally holds for changes in water depth, even when not induced by the tide. However, if counter currents occur in combination with an elevation change, something called super-resonant growth can occur. When one phenomenon decreases the wave speed, while the other one increases it, mutual compensation occurs. This super-resonance has shown to produce growth 10% larger than strict Proudman growth (Williams et al., 2020). Other research found that interaction between the meteotsunami and the tide altered the wave amplitude by 17% (Choi et al., 2014).

As for the flat-bottom assumption, it was found that in the case of a gentle upward-sloping bathymetry, the Froude numbers stayed near one and shoaling occurred (Williams et al., 2020). Other research found that once the atmospheric disturbance travels from deep to shallow water, the peak in amplitude occurs at shallower water depths than the depths for which the Froude number is equal to exactly one. Small and fast pressure disturbances on a mild slope create a significant peak, whereas peaks with larger Froude numbers are found at slower-moving speeds and steeper slopes (Chen and Niu, 2018).

Regarding the atmospheric assumptions, the largest uncertainty is found in the computation of the atmospheric-forcing speed. In general, cross-correlation is used to calculate this atmospheric forcing speed. Cross-correlation compares the atmospheric front at two moments in time. The atmospheric information is turned into a grid, where each grid point contains information about a small part of the front. Then, the atmospheric conditions for the next moment are also turned into a grid. In this second grid, a grid cell with similar properties to a grid point in the first moment has to be located. This will give information about the location of that part of the front over time (Belušić and Strelec Mahović, 2009). A visualization of this method is shown in Figure 2.3.

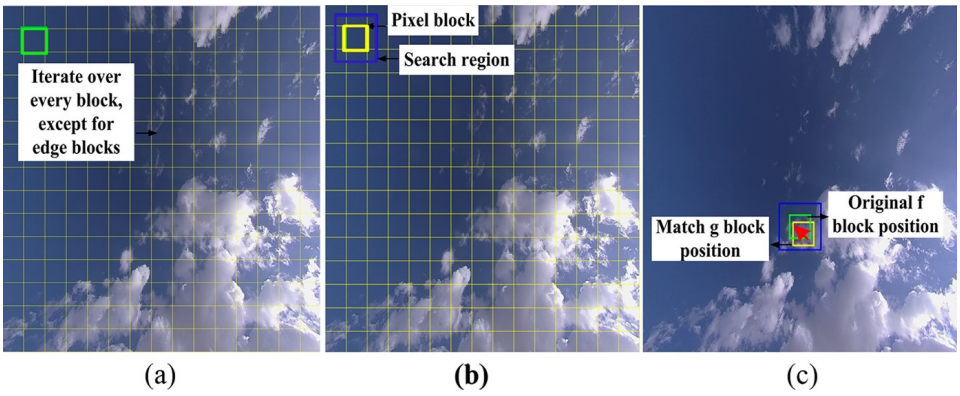

Figure 2.3: Explanation of cross correlation using clouds (Zuo et al., 2024). In figure (a) the cloud cover is turned into a grid. in (b) the next moment in time is compared and a search region is defined to find a pixel with similar properties to the selected pixel in figure (a). In figure (c) the original pixel (called f block) and the matching pixel (called g block) are shown.

For meteotsunamis, cross-correlation has been performed on satellite images of cloud tops in previous research (Belušić and Strelec Mahović, 2009). Other studies have performed cross-correlation on radar reflectivity. This radar reflectivity is calculated using the reflection of the water and ice particles. To minimize error estimation, the time difference between two consecutive images has been varied between 5 minutes and 1 hour (Wertman et al., 2014). The atmospheric forcing speed has also been correlated to more straightforward speeds, like the 500-hPa wind speed (Vilibić and Šepić, 2017). Further research even states that the mid-tropospheric wind speed can be used to approximate the atmospheric forcing speed (Markowski and Richardson, 2010).

Even when no assumptions for strict Proudman resonance are met, amplification still occurs. In literature, this is called near-Proudman resonance, which occurs at Froude numbers between 0.9 and 1.1 (Vilibić, 2008). More recent research has even shown that Froude numbers of 0.8 and 1.2 can still cause Proudman-like amplifications (Williams et al., 2020).

2.4. Identification of meteotsunamis

Information from the ocean and the atmosphere must be combined to identify a meteotsunami. Often, oceanographic data is used to select a potential event, and then the atmospheric conditions at that moment are reviewed to check whether they could have generated a meteotsunami. This section will discuss the identification methods in both fields.

2.4.1. Identification of the oceanic part via the classic approach

Generally, meteotsunamis are identified via one main method, referred to as the classic approach. In this approach, the elevation data is first filtered, and then an amplitude threshold is applied. The elevation data is often filtered with a Kaiser-Bessel window (Šepić et al., 2012), a Butterworth filter (Tappin et al., 2013), or a band-pass filtering (Williams et al., 2021). For the filters, the filter boundaries are determined by the shortest and longest wave period of meteotsunamis, 2 minutes (0.00833 Hz) and 2 hours (0.00014 Hz) (Monserrat et al., 2006). In cases where these filters did not produce satisfactory results, several studies performed a tidal analysis to filter out tidal components from the elevation data. This has been shown to produce an even clearer isolated peak at the moment of the meteotsunami (Pattiaratchi and Wijeratne, 2014). The leftover isolated signal is then further analyzed.

After signal filtering, the amplitude threshold is applied. In literature, the differentiation is made between an absolute and relative threshold (Monserrat et al., 2006). The absolute threshold is highly dependent on the ocean topography. This makes the absolute threshold highly region-dependent, fluctuating between 0.40 meters in wave height near Australia (Pattiaratchi and Wijeratne, 2014) to 5 centimeters in amplitude in the Eastern Yellow Sea (Kim et al., 2021b). For the Dutch coast, the only absolute threshold choices have been made by de Jong and Battjes (2004). They wrote about seiche events by atmospheric convection cells, that would now be classified as meteotsunamis. They take an absolute amplitude threshold of 0.25 meters to identify a seiche. Further absolute amplitude thresholds that could be relevant are found in the United Kingdom. Here wave height thresholds of 0.20 meters to 0.30 meters are often utilized (Lewis et al., 2023), which correspond to amplitude thresholds of 0.10 to 0.15 meters.

The relative threshold depends on the standard deviation of the dataset. Monserrat et al. (2006) was one of the first to define it as 3 to 4 times the standard deviation of the elevation data. However, more recent literature has proposed to increase the multiplication factor to 6 (Olabarrieta et al., 2017). Several studies apply both an absolute and relative threshold in their filtering methods (Dusek et al., 2019). An additional criterion to the thresholds to detect meteotsunamis, states that it has to be registered at at least two tide gauges to be classified as a meteotsunami (Lewis et al., 2023).

2.4.2. Identification of the oceanic part via Continuous Wavelet Analysis

Apart from the classic identification method, other studies apply Continuous Wavelet Analysis. The largest advantage of a wavelet analysis over a Fourier analysis, is its ability to show information about both the time and the frequency in the same analysis, while Fourier analysis can only show information on the frequency axis. (Picco et al., 2019).

Furthermore, to perform an FFT, the signal is divided into blocks over which the amplitude is averaged. Therefore, anomalies (like a meteotsunami) are smeared over the entire block length, troubling its detection. Reduction of the block length reduces the smearing but also decreases the frequency resolution of the Fourier analysis, an undesirable effect (GANESAN et al., 2004). This compromise between time and frequency resolution is resolved in wavelet analysis. The analysis is performed using a wavelet, a wavelike oscillation. This wavelet is slid along the signal, generating coefficients based on the similarity between the wavelet and signal. A high similarity results in high coefficients, and a low similarity in low coefficients. This process of sliding is repeated for multiple configurations of the same wavelet. This configuration is determined by a parameter called the scale. This parameter makes the change in time resolution per frequency possible, as each scale corresponds to a different frequency. Therefore, higher frequencies can have lower time resolutions and lower frequencies can have higher time resolutions. This differs from an FFT, where all frequencies have the same time resolution (Torrence and Compo, 1998)(Figure 2.4).

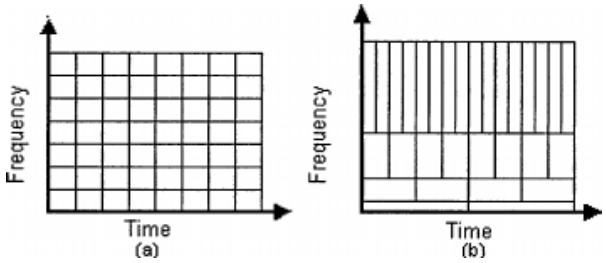

Figure 2.4: Difference in blocksize between an FFT (a) and wavelet analysis (b) (GANESAN et al., 2004). The blocks in the FFT all have the same size, resulting in the same frequency and time resolution. The blocks in the continuous wavelet analysis (b) have different sizes (because of the scales), and can thus vary in frequency and time resolution.

Since different scales generate different wavelet expansions, different wavelet coefficients are obtained per scale. Therefore, the right choice of scales will positively influence the results of a wavelet analysis. To choose the correct scales, the relation between scale and frequency needs to be understood. This relation is similar to frequency and period, as a lower frequency results in a wider wavelet and, thus a larger scale. Vice versa, a higher frequency results in a narrower wavelet and a smaller scale. Figure 2.5 shows an extension of Figure 2.4 to visualize the relation between period and scale.

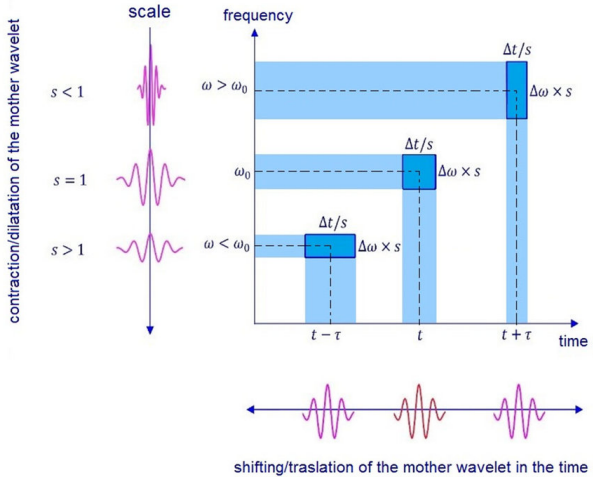

Figure 2.5: The relation between scaling and period explained (Magazù and Caccamo, 2018). As the scales increase, a narrower wavelet is compared to the original signal, shown at the x-axis. The case where s = 1 overlaps most with the original signal, and will result in the highest wavelet coefficients.

Even though the relation between frequency and period and frequency and scale are very alike, their exact relation differs by a given factor, called λ. λ depends on the choice of wavelet and therefore the relation between the scales and frequencies also differs for each wavelet.

The lower limit of the scales, called s_0 is equal to the Nyquist period, identical to Fourier. Thus, s_0 should correspond to a period equal to $2\delta t$. Since the elevation data is sampled at 15 seconds, the Nyquist period is twice that interval, resulting in 30 seconds. By multiplication of T_{nyq} with the relevant λ, the relevant s_0 per wavelet can be determined via Equation 2.6 (Torrence and Compo, 1998).

$$s_0 = T_{nyq} * \lambda \tag{2.6}$$

The larger scales are calculated as powers of 2, using s_0, via Equation 2.7.

$$s_j = s_0 2^{j\delta j}, \qquad j = 0, 1, ..., J \tag{2.7}$$

$$J = \delta j^{-1} \log_2 (N\delta t / s_0) \tag{2.8}$$

In Equation 2.7, N represents the length of the signal, δt is the sampling time, and s_0 is the lower limit of the scales. The final parameter in both equations is δj. δj determines the number of steps to reach the highest scale. The choice of δj has a lot of similarities to the choice of p in the Fourier analysis. Choosing it too low will result in too many scales, thus a lower frequency resolution. choosing it too large will decrease the reliability of the wavelet analysis.

2.4.2.1. Choice of wavelet

As the wavelet coefficients are determined by the coherence between the wavelet and the signal, a suitable wavelet will clarify the results. Even though choosing the correct wavelet might seem arbitrary, there are some guidelines for which wavelets to use in what situations, based on their properties.

Firstly, a wavelet can be either orthogonal or non-orthogonal. By the orthogonality of a wavelet, the overlap between sets of wavelets is described. If a wavelet is orthogonal, there is no overlap between wavelets, and each wavelet describes a discrete block in time. Therefore, orthogonal wavelets are linked to discrete wavelet analysis. In continuous wavelet analysis, the wavelets slide along the signal resulting in lots of redundant information. This redundancy means the wavelet will always be non-orthogonal regardless of the choice. (Torrence and Compo, 1998).

Secondly, a wavelet can be either real or complex. Like Fourier analysis, the real part of the transform will give information about the amplitude and the complex part of the phase. A complex wavelet gives amplitude and phase information, whereas a real wavelet only returns amplitude information. Therefore, a complex wavelet returns two coefficients, and a real wavelet only one. Phase information is beneficial if the analyzed signal contains two or more separate signals with different phases. In these situations, a complex wavelet would be superior. A benefit of a real wavelet over a complex wavelet is its ability to isolate peaks or discontinuities in the signal. (Torrence and Compo, 1998)

Thirdly, the width of the wavelet can influence the results of the analysis. Depending on the width of the wavelet, it will be more suitable for a higher frequency or time resolution. A wavelet that is wider in the time domain will give a worse frequency resolution and a narrower wavelet in the time domain will result in a better frequency resolution at the cost of the time resolution. As an example, two wavelets are shown in Figure 2.6b and Figure 2.6a, the Morlet wavelet (left) and the Mexican hat wavelet (right). The figure shows that the Morlet wavelet is narrower in the time domain and wider in the frequency domain, leading to a higher time and lower frequency resolution. For the Mexican hat wavelet, the inverse is true. (Torrence and Compo, 1998)

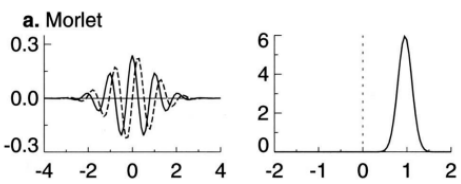

(a) The Morlet wavelet in the time domain (left) and frequency domain (right)(Torrence and Compo, 1998)

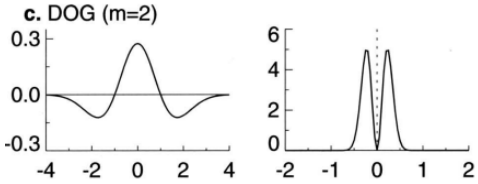

(b) The Mexican hat wavelet in the time domain (left) and frequency domain (right)(Torrence and Compo, 1998)

Figure 2.6: Comparison between the Morlet wavelet and the Mexican hat wavelet. In the time domain, the Morlet wavelet is narrower, thus the resolution in the frequency domain is better, resulting in a wider peak. Vice versa, the Mexican hat wavelet is wider in the time domain. this results in narrower peaks in the frequency domain and a worse frequency resolution.

Finally, the shape of the wavelet is interesting. As stated earlier, a higher correlation between the signal and the wavelet results in higher coefficients. Therefore a good fit in shape is beneficial. However, if the wavelet spectrum is the important conclusion of the analysis, the choice of the wavelet function is not critical, and similar qualitative results are obtained, regardless of the wavelet. (Torrence and Compo, 1998)

Generally, the Morlet wavelet is most suitable for geophysical processes (Torrence and Compo, 1998). This wavelet has also been used for the analysis of meteotsunamis in literature (Linares et al., 2016).

A second suitable wavelet, that has been used in the analysis of meteotsunamis is the Morse wavelet (Picco et al., 2019). These wavelets are complex-valued and only support the positive real axis. This wavelet is effective for analyzing discontinuities in a dataset. Therefore, it is deemed a suitable wavelet for meteotsunami detection. The Fourier Transform of the generalized Morse wavelet is shown in Equation 2.9 (Olhede and Walden, 2002).

$$\Psi_{P,\gamma}(\omega) = U(\omega) a_{P,\gamma} \omega^{P^2/\gamma} e^{-\omega^\gamma} \tag{2.9}$$

Here, $U(\omega)$ is the unit step, $a_{P,\gamma}$ is a normalizing constant, P^2 is the time-bandwidth product and γ determines the symmetry of the wavelet. P^2 is the parameter that is responsible for scaling the wavelet. citepLilly2009.

2.4.3. Identification of the atmospheric part

The final step to classify an event as a meteotsunami is the coupling of an atmospheric component. Meteotsunamis are always a consequence of mesoscale weather systems (Monserrat et al., 2006). These mesoscale weather systems are responsible for the pressure jumps resulting in the inverted barometer effect and the atmospheric forcing speeds resulting in Proudman resonance. As these pressure jumps are short, a small sampling interval is necessary to capture them. Unfortunately, most pressure data is sampled at 10-minute time intervals, with exceptions around the Mediterranean coast, where analog air pressure charts at 2 min resolution are available (Šepić et al., 2009). Since pressure jumps can be up to four times larger at 30 seconds than 10-minute sampling intervals (Vilibić, 2008), several methods are applied to overcome this undersampling. Some researchers adapt their pressure thresholds, using changes of plus or minus 1 mbar over 30 minutes or 3 mbar over 3 hours as a threshold (Monserrat et al., 2006). This does however not solve the issue.

Kim et al. (2021b) proposes the definition of a caution and warning zone in the relevant region. This caution zone consists of automatic weather stations (AWS) located offshore, that can be used for preliminary warnings. The weather stations in the warning zone are land-based and can be used to determine the propagation and direction of the pressure disturbance. To classify a disturbance as a potential source for a meteotsunami, the weather stations have to measure a pressure change that exceeds the set threshold of 1.5 hPa per 10 minutes. Furthermore, the disturbance has to propagate from at least one weather station in the caution zone to a weather station in the warning zone, since this means that the disturbance propagates towards shore, forming a potential danger.

Other research tries to overcome the oversampling by analysis of different parameters. The atmospheric pressure jumps can often be linked to precipitation events (Williams et al., 2021). Precipitating weather features are often linked to horizontal pressure gradients, and therefore fast pressure jumps (Johnson, 2001). This method fails to detect non-precipitation events, but can still form a solid basis for identification. Some research uses a categorization into four mesoscale systems, each with its criteria on whether a meteotsunami could have occurred. These systems are isolated cells, quasi-linear systems, non-linear clusters, and open-cellular convictions (Williams et al., 2021). Since precipitation data is available at much higher sampling frequencies, and could therefore be used as an alternative if the sampling intervals of the pressure data are too large.

Finally, several studies take a numerical approach, using atmospheric models, to resolve the undersampling issue of the sea level pressure data. Numerical modeling of meteotsunamis has already been performed in the Yellow Sea (Ha et al., 2018), the United States (Horvath and Vilibić, 2014), the Adriatic Sea (Šepić et al., 2009), and the Balearic Islands (Mourre et al., 2020). Near the Balearic Islands and the Adriatic Sea, this numerical modeling has been used to formulate meteotsunami prediction models, called AdriSC (Denamiel et al., 2019) and BRIFS (Mourre et al., 2020). The numerical modeling aims to decrease the time-step and increase the horizontal spatial resolution and vertical resolution in the first 2 kilometers above the earth's surface (Denamiel et al., 2019). The previously noted articles use the weather research and forecasting model (WRF) to run their numerical simulations. To model correct outputs, the right physical parameters have to be chosen. In Appendix C, the physical parameters of several articles modeling meteotsunamis are presented.

As stated, numerical modeling is beneficial to increase the horizontal spatial resolution of the area over which the pressure is reviewed. This resolution is determined by the horizontal grid spacing. For meteotsunamis, either two different grid spacings of 20 kilometers and 4 kilometers for the finer grid are used by Heo and Ha (2016), or three grid spacings, of 15 to 9 kilometers, 3 kilometers, and 1.5 to 1 kilometer by Denamiel et al.

(2019) and Horvath and Vilibić (2014). Most use a two-way nested horizontal grid spacing. If a grid is not two-way nested, the bigger outer grid is coupled to the smaller finer grid but does not receive any feedback from the smaller grid. A two-way nested grid does provide this feedback to the larger grid, and will therefore provide more accurate results. However, a two-way nested grid does make the simulation computationally heavier.

To determine the vertical resolution, vertical levels are used. These vertical levels determine the number of layers in the z-direction. In literature, they differ from 31 levels with the top at 50 hPa (Ha et al., 2018) to 81 levels with the top at 70 hPa (Horvath et al., 2018). The highest number of vertical levels used in the literature is 97 levels, with no top defined (Mourre et al., 2020). The final motivation for numerical modeling was the decrease in timestep. Mourre et al. (2020) decreased the timesteps to an output time of 2 minutes, with a computational time step of 10 seconds. Horvath and Vilibić (2014) used an even smaller computational time step of 6 seconds, with no noted output time.

3

Methodology

3.1. Sea Elevation Data

The identification of meteotsunami waves is done via the sea level elevation data at several locations in the North Sea over time. Data from eight tide gauges is used, all of which has been collected and distributed by Rijkswaterstaat (Rijkswaterstaat). These stations are located at the coordinates presented in the table below and visualized in Figure 3.1.

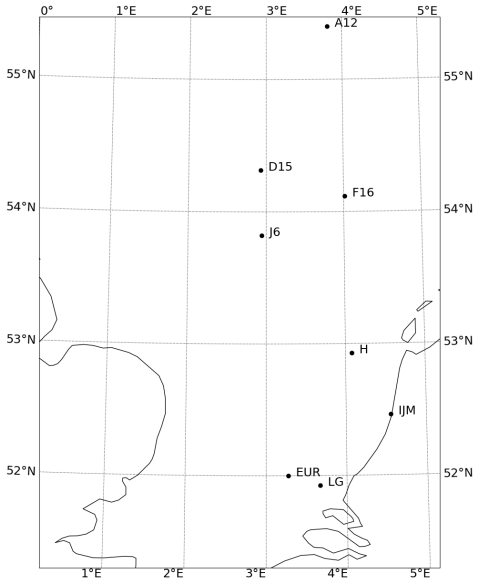

Figure 3.1: Locations of the stations on the map.

Station	Latitude [°]	Longitude [°]	Depth [m]
A12	55.400	3.810	29.91
D15	54.317	2.933	39.98
F16	54.116	4.011	46.04
J6	53.823	2.944	36.00
H	52.929	4.076	26.57
IJM	52.463	4.555	7.12
EUR	51.998	3.275	31.27
LG	51.926	3.670	23.70

Table 3.1: Coordinates of the measurement stations and the depths at those locations with respect to mean sea level.

These stations provide sea level data at a sampling frequency of 0.06 Hz, equal to a sampling interval of 15 seconds. This sampling frequency conforms to the prescribed sampling interval for meteotsunamis (Intergovernmental Oceanographic Commission, 2006). The set contains data from 2009 up to 2018. However, the data from the year 2009 contains multiple periods of missing points and has been excluded from this research. The remaining sea level elevation data is low-passed filtered at $f < 0.025 Hz$ in continuous blocks of 10 minutes (Kamminga, 2001). These blocks are concatenated to form the final dataset (Reniers et al., 2021).

3.2. Bathymetry Data Southern North Sea

The corresponding local water depth data is necessary to determine the characteristics and the propagation of the meteotsunami. This water depth is obtained from the European Marine Observation and Data Network (EMODnet) Bathymetry database (EMODnet Bathymetry Consortium, 2022), which has been composed of water depth data acquired up to December 2022. The data consists of bathymetric survey data from 64 data providers, Landsat 8 and Sentinel satellite images, and integrations of GEBCO 2022 and IBCAO V4. The resolution of the dataset is $\frac{1}{16} * \frac{1}{16}$ arc minute of longitude and latitude, which corresponds to circa $115 * 115$ meters at the equator.

From this database, the water depth data is acquired for latitudes between 47 and 60 degrees North and longitudes between 6 degrees West and 10 degrees East. Furthermore, the data resolution is downsampled to a resolution of $1000 * 1000$ meters, since this is consistent with the resolution of the atmospheric simulation. An overview of the bathymetry data is presented in Figure 3.2.

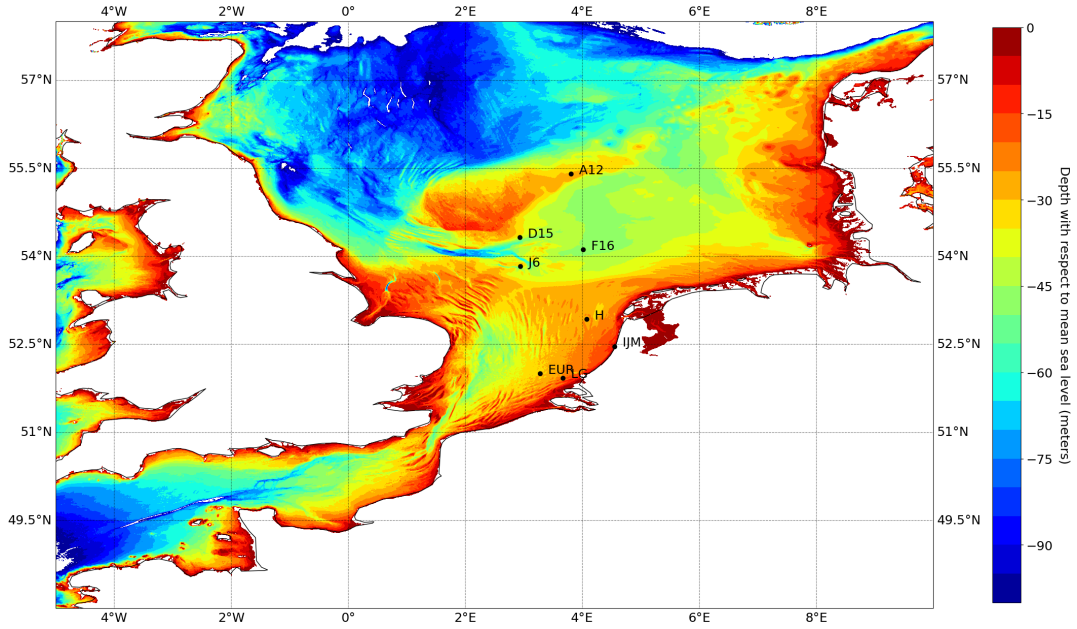

Figure 3.2: Bathymetry in meters below mean sea level, up to date until December 2022 (EMODnet Bathymetry Consortium, 2022). Downsampled to $1 * 1km$ resolution.

3.3. Numerical Modeling of the Atmospheric Parameters

As stated in the literature review, sea level pressure data with a sufficiently high temporal resolution for the identification of meteotsunamis is scarce. Therefore, the choice is made to numerically model the atmospheric conditions using the Weather Research and Forecasting (WRF) model. This model is used to dynamically downscale the ERA5 dataset (Hersbach et al., 2020), to both the spatial and temporal scales that are applicable for meteotsunami detection.

The full name list of input parameters needed to run the WRF model is added in Appendix B, the most relevant of which are shortly elaborated on. Firstly, the physical parameters relevant to the purpose of this research have to be established. Using Appendix C, the physical parameters in Table 3.2 have been selected.

Microphysics	Morisson 2 (Morrison et al., 2005)
Longwave radiation	RRTMG (Mlawer et al., 1997)
Shortwave radiation	RRTMG (Mlawer et al., 1997)
Planetary boundary layer	MYNN (Nakanishi and Niino, 2006)
Surface layer	ETA (Janjić, 1994)
Land surface model	Noah LSM (Ek et al., 2003)
Cumulus	Kain-Fritsch (Kain and Kain, 2004)

Table 3.2: Physical parametrization selected for the WRF model.

Additionally, the horizontal and vertical scales of the model are defined. For the vertical levels, 80 levels with a top at 50 hPa are used, consistent with Horvath et al. (2018). The relevant horizontal grid spacing depends on the minimum possible wavelength of the meteotsunamis. To calculate the minimum wavelength, the shallow water wavelength is used.

the shallow water wavelength can be used if the wavenumber k times the waterdepth d is well below one, following Equation 2.1. This is proven via Fenton's approximation (Equation 3.1) (Fenton and McKee, 1990) is applied.

$$kd \approx \alpha(tanh(\alpha))^{-\frac{1}{2}} \tag{3.1}$$

$$\alpha = k_0 d = \frac{\omega^2 d}{g} \tag{3.2}$$

Here k is the wave number, k_0 the deepwater wave number, d the water depth, g the gravitational constant and ω the angular frequency, equal to $2\pi/T$. To validate the shallow water conditions, the maximum kd should still be far below 1. This maximum kd is found when the shortest wave period and the largest water depth are combined. In the area of interest, the largest water depth is approximately 50 meters. Furthermore, the shortest period for a meteotsunami is 120 seconds. Following, Equation 3.1, these parameters would result in a kd of 0.11. This means that shallow water conditions have been verified. In shallow water, the wave speed is computed via Equation 3.3, where h is the water depth.

$$c_{shallow} = \sqrt{gh} \tag{3.3}$$

Since c is equal to L/T, the wavelength in shallow water can be calculated via Equation 3.4.

$$L_{shallow} = T\sqrt{gh} \tag{3.4}$$

Combining the shortest meteotsunami wave period (120 seconds) and the local depth leads to wavelengths around 2 kilometers over the entire basin. Generally, this resolution should suffice, except for certain shallower zones in the Southern North Sea. Therefore, the choice is made to use a reduced grid spacing of 1 kilometer.

The reanalysis data (the ERA5 dataset (Hersbach et al., 2020)) is sampled at a horizontal spacing of 30 kilometers. To transition smoothly toward the chosen 1 kilometer grid spacing, three domains are implemented, based on literature. These three domains have a horizontal grid spacing of 9 kilometers for the outer domain, 3 kilometers for the middle domain, and 1 kilometer for the finest scale. The domains are two-way nested, meaning the finer grid outputs are used as feedback for the coarser grid, and vice versa (Soriano et al., 2004).

It is beneficial to have the eight tide gauge locations within the finest domain, in order to properly link the outputs of the WRF model to the elevation data from these gauges. Therefore, the latitude boundaries of the finest domain are set from 51.272274 to 55.471222 degrees north, and the longitudinal boundaries at -0.01132202 and 5.309204 degrees east. This results in a grid of 220 cells West-East by 270 cells South-North. This is shown in Figure 3.3, together with the middle and coarsest domain, including their respective boundaries and cell counts.

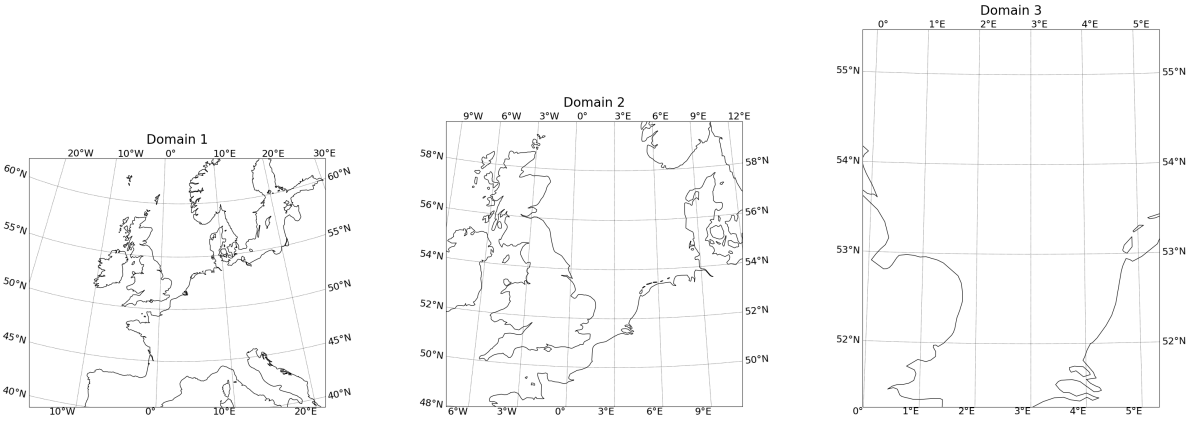

(a) Coarsest domain, with boundaries at 40.280525 to 63.143723 degrees north and -16.130157 to 21.493622 degrees east. A grid of 331 cells West-East by 454 cells South-North.

(b) Middle domain, with boundaries at 48.133255 to 59.637108 degrees north and -7.409851 and 10.9036255 degrees east. A grid of 346 cells West-East by 409 cells South-North.

(c) Finest domain, with boundaries at 51.272274 to 55.471222 degrees north and -0.01132202 and 5.309204 degrees east. A grid of 220 cells West-East by 270 cells South-North.

Figure 3.3: The three nested domains used for the numerical simulation in WRF, which have a horizontal grid resolution of 9, 3 and 1 kilometer for the outermost, middle, and innermost domain, respectively.

Finally, the output time to which the hourly ERA5 data should be downscaled is determined. As the shortest wave periods for meteotsunamis are equal to 2 minutes, the downscaled pressure data is also saved every 2 minutes. An integration time of 15 seconds is used to achieve this output time.

3.4. Preprocessing of the Elevation Data

In order to filter out measurement errors, the obtained sea level elevation dataset is preprocessed. At certain time intervals, the tide gauges fail to record measurements. At these moments, the output plateaus the last measured elevation, resulting in a sudden jump once measurements restart, as shown in Figure 3.4.

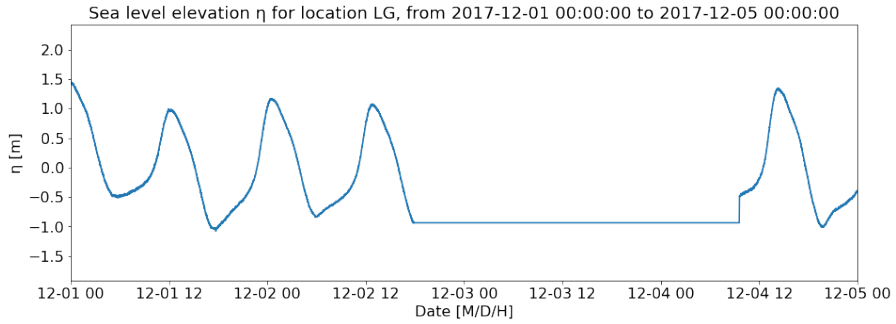

Figure 3.4: Example of faulty outputs of the measuring instruments for location LG at the beginning of December 2017.

These constant outputs are filtered out via a difference function between two consecutive values. A difference equal to zero could mean that the data has plateaued and is faulty. Unfortunately, the instruments record the sea level elevation in meters at only two decimal places, so the output frequently does not change over a single timestep. Thus, labeling all zero outputs of the difference function as a measurement error leads to the unnecessary removal of a lot of good data.

Additionally, the signal filtering to remove irrelevant wave types, mentioned in subsection 2.4.1, can only be applied when the signal length is at least as long as the longest relevant wave, which is a wave that can skew the amplitude filtering. For this research, this wave is formed by the spring-neap tidal cycle, with a period of two weeks. Therefore, if the signal is interrupted due to the removal of faulty data, these longest waves can not be filtered out, skewing the amplitude threshold filtering. This calls for a selection procedure based on the length of the consecutive constant output, as follows:

- If the stagnant output lasts shorter than 5 minutes, it is difficult to differentiate between faulty outputs and constant outputs caused by the low significance level. Accordingly, stagnant outputs shorter than 5 minutes are linearly interpolated to replace the faulty elevation data.
- If the stagnant output lasts between 5 minutes and half an hour, it is highly likely that this is caused by faulty measurements. Unfortunately, removing these faulty measurements could render several portions of the dataset unusable for signal filtering, because at least two weeks of consecutive data is needed. Therefore, it is beneficial to linearly interpolate these constant outputs before signal filtering, and to delete them once the irrelevant wavetypes have been filtered out.
- If the constant output is longer than half an hour, linear interpolation is no longer a good approximation of the missing elevation data, and the data is removed before the signal filtering.

3.5. Identification of the Oceanic Component of Meteotsunamis on the Southern North Sea

The oceanic component of meteotsunamis near the Dutch Coast is first analyzed using the classic identification approach for meteotsunamis. This includes a band-pass filtering step, an amplitude threshold filter, and a multiplicity principle. These filters will result in a list of potential events, out of which a few are selected. The selected events are subsequently reviewed using a Continuous Wavelet Analysis, to verify the stations at which the event was flagged. This results in a final list of selected meteotsunami events, including the locations at which these events were measured.

3.5.1. Band-Pass Filtering of the Elevation Data

The first step of the classic identification approach consists of signal filtering. In this research, a band-pass filter is applied to the data, using a Fast Fourier Transform (FFT) and a subsequent Inverse Fast Fourier Transform (IFFT). The boundaries of this filter are determined by the wave period of meteotsunamis. In Section 2.2, it was established that this period lies between 2 minutes and 2 hours, corresponding to frequencies between 0.008 and 0.00014 Hz. Setting these frequencies as the filter boundaries has the advantage that all potential meteotsunamis are included. Unfortunately, these boundaries also include several other wave types, because their wave periods overlap with meteotsunami wave periods. This research explores a narrower frequency band for the identification of meteotsunamis, specifically by setting the lower frequency boundary of the filter at a period of 30 minutes (instead of 2 hours), corresponding to a frequency of 0.0005 Hz. The upper frequency boundary is left at a period of 2 minutes, corresponding to 0.008 Hz. All waves with frequencies outside the set boundaries are removed from the elevation data.

As a consequence of the preprocessing steps, the elevation data is composed of several subsets of consecutive data. Before the band-pass filter is applied, these subsets are padded with constant values at the edges (Pywavelets, 2024). This padding prevents the occurrence of edge effects, caused by the sudden elevation cutoff at the edge of a subset. These edge effects show up in the filtered elevation data as a sudden elevation peak that could be misinterpreted as a meteotsunami. The constant is chosen to be equal to the last value at the given edge. Equal amounts of data points are added on both edges of the subset until the total length of the subset is equal to the next power of two (Torrence and Compo, 1998). After the FFT and IFFT are performed, the padding is removed from the dataset.

As stated in Section 3.4, the band-pass filtering can only be applied for time series consisting of at least two weeks of consecutive good data, in order to filter out the longest relevant waves. The subsets of consecutive data shorter than two weeks are therefore removed before the band-pass filtering. Afterwards, the neighboring subsets are concatenated and the removed subsets are replaced by zeros, to prevent misinterpretation of the correlating dates.

3.5.2. Threshold Filtering

After the band-pass filtering, increasingly distinct peaks become visible in the elevation data, indicating potential meteotsunamis. An amplitude threshold is set to detect these distinct peaks in the data. As stated in subsection 2.4.1, this threshold can be either absolute or relative. To limit the results of the threshold filtering to the peak amplitudes of potential meteotsunamis, the elevation data is down-sampled to daily maxima. Per station, the dates are flagged if their daily maximum exceeds the set threshold. A limitation of this approach is that it can not flag multiple potential meteotsunamis on the same date at the same location.

Based on the literature, two absolute and two relative thresholds are found, that could be applicable to detect meteotsunamis on the Southern North Sea:

- An absolute 0.25-meter amplitude threshold, based on de Jong and Battjes (2004)
- An absolute 0.10-meter amplitude threshold, based on Lewis et al. (2023)
- A relative 4σ amplitude based on Monserrat et al. (2006)
- A relative 6σ amplitude based on Williams et al. (2021)

Here σ represents the standard deviation of the dataset. The calculations of σ and the relative thresholds for each year and location are shown in Section D.1. These relative thresholds are generally much smaller than the absolute thresholds. All four thresholds are applied to the elevation data to draw conclusions on the most appropriate choice.

3.5.3. Multiplicity Principle

Apart from the band-pass and threshold filtering, an additional criterion is applied to improve the quality of the list of potential meteotsunamis. By utilizing the resonant properties of meteotsunamis, they can be distinguished from other waves that surpass the threshold as well. Given that meteotsunami generation is a resonant process, the wave grows as it travels over increasing distance. Therefore, the elevation increase should be detected at multiple tide gauges. As a result, the amplitude threshold should be exceeded in at least two locations on the same date to be included as a potential meteotsunami (Dusek et al., 2019). This multiplicity principle does not account for meteotsunamis that occur overnight, as they could be flagged by two stations on two separate days without being included.

This principle is validated for the elevation dataset using two known meteotsunamis. These known meteotsunamis occurred on the 3rd of January 2012 (Verhagen et al., 2014) and the 29th of May 2017 (Sibley et al., 2020). Applying both the threshold filtering and the multiplicity principle leads to the results in Table 3.3 and Table 3.4.

2012	A12	D15	F16	J6	H	IJM	EUR	Count
2012-01-03	1	0	0	1	0	1	0	3
2012-01-22	1	1	0	0	0	0	0	2
2012-08-15	0	0	0	0	1	1	0	2

Table 3.3: Dates where the daily maxima of two or more stations exceeded the absolute threshold of 0.10m in the year 2012.

2017	A12	F16	J6	H	IJM	EUR	LG	Count
2017-02-12	1	1	0	0	0	0	0	2
2017-05-29	0	0	0	1	1	1	1	4

Table 3.4: Dates where the daily maxima of two or more stations exceeded the absolute threshold of 0.10m in the year 2017.

On the 3rd of January 2012, the elevation data exceeded the set threshold at three different stations, and at four stations on the 29th of May 2017. An additional observation supporting the chosen multiplicity principle is the locations of exceedance on the 29th of May 2017. The four exceedances occur at the stations closest to the coast, in line with the expected growth due to amplification mechanisms. Thus, it is concluded that the multiplicity principle is a valid filtering criterion for meteotsunami detection that will be used to identify meteotsunamis in this research.

3.5.4. Visual Inspection

The dates on which the amplitude threshold was exceeded and on which the multiplicity criterion was passed are visually inspected. The visual inspection is used as an additional step to filter out faulty measurements, that were not removed via the applied preprocessing method. Possible errors include singular measurement errors, such as a disturbance by a collision of floating objects. An example of such a disturbance is presented in Figure 3.5.

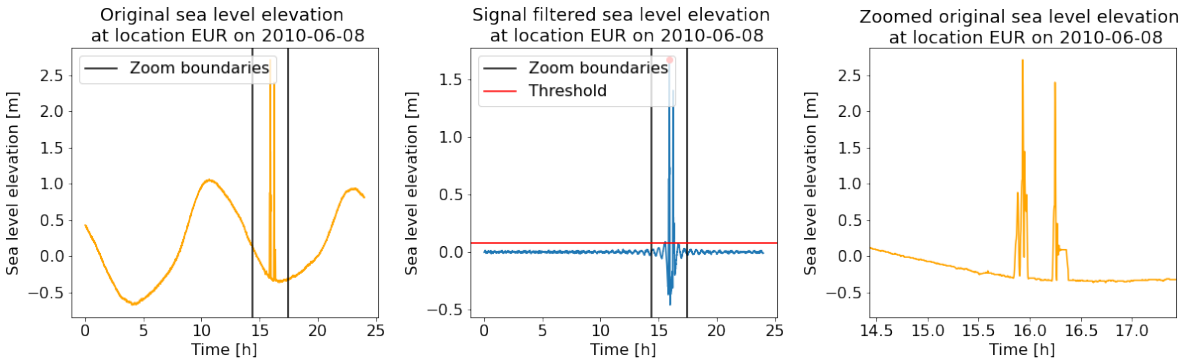

Figure 3.5: False flag due to a disturbance in the measurement, at location EUR on the 8th of June 2010. The left figure shows the original data, with the measurement error. The middle figure shows the band-pass filtered signal of this date. Here the measurement error looks quite similar to a meteotsunami, thus making filtering difficult. The black vertical lines in both figures represent the boundaries of the zoom in the right figure. This zoom emphasizes that the disturbance is indeed a measurement error, and not a meteotsunami.

A second category of faulty measurements that have yet to be filtered out are spontaneous large fluctuations, presented in Figure 3.6. These measurement errors are filtered out via visual inspections as well.

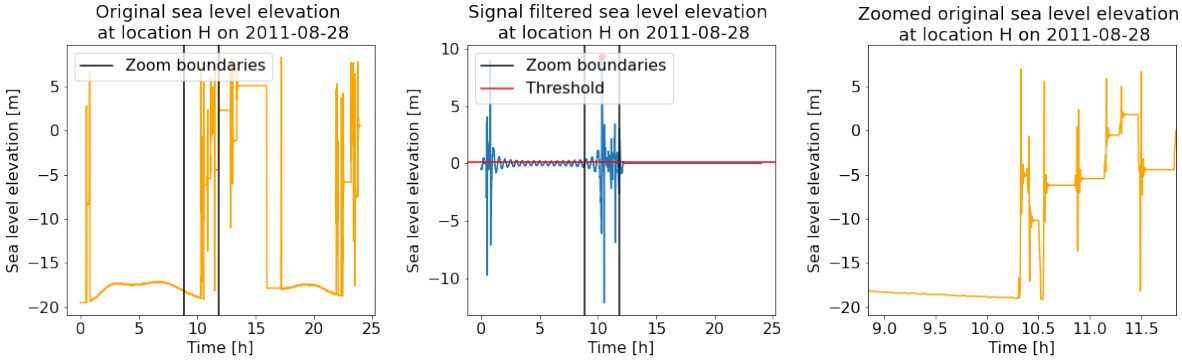

Figure 3.6: False flag due to large false fluctuations in the measurement, at location H on the 28th of August 2011. The left figure shows the original dataset, with clear errors in the elevation data. In the band-pass filtered dataset (middle), these disturbances are again less recognizable. However, given the excessive magnitude of the elevation, these errors can still be identified from these figures. The black vertical lines in both figures represent the boundaries of the zoom in the right figure. This zoom emphasizes that this data is indeed caused by malfunctioning equipment.

Situations similar to Figure 3.5 and Figure 3.6 are classified as false flags, and removed from the list of flags. Removal of these stations can cause the event to only occur at one station, thus not satisfying the multiplicity principle. Consequently, the event is removed from the list of potential meteotsunamis.

In addition to filtering out faulty measurements, visual inspection is used to differentiate between meteotsunamis and other large waves that exceed the threshold. A meteotsunami is characterized by a distinct peak isolated from the rest of the elevation data. Thus, the flag is removed if no isolated peak shows, an example of which is demonstrated in Figure 3.7.

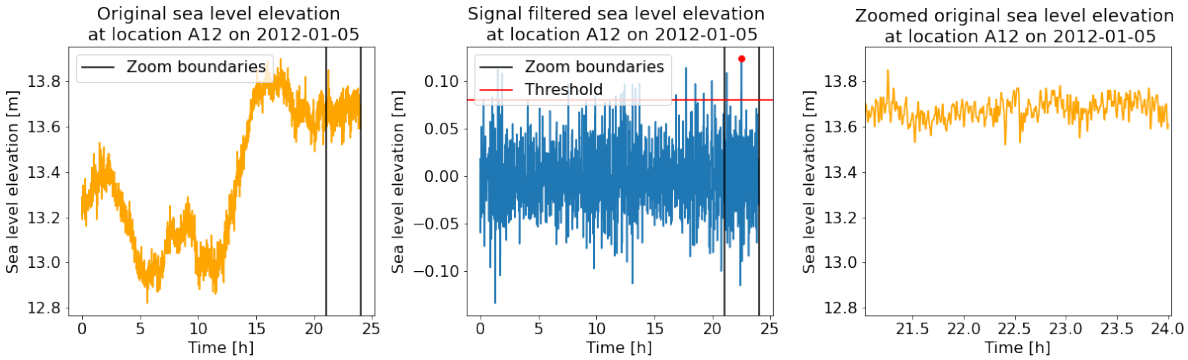

Figure 3.7: Flag without characteristic isolated peak, at location A12 on the 5th of January 2012. The left figure shows the original data, which is very noisy, and does not show a clear disturbance that is isolated from the rest of the data. The middle figure shows the filtered data, which contains a lot of threshold exceedances, aside from the maximum one. This is an indication that the exceedance is not caused by a meteotsunami. The black vertical lines represent the boundaries of the zoom presented in the right figure. This zoom emphasizes the absence of an isolated peak that would indicate the presence of a meteotsunami.

3.5.5. Block Diagram of the Classic Approach

The previously described identification method is visualized in a block diagram in Figure 3.8 on the next page, to give an insightful overview of the method.

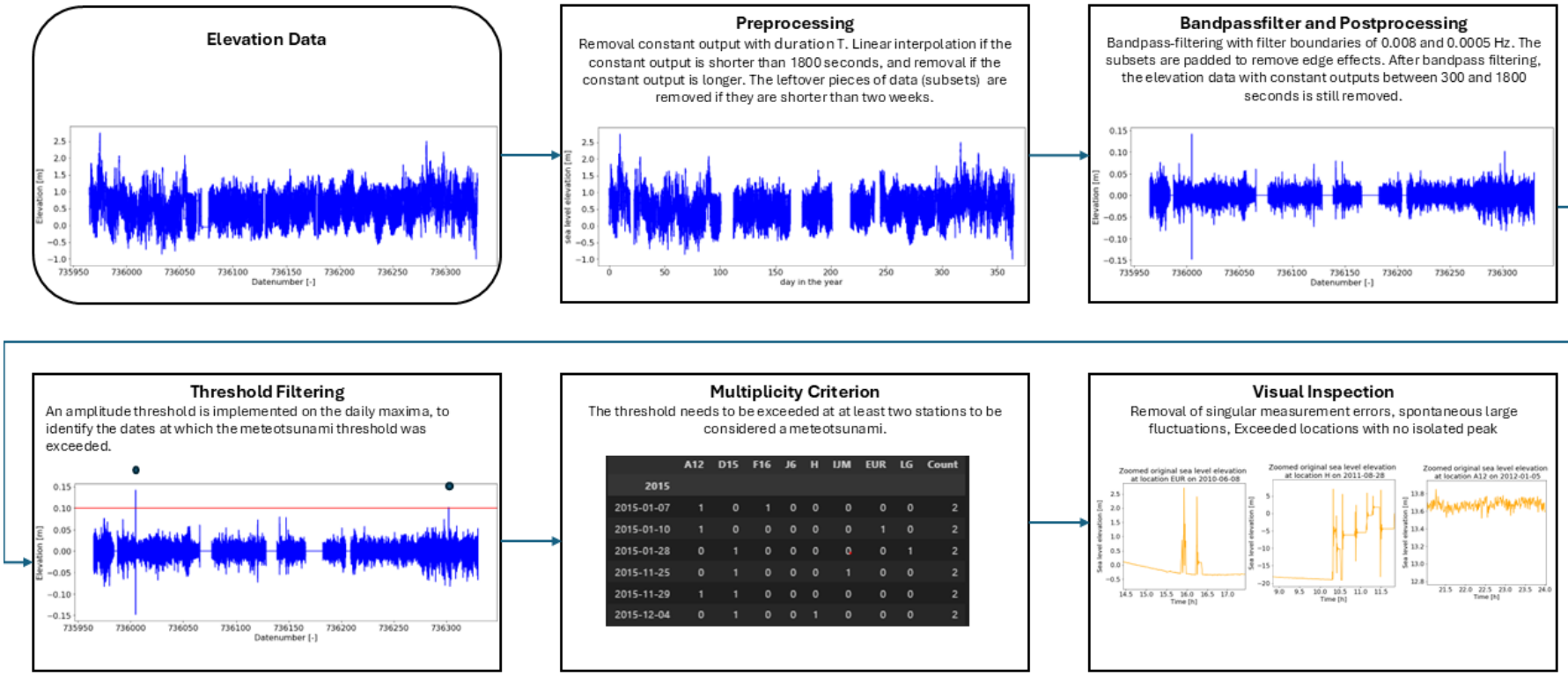

2015	A12	D15	F16	J6	H	IJM	EUR	LG	Count
2015-01-07	1	0	1	0	0	0	0	0	2
2015-01-10	1	0	0	0	0	0	1	0	2
2015-01-28	0	1	0	0	0	0	0	1	2
2015-11-25	0	1	0	0	0	1	0	0	2
2015-11-29	1	1	0	0	0	0	0	0	2
2015-12-04	0	1	0	0	1	0	0	0	2

Figure 3.8: Block diagram of the preprocessing and the classic identification approach.

3.5.6. Verification via the Continuous Wavelet Analysis

The events selected via the classic identification approach are verified via a second analysis technique, namely a Continuous Wavelet Analysis (CWT). Based on Picco et al. (2019), an analytic Morse wavelet with a standard γ of 3 is chosen for this analysis. This wavelet is included in the Matlab Wavelet Toolbox, which calculates the correct scales and generates corresponding wavelet coefficients and scalograms (Peyre, 2024). The analysis is run in Matlab R2023b.

The results of a CWT are visualized in a scalogram. This is a two-dimensional plot that shows the wavelet coefficients over time for each calculated scale. When a meteotsunami passes a station, the signal more closely overlaps with the wavelet configuration corresponding to meteotsunami wave periods (2 minutes to 30 minutes). The increased overlap results in higher wavelet coefficients at the moment of passing, which shows up as a clear anomaly in the scalogram.Figure 3.9 presents two scalograms. The left scalogram shows a clear anomaly within the relevant periods that could be a meteotsunami, whereas the right scalogram does not show any anomaly within the relevant periods. This property of the scalogram is used to verify the events that were flagged via the classic approach and to potentially add additional flagged stations to these events.

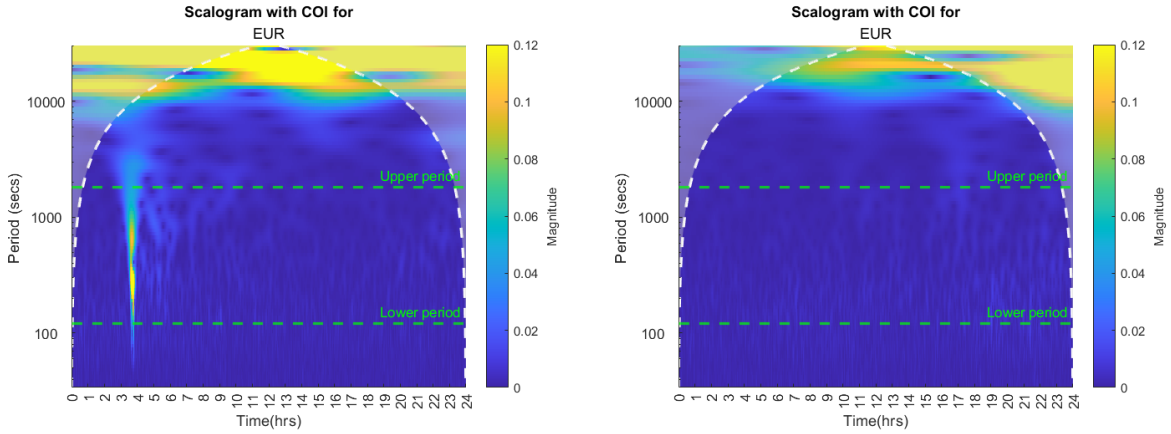

(a) Scalogram of the elevation data measured on station EUR on the 29th of May 2017.

(b) Scalogram of the elevation data measured on station EUR on the 15th of August 2012.

Figure 3.9: Example of a scalogram where a meteotsunami shows (left) and a scalogram without a meteotsunami (right)

3.5.7. The Time of Occurrence via the Continuous Wavelet Analysis

The anomalies in the scalogram do not only indicate whether a meteotsunami passed the station. They can also be used to determine the exact moment of arrival of the meteotsunami at the stations. The scalogram is decomposed by integrating the wavelet coefficients over the relevant wave period band (between 2 and 30 minutes). The peak in wavelet coefficients, when the meteotsunami passes the station, is visible in the integral of the relevant wavelet coefficients (Figure 3.10). The maximum value of this integral represents the exact moment the meteotsunami passes the station.

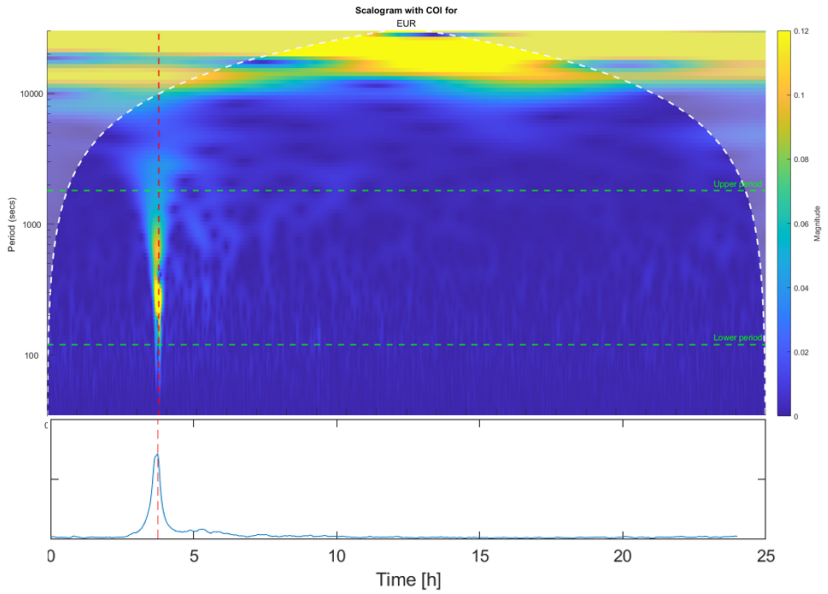

Figure 3.10: Scalogram of the 29th of May 2017 at station EUR. The graph below the scalogram represents the integral between wave periods of 2 and 30 minutes. The maximum value of this graph (shown by the dotted red line) is the moment when the tsunami passes the station.

3.6. Identification of the Atmospheric Component of Meteotsunamis

To determine whether an atmospheric pressure jump occurred on the identified dates of potential meteotsunami events, the sea level air pressure is analyzed in the finest domain, defined in Section 3.3. The used data is modeled by WRF, and is separated in windows of 30 minutes, equal to the longest pressure jumps capable of generating meteotsunamis (Lewis et al., 2023). Within these 30-minute windows, the maximum and minimum sea level pressures are localized to determine the height and duration of the potential pressure jump. The pressure change is computed for every five grid cells in both the x and y directions. This downsampling reduces computational cost, without significant impairing of the results of the analysis.

The identified sea level pressure changes are threshold filtered against a threshold of 2 hPa. This threshold is higher than the lowest pressure jump that can generate a meteotsunami, which is 1 hPa (Gusiakov, 2020). Changes in sea level pressure around 1 hPa occur regularly, resulting in a lot of noise and thus no clear indication of an atmospheric front. A threshold of 2 hPa reduces this noise. In cases where this selected threshold fails to provide results, the threshold is decreased until a lower limit of 1 hPa.

If the air pressure threshold is exceeded within a time window, the coordinates of the point are stored, together with the moment of exceedance (the start of the time window). For each analyzed event, this information is visualized on a map, which shows if and where the pressure threshold was exceeded. This process is explained in Figure 3.11 on the next page.

Together with the map, the sea level pressure at the moment of most exceedances is presented for each event. This data helps to visualize the atmospheric front responsible for the generation of the event. Additionally, the location where the maximum pressure change was measured is selected. At this location, the sea level air pressure is plotted over time to show the development of the atmospheric front.

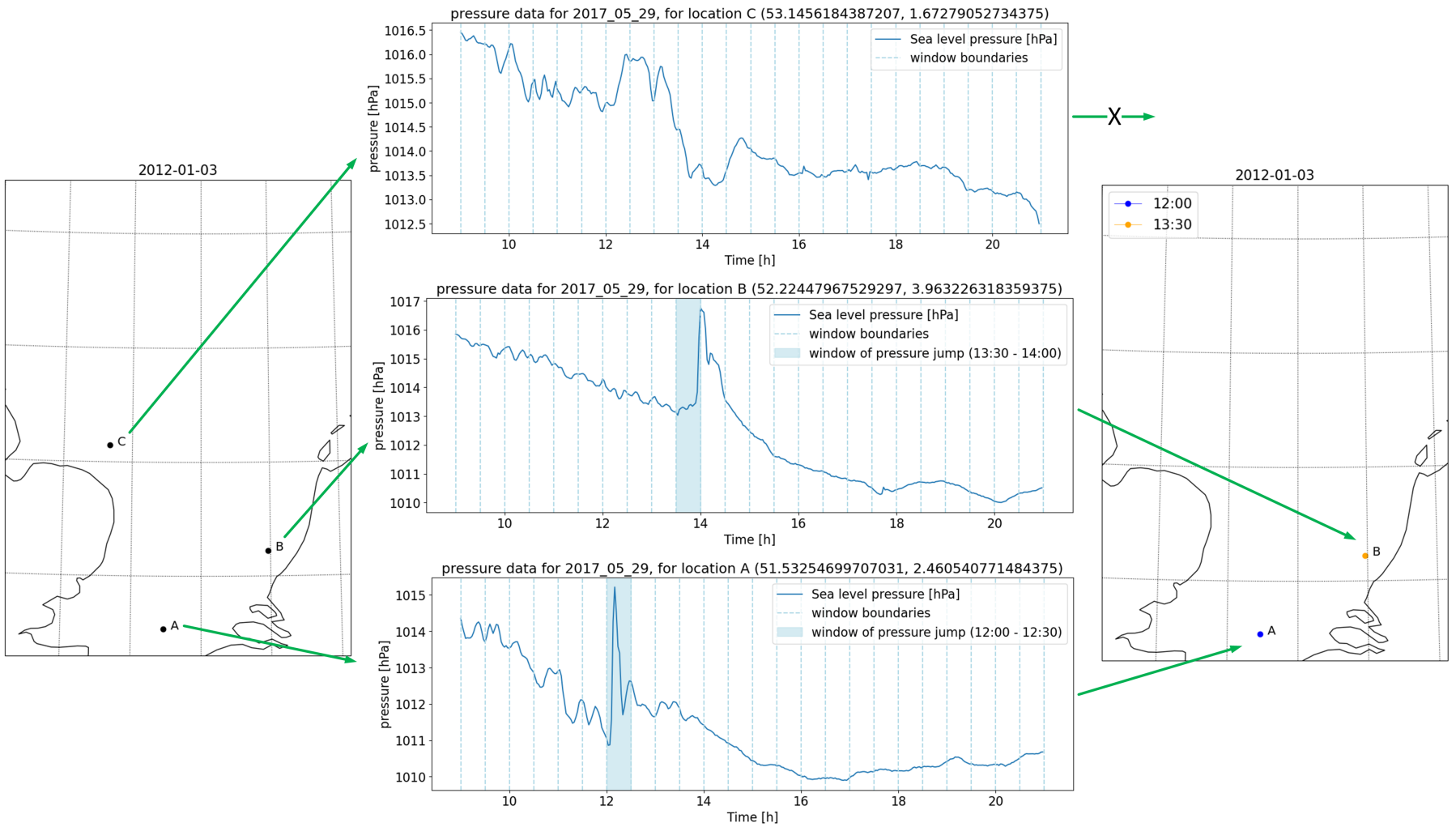

Figure 3.11: Process to identify a pressure jump explained. Three different locations are shown on the map on the left. For each location, the sea level pressure on the 29th of May 2017 is plotted. This data is divided into 30-minute windows, with the window where the pressure change exceeded the threshold marked in blue. The pressure jump does not pass location C, thus the location is not marked on the final map. The pressure jump does pass locations A and B, thus they are marked on the final map, with the color indicating the time of passing.

3.7. Characterization of the Identified Events

Once both the oceanic and the atmospheric components of the meteotsunami events are identified, the events are definitively classified as a meteotsunami and their characteristics are analysed. The properties that are characterized are the angle of incidence and wave speed, the wave period, and the wave height. Combining the characterizations of all selected events will produce an basis of the properties of meteotsunamis on the Southern North Sea.

3.7.1. Angle of Incidence and Meteotsunami Wave Speed

The angle of incidence provides important information about the trajectory of the meteotsunami. Furthermore, if it overlaps with the angle of incidence of the atmospheric front, the probability of Proudman resonance increases. This angle is derived by identifying a reference point, termed the hypothetical origin of the meteotsunami. Once this origin is established, the angle is calculated as the azimuthal difference between the meteotsunami's propagation path, extending from the hypothetical origin to each observation station, and the true North. The hypothetical origin does not represent the actual origin of the meteotsunami, as refraction and hindrance of land mass are not taken into account. It is used solely as a reference point.

The hypothetical origin is computed via triangulation, a method applied to locate the origin of seismically induced tsunamis. Triangulation uses the difference between the actual and calculated distance between the relevant stations and the hypothetical origin. The calculated distance is formulated as the multiplication of the wave speed and the time lag between the time of arrival at the stations and the time of generation at the hypothetical origin. The actual distance is calculated via Pythagoras over shorter distances or via the Haversine formula if the spherical shape of the earth has to be taken into account (Erukulla and Reddy, 2024). Using minimization, a location is found where the calculated and actual distance are almost equal for each relevant station, so that Equation 3.5 can be formulated.

$$v(t_n - t_0) = \sqrt{(x_n - x_0)^2 + (y_n - y_0)^2} \tag{3.5}$$

Here, v represents the wave speed, t_0 the time of generation at the hypothetical origin, and x_0 and y_0 the x- and y-location of the hypothetical origin. t_n, x_n, and y_n represent the time of arrival (known via Figure 3.10) at the relevant stations and their locations. The left side of the formula represents the calculated distance, and the right term represents the actual distance, via Pythagoras. Figure 3.12 presents an example of this calculation, with three known locations and three known times of arrival for a hypothetical earthquake. Equation 3.5 is solved to obtain a location and time of generation for the hypothetical origin.

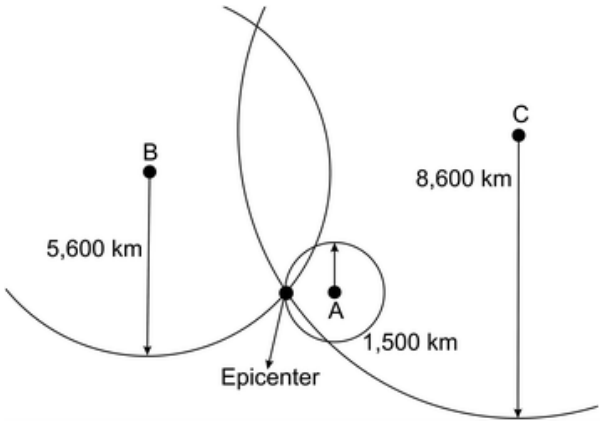

Figure 3.12: Process of triangulation explained for an earthquake. If the time of arrival and the location of point A, B, and C are known, a point can be located via Equation 3.5. From here, indicated as the epicenter, the earthquake must have originated. The distance from the epicenter to each station, divided by the velocity at which the wave travels, should result in the known time of arrival at each origin.

Triangulation is a process of difference minimization, since the aim is to derive the smallest difference between the actual distance and the calculated distance. This difference is called the distance error, formulated in Equation 3.6.

$$s_{actual} = \sqrt{(x_n - x_0)^2 + (y_n - y_0)^2} \tag{3.6}$$

$$s_{calculated} = v(t_n - t_0) \tag{3.7}$$

$$e_{distance} = s_{actual} - s_{calculated} \tag{3.8}$$

$$\tag{3.9}$$

Here s_{actual} represents the actual distance between the origin and station n, equal to the right side of Equation 3.5. $s_{calculated}$ represents the calculated distance, equal to the left side of Equation 3.5. $e_{distance}$ represents the distance error. The sum of the distance errors for each flagged station of an identified meteotsunami event, results in the total distance error. This distance error is minimized using the scipy.optimize.minimize function in Python 3.9.19. This triangulation leads to a location of the hypothetical origin, and a time at which the wave passed this point.

Normally, three known locations are necessary for triangulation. If location A would be removed from Figure 3.12, there would be two points of intersection and thus two possible epicenters instead of one. In the case of this research on meteotsunamis, some information about the location of origin is already known, as the responsible front is already identified. This can be used to select the more likely origin from the two options. Therefore, triangulation for meteotsunamis is also possible when only two locations are known.

A limitation of triangulation is the use of a constant wave speed v along the entire wave trajectory. For meteotsunamis, the wave speed is equal to the shallow water wave speed. It is therefore depth dependent, which means it differs along the trajectory. To account for this limitation, the wave speed of the meteotsunami is simplified to one estimated constant wave speed. The mean shallow water wave speed of the southern North Sea is 18.43 m/s. Accordingly, estimated wave speeds from 16 to 20 m/s are investigated for each event. The wave speed and origin that results in the smallest distance error are selected, to calculate the angle of incidence. Once the location of the hypothetical origin is known, the angle of incidence is calculated as the azimuthal difference between each trajectory and the north (visualized in Figure 3.13).

Figure 3.13: Azimuthal difference (shown as Az) between two locations. ϕ represents the latitude and λ the longitude of both locations (Dickey et al., 2020). In our application, the event would be the location of the hypothetical origin, and the station the location of the station. The red line is the trajectory between the two hypothetical origin and the black dotted line connects the origin to the north.

The azimuth difference is calculated via Equation 3.10 (Dickey et al., 2020).

$$\alpha = \arctan 2(\sin(\Delta\lambda)\cos(\phi_{station}),\ \cos(\phi_o)\sin(\phi_{station}) - \sin(\phi_o)\cos(\phi_{station})\cos(\Delta\lambda)) \tag{3.10}$$

where α is the azimuth difference (thus the angle of incidence), $\Delta\lambda$ represents the difference in longitude between the hypothetical origin and the station, ϕ_o the latitude at the hypothetical origin, and $\phi_{station}$ the latitude at the station. Via this equation, the angle of incidence towards each flagged station is calculated. To finally get one angle of incidence, the mean angle of incidence out of all stations is calculated and used as the final direction of the meteotsunami.

3.7.2. Wave Period and Wave Height

To determine the wave periods, two separate analyses are performed. Their results are combined to determine the definitive wave period of each identified event.

The first method estimates the period using the scalograms that are generated from the results of the CWT. These contain information about the wave period on the vertical axis. When a meteotsunami passes a station, the highest wavelet coefficients on the vertical axis will be found for the wave period corresponding to the tsunami period. This property is used to identify the meteotsunami period. Since the time of occurrence is known, the wavelet coefficients along the vertical axis at that moment will give a relative estimation of what periods are most distinguished. These periods are identified via the local maxima of the wavelet coefficients at the time of occurrence. For each station where the tsunami event was flagged, the local maxima are defined, to scan for overlapping periods between stations. The local maximum that occurs at most stations is linked to the meteotsunami wave, resulting in a small period band (as the local maxima will not be exactly equal).

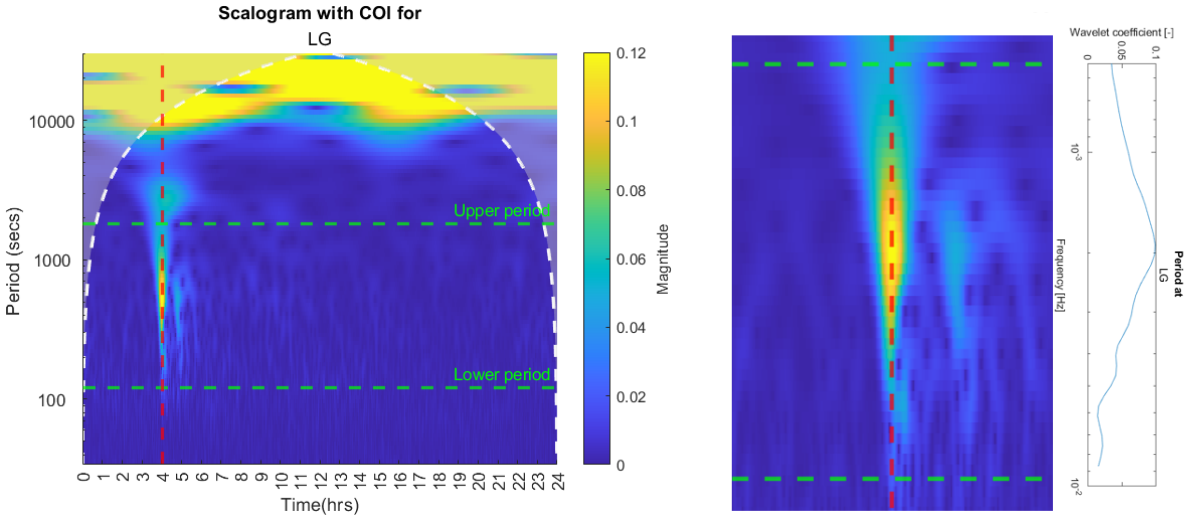

Figure 3.14: The left figure presents the scalogram of station LG on the 29th of May with a clear anomaly, classified as a meteotsunami. The moment the meteotsunami passes is highlighted by the red dotted line. the right figure zooms in on this anomaly, with the wavelet coefficients along the red dotted line shown in the graph. The local maxima in this graph give information about the prominent wave period of this event.

The second method used to determine the wave period of the tsunami events is via a zero-down crossing analysis. This analysis detects waves in the elevation data by identifying the moments where the elevation goes from a positive elevation to a negative elevation, called a zero-down crossing (Figure 3.15).

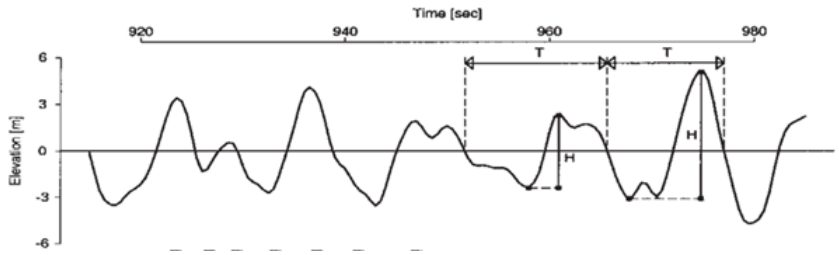

Figure 3.15: Example of the zero-down crossing method (Podgórski et al., 2000). The waveheight is shown by H and the waveperiod is shown by T, where both are determined between two zero-down crossings.

To perform the zero-down crossing analysis, the filtered elevation data is used, as the tidal elevations would negatively impact the results of the analysis. The exact moment of occurrence, identified via the wavelet analysis, is used to isolate the tsunami wave within the dataset. To include the start and end of the wave and its zero-down crossings, the analyzed time window spans an hour (30 minutes before and after the moment of occurrence). In this window, the highest wave is classified as the tsunami wave. The timespan between two zero-down crossings represents the period of the wave. Via the zero-down crossing analysis, also the wave height of the tsunami wave is determined, using the maximum and minimum amplitude between two zero-down crossings. The result is an exact wave height at each flagged location.

3.8. Influence of Proudman Resonance on the Identified Events

Since Proudman resonance is the most prominent mechanism in the amplification of meteotsunamis, its potential influence on the identified events will be the focus of this chapter. To establish whether Proudman resonance influenced the found events, the atmospheric forcing speed is computed, and compared to the shallow water speed. Furthermore, the area covered by the front and the meteotsunami are compared.

3.8.1. Atmospheric Forcing Speed

The area covered by the front is determined via the pressure jumps calculated in the identification chapter. Based on the found locations and their timestamp, a rough estimate of the trajectory of the front is already possible. If the pressure jump would be constant over time, following it would result in an overview of the covered area by the front. Unfortunately, a front is a dynamic system, thus the change in pressure at moment one will likely differ from the pressure jump at moment two, even though they represent the same location in the front. Therefore, the number of points that exceed the pressure threshold varies over time. This issue also makes cross-correlation as prescribed in literature difficult when tracking pressure jumps.

The front is simplified to a straight line to overcome the changing pressure jumps. The line is drawn between the two outer points of the found exceedances for each timestep. These line approximations of the fronts at each timestep are interpolated to 5 points. tracking these 5 points over time results in 5 separate trajectories, and thus five atmospheric forcing speeds for each time window. The distance between two points is known, as well as the time window over which the front propagates between the two points, hence the atmospheric forcing speed is found. These 5 speeds are averaged, to obtain an atmospheric forcing speed for that time window. This process is visualized in Figure 3.16.

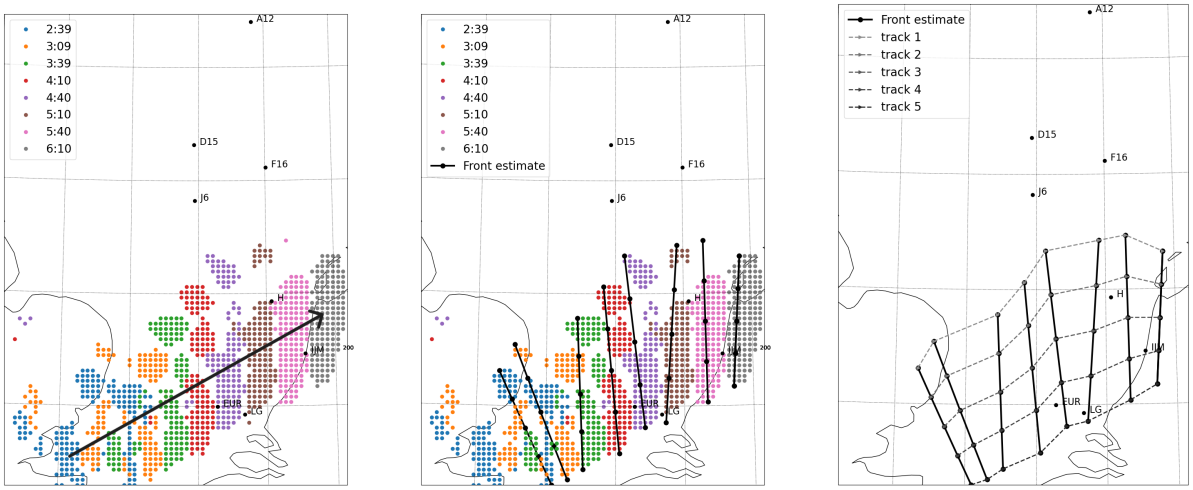

(a) Locations where the Sea level pressure threshold is exceeded for every half an hour window, colored by the respective time window. The arrow indicates the direction of propagation of the front.

(b) Line approximations of the front for each half an hour window. These lines are drawn between the two outer points of the front, and then linear interpolated to five points.

(c) The line approximations are connected, resulting in five trajectories that approximate the trajectory of the front.

Figure 3.16: A visual representation of the method to determine the atmospheric forcing speed.

3.8.2. Check for Proudman Resonance

It is assumed that in one half an hour window, the atmospheric forcing speed does not change. Therefore an area over which the front has propagated at that speed is found. In this area, the shallow water wave speed is calculated using the bathymetry data. To check whether Proudman resonance occurred, this wave speed is compared to the atmospheric forcing speed, using the Froude numbers. If these lie between 0.8 and 1.2, they are shown, and Proudman resonance could have occurred in that area.

The final step is then to verify whether the front overlapped with the meteotsunami, while the Froude number was close to 1. Every half an hour, the area covered by both the meteotsunami and the front are overlaid to check for potential overlap. If overlap occurs when the Froude numbers are close to 1, the conclusion is drawn that Proudman resonance was relevant in the amplification of the event.

4

Results: Identification of the Oceanic Component of Meteotsunamis on the Southern North Sea

4.1. Identification of the Oceanic Component via the Classic Method

The classic identification method starts with establishing a suitable amplitude threshold for the identification of meteotsunamis in the Southern North Sea. After a threshold is selected, a list of potential meteotsunamis is made. From this list a selection is made, dependent on the probability of correct classification.

4.1.1. Amplitude Threshold Filtering

Following the classic approach, threshold filtering is performed on the band-pass filtered elevation data. The results for each selected amplitude threshold are presented in Table 4.1.

Threshold	Threshold filter	Multiplicity criterion	Visual inspection
0.25	123	7	1
0.10	279	38	14
6 σ	996	324	-
4 σ	2364	1591	-

Table 4.1: Number of flagged dates for each threshold, per step in the process. The visual inspection of the relative thresholds is not performed, because of the abundance of potential events after the first two steps.

The relative thresholds result in many more flags than the absolute thresholds since they are generally much smaller. Because of this abundance of potential meteotsunamis with the relative thresholds, the visual inspection of all flagged events would be a lengthy and labor-intensive process. It would have been beneficial to eliminate this step, as it is hypothesized that these thresholds even with visual inspection result in a much higher number of potential meteotsunamis than the two absolute thresholds. Unfortunately, in this research, the validity of the outputs of the relative thresholds cannot be verified since no visual inspection is performed. Therefore, they are not used to select potential tsunami dates.

The absolute thresholds have been inspected visually. The results of this visual inspection are shown in Section D.2. For the 0.25-meter threshold, the only flagged date left is the 29th of May 2017. This event is the most significant meteotsunami reaching the Dutch Coast in the past decade, explaining why it is one of the only events documented in the literature. It is however deemed unlikely that only one meteotsunami has arrived near the Dutch coast in 8 years of data. This hypothesis is supported by the result of the lower absolute threshold, which shows 14 potential meteotsunami events after visual inspection. An explanation for this excessive height is found in the article from de Jong and Battjes (2004) that proposed this threshold. Their research focused on seiches, not on meteotsunamis. These seiches amplify the meteotsunamis significantly, making a higher threshold more appropriate. However, this threshold is too high to detect waves like meteotsunamis before they are amplified by seiching.

The only threshold resulting in a practical number of potential meteotsunamis is the 0.10-meter threshold,

proposed by Lewis et al. (2023). After the application of the multiplicity criterion, 38 potential meteotsunamis were detected, After visual inspection, this amount decreased to 14 potential meteotsunamis. Therefore based on this research, the absolute threshold of 0.10 meters is suggested to identify meteotsunamis towards the Dutch coast.

4.1.2. Selection of Further Analyzed Events

Out of the fourteen potential meteotsunamis, a selection of six is made, as analyzing all fourteen was not feasible given the duration of this research. The selected events for the case studies and the substantiation for this selection are presented in this section.

The first selected meteotsunami occurred on the 29th of May 2017. This event is the only one that exceeded the threshold of 0.25 meters. Furthermore, it is one of the only meteotsunamis on the Dutch coast that has been documented in earlier studies (Sibley et al., 2020). Therefore, it is expected the characterization of this event will produce the clearest results out of the six selected events. This event will be referenced as the spring event of 2017.

The second selected event occurred on January 3rd 2012. This event was detected at three different stations and has also been documented in literature before. This event will be referenced as the winter event of 2012. An additional point of interest is the time of the year when the first two events appeared. The first event occurred during summer and the second during winter, which is expected to influence the atmospheric source responsible for its generation.

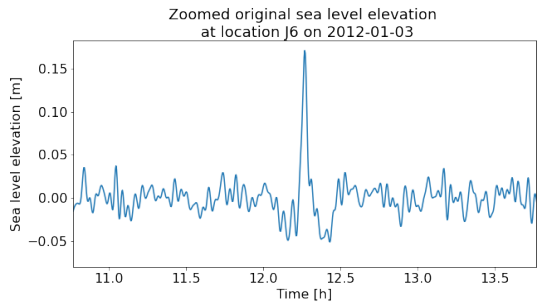

(a) Signal filtered elevation data on the 3rd of January 2012, showing the potential meteotsunami at station J6.

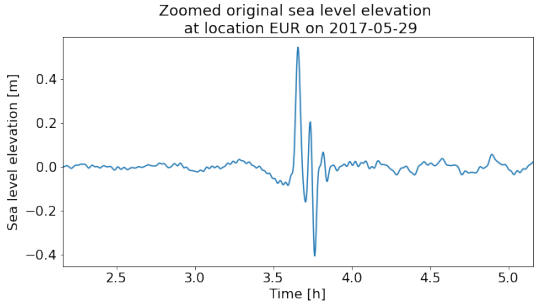

(b) Signal filtered elevation data on the 29th of May 2017, showing the potential meteotsunami at station EUR.

Figure 4.1: a zoom of the signal filtered elevation data of the first two selected events.

The third and fourth selected events occurred on the night of July 18th to 19th, 2014. Since these events occurred on two consecutive dates, they might be related or be the same event. This will be further investigated in Section 4.3. If the flagged stations on both dates represent the same event, six stations are exceeded for one event. This would be the highest number of flags out of all found dates, thus these dates are also selected to be further analyzed and characterized. These events will be referenced as the consecutive summer events of 2014.

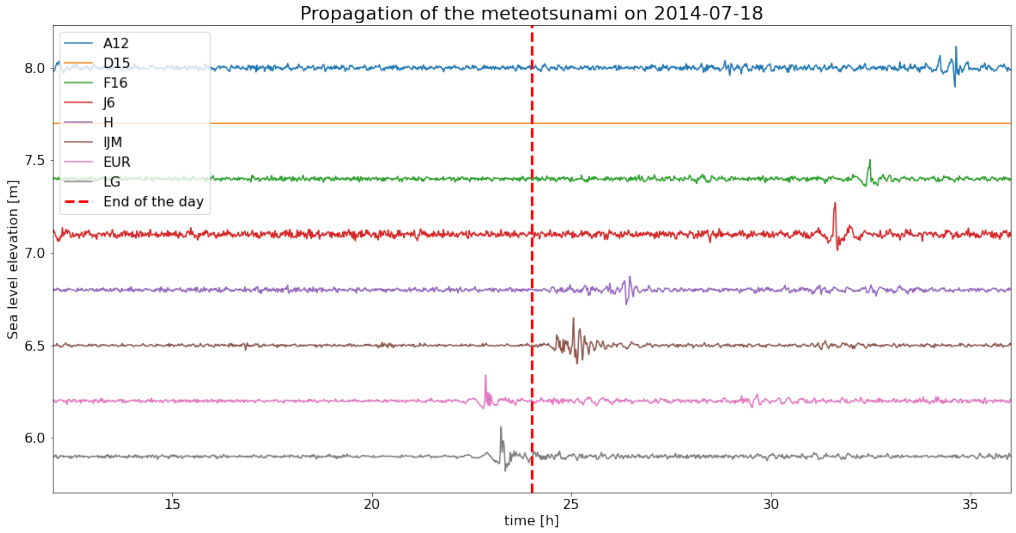

Figure 4.2: Signal filtered elevation data for all stations on the night between the 18th and 19th of July (separated by the vertical red dotted line).

The final two events were detected on the 28th of January 2015 and the 15th of August 2012. These events have been selected to include an extra winter and summer event in the case studies, to decrease the chance of coincidence for the conclusions about the seasonality of the events. Additionally, since these events were only flagged at two stations, they will likely be less clearly visible in further analysis, which could give additional information on the effectiveness of the second identification method. These events will be referenced as the winter event of 2015 and the summer event of 2012.

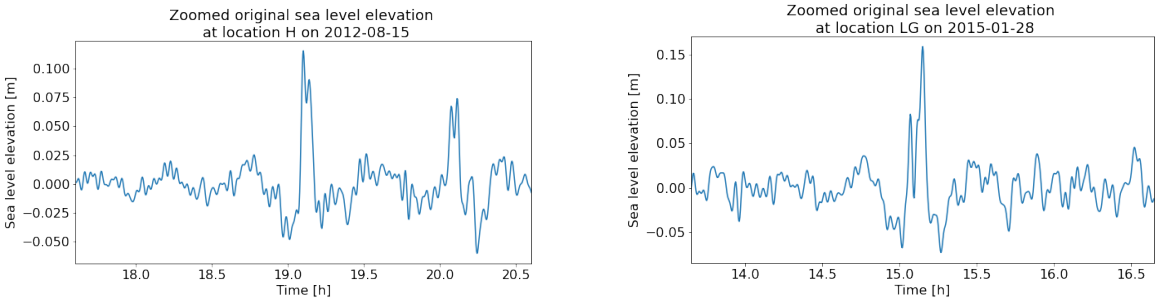

(a) Signal filtered elevation data on the 15th of August 2012, showing the potential meteotsunami at station H.

(b) Signal filtered elevation data on the 28th of January 2015, showing the potential meteotsunami at station LG.

Figure 4.3: a zoom of the signal filtered elevation data of the final two selected events.

In summary, the six selected dates are shown, with the stations where the 0.10-meter threshold was exceeded are shown in Table 4.2. The elevation data of the six selected dates are presented in Appendix E.

	A12	D15	F16	J6	H	IJM	EUR	LG	Count
Winter event of 2012	1	0	0	1	0	1	0	-	3
Summer event of 2012	0	0	0	0	1	1	0	-	2
First summer event of 2014	0	0	0	0	0	0	1	1	2
Consecutive summer event of 2014	1	0	1	1	0	1	0	0	4
Winter event of 2015	0	1	0	0	0	0	0	1	2
Spring event of 2017	0	-	0	0	1	1	1	1	4

Table 4.2: Per selected event the stations that exceed the threshold of 0.10-meter. The most right column presents the sum of the exceeded stations per date, to show that all of them exceed the multiplicity criterion. If no value is shown at a station, no data is available.

4.2. Verification of the Events via the Continuous Wavelet Analysis

The scalograms of the selected events are shown in Appendix F. Using these scalograms, a similar table to Table 4.2 is constructed, Table 4.3. The flagged stations marked red show an anomaly indicating a potential meteotsunami, while not being flagged in the classic analysis. The flagged stations marked yellow were flagged in the classic approach but resulted in scalograms that did not show a clear anomaly within the meteotsunami frequency boundaries.

	A12	D15	F16	J6	H	IJM	EUR	LG	Count
Winter event of 2012	1	0	0	1	0	1	1	-	4
Summer event of 2012	0	0	0	0	1	1	0	-	2
First summer event of 2014	0	0	0	0	0	0	1	1	2
Consecutive summer event of 2014	1	0	1	1	0	1	0	0	4
Winter event of 2015	0	1	0	0	0	0	1	1	3
Spring event of 2017	0	-	0	0	1	1	1	1	4

Table 4.3: Per selected event the stations where a clear anomaly within the meteotsunami frequencies was showing on the scalograms. The most right column presents the sum of the exceeded stations per date, to show that all of them exceed the multiplicity criterion. If no value is shown at a station, no data is available.

The winter event of 2012 is the only event where the scalograms of the flagged locations (shown in Figure 4.4) significantly differ from the scalograms of the other flagged stations. Both of them show an anomaly within the relevant frequency boundaries, but mainly very high wavelet coefficients outside of these boundaries. These stations will still be taken into account in the characterization of this event, but will carefully be inspected.

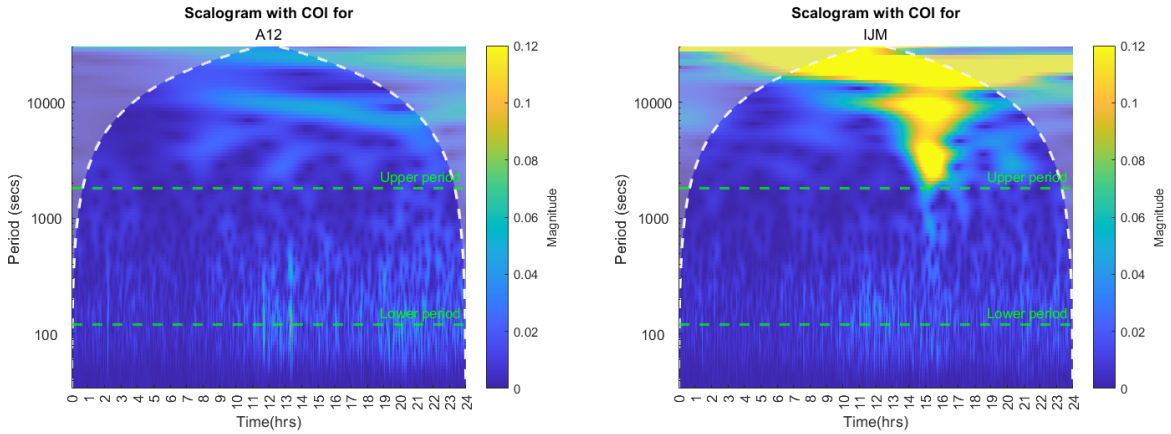

(a) Scalogram of location A12 during the winter event of 2012.

(b) Scalogram of location IJM during the winter event of 2012.

Figure 4.4: Examples of a scalogram of a location flagged in the classic approach that looks different in the scalograms

In addition to the stations that were already flagged in the classic analysis, for two events (both winter events) the station EUR is added since a clear anomaly shows in the scalograms (Figure 4.5). These stations did not flag in the classic approach because of the limitations imposed by the band-pass filter. For the FFT, two consecutive weeks of good data were necessary to filter out the longest irrelevant waves, at the cost of some valid data. Since the continuous wavelet analysis is performed on the unfiltered dataset, this valid data is not deleted, and can therefore produce additional points where the meteotsunamis are flagged. It should be checked in further research if the CWT still results in less data removal when the data is preprocessed first.

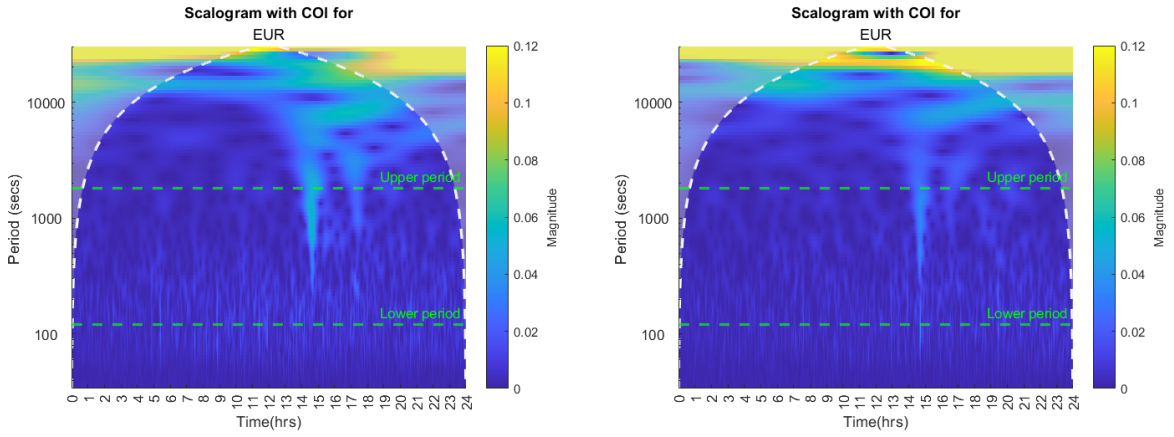

(a) Scalogram of location EUR during the winter event of 2012.

(b) Scalogram of location EUR during the winter event of 2015.

Figure 4.5: Examples of a scalogram of locations that were not flagged in the classic approach that should have been flagged according to the scalograms

4.3. The Time of Occurrence via the Continuous Wavelet Analysis

The exact moment when a meteotsunami passes a station provides valuable information to compute the angle of incidence and further characterize the wave. To determine this moment, the scalograms (shown in Appendix F) are revised to determine an exact moment of occurrence at the relevant stations, including the additional stations from Section 4.2. These results are summarized in Table 4.4.

	A12	D15	F16	J6	H	IJM	EUR	LG
Winter event of 2012	13:21	-	-	12:16	-	15:14	14:39	-
Summer event of 2012	-	-	-	-	19:06	19:07	-	-
First summer event of 2014	-	-	-	-	-	-	22:52	23:15
Consecutive summer event of 2014	10:37	-	08:29	07:36	-	01:03	-	-
Winter event of 2015	-	12:43	-	-	-	-	14:43	15:07
Spring event of 2017	-	-	-	-	05:20	05:18	03:44	04:02

Table 4.4: times of occurrence of each event at each measuring station

Most of these results are sensible when they are compared to the locations of the stations, except for the results of the winter event of 2012. It is namely physically not possible for the wave to first arrive at station J6, then arrive at station A12 1 hour later, and then arrive at stations EUR and LG 2 hours later. In Section 4.2, the scalogram of station A12 was already flagged, as it looked different from the other stations. Therefore, based on these two observations, station A12 is excluded from further analysis for this event.

The time of occurrence is a necessity for the further characterization of each event. Additionally, it is also used to determine whether the events on the 18th and 19th of July 2014 might have been the same event. The gap between the two flagged dates is the smallest between station J6 and IJM, namely 6 hours and 33 minutes. These stations are located 185.8 kilometers from one another. To cover this distance in the found period, the meteotsunami has to propagate at a mean speed of 7.87 m/s.

The actual wave speed, is fully dependent on the depth profile along the trajectory between the two stations, as it propagates at shallow water wave speed. This results in a mean wave speed of 16.32 m/s, twice as big as the wave speed computed via the moments when the event passed the stations. Therefore, even though the events occur on two consecutive dates, they are classified as separate events.

5

Results: Identification of the Atmospheric Component of Meteotsunamis on the Southern North Sea

For the six selected dates, the atmospheric conditions are modeled by WRF. For each event, a map visualizes the positions that exceeded the pressure threshold per time window. Next, the pressure data at the time window with the most exceedances is shown to establish the responsible front. The events are categorized based on the season in which they occurred, as a strong seasonal overlap in atmospheric conditions is observed.

5.1. Winter Events

The winter event of 2015 is the only event that did not meet the pressure threshold of 2 hPa. By lowering the threshold to 1.5 hPa, a front still occurs. This front is shown on the map in Figure 5.1a, together with the pressure data for 13:00 (the moment with the highest number of exceeded points) in Figure 5.1b. Though the front first appears on land, from 13:30 onwards, the front travels over the sea, making meteotsunami generation possible.

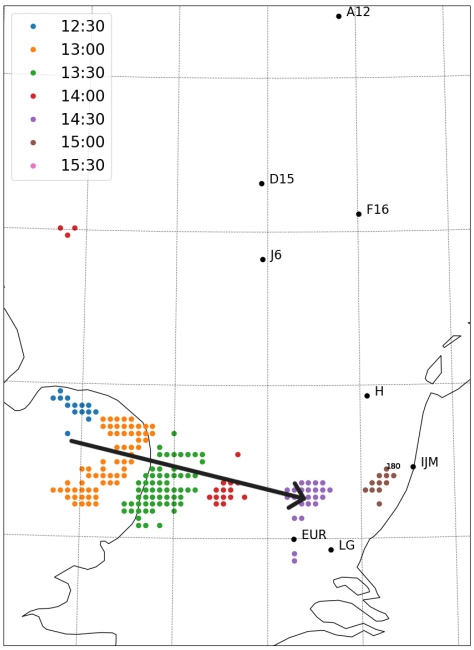

(a) Locations where the threshold of 1.5 hPa is exceeded, colored by the time of exceedance. The arrow indicates the direction of propagation of the front.

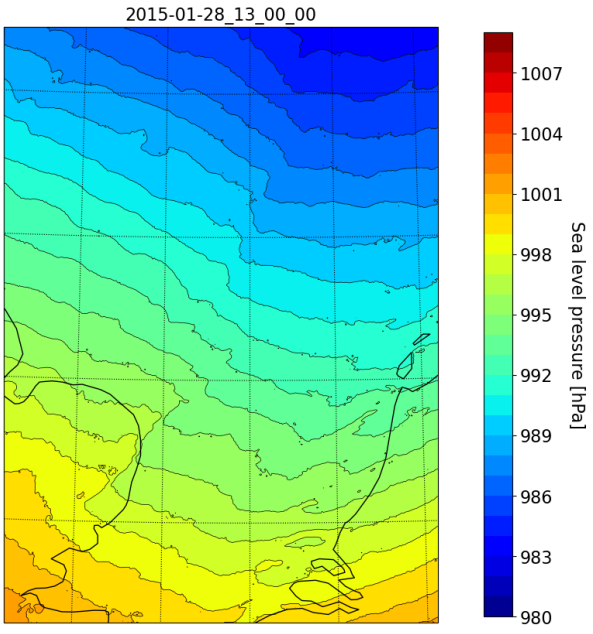

(b) Sea level pressure data at the moment of most exceedances, 13:00.

Figure 5.1: Atmospheric components of the meteotsunami on winter event of 2015.

Figure 5.2 reveals that the pressure jump is smaller than 2 hPa, with the maximum pressure jump being 1.9 hPa. This maximum pressure jump occurs at 52.876 degrees North and 0.853 degrees East.

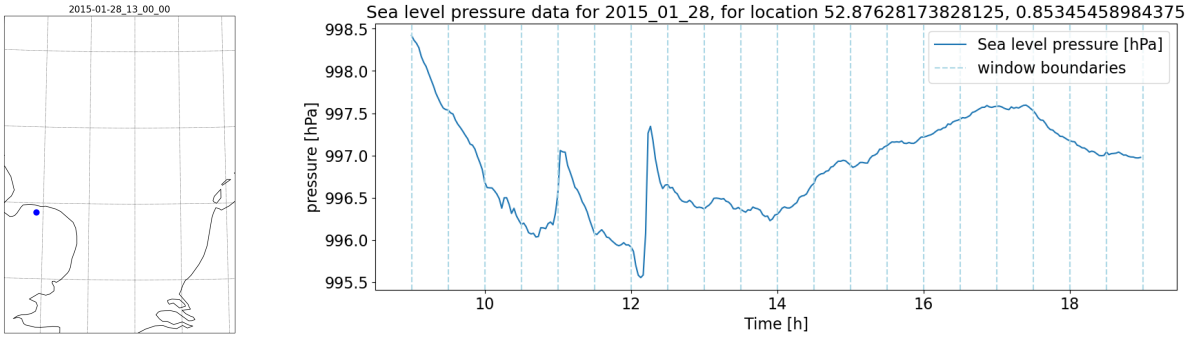

Figure 5.2: The left figure shows the location where the pressure disturbance is largest, at 52.876 degrees North and 0.853 degrees East, with a blue dot. The right figure shows the corresponding pressure data at sea level for the 28th of January 2015.

Figure 5.3a shows the map of the winter event of 2012. The threshold is exceeded at several locations located over the southern North Sea. The clouds of points form a vertical line spanning the southern North Sea, where the highest number of exceedances occurs at 12:30 (the purple dots in Figure 5.3a). The pressure data corresponding to this time is shown in Figure 5.3b. The westernmost points of the time window 12:30 correspond to the vertical line detected in the pressure data. Therefore, this front is responsible for the detected pressure change, that likely caused the meteotsunami. The shape of the front of both winter events is very much alike, which could be related to their seasonality.

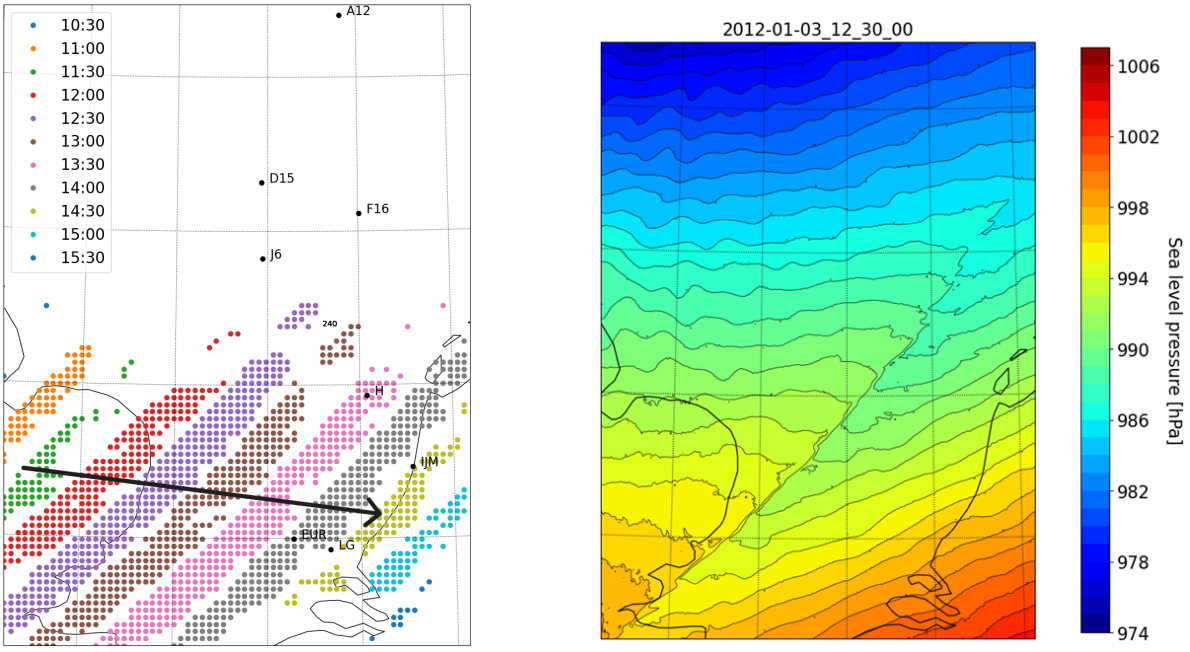

(a) Locations where the threshold of 2 hPa is exceeded, colored by the respective time window. The arrow indicates the direction of propagation of the front.

(b) Sea level pressure data at the moment of most exceedances, 12:30.

Figure 5.3: Atmospheric components of the winter event of 2012.

The largest pressure disturbance on this date was found at location 52.317 degrees North and 2.013 degrees East. This location is shown on a map with the corresponding pressure data in Figure 5.4. It consists of a sudden increase of 3 hPa, after which the pressure steadily increases. This can be attributed to the outline of the front. The map at Figure 5.3b shows a zigzag in the horizontal pressure isobars, which looks like a diagonal line spanning the southern North Sea. Once the line has passed, the pressure field returns to its original state, except for the fact that it is a few hPa higher, which is in line with the information in the graph in Figure 5.3b.

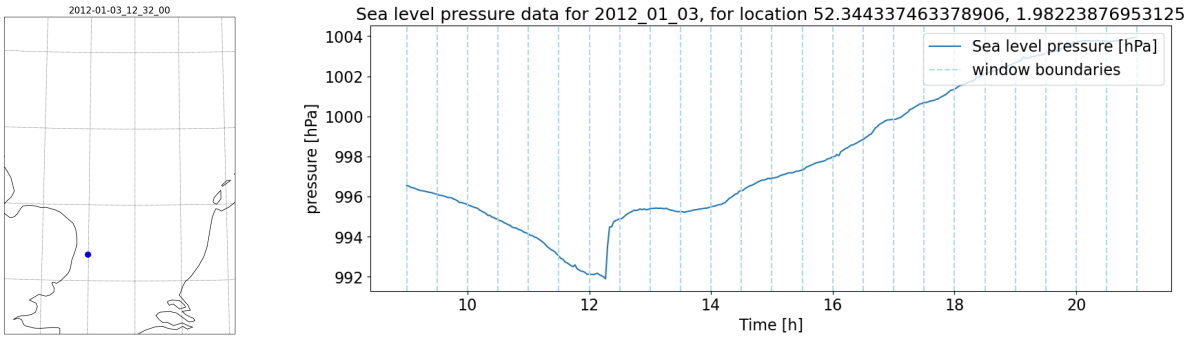

Figure 5.4: The left figure shows the location where the pressure disturbance is largest, at 52.317 degrees North and 2.013 degrees East, with a blue dot. The right figure shows the corresponding pressure data at sea level for the winter event of 2012

5.2. Summer Events

For the summer event of 2012, the map in Figure 5.5a shows multiple exceedances of the threshold of 2 hPa, mainly located over land. Of these, the highest number occurs at 19:00. The corresponding sea level pressure data at this time is shown in Figure 5.5b. The front propagating over station IJM at 19:00 in Figure 5.5b corresponds to the location of the cloud of points at that time window in Figure 5.5a, and is thus linked to the pressure jump.

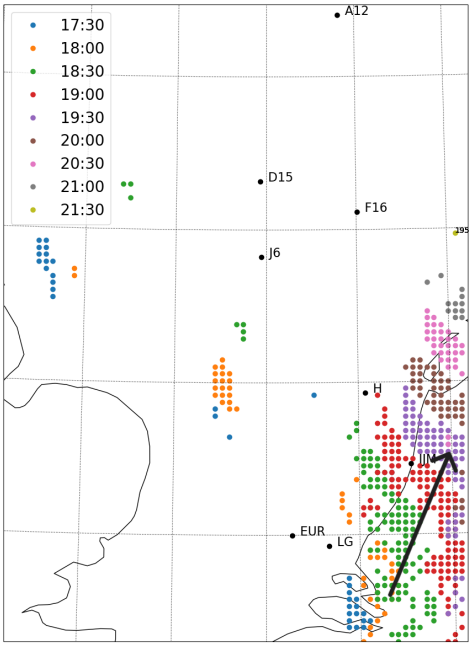

(a) Locations where the threshold of 2 hPa is exceeded, colored by the respective time window. The arrow indicates the direction of propagation of the front.

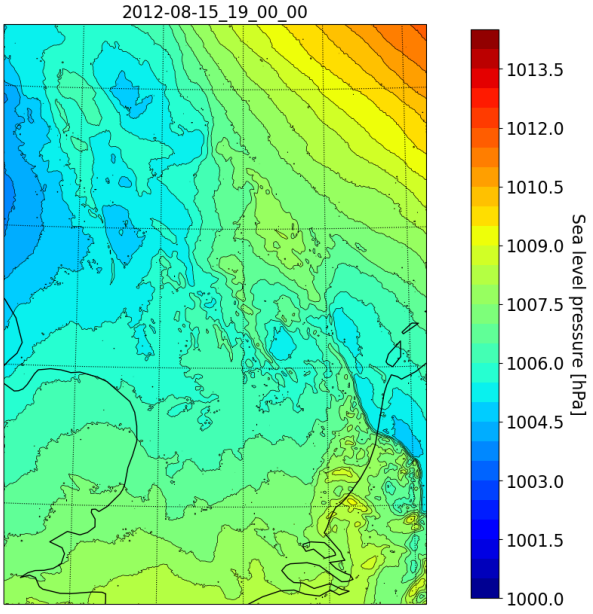

(b) Sea level Pressure data at the moment of most exceedances, 19:00.

Figure 5.5: Atmospheric components of the meteotsunami on the summer event of 2012.

Figure 5.5a and Figure 5.5b show some points over the water near the Dutch coast that could have caused a disturbance in sea level elevation. This is also where the biggest pressure jump occurs, at an exact location of 52.156 degrees North and 4.369 degrees East (Figure 5.6).

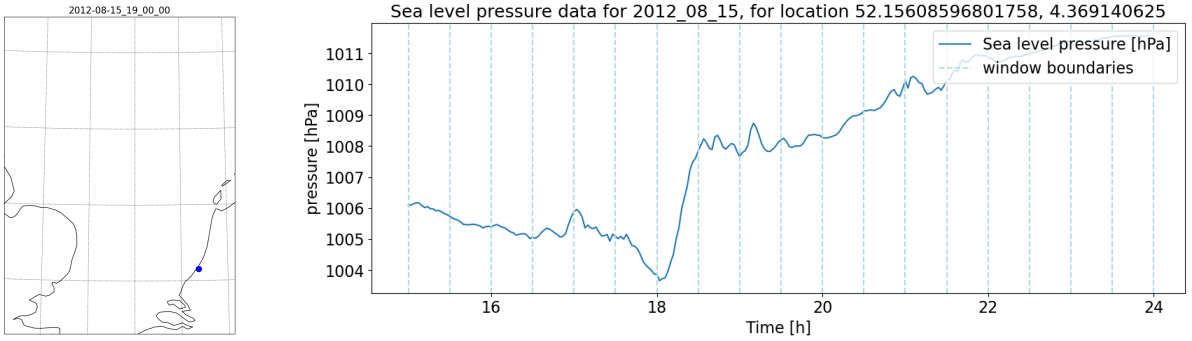

Figure 5.6: The left figure shows the location where the pressure disturbance is largest, at 52.129 degrees North and 4.308 degrees East, with a blue dot. The right figure shows the corresponding pressure data at sea level for the summer event of 2012

The increase of pressure at this location is 4.6 hPa at maximum, resulting in waves of 4.6 cm without external amplification mechanisms. This is lower than the elevation threshold of 10 cm, making it unlikely that the event was generated at this location. Therefore, it is checked whether the front passed the water mass at a lower latitude, outside the smallest simulated grid. The data at a larger grid is reviewed, using the grid with a 3 km horizontal spacing. The front appears in Figure 5.7c over land, but is undetectable at the other timestamps. Thus, the front did also not propagate over water at a lower latitude, unless it did at even lower latitude, outside of the larger grid or within the six-hour timesteps of the larger grid. As the front travels mostly over land, it is difficult to determine whether this event was a meteotsunami, since there is a front with a sufficient pressure jump, but no detectable origin.

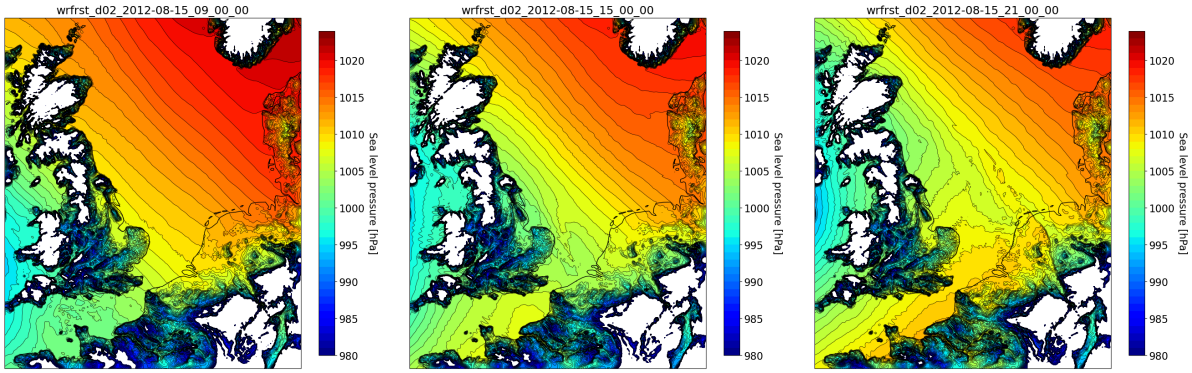

(a) Sea level Pressure data at 9:00

(b) Sea level pressure data at 15:00

(c) Sea level pressure data at 21:00.

Figure 5.7: Sea level pressure data for the 3-km grid for the summer event 2012.

For the consecutive summer events of 2014, a similar problem arises. Several pressure anomalies exceed the 2 hPa threshold, but all of them travel mainly over land within the reviewed grid space (Figure 5.8a). The highest number of grid points occurs at 7:00, corresponding to the pressure data in Figure 5.8b. This sea level pressure data shows a clear front that overlaps with the cloud of exceeded points, which is deemed responsible for the measured disturbance.

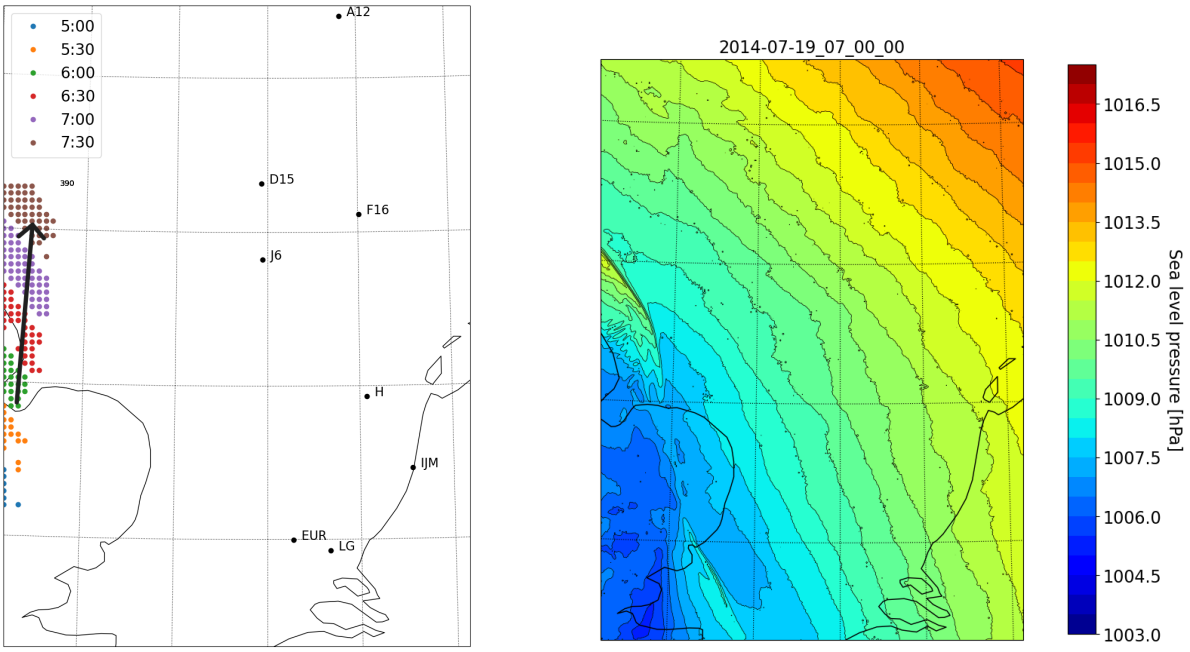

(a) Locations where the threshold of 2 hPa is exceeded, colored by the time of exceedance. The arrow indicates the direction of propagation of the front.

(b) Sea level pressure data at the moment of most exceedances, 7:00.

Figure 5.8: Atmospheric components of the meteotsunami during the consecutive summer events of 2014

The maximum disturbance occurred at 54.255 degrees North and 0.065 degrees East. This point is shown on a map, together with the sea level pressure at this location in Figure 5.9. In contrast to the other two events, the anomaly in the pressure data looks like a sharp peak, with a height of 3.6 hPa. This is attributed to the narrow width of the front, resulting in only a short duration of the increased pressure before returning to the original state.

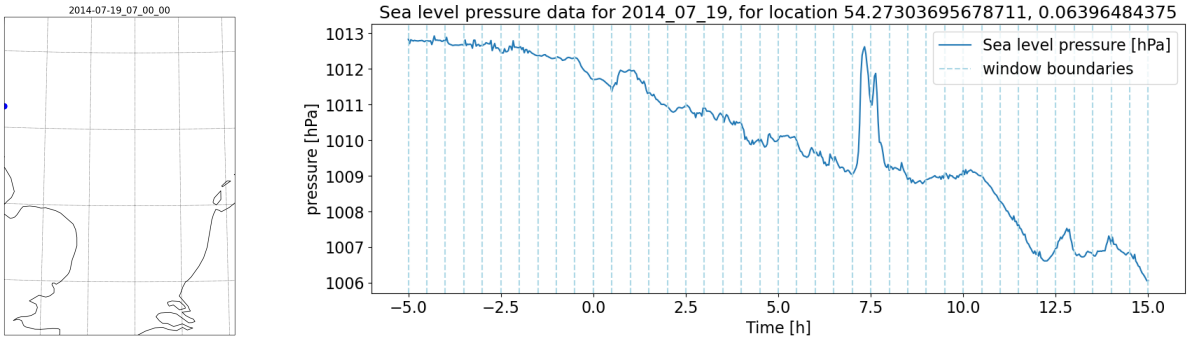

Figure 5.9: The left figure shows the location where the pressure disturbance is largest, at 54.255 degrees North and 0.065 degrees East, with a blue dot. The right figure shows the corresponding pressure data at sea level for the consecutive events of 2014

The front travels over the sea around 7:00 in the morning. This time does fit in the timeline of the second event but is too late to have been responsible for the first one. It is expected that this event was generated while the front passed over the sea at a lower latitude. To verify this, the larger grid is inspected. Unlike the summer event of 2012, the front responsible for this event is detected propagating over water at a lower latitude, as shown in Figure 5.10b. The front crosses the sea between France and England over the English Channel. Therefore, it is likely this front is responsible for the generation of the first event.

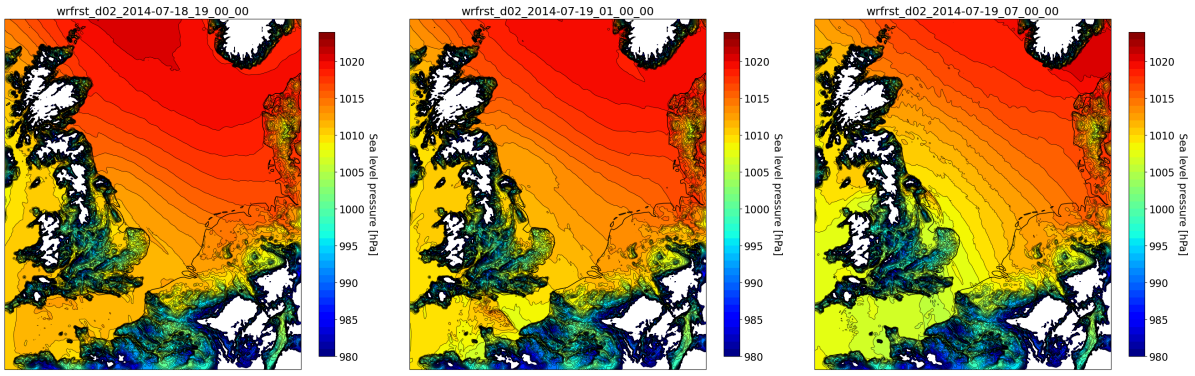

(a) Sea level pressure data at 19:00.

(b) Sea level pressure data at 1:00.

(c) Sea level pressure data at 7:00.

Figure 5.10: Sea level pressure data for the 3-km grid for the consecutive summer events of 2014.

5.3. Spring Event

Finally, the spring event of 2017 is analyzed. As this event generated the highest wave, it is expected that the responsible front would contain a big pressure jump. The threshold of 2 hPa is exceeded by several locations (Figure 5.11b), being exceeded the most at 4:40. The pressure data for this time moment is visualized in Figure 5.12. At this moment, a very clear front is propagating over the Southern North Sea, responsible for the large pressure jumps.

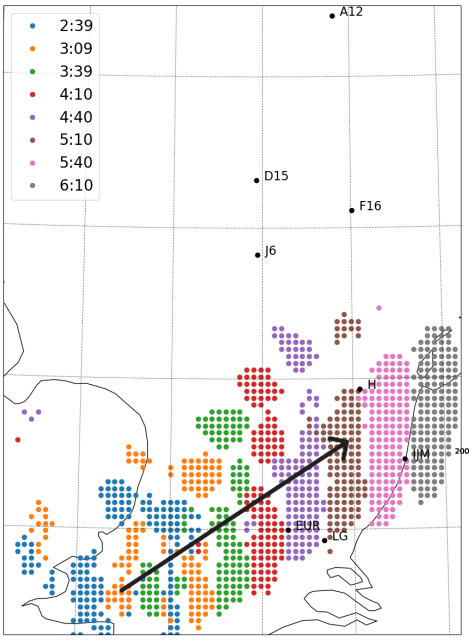

(a) Locations where the threshold of 2 hPa is exceeded, colored by the time of exceedance. The arrow indicates the direction of propagation of the front.

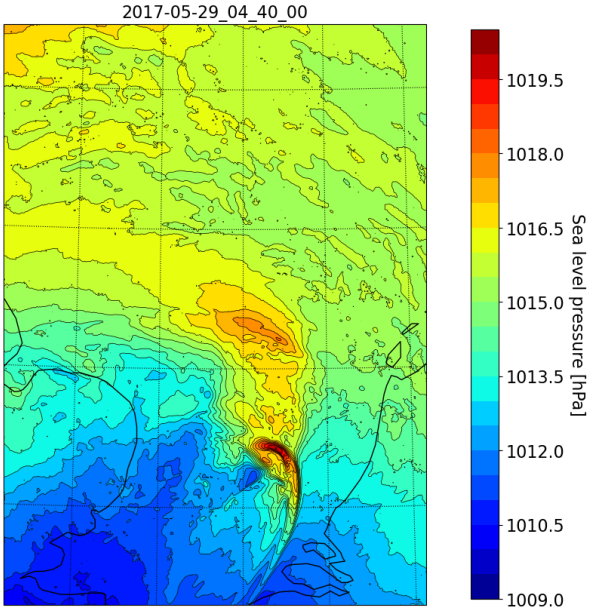

(b) Sea level pressure data for the moment of most exceedances, 4:40.

Figure 5.11: Atmospheric components of the spring event of 2017.

The maximum pressure jump occurs at 52.145 degrees North and 3.057 degrees East. For this location, the sea level pressure data is shown in Figure 5.12. The pressure anomaly shows a big increase of 6.7 hPa, as expected since this event is also responsible for the largest measured waves. The increase is shortly followed by an even larger decrease, resembling the pressure development of the 18th and 19th of July event.

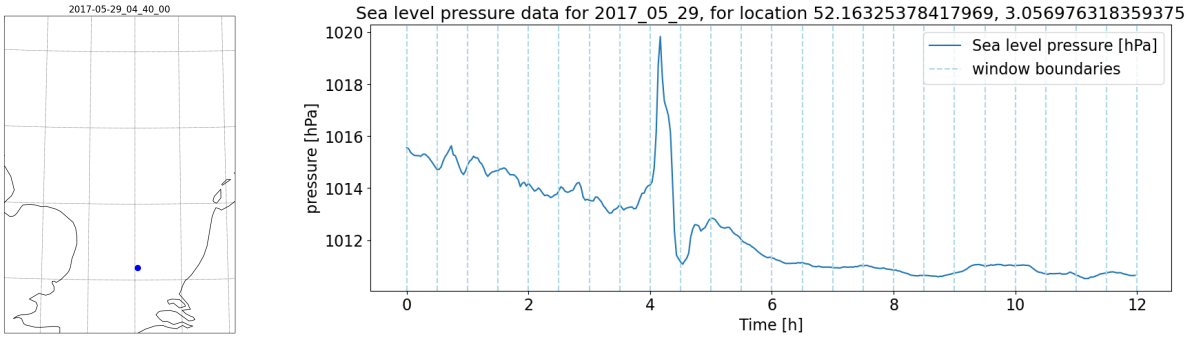

Figure 5.12: The left figure shows the location where the pressure disturbance is largest, at 52.145 degrees North and 3.057 degrees East, with a red dot. The right figure shows the corresponding pressure data at sea level for the 29th of May 2017

5.4. Summary Atmospheric Components

For all six events pressure jumps were found larger than 1 hPa, and for 5 out of 6, also the increased threshold of 2 hPa was exceeded. The only event that did not exceed the 2 hPa threshold (the 28th of January 2015), had its maximum pressure at 1.9 hPa, and therefore the increased threshold is deemed a good threshold to reduce noise, but it cannot be used as a new lower limit for the pressure jump.

Furthermore, the fronts detected for the summer event of 2012 and the consecutive summer events of 2014 travel mainly over land in the smallest simulation grid. In the larger simulation grid it shows that for the summer events of 2014, the front does propagate over the sea at lower latitude, still able to generate a meteotsunami. For the summer event of 2012, this overlap is not found, and therefore, this event cannot definitively be classified as a meteotsunami. The other five are classified as meteotsunamis.

6

Results: Characterization of the Identified Meteotsunamis

6.1. Angle of Incidence and Wavespeeds

For a range of explored wave speeds ranges from 16 to 20 m/s, the location with the smallest distance error is determined via triangulation. This results in a hypothetical origin, that is used to determine the angle of incidence. The locations of the found hypothetical origins are shown in Appendix G, for each considered wave speed per event.

6.1.1. Winter Events

For the winter events, the distance errors are shown in Table 6.1 and Table 6.2.

wave speed [m/s]	J6	IJM	EUR	total
16	32	1442	0	1473
17	224	2504	0	2728
18	9	10689	44	10732
19	5	19132	1	19138
20	0	28277	130	284808

Table 6.1: Distance error for the winter event of 2012.

wave speed [m/s]	D15	EUR	LG	total
16	0	1943	2159	4101
17	0	1313	1485	2798
18	0	184	935	1120
19	0	25	194	219
20	0	1258	194	1552

Table 6.2: Distance error for the winter event of 2015.

For both winter events, all hypothetical origins are located northwest of the stations. For the winter event of 2012, the smallest distance error is found when calculating the hypothetical origin using a mean wave speed of 16 m/s. This wave speed results in the angles of incidence varying between 112 and 126 degrees between the stations (as shown in Figure 6.1a). For the winter event of 2015, the smallest distance error is found when calculating the hypothetical origin with a wave speed of 19 m/s, resulting in angles of incidence between 98 and 111 degrees (as shown in Figure 6.2a).

The mean angles of incidence are close for the two events, with the final angle being 118.65 degrees with respect to the true North for the winter event of 2012 (as shown in Figure 6.1b) and 106.79 degrees with respect to the true North for the winter event of 2015 (as shown in Figure 6.2b). This means both winter events propagated from the Northern part of the North Sea towards the Dutch coast.

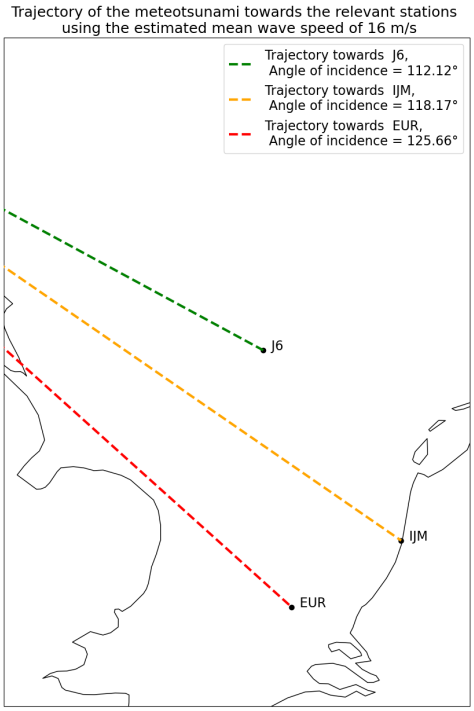

(a) Trajectory of the meteotsunami towards each relevant station, based on the location of the hypothetical origin, calculated via the mean wave speed of 16 m/s.

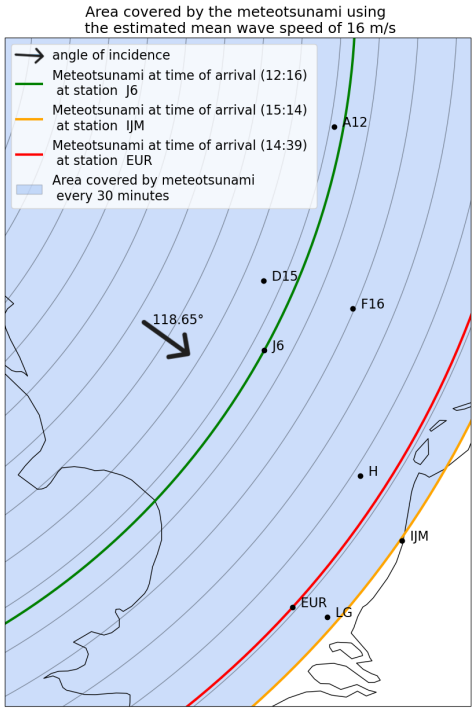

(b) Area traveled by the meteotsunami based on the mean wave speed of 16 m/s. The moments the meteotsunami arrives at the stations are also marked in a different colour.

Figure 6.1: The trajectories of the meteotsunami towards each station and the combined angle of incidence for the winter event of 2012.

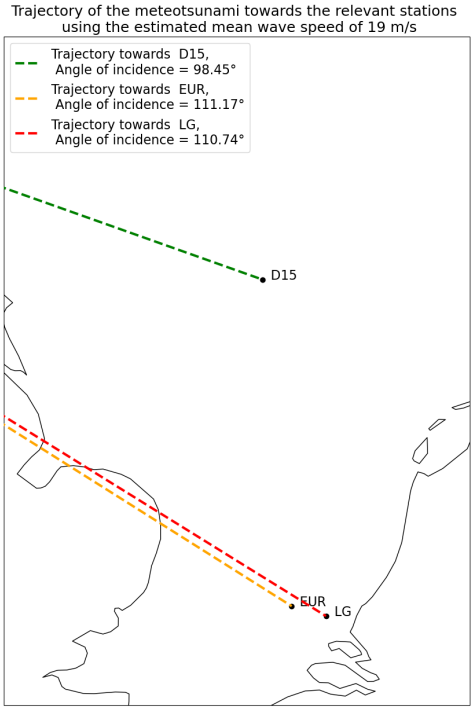

(a) Trajectory of the meteotsunami towards each relevant station, based on the location of the hypothetical origin, calculated via the mean wave speed of 19 m/s.

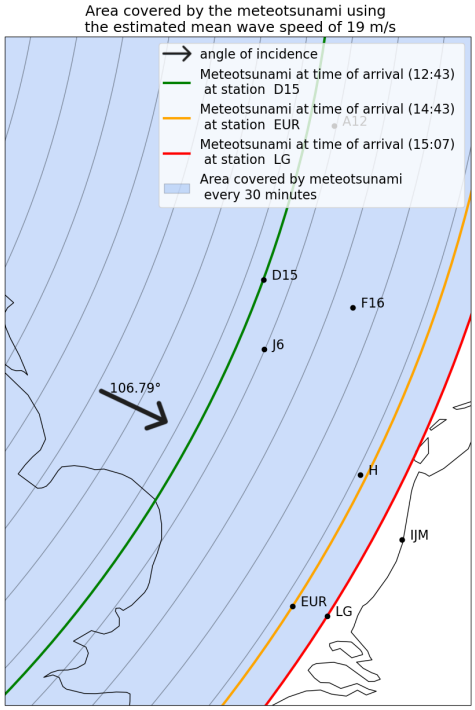

(b) Area traveled by the meteotsunami based on the mean wave speed of 19 m/s. The moments the meteotsunami arrives at the stations are also marked in a different colour.

Figure 6.2: The trajectories of the meteotsunami towards each station and the combined angle of incidence for the winter event of 2015.

6.1.2. Summer Events

Out of the summer events, one is flagged at only two stations, namely the summer event of 2012. This makes it possible that the wave could have traveled either from the northeast towards station H and IJM or from the southwest. Since the front responsible for the generation of this event propagated from the south, it is more plausible that the meteotsunami propagated from the southwest. For these hypothetical origins, the distance errors for the summer event of 2012 are shown in Table 6.3.

wave speed [m/s]	H	IJM	total
16	3	5549	5552
17	82	3625	3707
18	16248	14	16262
19	9024	10	9034
20	3132	4	3136

Table 6.3: Distance error for the summer event of 2012.

These tables show that the distance error is smallest for the origin related to the mean wave speed of 20 m/s. For this wave speed, the angles of incidence are 44 and 46 degrees for station H and IJM, with a mean angle of incidence of 45.17 degrees. This angle is supported by the identical time of occurrence at both stations. For this to happen, the wave must have traveled approximately perpendicular to the stations, resulting in a wave angle of approximately 45 degrees. This means the wave most likely propagated from the English Channel towards the Southern North Sea.

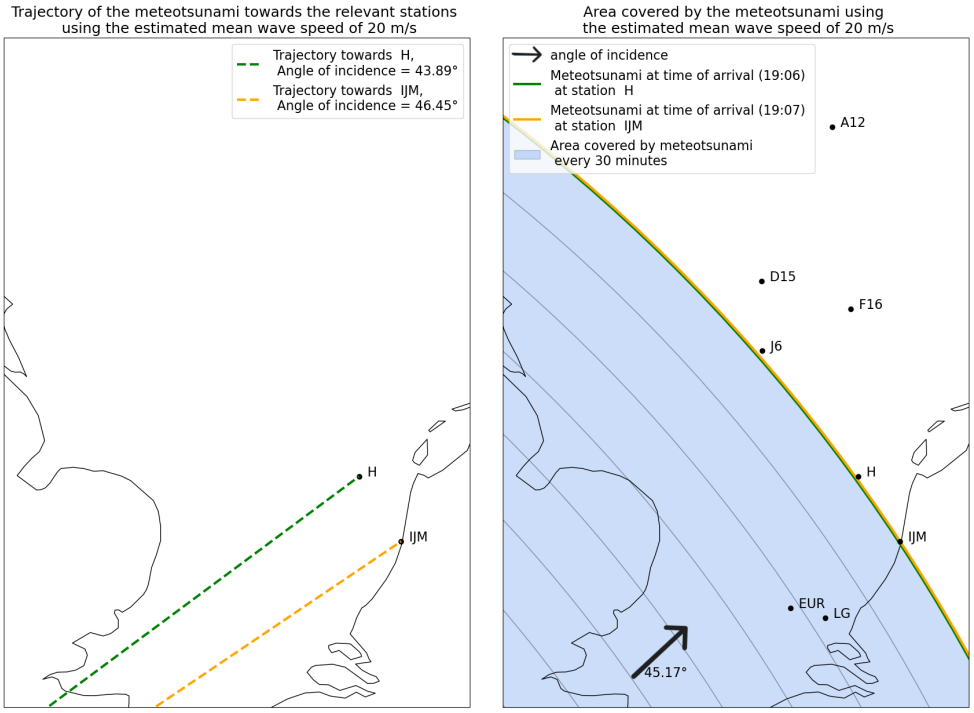

(a) Trajectory of the meteotsunami towards each relevant station, based on the location of the hypothetical origin, calculated via the mean wave speed of 20 m/s.

(b) Area traveled by the meteotsunami based on the mean wave speed of 19 m/s. The moments the meteotsunami arrives at the stations are also marked in a different colour.

Figure 6.3: The trajectories of the meteotsunami towards each station and the combined angle of incidence for the summer event of 2012.

For the consecutive summer events of 2014, the distance errors are shown in Table 6.4 and Table 6.5.

wave speed [m/s]	IJM	EUR	LG	Total
16	22897	1250	0	24147
17	27841	4166	0	32007
18	34504	5366	0	39870
19	40844	6882	0	47727
20	48908	6679	0	55586

Table 6.4: Distance error for the first summer event of 2014.

wave speed [m/s]	A12	F16	J6	total
16	0	0	0	0
17	137	0	248	385
18	11237	1	0	11238
19	21946	0	149	22095
20	31467	0	1488	32955

Table 6.5: Distance error for the consecutive summer event of 2014.

The hypothetical origin calculated with the mean wave speed of 16 m/s resulted in the smallest distance error for both stations. For both cases, the hypothetical origin related to this wave speed is located within the finest domain. In this area, no atmospheric component is found at the times of generation (20:56 on the 18th of July and 1:55 on the 19th of July) that are linked to these origins, as shown in Figure 6.4a and Figure 6.4b. Because of this, these hypothetical origins are not used to compute the angle of incidence.

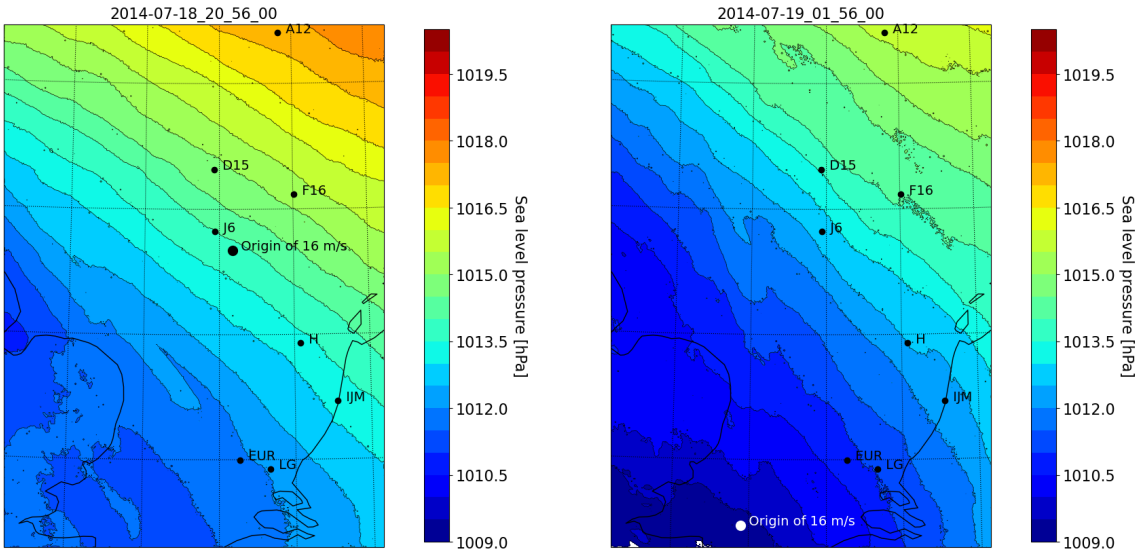

(a) Sea level pressure on 20:56 at the first summer event of 2014.

(b) Sea level pressure on 1:56 during the consecutive summer event of 2014.

Figure 6.4: Sea level pressure for both summer events of 2014. The hypothetical origins computed with the mean wave speed of 16 m/s are marked. In both cases, no atmospheric front shows, and therefore it is not feasible that at these moments, the tsunami events were generated.

The second lowest distance error for both events occurs at the hypothetical origin found with the mean wave speed of 17 m/s. It should be noted that in general, the distance error of the first event is very large, and therefore, the angle of incidence that is found should be interpreted with care. For the first event, this hypothetical origin results in angles of incidence varying between 47 and 48 degrees (as shown in Figure 6.5a, with the mean angle of incidence being 47.73 degrees to the North (as shown in Figure 6.5b). For the consecutive event, the angles of incidence are smaller, varying between 15 and 20 degrees (as shown in Figure 6.6a), with a mean angle of incidence of 16.33 degrees to the North (as shown in Figure 6.6b). This means that most likely this summer event also propagated towards the Southern North Sea from the English channel, which is in line with the conclusions of the atmospheric part of this event, shown in Section 5.2.

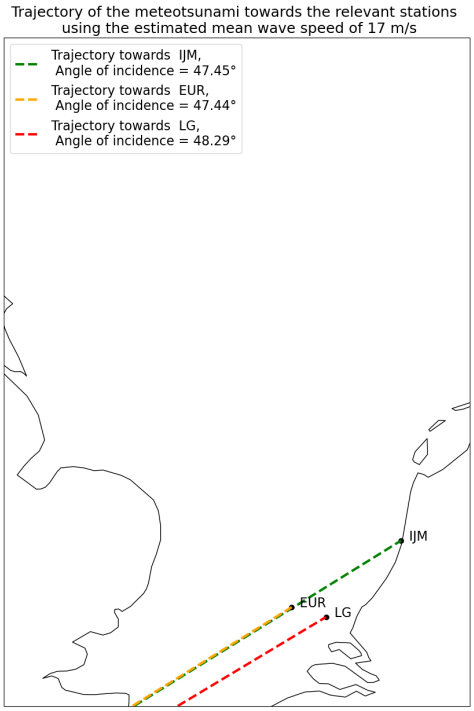

(a) Trajectory of the meteotsunami towards each relevant station, based on the location of the hypothetical origin, calculated via the mean wave speed of 17 m/s.

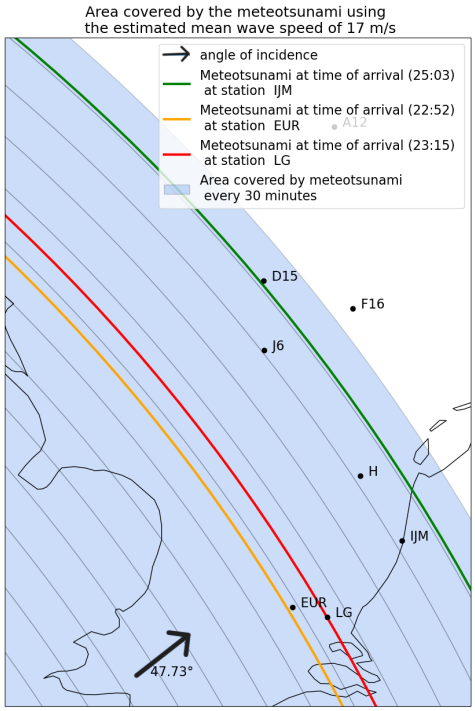

(b) Area traveled by the meteotsunami based on the mean wave speed of 17 m/s. The moments the meteotsunami arrives at the stations are also marked in a different colour.

Figure 6.5: The trajectories of the meteotsunami towards each station and the combined angle of incidence for the first summer event of 2014.

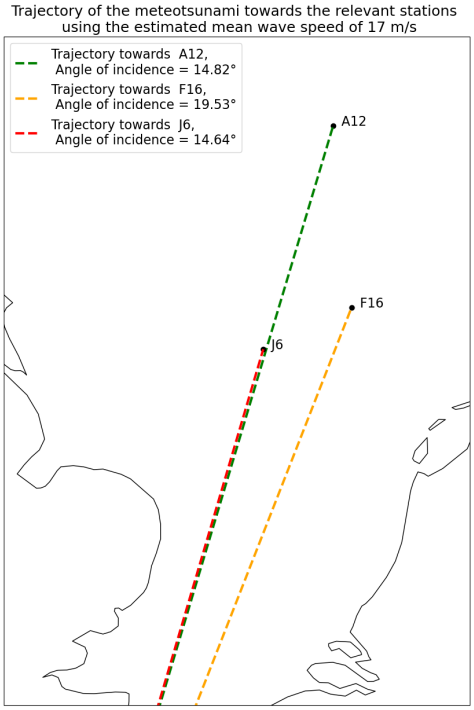

(a) Trajectory of the meteotsunami towards each relevant station, based on the location of the hypothetical origin, calculated via the mean wave speed of 17 m/s.

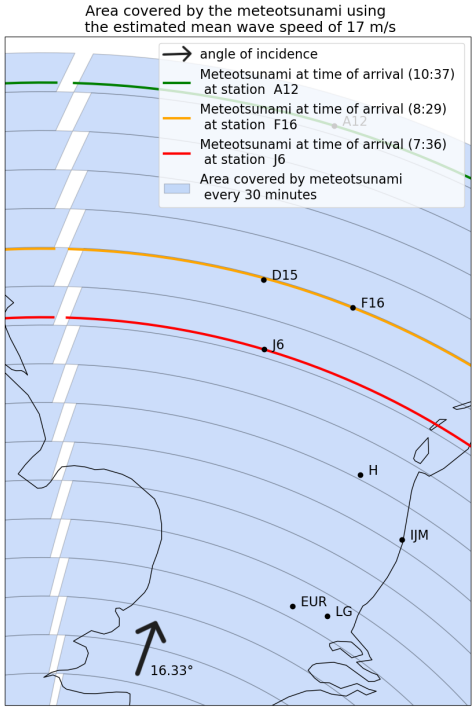

(b) Area traveled by the meteotsunami based on the mean wave speed of 17 m/s. The moments the meteotsunami arrives at the stations are also marked in a different colour.

Figure 6.6: The trajectories of the meteotsunami towards each station and the combined angle of incidence for the consecutive summer event of 2014.

6.1.3. Spring Event

Finally, the potential origins found for the Spring event of 2017, the distance errors are shown in Table 6.6.

	H	IJM	EUR	LG	total
16	16	301	8761	0	9078
17	0	43	5013	29	5085
18	1	12	78	0	91
19	1	5557	3	0	5561
20	0	11064	370	0	11434

Table 6.6: Distance error for the spring event of 2017

The smallest distance error is found for the origin found with the mean wave speed of 18 m/s. This mean wave speed resulted in angles of incidence varying between 47 and 57 degrees (as shown in Figure 6.7a), with the mean angle of incidence being 53.61 degrees from the North. This angle is fairly close to the angles found for the summer event of 2012 and the first summer event of 2014. Furthermore, this angle also overlaps with the trajectory of the atmospheric front, increasing the chances of Proudman resonance. Finally, this angle of incidence shows that the spring event propagated from the English Channel towards the Southern North Sea, like the summer events.

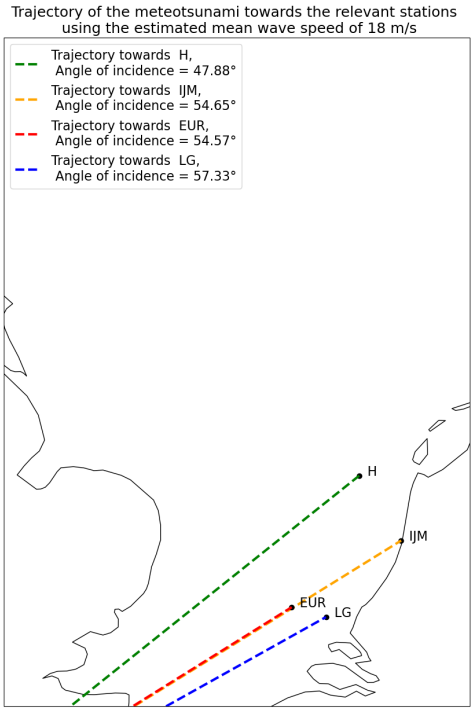

(a) Trajectory of the meteotsunami towards each relevant station, based on the location of the hypothetical origin, calculated via the mean wave speed of 18 m/s.

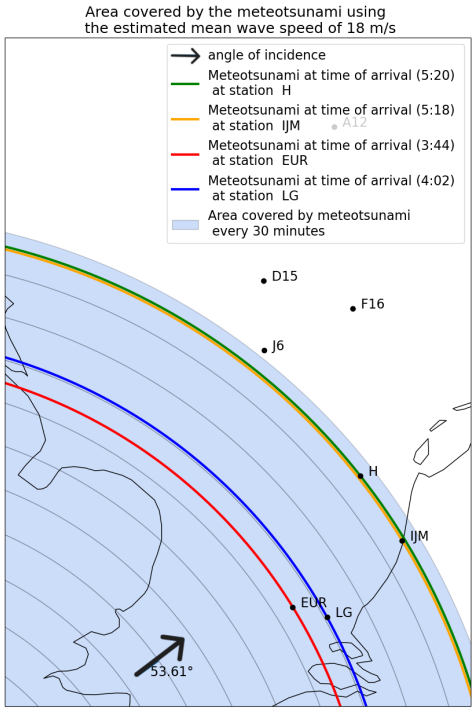

(b) Area traveled by the meteotsunami based on the mean wave speed of 18 m/s. The moments the meteotsunami arrives at the stations are also marked in a different colour.

Figure 6.7: The trajectories of the meteotsunami towards each station and the combined angle of incidence for the spring event of 2017.

6.2. Period

The wave period of each event is determined by comparing the results of the continuous wavelet analysis and the zero-down crossing analysis. The scalograms from which the wavelet coefficients are obtained are presented in Appendix F and the full zero down crossing analysis of each event is presented in Appendix H. For the stations that were added in Section 4.2, no zero-down crossing analysis is available, as the elevation data at these locations is removed during preprocessing, and thus not available.

6.2.1. Winter Events

In Figure 6.8, the wavelet coefficients of the winter event of 2012 are shown over the period axis at the moment of occurrence. All stations show a local maximum at 0.001 Hz, with the exact location at 0.0012 Hz for stations J6 and IJM and 0.0013 Hz for station EUR. These frequencies convert to wave periods of 13 minutes and 53 seconds and 12 minutes and 49 seconds.

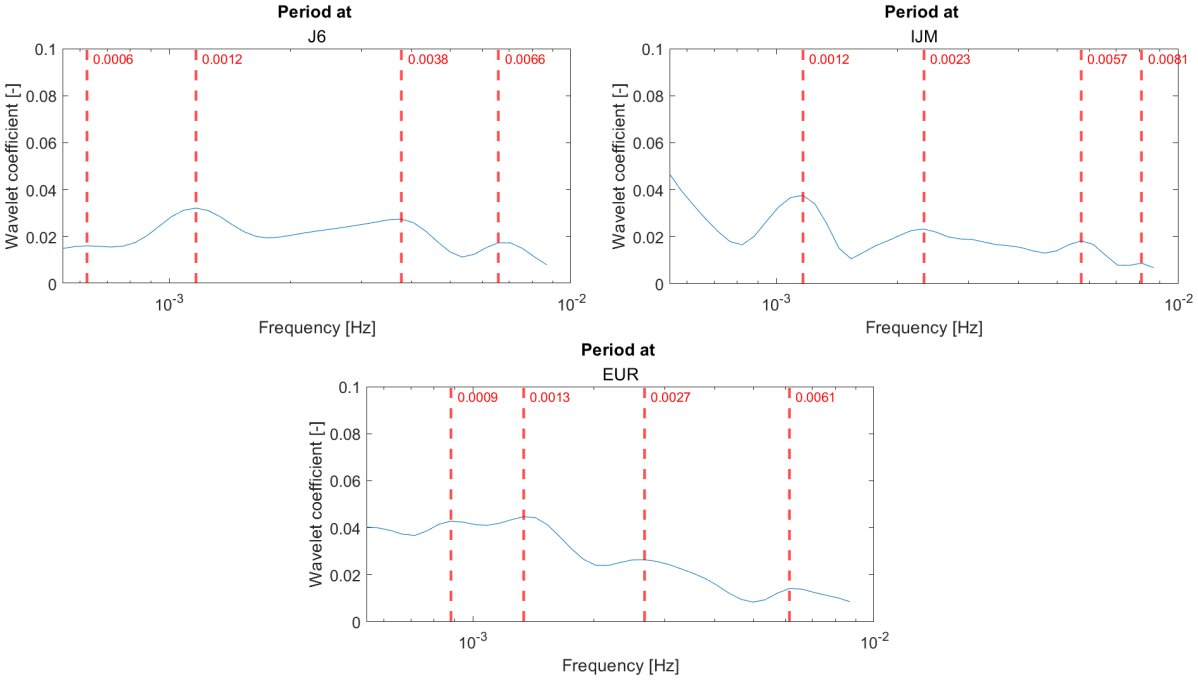

Figure 6.8: Wavelet coefficients at the flagged locations for the winter event of 2012 on the moment of occurrence.

Station IJM also shows a large increase near the 30-minute limit (0.0005 Hz). The scalogram in Section F.1 shows that these higher wavelet coefficients are visible at wave periods around 2 hours. This explains why the elevation data at station IJM looks significantly different from the other two stations, where the wavelet coefficients do not increase around the 2-hour wave period (Figure 6.9).

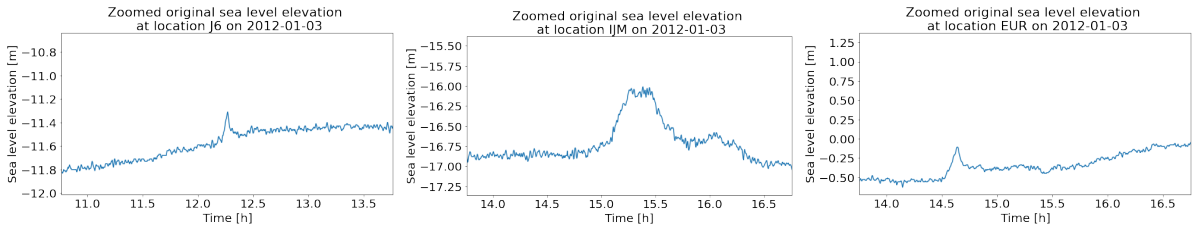

Figure 6.9: Sea level elevation at the relevant stations during the winter event of 2012.

Despite the large increase at the boundary of the frequency limits at station IJM, all stations show a local maximum at wave periods of 13 minutes and 53 seconds and 12 minutes and 49 seconds. The results of the zero-down crossing analysis further support these periods, with the tsunami wave's wave periods found at

13 minutes and 24 seconds at station J6 and 12 minutes at station IJM. This results in a final wave period between 12 and 14 minutes.

For the second winter event, the winter event of 2015, the wavelet coefficients over the period axis are shown in Figure 6.10. Stations D15 and EUR show several local maxima, of which the ones at the lower frequencies (0.0007 and 0.0012 Hz) overlap. the smallest of these also occurs at station LG at 0.0008 Hz. These frequencies of 0.0007 and 0.0008 Hz corresponds to a wave period of 23 minutes and 48 seconds and 20 minutes and 50 seconds.

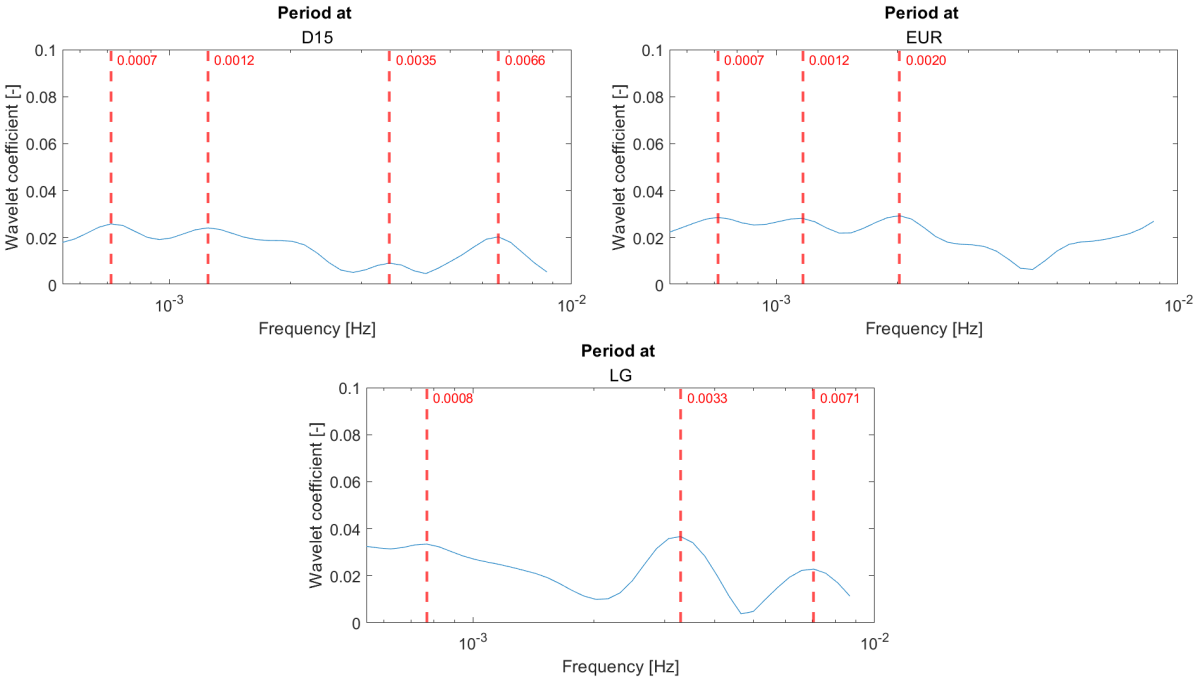

Figure 6.10: wavelet coefficients at the flagged locations for the winter event of 2015

The zero-down crossing analysis is inconclusive for this event, as the stations for which the zero-down crossing is possible show very different wave periods (Figure 6.11). Therefore, the wave period of 20 minutes and 50 seconds to 23 minutes and 48 seconds found via the wavelet method is deemed the most plausible wave period of the winter event of 2015.

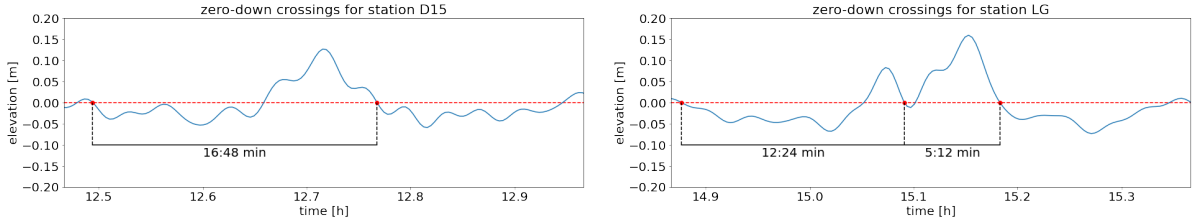

Figure 6.11: Zero-down crossing analysis at the flagged locations for the winter event of 2015.

6.2.2. Summer Events

In Figure 6.12, the wavelet coefficients are shown over the period axis for the summer event of 2012. These coefficients correspond to the moments of occurrence at the flagged stations. The two relevant stations have four local maxima, of which two show up at both, namely the local maximum around 0.0006 Hz and the maximum at 0.0015 and 0.0018 Hz. These correspond to a period of 27 minutes and 47 seconds for the first local maximum and a period range between 11 minutes and 6 seconds to 9 minutes and 15 seconds at the second local maximum.

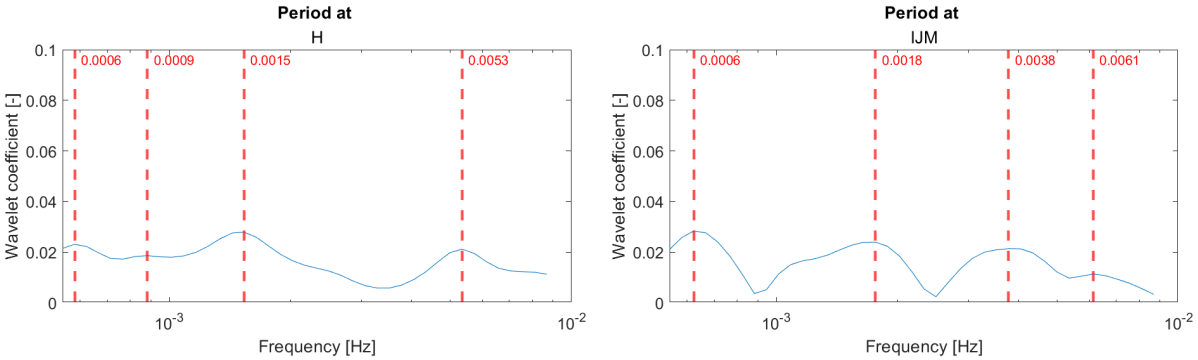

Figure 6.12: wavelet coefficients at the flagged locations for the summer event of 2012

The zero-down crossing shows waves with periods of around 20 minutes, right in the middle of the shorter and longer periods found in the wavelet analysis. When reviewing the graphs for this event, a very small local maximum is visible at station H at 0.0009 Hz, corresponding to 19 minutes. Therefore, the period for this event is estimated to be between 19 and 20 minutes.

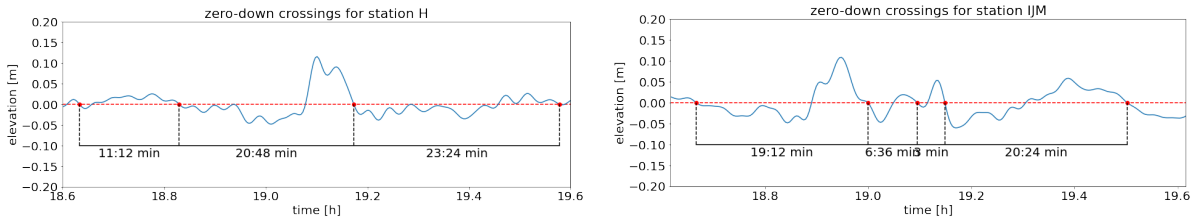

Figure 6.13: Zero-down crossing analysis at the flagged locations for the summer event of 2012

For the first summer event of 2014, the most significant peak in wavelet coefficients shows at 9 minutes and 15 seconds. This period overlaps exactly with the wave period found in the zero-down crossing for this station, as shown in Figure 6.14.

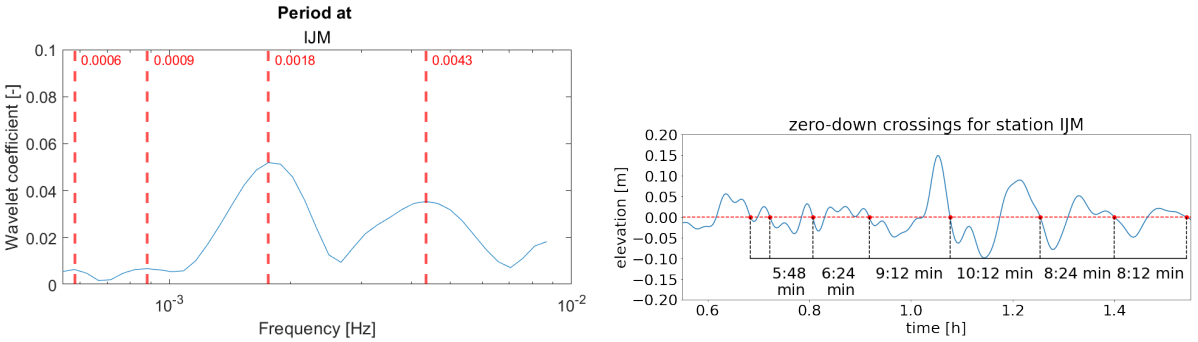

Figure 6.14: Wavelet coefficients and zero down crossing analysis at station IJM for the first summer event of 2014.

Unfortunately, this peak does not appear at the other stations and is therefore unlikely the wave period of the meteotsunami. Figure 6.15 shows the wavelet coefficients over the period axis for the other two stations, corresponding to the time of occurrence at each station. Based on the local maxima, three potential wave periods could be linked to the meteotsunami on this date: 27 minutes and 46 seconds (0.0006 Hz), which occurs at location IJM and EUR, 18 minutes and 31 seconds (0.0009 Hz), which occurs at IJM and LG, and 4 minutes and 23 seconds (0.0038 Hz), which occurs at all three stations.

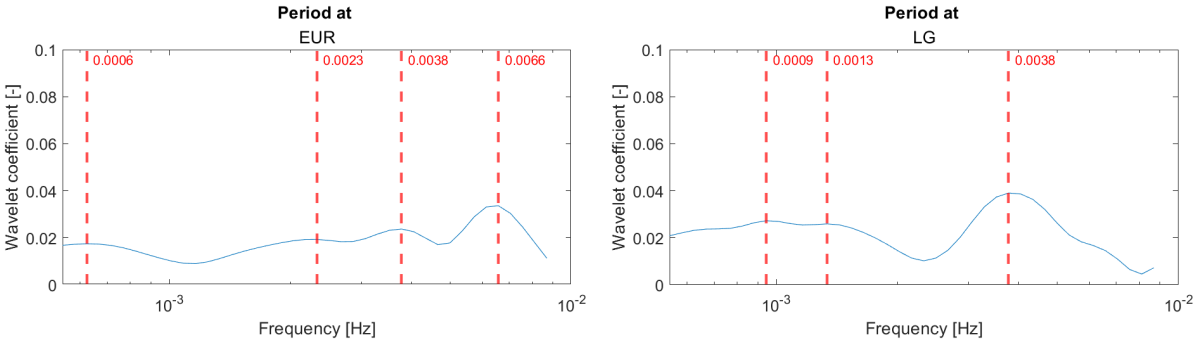

Figure 6.15: Wavelet coefficients at the flagged locations for the first summer event of 2014.

Out of these three, the period of 18 minutes and 31 seconds is closest to the results of the zero-down crossing analysis of station EUR and LG, which determined wave periods of 14 minutes and 12 seconds at EUR and 19 minutes and 24 seconds at station LG. Therefore, based on both analyses, a period band between 14 and 19:30 minutes is estimated for this event, which is quite a broad band.

The consecutive summer event of 2014 shows the most significant local maximum at 5 minutes and 44 seconds (0.0029 Hz) at station A12. This period is in line with the results of the zero-down crossing analysis for this station, similar to the first summer event of 2014 (Figure 6.16).

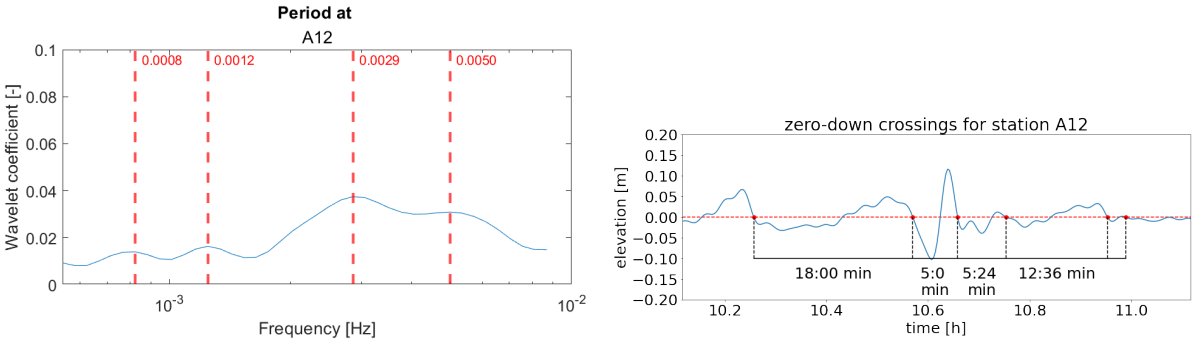

Figure 6.16: wavelet coefficients at the flagged locations for the consecutive summer event of 2014

The wavelet coefficients of the other stations are presented in Figure 6.17. The local maximum found at station A12 at 0.0028 Hz also appears at station J6, at 0.0025 Hz, but does not at station F16. the only wave period that occurs at all three stations is around 20 minutes, with 20 minutes and 50 seconds (0.0008 Hz) at station A12, 18 minutes and 31 seconds (0.0009 Hz) at station F16 and 23 minutes and 48 seconds at station J6.

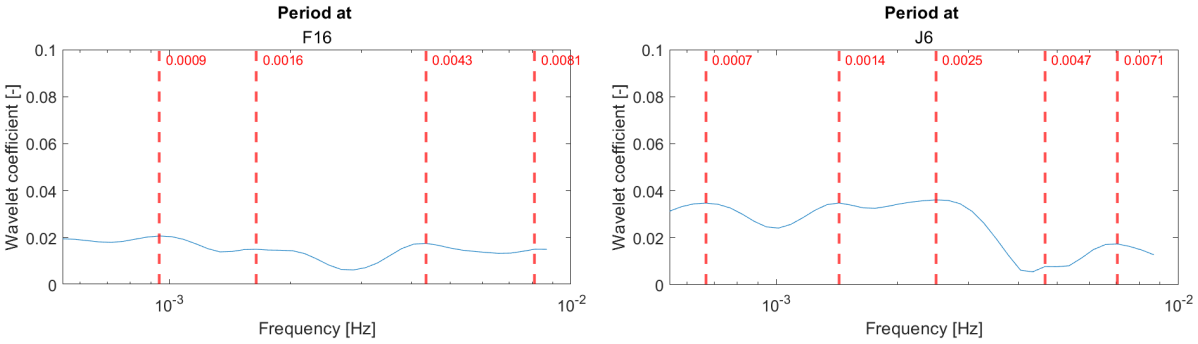

Figure 6.17: wavelet coefficients at the flagged locations for the consecutive summer event of 2014

The zero-down crossing method results in wave periods slightly lower than the results of the wavelet analysis, at wave periods of 17 minutes and 36 seconds for stations F16 and J6. Since the same wave period is found at both stations using the zero-down crossing analysis, these results seem more plausible. Thus the period band is estimated between 17:30 and 18:00 minutes.

6.2.3. Spring Event

Finally, the wavelet coefficients over the period axis of the spring event of 2017 are analyzed. These results are shown in Figure 6.18. One local maximum occurs at all four stations, between 0.001 and 0.002 Hz. The exact locations of these peaks are 0.0018, 0.0013, 0.0012, and 0.0015 Hz at stations LG, H, IJM, and EUR respectively. These correspond to wave periods of 8 minutes and 49 seconds, 12 minutes and 28 seconds, 13 minutes and 22 seconds, and 10 minutes and 51 seconds.

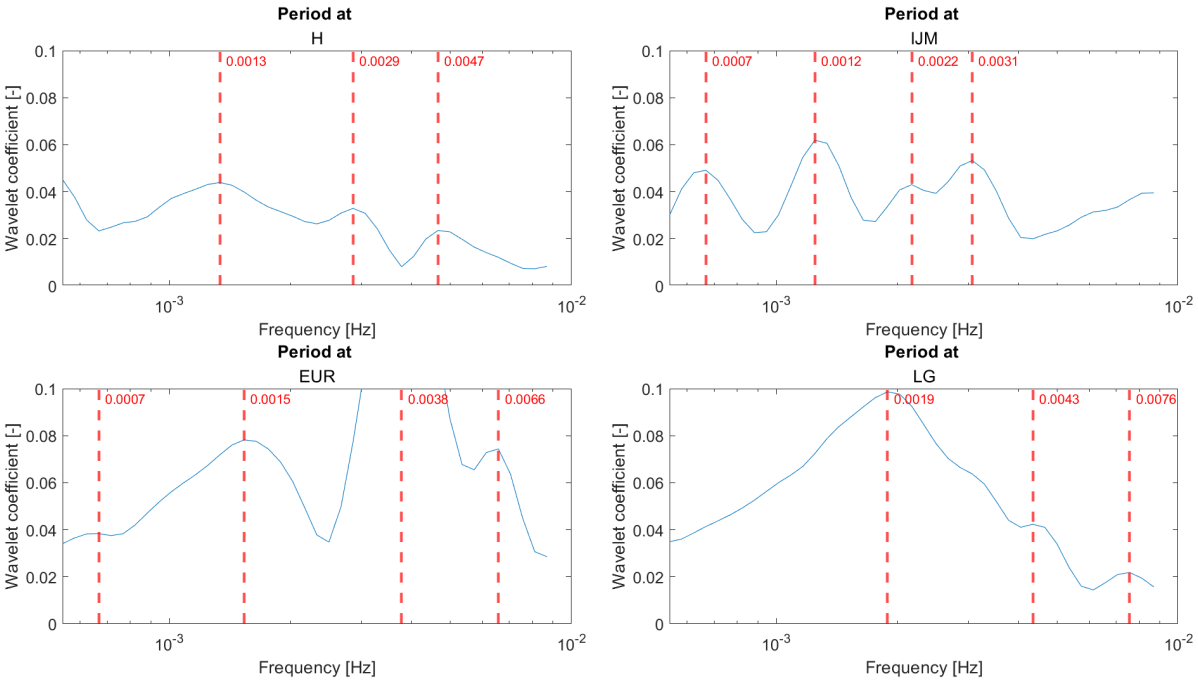

Figure 6.18: wavelet coefficients at the flagged locations for the spring event of 2017

The zero-down crossing analysis resulted in wave periods that are closer together, though a bit higher than the wave periods from the wavelet analysis. These results are shown in Figure 6.19. A wave with a period of approximately 16 minutes passes all four stations. Since the results of the zero-down crossing analysis lie closer together, they are deemed more plausible, thus a period band between 15 and 16:30 minutes is estimated.

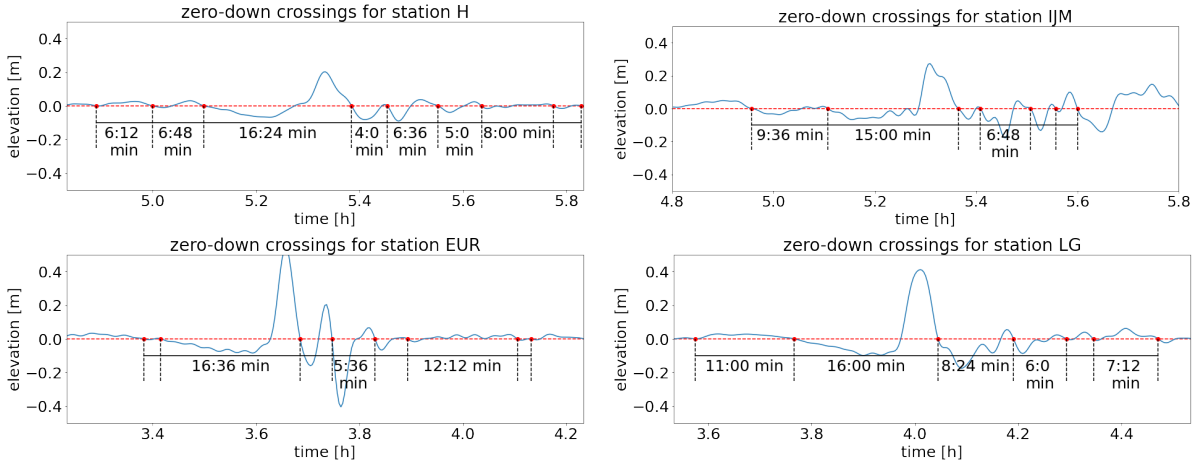

Figure 6.19: Zero-down crossing analysis at the flagged locations for the spring event of 2017

6.3. Wave Height Analysis

The zero-down crossing analysis performed in Appendix H also resulted in a wave height for each relevant station. These results are presented in this section, and put in perspective with the times of occurrence found in Section 4.3.

6.3.1. Winter Events

For the winter event of 2012, the highest wave height is found at station J6 at 22 centimeters. The maximum wave height at location J6 contrasts with the expected growth, as it arrives at this station before the other stations. Therefore, the maximum wave height was expected at station IJM, due to the later arrival time. Likely, the wave has already dissipated some of its energy before reaching the Dutch coast, decreasing the wave height. The identified wave heights are visualized in Figure 6.20.

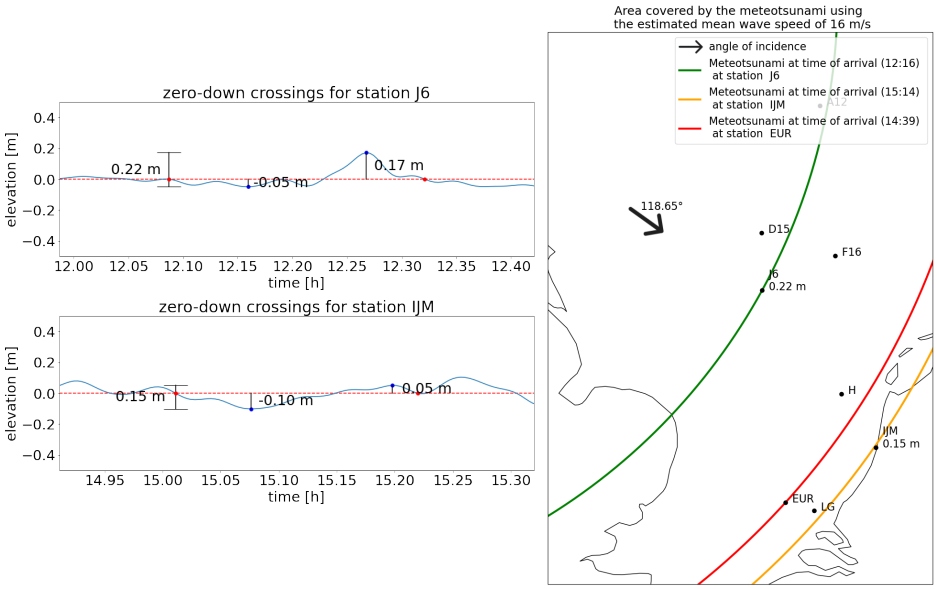

Figure 6.20: Wave height results of the zero-down crossing analysis for the winter event of 2012. The graphs on the left show the minimum and maximum amplitude and the wave height of the relevant wave. The map on the right shows how these wave heights relate to the times of arrival and angle of incidence of the meteotsunami.

For the winter event of 2015, the wave heights at the stations are almost equal, even though they are located pretty far apart. This is likely caused by other mechanisms that amplify and dissipate the energy of the meteotsunami. These waveheights are visualized in Figure 6.21.

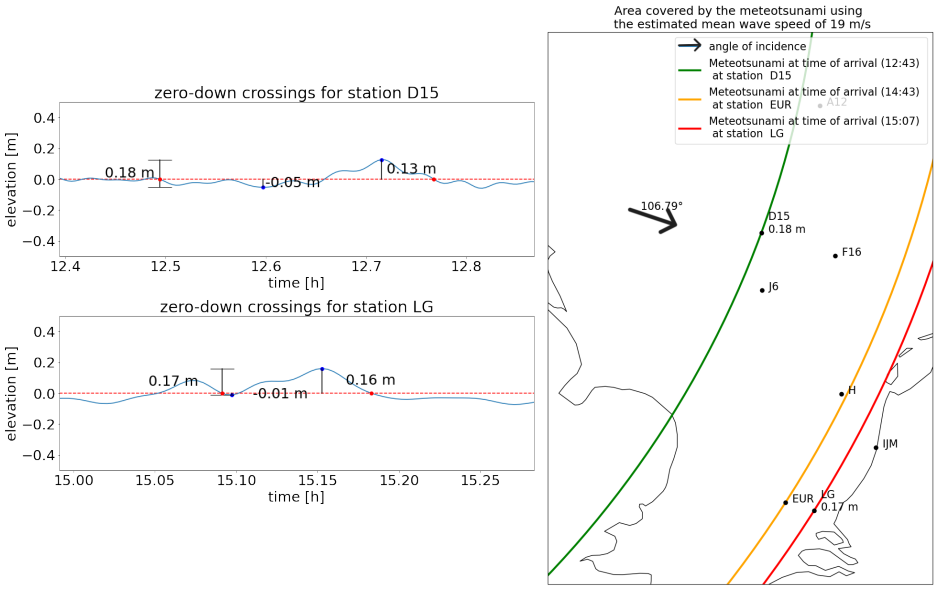

Figure 6.21: Wave height results of the zero-down crossing analysis for the winter event of 2015. The graphs on the left show the minimum and maximum amplitude of the relevant wave and the wave height. The map on the right shows how these wave heights relate to the times of arrival and angle of incidence of the meteotsunami.

6.3.2. Summer Events

The summer event of 2012 reaches its maximum wave height of 16.36 centimeters at location H. The difference in wave heights at both stations is small since both waves arrive at each station at approximately the same moment. Therefore, similar wave heights at both stations are in line with expectations. These wave heights are visualized in Figure 6.22.

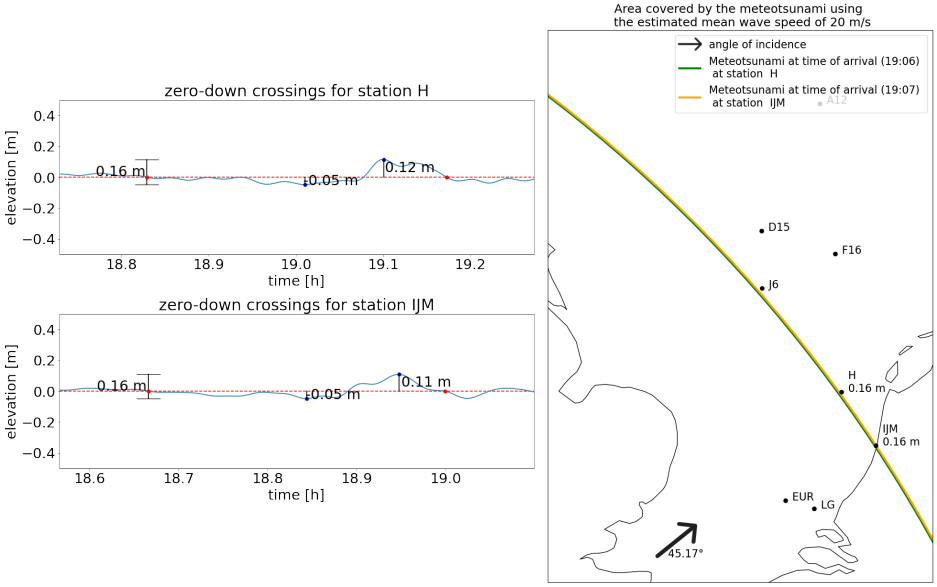

Figure 6.22: Wave height results of the zero-down crossing analysis for the summer event of 2012. The graphs on the left show the minimum and maximum amplitude of the relevant wave and the wave height. The map on the right shows how these wave heights relate to the times of arrival and angle of incidence of the meteotsunami

The first summer event of 2014 shows a gradual increase from the offshore stations to the onshore stations, with the highest wave height at 0.20 meters at stations IJM and LG. The consecutive event shows, the highest amplitude, found at station A12 is close to the wave height at station J6, while the waveheight at station F16 is lower. This is odd, since the wave arrives first at station J6, then at station F16, and then at station A12. The waveheights of both events are visualized in Figure 6.23 and Figure 6.24.

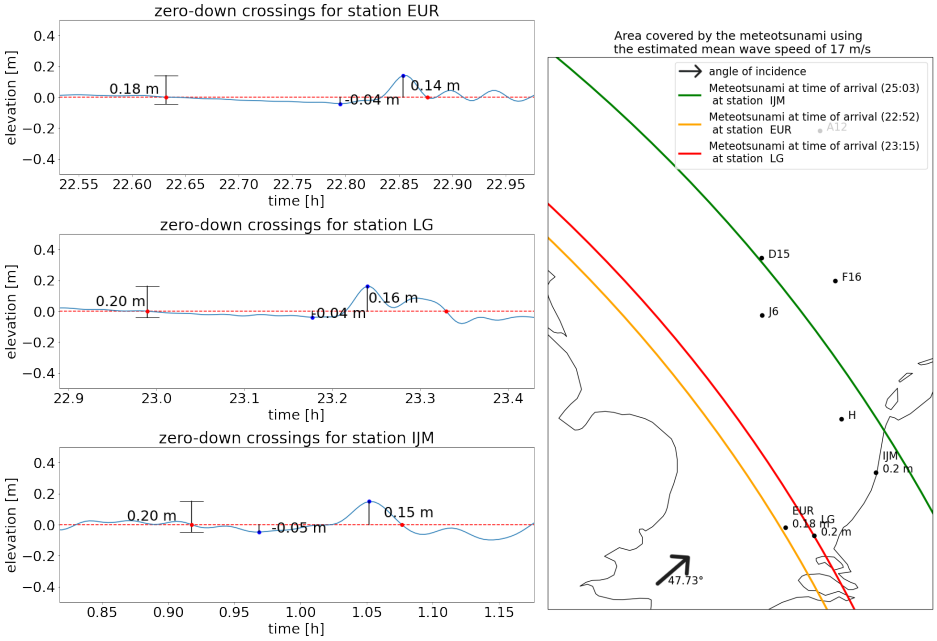

Figure 6.23: Wave height results of the zero-down crossing analysis for the first summer event of 2014. The graphs on the left show the minimum and maximum amplitude of the relevant wave and the wave height. The map on the right shows how these wave heights relate to the times of arrival and angle of incidence of the meteotsunami.

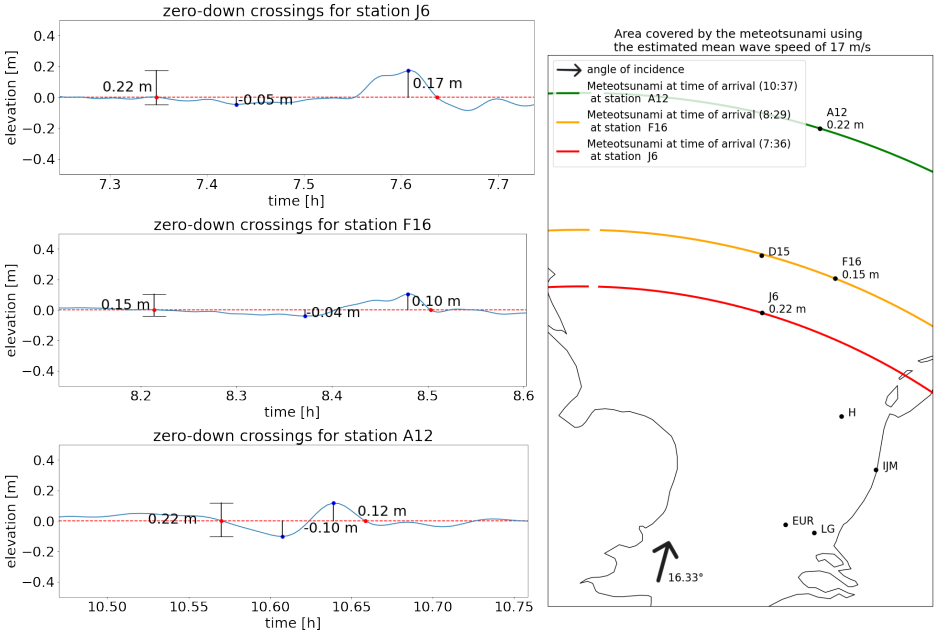

Figure 6.24: Wave height results of the zero-down crossing analysis for the consecutive summer event of 2014. The graphs on the left show the minimum and maximum amplitude of the relevant wave and the wave height. The map on the right shows how these wave heights relate to the times of arrival and angle of incidence of the meteotsunami.

6.3.3. Spring Event

The highest wave height of all events occurred during the spring event of 2017 at station EUR, with a wave height of 62.71 cm. After this station, the wave starts decreasing in height, as at the other stations, even though the wave arrival time is later, the wave height is lower. Also interesting is the difference between the wave heights at station H and IJM, as the waves arrive at approximately the same time. This could be because of the more onshore location of station IJM.

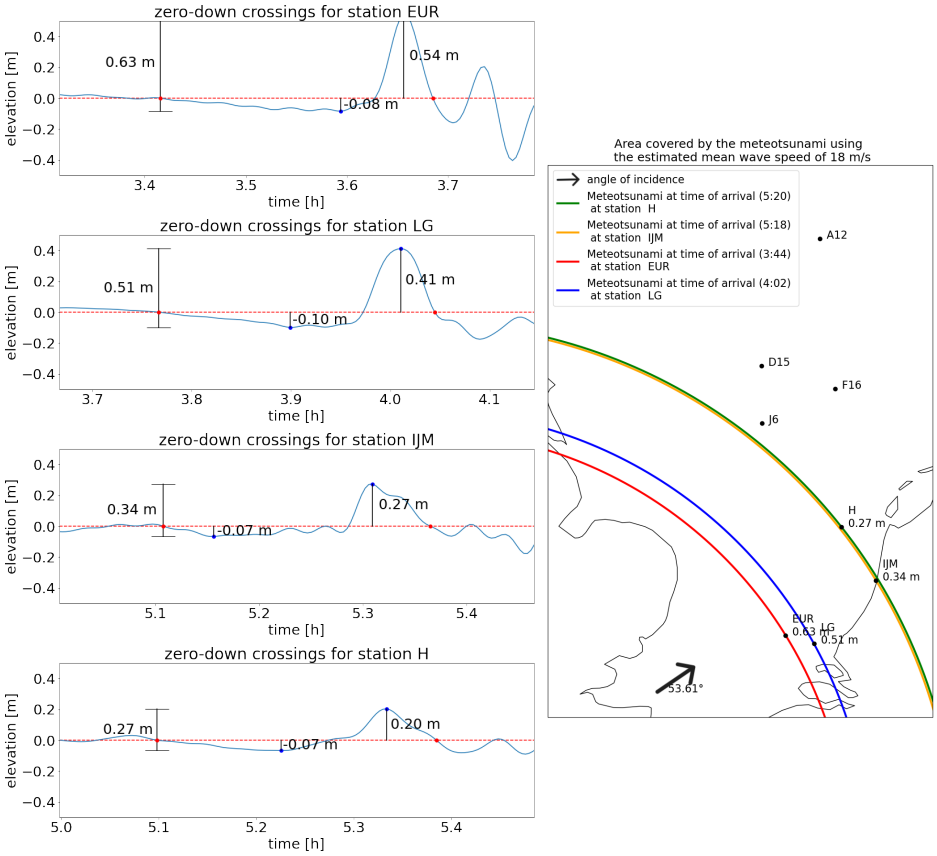

Figure 6.26: Wave height results of the zero-downcrossing analysis for the spring event of 2017. The graphs on the left show the minimum and maximum amplitude of the relevant wave and the wave height. The map on the right shows how these wave height relate to the times of arrival and angle of incidence of the meteotsunami

7

Results: Check for Proudman Resonance in the Identified Events

7.1. Front Trajectory and Atmospheric Forcing Speed

Via the pressure jumps identified in chapter 5, for each event the area covered by the front is determined, as well as the atmospheric forcing speed, when relevant.

7.1.1. Summer Events

The atmospheric fronts of the summer events did not propagate over the ocean grid. Figure 7.1 presents the areas covered by the front over time for all summer events. A distinction, shown by the different colors, is made in the height of the pressure jump within the area covered, to show the layering of the front.

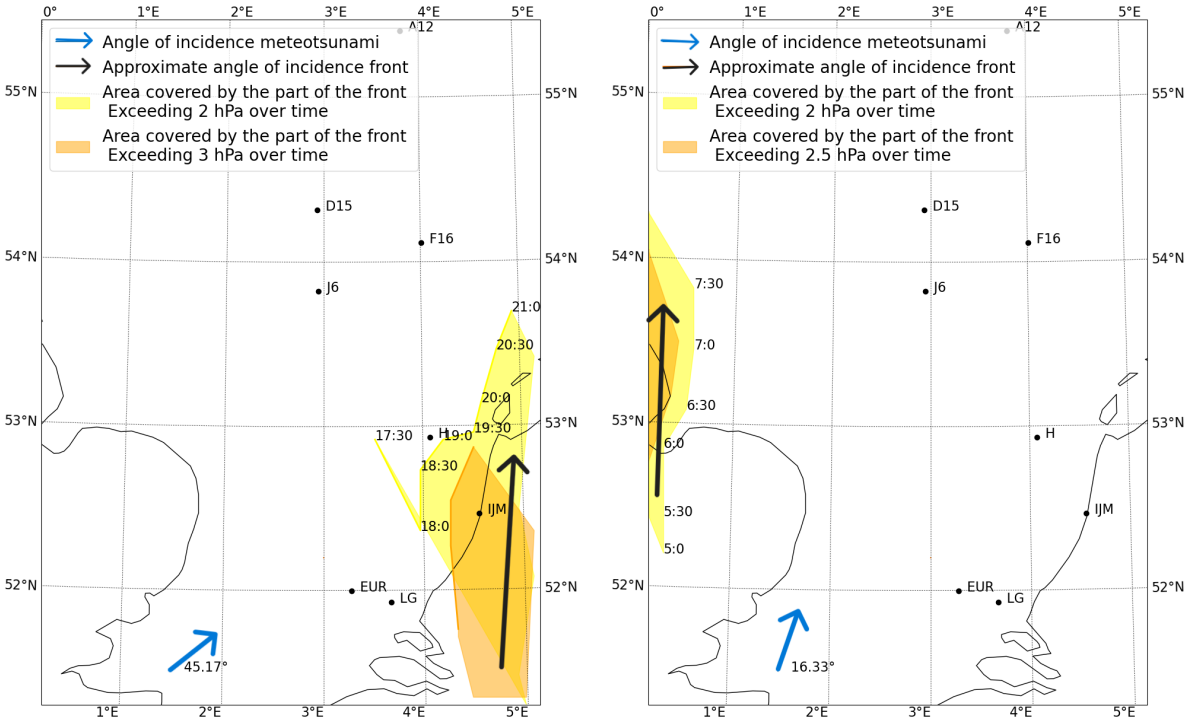

(a) The summer event of 2012.

(b) The summer events of 2014.

Figure 7.1: The covered area by the fronts detected on both events. The color of the zone indicates the pressure jump linked to the location in the front. The darker the color, the higher the pressure jumps within that part of the front. The numbers on the boundaries represent the times at which the pressure jump arrived at that location. The black arrow presents the direction of propagation of the front, while the blue arrow represents the direction of the meteotsunami.

Since Proudman resonance occurs via the interaction between wave speed and atmospheric forcing speed, no Proudman resonance will occur while the front propagates over land. For the summer events of 2014, the front propagates along the western boundary of the investigated grid. In chapter 5, it was found that outside of this investigated grid, the front passes over the sea between England and France, South of the covered area of the front shown here. Connecting the known location outside the investigated grid to the trajectory found within the investigated grid, it is concluded that the front propagated Northward over the English mainland between them. The angles of incidence support the hypothesis that the front was generated at a lower latitude. However, after generation, the front propagates over land, and thus no further amplification by Proudman resonance can occur. Therefore the atmospheric forcing speed is not calculated.

The front of the summer event also mainly propagates over land, though around 18:00 it starts propagating overseas (Figure 7.1a). At this moment, Proudman resonance could potentially still amplify the wave. Figure 7.2 shows that the meteotsunami indeed overlaps with the front around the moment of arrival at the stations (approximately 19:00). In this area, Proudman resonance could still occur, but only around the time the wave arrives at station H and IJM. Before this time, the front still propagated over land, making Proudman resonance impossible. Therefore, Proudman resonance can not have played a role in the wave growth before the wave arrives at the stations, and thus the atmospheric forcing speed is not further investigated.

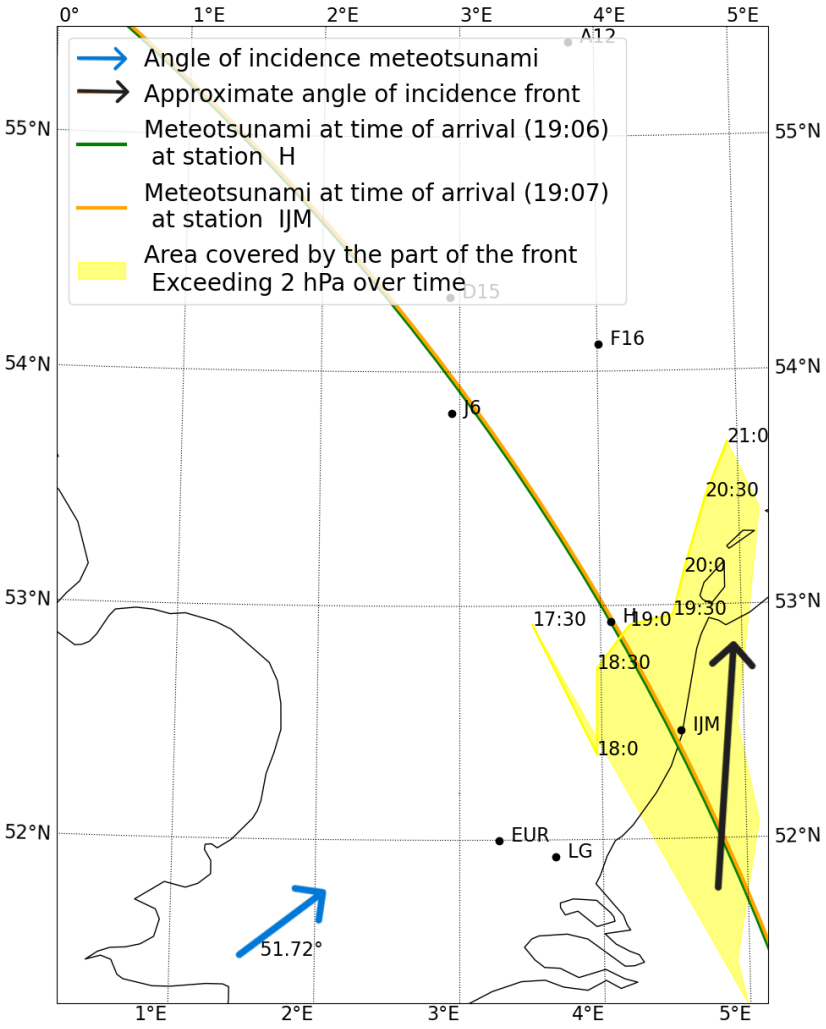

Figure 7.2: Overlap between the atmospheric front and the meteotsunami wae. The numbers at the boundaries show the time at which the front was at that location, and the lines show the times of arrival of the wave at the station. This figure shows a clear overlap between the meteotsunami and the front at these moments.

7.1.2. Winter Events

The two winter events are linked to fronts that propagated overseas, resulting in potential Proudman resonance. The first analyzed event is the winter event of 2012. The trajectory of the front over time and the linear estimates of this trajectory are shown in Figure 7.3a and Figure 7.3b.

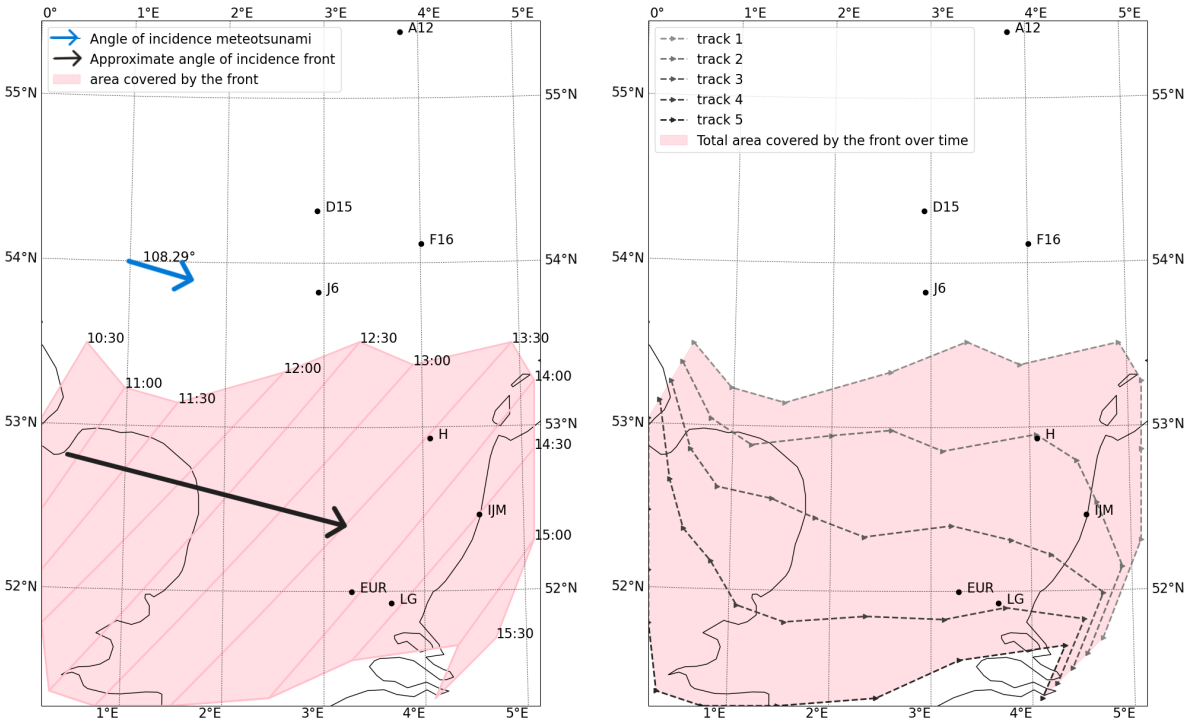

(a) Area surpassed by the relevant part of the front per timestep.

(b) Linear estimations of the fronts trajectory

Figure 7.3: The trajectory of the front that is linked to the winter event of 2012. Based on the zones defined in the left figure, 5 points are identified along each vertical boundary. These points have been connected between the zones to create the five trajectories shown in the right figure.

The tracks in Figure 7.3b are used to calculate the propagation speed of the trajectory (Table 7.1). Per time window, the mean of the speeds of the tracks estimates the speed of the front. The speeds vary between 20 and 30 m/s over time, without a clear rising or falling trend. The table shows that the speeds of the tracks further from the center generally differ more from the mean calculated speed.

Track	10:30-11:00	11:00-11:30	11:30-12:00	12:00-12:30	12:30-13:00
1	22.30	20.82	41.64	30.78	21.76
2	23.98	18.17	30.58	22.68	20.86
3	26.72	17.59	21.00	17.91	19.96
4	30.23	19.32	16.12	19.28	19.06
5	34.27	22.87	20.03	25.93	18.15
Mean	27.50	19.75	25.87	23.32	19.96
Track	13:00-13:30	13:30-14:00	14:00-14:30	14:30-15:00	15:00-15:30
1	38.13	16.64	25.69	34.28	39.86
2	35.78	18.245	17.23	26.06	35.35
3	33.42	23.11	16.17	24.24	30.84
4	31.05	29.80	23.69	30.13	26.32
5	28.71	37.44	34.68	40.58	21.81
Mean	33.42	25.05	23.49	31.06	30.84

Table 7.1: Calculated atmospheric forcing speeds (in m/s) for the tracks defined in Figure 7.3b, for the winter event of 2012. The times on top represent the time window over which the speed was calculated.

The covered area of the front over time and the linear estimates of the trajectory for the winter tsunami of 2015 are shown in Figure 7.4a and Figure 7.4b. It should be noted that the timestep between points is 1 hour between 4:30 and 5:30, since the flagged points at 5:00 were not representative of the rest of the trajectory and were therefore classified as outliers.

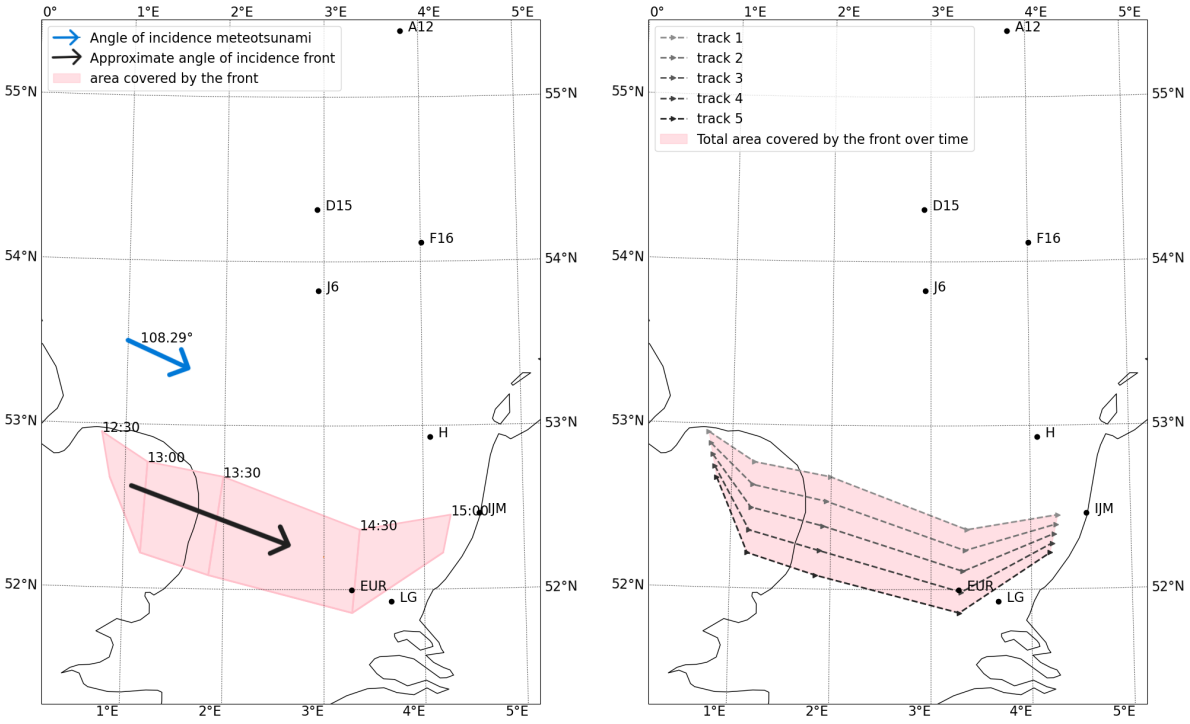

(a) Covered area by the front per timestep for the winter event of 2015

(b) Front trajectory for the winter event of 2015.

Figure 7.4: The trajectory of the front that was detected for the winter event of 2015. Based on the zones defined in the left figure, 5 points are identified along each vertical boundary. These points have been connected between the zones to create the five trajectories shown in the right figure.

For the tracks defined in Figure 7.4b, the atmospheric forcing speeds are computed for each time window, shown in Table 7.2. These show a general mean wave speed of around 27 m/s, with a much higher mean wave speed for the final window, the shape of this trajectory can explain that. Since the tracks converge, a longer distance is covered over this time window, resulting in a larger velocity. These converging tracks are a consequence of the definition of the front. Since a front is a dynamic system, over time the pressure change that first surpassed the threshold might have decreased. Due to the methodology, this point will then not be showing in the trajectory anymore. This means the track continues to the closest point that still exceeds the threshold, which is often closer to the center of the front, resulting in the converging tracks.

track	12:30-13:00	13:00-13:30	13:30-14:30	14:30-15:00
1	20.63	29.00	27.65	34.85
2	22.25	28.66	27.74	35.81
3	24.60	28.15	27.86	37.25
4	27.50	27.66	28.00	39.10
5	30.79	27.19	28.17	41.32
mean	25.15	28.13	27.88	37.67

Table 7.2: Calculated atmospheric forcing speeds (in m/s) for the tracks defined in Figure 7.4b, for the winter event of 2015. The times on top represent the time window over which the speed was calculated.

7.1.3. Spring Event

The final event for which the atmospheric forcing speed has been computed is the spring event of 2017. As shown in chapter 5, the pressure disturbance is characterized by a strong increase and decrease in pressure. Therefore instead of only the threshold of 2 hPa, multiple areas based on multiple thresholds have been computed. These are shown in Figure 7.5.

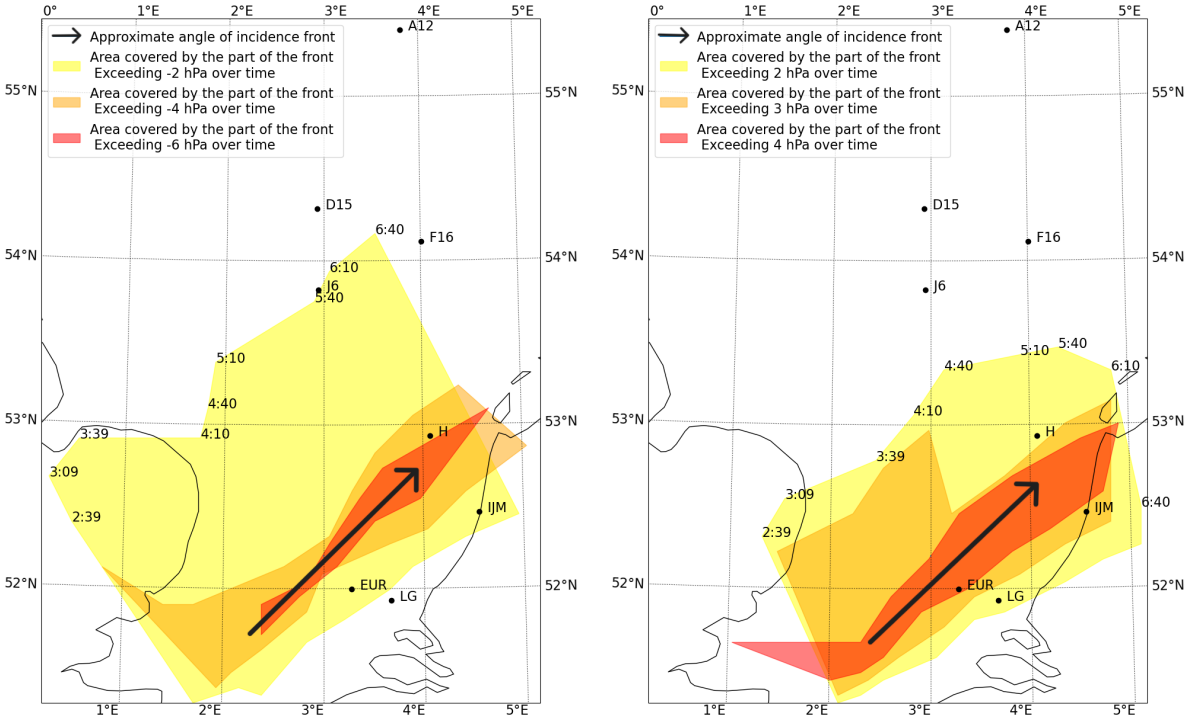

(a) Covered area by the front, dependent on the pressure threshold for which it was calculated, for the spring event of 2017. For this figure the pressure thresholds used are negative, representing the pressure drop.

(b) Covered area by the front, dependent on the pressure threshold for which it was calculated, for the spring event of 2017. For this figure the pressure thresholds used are positive, representing the pressurejump.

Figure 7.5: covered areas by the front linked to the spring event of 2017. The formulated fronts for both the pressure increase and decrease are shown.

Both figures show that a higher pressure-threshold results in a narrower trajectory. These narrower trajectories have a smaller standard deviation of the mean wave speed, as the covered distances by the different parts of the fronts lay closer together. For a wider front, it is much more likely the outer boundaries travel at different wave speeds, resulting in a bigger standard deviation from the computed mean wave speed.

The downside to this is that only using the part of the front that is exceeded by a very high threshold removes a large part of the information on the rest of the front. For example, the area covered by the front bounded by a pressure decrease larger than 6 hPa, might result in an accurate estimate of the forcing speed of this area. Yet, the forcing speeds of the upper boundary of the front bounded by a decrease of 2 hPa are not represented by this main wave speed, even though this part of the front could generate and amplify a meteotsunami.

Based on these arguments, the choice is made to use a mean wave speed that represents the full front, even with larger standard deviations. Therefore, the choice is made to use the front bounded by a pressure jump of 2 hPa for this event. The area covered by this front and its estimated trajectories are shown in Figure 7.6a and Figure 7.6b.

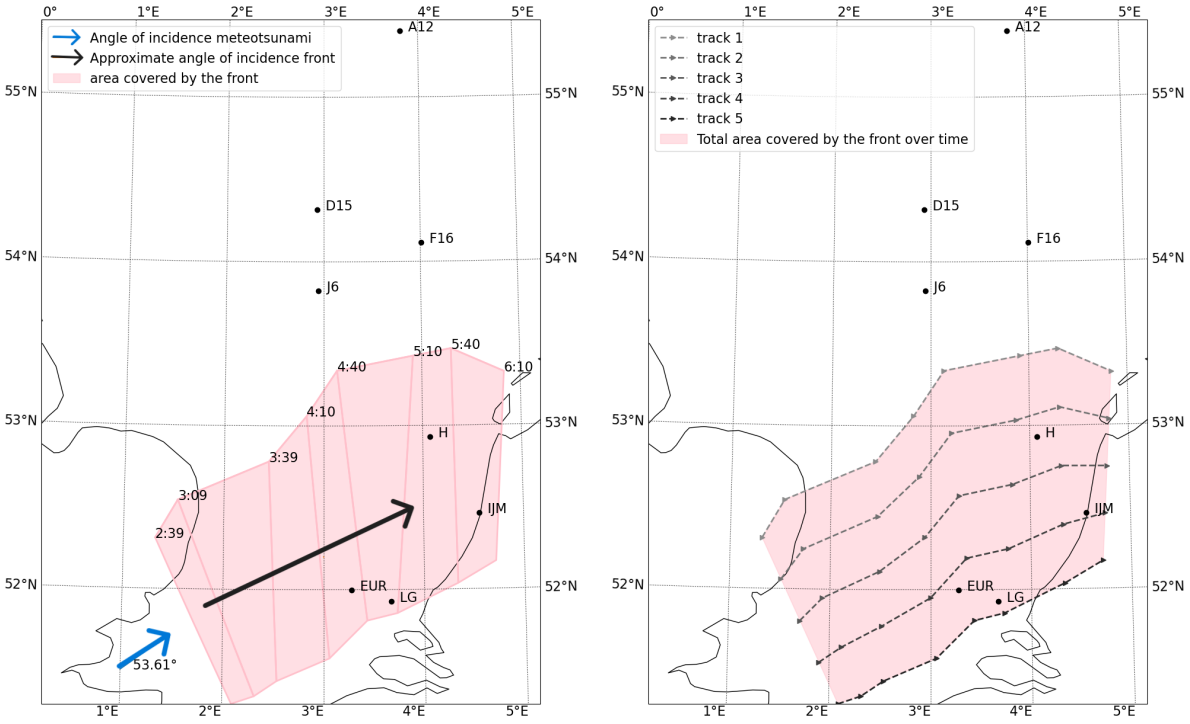

(a) Covered area by the front per timestep for the spring event of 2017

(b) Front trajectory for the spring event of 2017.

Figure 7.6: The trajectory of the front that was detected for the spring event of 2017. Based on the zones defined in the left figure, 5 points are identified along each vertical boundary. These points have been connected between the zones to create the five trajectories shown in the right figure.

Via the defined tracks, the atmospheric forcing speeds shown in Table 7.3 are calculated. It shows that the most southern track contains some outliers compared to the other forcing speeds. However, this is a plausible result since it is furthest from the center of the front. the mean atmospheric forcing speed does not develop by a lot over time and fluctuates around 20 m/s.

track	2:39-3:09	3:09-3:39	3:39-4:10	4:10-4:40	4:40-5:10	5:10-5:40	5:40-6:10
1	9.07	10.34	21.85	20.26	11.82	25.64	16.71
2	10.32	17.11	21.48	20.26	16.27	22.72	16.36
3	12.13	23.88	21.44	20.31	20.64	19.88	17.22
4	14.29	30.59	21.72	20.43	24.94	17.15	19.11
5	16.68	37.22	22.32	20.59	29.16	14.57	21.76
mean	12.50	23.82	21.76	20.37	20.57	19.99	18.23

Table 7.3: Calculated atmospheric forcing speeds (in m/s) for the tracks defined in Figure 7.6b, for the spring event of 2017. The times on top represent the time window over which the speed was calculated.

7.2. Check for Proudman Resonance

For the three events that have a front propagating over water, it is verified whether Proudman resonance could have occurred. For this to happen, it is checked whether the atmospheric forcing speed overlaps with the shallow water wave speed, so that the Froude number is close to 1. Furthermore, it is checked whether the front overlaps with the meteotsunami for each point in time. If both of those criteria are met, the chances of Proudman resonance are very likely. In Appendix I, the entire time window over which the front propagates over the Southern North Sea is shown for each event. In this section, the time windows where Proudman resonance could have occurred are highlighted.

7.2.1. Winter Events

For the winter event of 2012, the atmospheric forcing speeds of the front are close to the shallow water wave speeds of the regions the front passes. This overlap is strongest in the later stages of the event, In the earlier stages, the found Froudnumbers are a bit above 1. Over time, the Froude numbers lower, reaching 1 between 11:30 and 12:00 and changing to Froude numbers below 1 at the later stages of the trajectory (Figure 7.7a).

Comparing the area covered by both the front and the meteotsunami, a strong overlap is visible, especially in the earlier stages. Over time, the front travels faster than the meteotsunami, decreasing the overlap between the two (Figure 7.7b). It is feasible that also at these later time windows, a stronger overlap between the front and the meteotsunami occurs than shown in these figures, as the area covered by the meteotsunami is calculated using one mean wave speed, instead of the varying depth-dependent shallow water wave speed.

For this event, the Froude numbers are within near-Proudman resonant conditions along the entire timespan of the front. Furthermore, a significant overlap between the area covered by the front and the meteotsunami is observed. Therefore, Proudman resonance has very likely amplified this meteotsunami event.

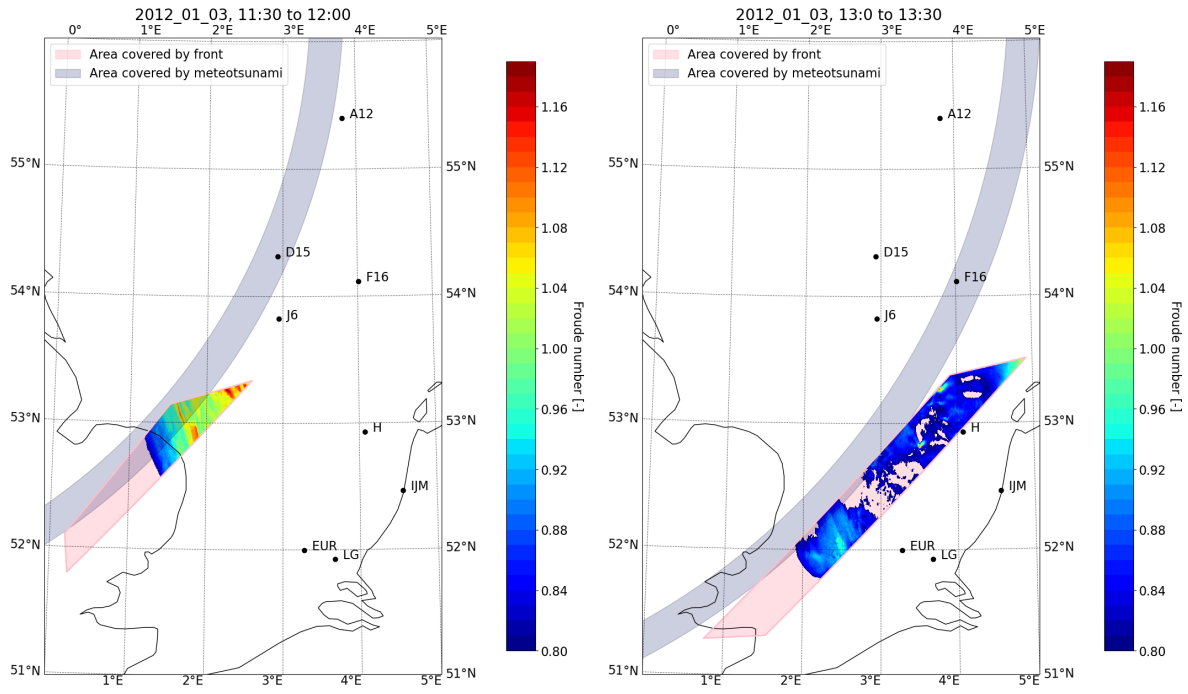

(a) Propagation of the meteotsunami and the atmospheric front between 11:30 and 12:00.

(b) Propagation of the meteotsunami and the atmospheric front between 13:00 and 13:30.

Figure 7.7: Proudman simulations for the winter event of 2012. The colored area represents the Froude numbers in the area the front passes during this time window.

For the other winter event, the winter event of 2015, the areas covered by the front and the meteotsunami overlap even more than during the winter event of 2012. Especially between 13:30 and 14:30, the area covered by the front and the meteotsunami is almost identical. Over this period, the Froude numbers are in near Proudman-resonant conditions, with some areas even close to strict Proudman-resonant conditions. Similar to the other winter event, Proudman resonant conditions appear along the entire trajectory of the front (Figure 7.8). The strong overlap between the meteotsunami and the front combined with the constant near Proudman-resonant conditions make it highly likely that Proudman resonance also amplified this meteotsunami event.

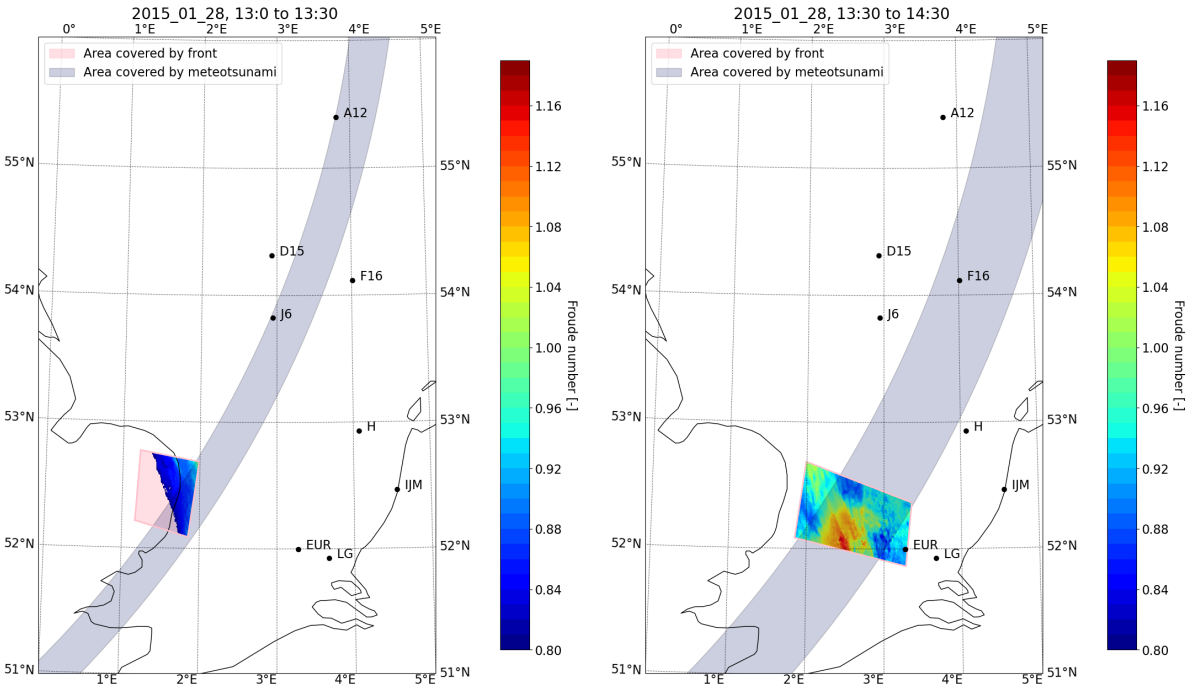

(a) Propagation of the meteotsunami and the atmospheric front between 13:00 and 13:30.

(b) Propagation of the meteotsunami and the atmospheric front between 13:30 and 14:30.

Figure 7.8: Proudman simulations for the winter event of 2015. The colored area represents the Froude numbers in the area the front passes during this time window.

7.2.2. Spring Event

Finally, the spring event of 2017 is analyzed. For this event, several zones where near Proudman resonance could occur are identified, mainly in the earlier stages of the front trajectory. Here, the Froude numbers vary mainly between 1 and 1.2, showing potential for Proudman resonance.

The trajectory of the tsunami overlaps with the northern part of the front over the entire timespan. It is possible the wave and the front overlap even more than is shown in the figures, as variations in wave speed are not accounted for. This strong overlap between the area covered by the meteotsunami and the front is strong combined with the near-one Froude numbers over the entire timespan, make it highly likely again Proudman resonance amplified this event. The atmospheric front originates Southwest of the investigated grid, in line with the wave. It is hypothesized that in this area, an even stronger overlap of both the wave and the front, as well as the front speed and wave speed is found, resulting in an even larger amplification. Unfortunately, this cannot be verified since the atmospheric pressure data is not available in these areas.

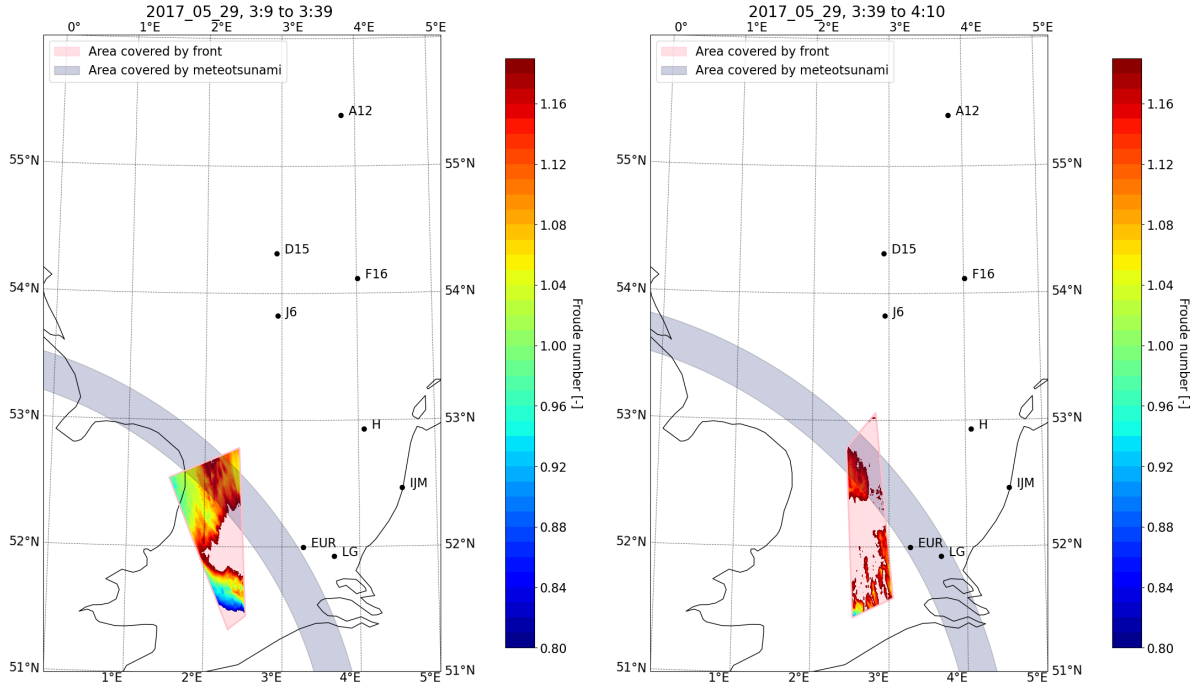

(a) Propagation of the meteotsunami and the atmospheric front between 3:09 and 3:39.

(b) Propagation of the meteotsunami and the atmospheric front between 3:39 and 4:09.

Figure 7.9: Proudman simulations for the spring event of 2017. The colored area represents the Froude numbers in the area the front passes during this time window.

8

Discussion

Having presented all results, this chapter will first focus on their interpretation. The results of this thesis will be compared to previous research, to verify the results and explain differences in outcomes. Additionally, the important assumptions are discussed, together with their influence on the results, so that a good overview is created of the reliability of the outcome of the different analyses. Finally, the limitations that enforced some research choices are discussed, together with the proposed methods if these limitations had not been there.

8.1. Interpretation of the Results

The research started with an analysis of the elevation data, to identify potential meteotsunamis. This data was first band-pass filtered with filtering boundaries between 2 and 30 minutes, after which an amplitude threshold of 0.10 meters was applied. These two steps resulted in the identification of 279 potential meteotsunamis over 9 years, equal to 31 events per year. In literature, the only other study that identified meteotsunamis near the Dutch coast, identified 32 meteotsunamis over 3 years, equal to 11 events per year. This study used a Butterworth filter and an amplitude filter of 12.5 cm (Williams et al., 2021). The difference in identified events between the two studies is primarily attributed to the difference in amplitude threshold. Furthermore, it is expected that the more extensive preprocessing done in the study by Williams et al. (2021) also decreased their number of potential meteotsunamis.

For signal filtering, previous research uses filter boundaries between 2 minutes and 2 hours (Monserrat et al., 2006), causing overlap with other wave types. As previously stated, this research explored a narrower filter band, between 2 minutes and 30 minutes. The six case studies found meteotsunami periods from 10 minutes to 25 minutes. Based on these case studies, the narrower period band did not seem to negatively influence the detectability of the meteotsunamis, since all found periods were well below the 30-minute filter boundary. Before this narrower filter band for Dutch meteotsunamis can be implemented, a larger set of potential events should be analyzed.

After the amplitude threshold, the multiplicity principle resulted in a reduction of potential meteotsunamis of approximately 85 percent. Dusek et al. (2019) also used the multiplicity principle to identify potential meteotsunamis. Their study used 125 tidal gauges and the criterion that at least two tide gauges had to flag the event. This resulted in 548 identified meteotsunamis between 1996 and 2017 near the U.S. Coast. Out of those, 84 percent was measured by five or fewer tide gauges. Scaling their number of tide gauges to our number of tide gauges, the decrease of 85 percent seems feasible. Additionally, since our research uses the data of only 8 tide gauges instead of 125, the implementation of the multiplicity criterion might have been too strict of a filter. This potentially resulted in an underestimation of the actual frequency of occurrence of meteotsunamis near the Dutch Coast.

The verification via the wavelet analysis resulted in the addition of a few stations. It is not known whether these stations would have also been detected on a preprocessed dataset. Therefore, it remains unclear how effective the verification via the wavelet analysis would be in other research.

Once the identification of the oceanic component had been performed, six events were selected to investigate their atmospheric component. For these events, the threshold for a pressure jump was put at 2 hPa, to remove noise. Previous research looked into pressure jumps between 1 and 3 hPa (Gusiakov, 2020). The selected threshold for this research was sufficient to identify a pressure jump for 5 out of 6 selected events. Therefore,

based on the case studies, meteotsunamis of significant height can often be detected via a pressure threshold of 2 hPa. This pressure threshold results in the removal of a lot of noise, while still capturing the large events.

Out of the six events, two events have been investigated in literature before, namely the winter event of 2012 and the spring event of 2017. For the spring event of 2017, Sibley et al. (2020) states that the responsible front propagates from the English Channel to the Southern North Sea. This is in line with our results regarding the propagation of the front. Verhagen et al. (2014) looked into the precipitation during the winter event of 2012. They presented a precipitating front that looks very similar to the front that was identified in our research. The identified fronts from both researches are presented in Figure 8.1.

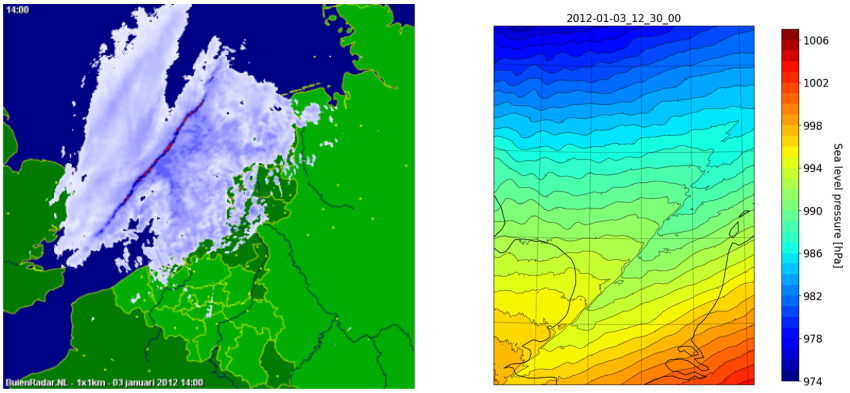

Figure 8.1: Atmospheric front identified by Verhagen et al. (2014) (left) and numerical simulation in this thesis (right) for the winter event of 2012.

After the identification of the atmospheric component, the six events were all classified as meteotsunamis and characterized. For all six, the angle of incidence, wave period, and wave height were identified. Regarding the angle of incidence, the winter event of 2012 is noted to have arrived on the Dutch west coast, following the precipitation front presented in Figure 8.1 (Verhagen et al., 2014). The article presents this front propagating from the North East, supporting the angle of incidence we found.

Because the spring event of 2017 was such a large event, it was simulated by Deltares. Their simulation shows the meteotsunami propagating over the Southern North Sea, from the English Channel northwards. Figure 8.2 presents a snapshot of their simulation, showing the northwards propagation direction. Compared to our research, the angle of incidence we determined seems in line with their simulation.

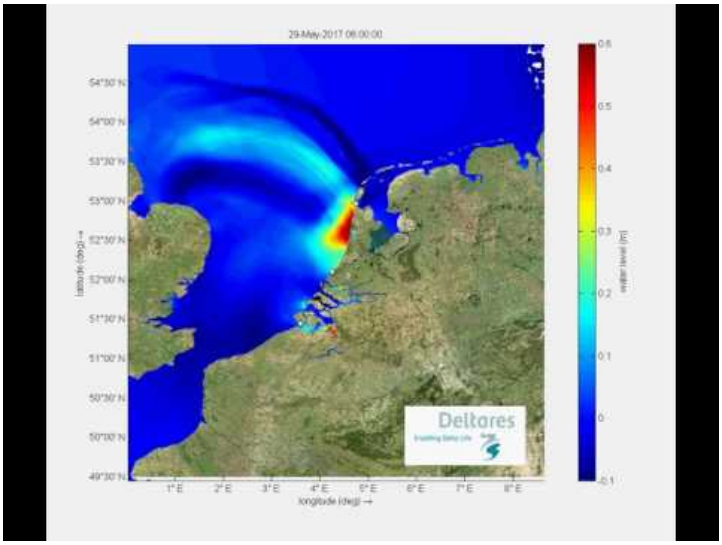

Figure 8.2: Snapshot of the simulation of the spring event of 2017. From a YouTube video by Deltares.

In the computation of the wave period, both methods showed several hiccups. Often the wavelet analysis was inconclusive, with the peaks not occurring at the same periods between the stations. For the zero-down crossing analysis, the results might have been clouded sometimes by false zero-down crossings, caused by other wave types that could not be filtered from the elevation data. Despite the disadvantages of both methods, combining them resulted in a good estimate of the wave period of each event.

The final parameter to be estimated in the characterization of the six selected events was the wave height. The largest wave height measured was 0.60 meters, for the spring event of 2017. Much greater wave heights were observed in literature, with wave heights of 2 meters for the same event (Sibley et al., 2020). This is likely explained by the limited amount of tide gauges for this research, which gives a small sample size from which to determine the maximum wave height. Their research shows two overlapping locations at which the wave height was measured, namely IJmuiden (station IJM) and Europlatform (station EUR). In the research of Sibley et al. (2020), wave heights between 0.44 and 0.50 meters were measured at IJmuiden, and waves with amplitude around 0.78 meters at Europlatform. Our research found wave heights of 0.34 meters at IJmuiden and 0.63 meters at Europlatform, which is slightly lower in both cases.

For the winter event of 2012, again an overlapping wave height measurement is found at IJmuiden. While our research found a wave height of approximately 0.15 meters at this station, Verhagen et al. (2014) denoted a wave height of 1 meter at the same location. Based on these two papers, our wave height estimates might have been an underestimate of the real wave heights of the events.

Finally, the six events were checked for Proudman resonance. In the computation of the atmospheric forcing speeds generally, speeds ranged between 20 and 30 m/s. These wind speeds are correlated to the 500-hPa wave speed (Vilibić and Šepić, 2017). It was found that for our events, indeed the atmospheric forcing speed is in the same range as the 500-hPa wind speed for the six selected events. Finally, all events where the atmospheric front propagated over the sea, Proudman resonance likely occurred, supporting the statement in literature that Proudman resonance is the most important amplification mechanism for meteotsunamis (Monserrat et al., 2006).

8.2. Assumptions

Several assumptions were made during this research, that should be elaborated on. The most important assumptions were made in the computation of the angle of incidence and the atmospheric forcing speed.

To compute the angle of incidence, one mean wave speed along the entire trajectory of the meteotsunami was assumed. Since the waves travel at shallow water wave speed, their speed is fully depth dependent, and therefore using only one mean wave speed is a simplification of the actual wave speed. Use of the actual wave speed could lead to differences in the covered area by the meteotsunami over time. This can either increase or decrease overlap between the meteotsunami and the atmospheric front, influencing the probability of Proudman resonance. Therefore, implementing the actual wave speed would improve the reliability of the conclusions drawn on the probability of Proudman resonance.

In the computation of the atmospheric forcing speed, again one mean speed is used to determine the atmospheric forcing speed of the front over half an hour. However, this assumption is less valid for larger fronts, since variations in front speed are larger. For fronts as clearly detectable as the identified events, it is recommended to determine the atmospheric forcing speed for smaller areas. Here, the front was subdivided into 5 tracks, over which an average was taken. This might have resulted in an over- or underestimation of the zones where the Froude numbers were close to one. Increasing the number of tracks could result in a full grid where the atmospheric forcing speeds are known at each location within the front. This gives a more accurate representation of the front its atmospheric forcing speed, and therefore again improves the reliability of the check for Proudman resonance.

8.3. Limitations of the Research

Finally, the limiting factors during this research are discussed, together with their consequence on the outcome of this research.

The biggest limiting factor in the identification of the oceanic component was the visual inspection. Both the relative thresholds by Monserrat et al. and Olabarrieta et al. gave more than 300 events, even after the multiplicity criterion. This number of events could not be visually inspected within the timespan of this research, and thus no conclusion could be drawn on the applicability of a relative threshold for meteotsunamis on the Southern North Sea. Because of this, the choice of thresholds was limited only to the absolute thresholds, which might have led to unidentified meteotsunamis. Removal of the step of visual inspection from the analysis via better preprocessing of the data, could improve the quality of this identification and also reduce the duration.

A second limiting factor in the identification of the oceanic component was the necessity to use daily maxima. A consequence of this choice was that overnight meteotsunamis could not be detected, as the multiplicity principle would likely filter these out. If higher computational force had been available, hourly maxima could have been used. These hourly maxima could have been used to perform a 24-hour running identification method that would have been able to identify overnight events. This limitation in computational power again might have led to unidentified meteotsunamis.

The identification of the atmospheric component was limited by the same computational power issue as the oceanic component. It would have been beneficial for the identification of the pressure jump if it could have been computed via a running maximum and minimum value. This running analysis would have prevented the undersampling of pressure that occurred on exactly the edge of a time window. Using a running maximum and minimum over half an hour, the potential of a jump at the boundary between two windows is removed, which would have led to a full capture of the pressure jump. Since this running analysis was not possible, the found pressure jumps might have been underestimated.

These running maxima would also help improve the resolution over which the atmospheric forcing speed is computed. Combined with the previously noted improvements, the result could be a 2d grid, where at each time moment the location and atmospheric forcing speed are known, resulting in a better representation of the front and its behavior.

The main limiting factor in the characterization of our selected events was the number of available tide gauges. The limited availability made it difficult to correctly estimate the wave period and the development of the wave height. If more stations were available, the inconclusiveness of some stations in the wave period identification would not have influenced the results as much, and identification of overlapping periods between stations would have been easier. An additional benefit of a higher number of tide gauges would have been that identification would have also become easier since it would be more likely that an event passed the multiplicity criterion.

9

Conclusion

Because of the lack of research, very little is known about meteotsunamis near the Dutch coast. To improve knowledge on this topic, this thesis researched the identification and generation of meteotsunamis in the Southern North Sea. In this chapter, the research questions presented in the introduction will be answered through a summary of the research results.

Research Question 1) How frequently do meteotsunamis occur on the Southern North Sea?

To determine the frequency of meteotsunamis on the Southern North Sea, the elevation data from Rijkswaterstaat (Rijkswaterstaat), was bandpass-filtered with filtering boundaries of 0.008 Hz and 0.0005 Hz (equal to wave periods of 2 minutes and 30 minutes). After this filtering, the data was threshold-filtered against an amplitude threshold of 0.10 meters. This threshold resulted in 279 potential events after threshold filtering, 38 events after the application of the multiplicity criterion, and 14 events after visual inspection. Out of these 14 events, six dates were selected based on their probability of correct classification. These events included two winter events (in 2012 and 2015), three summer events (in 2012 and two consecutive ones in 2014), and one spring event (in 2017). These six events were subjected to a continuous wavelet analysis, which led to the flagging of two additional stations (one for the winter event of 2012 and one for the winter event of 2015).

Finally, the atmospheric conditions were simulated for the six selected events, which resulted in the identification of an atmospheric pressure jump for all six events. Therefore, over the past 9 years, six definitive events have been identified as meteotsunamis, of which four had never been classified before. Apart from these six, 8 other events were classified as potential meteotsunamis, though atmospheric conditions were not checked.

Research Question 2) What are the atmospheric conditions generating meteotsunamis on the Southern North Sea?

To determine what atmospheric conditions generate meteotsunamis near the Dutch coast, the previously mentioned atmospheric simulations were analyzed. Based on these, five out of six events showed a pressure jump that exceeded the 2 hPa set threshold. The one event that did not exceed the threshold (the winter event of 2015) was identified when the threshold was lowered to 1.5 hPa, with the maximum pressure jump being 1.9 hPa. It is therefore concluded that based on the six case studies, meteotsunamis with an amplitude larger than 0.10 meters can be linked to a pressure jump of at least 2 hPa, though for events with amplitudes close to 0.10 meters, this threshold might be too strict. Additionally, a clear overlap is found between the height of the identified pressure jump and the wave height of the event. The event with the highest wave height, the spring event of 2017, was linked to a maximum pressure jump of 6.6 hPa. For the summer events, the maximum pressure jump was 4.6 hPa for the event of 2012 and 3.6 hPa for the event of 2014. Finally, for the winter event of 2012, a maximum pressure jump of 3 hPa was identified.

Regarding the shape of the front, a strong seasonality was identified. The fronts linked to the winter events showed a very long and narrow shape, whereas the summer and spring events were linked to a front where the highest pressure changes were found in the center of the front. Both winter events and the spring event of 2017 showed a clear front propagating overseas, while the summer events of 2012 and 2014 were both linked to a front that mainly propagated over land. For the summer event of 2014, a moment was found where the identified front propagated over water at a lower latitude, where the event could have been generated.

Research Question 3) What are the characteristics of meteotsunamis on the Southern North Sea?

The characteristics of meteotsunamis towards the Dutch coast were determined via case studies of the six selected events. Given that only six events are analyzed in this study, the conclusions regarding the characteristics of meteotsunamis along the Dutch coast should be interpreted as a basis for future investigations. For these six events, the angle of incidence, the wave period, and the wave height were computed. First, the angles of incidence were determined. Both winter events propagated from the North West towards the Dutch coast, with the angles of incidence shown in Table 9.1.

Event	Angle of incidence [°]
Winter event of 2012	118.65
Winter event of 2015	106.79

Table 9.1: Angles of incidence of the winter events of 2012 and 2015 with respect to the true North.

The summer events of 2012 and 2014 and the spring event of 2017 all propagated from the South through the English Channel, with the angles of incidence shown in Table 9.2.

Event	Angle of incidence [°]
Summer event of 2012	45.17
First summer event of 2014	47.73
Consecutive summer event of 2014	16.33
Spring event of 2017	53.61

Table 9.2: Angles of incidence of the summer events of 2012 and 2014 and the spring event of 2017 with respect to the true North.

Based on these six case studies, the winter events generally seem to propagate from the North west, while summer and spring events propagate from the South through the english channel.

The second characteristic to be determined was the wave period. Table 9.3 shows the estimated wave periods based on both the continuous wavelet analysis and the zero-down crossing analysis. Based on these case studies, The period of meteotsunamis on the Southern North sea generally ranges between 10 and 25 minutes.

Date	Period [min]
Winter event of 2012	12:00 - 14:00
Winter event of 2015	21:00 - 24:00
Summer event of 2012	19:00 - 20:00
First summer event of 2014	18:30 - 19:00
Consecutive summer event of 2014	17:30 - 20:00
Spring event of 2017	15:00 - 16:30

Table 9.3: Estimated periods for each event based on the continuous wavelet transform and the zero-down crossing analysis

The final characteristic is the wave height. Table 9.4 presents the identified wave heights at the relevant stations for all six events. The largest detected wave height was 0.63 meters, with the general wave height being around 20 centimeters.

	A12	D15	F16	J6	H	IJM	EUR	LG
Winter event of 2012	-	-	-	0.22	-	0.15	-	-
Winter event of 2015	-	0.18	-	-	-	-	-	0.17
Summer event of 2012	-	-	-	-	0.16	0.16	-	-
First summer event of 2014	-	-	-	-	-	0.20	0.18	0.20
Consecutive summer event of 2014	0.22	-	0.15	0.22	-	-	-	-
Spring event of 2017	-	-	-	-	0.27	0.34	0.63	0.51

Table 9.4: results of the zero-down crossing analysis, for the wave height in meters.

Research Question 4) What role does Proudman resonance play in meteotsunami amplification on the Southern North Sea?

To determine whether Proudman resonance occurred first it is verified whether the front propagated overseas within the simulation grid. It is found that for the summer events of 2012 and 2014, this is not the case, and therefore no Proudman resonance can have occurred. on the other three dates, the front did propagate overseas, with atmospheric forcing speeds varying between 20 and 30 m/s.

All three events showed a clear overlap between the front and the wave, with the clearest overlap occurring during the winter event of 2015. Furthermore, for all three events, the shallow water wave speeds were close to the atmospheric forcing speeds, creating near Proudman resonant conditions during all three events. Therefore, it is concluded that all three events were likely amplified by Proudman resonance, making the role of Proudman resonance very significant in the amplification of meteotsunamis on the Southern North Sea.

With the four research questions answered, a foundation is laid for future research on meteotsunamis on the Southern North sea, with an increased knowledge about their frequencies and properties. Furthermore, more insight is obtained in their generation and propagation in this area.

10

Recommendations

In this chapter, the recommendations for future works are presented. Most recommendations are made on future works on the identification of meteotsuanmis.

In the identification of the oceanic component, it would be recommended to further investigate the choice of amplitude threshold. Firstly, the relative thresholds should be properly tested, to explore their ability to identify meteotsunamis on the Southern North Sea. To explore this, it would be beneficial to further research the ratio between flagged dates and actual meteotsunamis for these thresholds. If the results contain a lot of false flags, a higher relative threshold should be proposed, in the order of 8 times the standard deviation or even higher.

Additionally, more research should be performed on the multiplicity criterion. Since only eight stations were available for this research, an increase of the multiplicity criterion was not feasible, but if more stations had been available the ratio between flagged dates and actual meteotsunamis is expected to become even better. In further research, given there are more stations, it should be researched whether an increase of the multiplicity criterion results in a better ratio of flagged dates and actual meteotsunamis.

In this research, the wavelet analysis was only used to verify already identified events. For future research, it should be investigated whether the wavelet analysis can be used to not only verify but also identify meteotsunamis. During this research, it was found that the integrated wavelet coefficients show a great resemblance with the absolute value of the band-pass filtered elevation data. Because of this resemblance, a similar approach to the classic analysis is proposed for the identification via wavelet analysis. A threshold will have to be established, based on the wavelet coefficients. This would give a more insightful identification method, as direct period/frequency information is available about flagged dates.

For future research into the atmospheric component of meteotsunamis on the Southern North Sea, it is recommended to implement a larger grid. For each analyzed event a pressure jump exceeding the threshold was found, but for the summer event of 2012 and the summer events of 2014, the front is cut off by the boundaries of the simulation grid. A bigger grid would resolve this and give more insight into the potential overlap between the front and the sea. It would be recommended to first expand the grid southward, as the area around the English channel has been identified as an area of interest for Dutch meteotsunamis.

Furthermore, a strong seasonality is found in the shape of the fronts. For the three summer events, the pressure jump is generated by a small and localized front, where the highest pressure changes occur in the middle of the front, and the pressure change decreases further away from the center. The pressure change of the two winter events is caused by a long diagonal line. More research should be done to validate whether this seasonality holds up over a larger group of events. Finally, this research focuses only on the role of Proudman resonance in the amplification process of the identified events. However, future research could focus more on the influence of the other amplification mechanisms that also have a known influence on the amplification of meteotsunamis (Williams, 2019). This will create a more complete and conclusive case study of the events. Apart from widening the research to other amplification mechanisms, it would also be interesting to further explore whether the Proudman Resonance could be quantified for the events that are linked to potential Proudman resonance.

Appendices

Bibliography

Toshiyuki Asano, Toru Yamashiro, and Norihiro Nishimura. Field observations of meteotsunami locally called "abiki" in urauchi bay, kami-koshiki island, japan. Natural Hazards, 64(2):1685–1706, August 2012. ISSN 1573-0840. doi: 10.1007/s11069-012-0330-2. URL http://dx.doi.org/10.1007/s11069-012-0330-2.

Danijel Belušić and Nataša Strelec Mahović. Detecting and following atmospheric disturbances with a potential to generate meteotsunamis in the adriatic. Physics and Chemistry of the Earth, Parts A/B/C, 34(17–18): 918–927, January 2009. ISSN 1474-7065. doi: 10.1016/j.pce.2009.08.009. URL http://dx.doi.org/10.1016/j.pce.2009.08.009.

Lance Bode and Thomas A. Hardy. Progress and recent developments in storm surge modeling. Journal of Hydraulic Engineering, 123(4):315–331, April 1997. ISSN 1943-7900. doi: 10.1061/(asce)0733-9429(1997)123:4(315). URL http://dx.doi.org/10.1061/(ASCE)0733-9429(1997)123:4(315).

Yixiang Chen and Xiaojing Niu. Forced wave induced by an atmospheric pressure disturbance moving towards shore. Continental Shelf Research, 160:1–9, May 2018. ISSN 0278-4343. doi: 10.1016/j.csr.2018.03.007. URL http://dx.doi.org/10.1016/j.csr.2018.03.007.

Byoung-Ju Choi, Chorong Hwang, and Sang-Ho Lee. Meteotsunami-tide interactions and high-frequency sea level oscillations in the eastern <scp>y</scp>ellow <scp>s</scp>ea. Journal of Geophysical Research: Oceans, 119(10):6725–6742, October 2014. ISSN 2169-9291. doi: 10.1002/2013jc009788. URL http://dx.doi.org/10.1002/2013JC009788.

Martijn P. C. de Jong and J.A. Battjes. Origin and prediction of seiches in Rotterdam harbour basins. TU Delft, 2004.

Cléa Denamiel, Jadranka Šepić, Damir Ivanković, and Ivica Vilibić. The adriatic sea and coast modelling suite: Evaluation of the meteotsunami forecast component. Ocean Modelling, 135:71–93, March 2019. ISSN 1463-5003. doi: 10.1016/j.ocemod.2019.02.003. URL http://dx.doi.org/10.1016/j.ocemod.2019.02.003.

Joshua Dickey, Brett Borghetti, and William Junek. Baznet: A deep neural network for confident three-component backazimuth prediction. Pure and Applied Geophysics, 178(7):2459–2473, October 2020. ISSN 1420-9136. doi: 10.1007/s00024-020-02578-x. URL http://dx.doi.org/10.1007/s00024-020-02578-x.

Gregory Dusek, Christopher DiVeglio, Louis Licate, Lorraine Heilman, Katie Kirk, Christopher Paternostro, and Ashley Miller. A meteotsunami climatology along the u.s. east coast. Bulletin of the American Meteorological Society, 100(7):1329–1345, July 2019. ISSN 1520-0477. doi: 10.1175/bams-d-18-0206.1. URL http://dx.doi.org/10.1175/BAMS-D-18-0206.1.

Anna Dzvonkovskaya, Dejan Nikolic, Vladimir Orlic, Miroslav V. Peric, and Nikola Tosic. Remote observation of a small meteotsunami in the bight of benin using hf radar operating in lower hf band. IEEE Access, 7: 88601–88608, 2019. ISSN 2169-3536. doi: 10.1109/access.2019.2926213. URL http://dx.doi.org/10.1109/ACCESS.2019.2926213.

M. B. Ek, K. E. Mitchell, Y. Lin, E. Rogers, P. Grunmann, V. Koren, G. Gayno, and J. D. Tarpley. Implementation of noah land surface model advances in the national centers for environmental prediction operational mesoscale eta model. Journal of Geophysical Research: Atmospheres, 108(D22), November 2003. ISSN 0148-0227. doi: 10.1029/2002jd003296. URL http://dx.doi.org/10.1029/2002JD003296.

EMODnet Bathymetry Consortium. Emodnet digital bathymetry (dtm 2022), 2022. URL https://sextant.ifremer.fr/record/ff3aff8a-cff1-44a3-a2c8-1910bf109f85.

Spandan Erukulla and Poli Lokeshwara Reddy. Tsunami Prediction via Seismic Triangulation and Earthquake Magnitude Estimation Using Ground Based Seismic Data, page 447–457. Springer Nature Singapore, 2024. ISBN 9789819761036. doi: 10.1007/978-981-97-6103-6_28. URL http://dx.doi.org/10.1007/978-981-97-6103-6_28.

J.D. Fenton and W.D. McKee. On calculating the lengths of water waves. Coastal Engineering, 14(6):499–513, December 1990. ISSN 0378-3839. doi: 10.1016/0378-3839(90)90032-r. URL http://dx.doi.org/10.1016/0378-3839(90)90032-R.

RAJESH GANESAN, TAPAS K. DAS, and VIVEKANAND VENKATARAMAN. Wavelet-based multiscale statistical process monitoring: A literature review. IIE Transactions, 36(9):787–806, September 2004. ISSN 1545-8830. doi: 10.1080/07408170490473060. URL http://dx.doi.org/10.1080/07408170490473060.

Théo Gravalon, Lucia Seoane, José Darrozes, and Guillaume Ramillien. Can gnss-r help us to monitor the effects of inverse barometer in coastal areas? EGU General Assembly 2021, March 2021. doi: 10.5194/egusphere-egu21-12499. URL http://dx.doi.org/10.5194/egusphere-egu21-12499.

Esq. Green, George. On the Motion of Waves in a variable Canal of small Depth and Width. Transactions of the Cambridge Philosophical Society, 6:457, January 1838.

H. P. Greenspan. The generation of edge waves by moving pressure distributions. Journal of Fluid Mechanics, 1(06):574, December 1956. ISSN 1469-7645. doi: 10.1017/s002211205600038x. URL http://dx.doi.org/10.1017/S002211205600038X.

Viacheslav K. Gusiakov. Meteotsunamis at global scale: problems of event identification, parameterization and cataloguing. Natural Hazards, 106(2):1105–1123, August 2020. ISSN 1573-0840. doi: 10.1007/s11069-020-04230-2. URL http://dx.doi.org/10.1007/s11069-020-04230-2.

Taemin Ha, Jae-Seon Yoon, and Ki-Young Heo. Numerical simulations of a meteotsunami using both atmospheric and phase-resolving wave models in the yellow sea. Journal of Coastal Research, 85:786–790, May 2018. ISSN 1551-5036. doi: 10.2112/si85-158.1. URL http://dx.doi.org/10.2112/SI85-158.1.

Ki-Young Heo and Taemin Ha. Producing the hindcast of wind and waves using a high-resolution atmospheric reanalysis around korea. Journal of Coastal Research, 75(sp1):1107–1111, March 2016. ISSN 1551-5036. doi: 10.2112/si75-222.1. URL http://dx.doi.org/10.2112/SI75-222.1.

Hans Hersbach, Bill Bell, Paul Berrisford, Shoji Hirahara, András Horányi, Joaquín Muñoz-Sabater, Julien Nicolas, Carole Peubey, Raluca Radu, Dinand Schepers, Adrian Simmons, Cornel Soci, Saleh Abdalla, Xavier Abellan, Gianpaolo Balsamo, Peter Bechtold, Gionata Biavati, Jean Bidlot, Massimo Bonavita, Giovanna De Chiara, Per Dahlgren, Dick Dee, Michail Diamantakis, Rossana Dragani, Johannes Flemming, Richard Forbes, Manuel Fuentes, Alan Geer, Leo Haimberger, Sean Healy, Robin J. Hogan, Elías Hólm, Marta Janisková, Sarah Keeley, Patrick Laloyaux, Philippe Lopez, Cristina Lupu, Gabor Radnoti, Patricia de Rosnay, Iryna Rozum, Freja Vamborg, Sebastien Villaume, and Jean-Noël Thépaut. The era5 global reanalysis. Quarterly Journal of the Royal Meteorological Society, 146(730):1999–2049, June 2020. ISSN 1477-870X. doi: 10.1002/qj.3803. URL http://dx.doi.org/10.1002/qj.3803.

Simon J. Holgate, Andrew Matthews, Philip L. Woodworth, Lesley J. Rickards, Mark E. Tamisiea, Elizabeth Bradshaw, Peter R. Foden, Kathleen M. Gordon, Svetlana Jevrejeva, and Jeff Pugh. New Data Systems and Products at the Permanent Service for Mean Sea Level. Journal of Coastal Research, 29(3):493–504, 12 2012. ISSN 0749-0208. doi: 10.2112/JCOASTRES-D-12-00175.1. URL https://doi.org/10.2112/JCOASTRES-D-12-00175.1.

Leo H. Holthuijsen. Waves in Oceanic and Coastal Waters. Cambridge University Press, January 2007. ISBN 9780521129954. doi: 10.1017/cbo9780511618536. URL http://dx.doi.org/10.1017/CBO9780511618536.

Kristian Horvath and Ivica Vilibić. Atmospheric mesoscale conditions during the boothbay meteotsunami: a numerical sensitivity study using a high-resolution mesoscale model. Natural Hazards, 74(1):55–74, February 2014. ISSN 1573-0840. doi: 10.1007/s11069-014-1055-1. URL http://dx.doi.org/10.1007/s11069-014-1055-1.

Kristian Horvath, Jadranka Šepić, and Maja Telišman Prtenjak. Atmospheric forcing conducive for the adriatic 25 june 2014 meteotsunami event. Pure and Applied Geophysics, 175(11):3817–3837, June 2018. ISSN 1420-9136. doi: 10.1007/s00024-018-1902-1. URL http://dx.doi.org/10.1007/s00024-018-1902-1.

Kristian Horvath, Jadranka Šepić, and Maja TelišMan Prtenjak. Atmospheric Forcing Conducive for the Adriatic 25 June 2014 Meteotsunami Event, page 97–117. Springer International Publishing, 2019. ISBN 9783030119584. doi: 10.1007/978-3-030-11958-4_7. URL http://dx.doi.org/10.1007/978-3-030-11958-4_7.

M.J. Howarth. North Sea Circulation, page 73–81. Elsevier, 2001. ISBN 9780123744739. doi: 10.1016/b978-012374473-9.00382-9. URL http://dx.doi.org/10.1016/B978-012374473-9.00382-9.

Intergovernmental Oceanographic Commission. Manual on sea level measurement and interpretation. volume iv - an update to 2006., 2006. URL https://repository.oceanbestpractices.org/handle/11329/213.

Derek W.T. Jackson and Andrew D. Short. Sandy Beach Morphodynamics. Elsevier, 2020. ISBN 9780081029275. doi: 10.1016/c2018-0-02420-2. URL http://dx.doi.org/10.1016/C2018-0-02420-2.

Zaviša I. Janjić. The step-mountain eta coordinate model: Further developments of the convection, viscous sublayer, and turbulence closure schemes. Monthly Weather Review, 122(5):927–945, May 1994. ISSN 1520-0493. doi: 10.1175/1520-0493(1994)122<0927:tsmecm>2.0.co;2. URL http://dx.doi.org/10.1175/1520-0493(1994)122<0927:TSMECM>2.0.CO;2.

Harold Jeffreys. Causes contributory to the annual variation of latitude. (plate 8.). Monthly Notices of the Royal Astronomical Society, 76(6):499–525, April 1916. ISSN 1365-2966. doi: 10.1093/mnras/76.6.499. URL http://dx.doi.org/10.1093/mnras/76.6.499.

Richard H. Johnson. Surface mesohighs and mesolows. Bulletin of the American Meteorological Society, 82 (1):13–31, January 2001. ISSN 1520-0477. doi: 10.1175/1520-0477(2001)082<0013:smam>2.3.co;2. URL http://dx.doi.org/10.1175/1520-0477(2001)082<0013:SMAM>2.3.CO;2.

J.S. Kain and J. Kain. The kain - fritsch convective parameterization: An update. Journal of Applied Meteorology, 43:170–181, 01 2004. doi: 10.1175/1520-0450(2004)04360;0170:tkcpau62;2.0.co;2.

S.D. Kamminga. Een algoritme voor de opslag van data van lange golven. Technical report, Rijkswaterstaat, RIKZ, 2001.

Jihwan Kim, Byoung-Ju Choi, and Rachid Omira. On the greenspan resonance of meteotsunamis in the yellow sea - insights from the newly discovered 2009 event. August 2021a. doi: 10.21203/rs.3.rs-804240/v1. URL http://dx.doi.org/10.21203/rs.3.rs-804240/v1.

Myung-Seok Kim, Seung-Buhm Woo, Hyunmin Eom, and Sung Hyup You. Occurrence of pressure-forced meteotsunami events in the eastern yellow sea during 2010–2019. Natural Hazards and Earth System Sciences, 21(11):3323–3337, November 2021b. ISSN 1684-9981. doi: 10.5194/nhess-21-3323-2021. URL http://dx.doi.org/10.5194/nhess-21-3323-2021.

Arnida L. Latifah, Henokh Lugo Hariyanto, and Rido Dwi Ismanto. Effect of bathymetry data on tsunami wave ray tracing in the western banten sea. Continental Shelf Research, 277:105247, June 2024. ISSN 0278-4343. doi: 10.1016/j.csr.2024.105247. URL http://dx.doi.org/10.1016/j.csr.2024.105247.

Boris W. Levin and Mikhail Nosov. Physics of Tsunamis. Springer International Publishing, 2016. ISBN 9783319240374. doi: 10.1007/978-3-319-24037-4. URL http://dx.doi.org/10.1007/978-3-319-24037-4.

Clare Lewis, Tim Smyth, David Williams, Jess Neumann, and Hannah Cloke. Meteotsunami in the united kingdom: the hidden hazard. Natural Hazards and Earth System Sciences, 23(7):2531–2546, July 2023. ISSN 1684-9981. doi: 10.5194/nhess-23-2531-2023. URL http://dx.doi.org/10.5194/nhess-23-2531-2023.

Álvaro Linares, Adam J. Bechle, and Chin H. Wu. Characterization and assessment of the meteotsunami hazard in northern <scp>l</scp>ake <scp>m</scp>ichigan. Journal of Geophysical Research: Oceans, 121 (9):7141–7158, September 2016. ISSN 2169-9291. doi: 10.1002/2016jc011979. URL http://dx.doi.org/10.1002/2016JC011979.

S. Magazù and M. T. Caccamo. Variable length pendulum analyzed by a comparative fourier and wavelet approach. Revista Mexicana de Física E, 64(1 Jan-Jun):81–86, April 2018. ISSN 1870-3542. doi: 10.31349/revmexfise.64.81. URL http://dx.doi.org/10.31349/RevMexFisE.64.81.

Paul Markowski and Yvette Richardson. Mesoscale Meteorology in Midlatitudes. Wiley, February 2010. ISBN 9780470682104. doi: 10.1002/9780470682104. URL http://dx.doi.org/10.1002/9780470682104.

Anton McLachlan and Omar Defeo. The Physical Environment, page 5–35. Elsevier, 2018. doi: 10.1016/b978-0-12-809467-9.00002-3. URL http://dx.doi.org/10.1016/B978-0-12-809467-9.00002-3.

Eli J. Mlawer, Steven J. Taubman, Patrick D. Brown, Michael J. Iacono, and Shepard A. Clough. Radiative transfer for inhomogeneous atmospheres: Rrtm, a validated correlated-k model for the longwave. Journal of Geophysical Research: Atmospheres, 102(D14):16663–16682, July 1997. ISSN 0148-0227. doi: 10.1029/97jd00237. URL http://dx.doi.org/10.1029/97JD00237.

S. Monserrat, I. Vilibić, and A. B. Rabinovich. Meteotsunamis: atmospherically induced destructive ocean waves in the tsunami frequency band. Natural Hazards and Earth System Sciences, 6(6):1035–1051, December 2006. ISSN 1684-9981. doi: 10.5194/nhess-6-1035-2006. URL http://dx.doi.org/10.5194/nhess-6-1035-2006.

H. Morrison, J. A. Curry, and V. I. Khvorostyanov. A new double-moment microphysics parameterization for application in cloud and climate models. part i: Description. Journal of the Atmospheric Sciences, 62 (6):1665–1677, June 2005. ISSN 0022-4928. doi: 10.1175/jas3446.1. URL http://dx.doi.org/10.1175/JAS3446.1.

B. Mourre, A. Santana, A. Builes, L. Gautreau, M. Ličer, A. Jansà, B. Casas, B. Amengual, and J. Tintoré. On the potential of ensemble forecasting for the prediction of meteotsunamis in the balearic islands: sensitivity to atmospheric model parameterizations. Natural Hazards, 106(2):1315–1336, April 2020. ISSN 1573-0840. doi: 10.1007/s11069-020-03908-x. URL http://dx.doi.org/10.1007/s11069-020-03908-x.

Mikio Nakanishi and Hiroshi Niino. An improved mellor–yamada level-3 model: Its numerical stability and application to a regional prediction of advection fog. Boundary-Layer Meteorology, 119(2):397–407, March 2006. ISSN 1573-1472. doi: 10.1007/s10546-005-9030-8. URL http://dx.doi.org/10.1007/s10546-005-9030-8.

Maitane Olabarrieta, Arnoldo Valle-Levinson, Christopher J. Martinez, Charitha Pattiaratchi, and Luming Shi. Meteotsunamis in the northeastern gulf of mexico and their possible link to el niño southern oscillation. Natural Hazards, 88(3):1325–1346, May 2017. ISSN 1573-0840. doi: 10.1007/s11069-017-2922-3. URL http://dx.doi.org/10.1007/s11069-017-2922-3.

S.C. Olhede and A.T. Walden. Generalized morse wavelets. IEEE Transactions on Signal Processing, 50(11): 2661–2670, November 2002. ISSN 1053-587X. doi: 10.1109/tsp.2002.804066. URL http://dx.doi.org/10.1109/TSP.2002.804066.

Ozgun Ozsoy, Ivan D. Haigh, Matthew P. Wadey, Robert J. Nicholls, and Neil C. Wells. High-frequency sea level variations and implications for coastal flooding: A case study of the solent, uk. Continental Shelf Research, 122:1–13, July 2016. ISSN 0278-4343. doi: 10.1016/j.csr.2016.03.021. URL http://dx.doi.org/10.1016/j.csr.2016.03.021.

S. Pasquet, I. Vilibić, and J. Šepić. A survey of strong high-frequency sea level oscillations along the us east coast between 2006 and 2011. Natural Hazards and Earth System Sciences, 13(2):473–482, February 2013. ISSN 1684-9981. doi: 10.5194/nhess-13-473-2013. URL http://dx.doi.org/10.5194/nhess-13-473-2013.

Charitha Pattiaratchi and E. M. S. Wijeratne. Observations of meteorological tsunamis along the south-west australian coast. Natural Hazards, 74(1):281–303, June 2014. ISSN 1573-0840. doi: 10.1007/s11069-014-1263-8. URL http://dx.doi.org/10.1007/s11069-014-1263-8.

Gabriel Peyre. Toolbox wavelets, 2024. URL https://www.mathworks.com/matlabcentral/fileexchange/5104-toolbox-wavelets.

Paola Picco, Maria Elisabetta Schiano, Silvio Incardone, Luca Repetti, Maurizio Demarte, Sara Pensieri, and Roberto Bozzano. Detection and characterization of meteotsunamis in the gulf of genoa. Journal of Marine Science and Engineering, 7(8):275, August 2019. ISSN 2077-1312. doi: 10.3390/jmse7080275. URL http://dx.doi.org/10.3390/jmse7080275.

Christopher G. Piecuch and Rui M. Ponte. Inverted barometer contributions to recent sea level changes along the northeast coast of north america. Geophysical Research Letters, 42(14):5918–5925, July 2015. ISSN 1944-8007. doi: 10.1002/2015gl064580. URL http://dx.doi.org/10.1002/2015GL064580.

Krzysztof Podgórski, Igor Rychlik, and Ulla E.B. Machado. Exact distributions for apparent waves in irregular seas. Ocean Engineering, 27(9):979–1016, April 2000. ISSN 0029-8018. doi: 10.1016/s0029-8018(99)00030-x. URL http://dx.doi.org/10.1016/S0029-8018(99)00030-X.

J. Proudman. The effects on the sea of changes in atmospheric pressure. Geophysical Journal International, 2:197–209, October 1929. ISSN 1365-246X. doi: 10.1111/j.1365-246x.1929.tb05408.x. URL http://dx.doi.org/10.1111/j.1365-246X.1929.tb05408.x.

David Pugh and Philip Woodworth. Sea-Level Science: Understanding Tides, Surges, Tsunamis and Mean Sea-Level Changes. Cambridge University Press, April 2014. ISBN 9781139235778. doi: 10.1017/cbo9781139235778. URL http://dx.doi.org/10.1017/CBO9781139235778.

Pywavelets. Continuous wavelet analysis. Pywavelets documentation, 2024. URL https://pywavelets.readthedocs.io/en/latest/ref/cwt.html.

Alexander B. Rabinovich. Seiches and Harbor Oscillations, page 193–236. WORLD SCIENTIFIC, September 2009. ISBN 9789812819307. doi: 10.1142/9789812819307_0009. URL http://dx.doi.org/10.1142/9789812819307_0009.

Ad J.H.M. Reniers, Remy Naporowski, Marion F. S. Tissier, Matthieu A. de Schipper, Gal Akrish, and Dirk P. Rijnsdorp. North sea infragravity wave observations. Journal of Marine Science and Engineering, 9(2):141, January 2021. ISSN 2077-1312. doi: 10.3390/jmse9020141. URL http://dx.doi.org/10.3390/jmse9020141.

Rijkswaterstaat. URL https://waterinfo.rws.nl/#/publiek/astronomische-getij.

Dirk P. Rijnsdorp, Ad J. H. M. Reniers, and Marcel Zijlema. Free infragravity waves in the north sea. Journal of Geophysical Research: Oceans, 126(8), August 2021. ISSN 2169-9291. doi: 10.1029/2021jc017368. URL http://dx.doi.org/10.1029/2021JC017368.

Giovanni Battista Rossi, Andrea Cannata, Antonio Iengo, Maurizio Migliaccio, Gabriele Nardone, Vincenzo Piscopo, and Enrico Zambianchi. Measurement of sea waves. Sensors, 22(1):78, December 2021. ISSN 1424-8220. doi: 10.3390/s22010078. URL http://dx.doi.org/10.3390/s22010078.

Alvaro Semedo, Roberto Vettor, Øyvind Breivik, Andreas Sterl, Magnar Reistad, Carlos Guedes Soares, and Daniela Lima. The wind sea and swell waves climate in the nordic seas. Ocean Dynamics, 65(2):223–240, November 2014. ISSN 1616-7228. doi: 10.1007/s10236-014-0788-4. URL http://dx.doi.org/10.1007/s10236-014-0788-4.

SHOM DOPS/HOM/MAC. Données du réseau de référence des observations marégraphiques (refmar), 2018. URL http://data.shom.fr/donnees/refmar.

Andrew M. Sibley, Dave Cox, and David R. Tappin. Convective rear-flank downdraft as driver for meteotsunami along english channel and north sea coasts 28–29 may 2017. Natural Hazards, 106(2):1445–1465, October 2020. ISSN 1573-0840. doi: 10.1007/s11069-020-04328-7. URL http://dx.doi.org/10.1007/s11069-020-04328-7.

Polina Silivanova. Water Waves in Gray Scale. Silivanova, Polina, Feb 2021. URL https://unsplash.com/photos/water-waves-in-grayscale-photography-drDXXCDNlYo.

R.M. Sorensen. Basic Coastal Engineering. Springer Science & Business Media, 2006.

Cecilia Soriano, Oriol Jorba, and José Baldasano. One-Way Nesting Versus Two-Way Nesting: Does It Really Make a Difference?, pages 177–185. 01 2004. ISBN 0-306-47294-5. doi: 10.1007/0-306-47813-7_18.

James L Sumich. Introduction to the biology of marine life. Brown (William C.), Dubuque, IA, 5 edition, 01 1992.

David R. Tappin, Andrew Sibley, Kevin Horsburgh, Camille Daubord, Dave Cox, and Dave Long. The english channel 'tsunami' of 27 june 2011 – a probable meteorological source. Weather, 68(6):144–152, May 2013. ISSN 1477-8696. doi: 10.1002/wea.2061. URL http://dx.doi.org/10.1002/wea.2061.

Christopher Torrence and Gilbert P. Compo. A practical guide to wavelet analysis. Bulletin of the American Meteorological Society, 79(1):61–78, January 1998. ISSN 1520-0477. doi: 10.1175/1520-0477(1998)079<0061:apgtwa>2.0.co;2. URL http://dx.doi.org/10.1175/1520-0477(1998)079<0061:APGTWA>2.0.CO;2.

H.J. Verhagen, M. Klein Breteler, and M. Bottema. Tsunami's langs de nederlandse noordzeekust. Technical report, TU Delft, Deltares, Rijkswaterstaat, 2014. URL http://resolver.tudelft.nl/uuid:baf75641-3b3e-4ffd-93f7-8e5c76f71032.

Ivica Vilibić. Numerical simulations of the proudman resonance. Continental Shelf Research, 28(4–5):574–581, March 2008. ISSN 0278-4343. doi: 10.1016/j.csr.2007.11.005. URL http://dx.doi.org/10.1016/j.csr.2007.11.005.

Ivica Vilibić and Jadranka Šepić. Global mapping of nonseismic sea level oscillations at tsunami timescales. Scientific Reports, 7(1), January 2017. ISSN 2045-2322. doi: 10.1038/srep40818. URL http://dx.doi.org/10.1038/srep40818.

D.J. Webb. A model of continental-shelf resonances. Deep Sea Research and Oceanographic Abstracts, 23(1):1–15, January 1976. ISSN 0011-7471. doi: 10.1016/0011-7471(76)90804-4. URL http://dx.doi.org/10.1016/0011-7471(76)90804-4.

Christina A. Wertman, Richard M. Yablonsky, Yang Shen, John Merrill, Christopher R. Kincaid, and Robert A. Pockalny. Mesoscale convective system surface pressure anomalies responsible for meteotsunamis along the u.s. east coast on june 13th, 2013. Scientific Reports, 4(1), November 2014. ISSN 2045-2322. doi: 10.1038/srep07143. URL http://dx.doi.org/10.1038/srep07143.

David A. Williams, Kevin J. Horsburgh, David M. Schultz, and Chris W. Hughes. Examination of generation mechanisms for an english channel meteotsunami: Combining observations and modeling. Journal of Physical Oceanography, 49(1):103–120, January 2019. ISSN 1520-0485. doi: 10.1175/jpo-d-18-0161.1. URL http://dx.doi.org/10.1175/JPO-D-18-0161.1.

David A. Williams, Kevin J. Horsburgh, David M. Schultz, and Chris W. Hughes. Proudman resonance with tides, bathymetry and variable atmospheric forcings. Natural Hazards, 106(2):1169–1194, March 2020. ISSN 1573-0840. doi: 10.1007/s11069-020-03896-y. URL http://dx.doi.org/10.1007/s11069-020-03896-y.

David A. Williams, David M. Schultz, Kevin J. Horsburgh, and Chris W. Hughes. An 8-yr meteotsunami climatology across northwest europe: 2010–17. Journal of Physical Oceanography, 51(4):1145–1161, April 2021. ISSN 1520-0485. doi: 10.1175/jpo-d-20-0175.1. URL http://dx.doi.org/10.1175/JPO-D-20-0175.1.

David Alan Williams. Meteotsunami generation, amplification and occurence in north-west Europe. PhD thesis, University of Liverpool, 2019.

Hui-Min Zuo, Jun Qiu, and Fang-Fang Li. An improved cross-correlation method for efficient clouds forecasting. Theoretical and Applied Climatology, 155(7):6491–6505, May 2024. ISSN 1434-4483. doi: 10.1007/s00704-024-04985-9. URL http://dx.doi.org/10.1007/s00704-024-04985-9.

Jadranka Šepić, Ivica Vilibić, and Danijel Belušić. Source of the 2007 ist meteotsunami (adriatic sea). Journal of Geophysical Research: Oceans, 114(C3), March 2009. ISSN 0148-0227. doi: 10.1029/2008jc005092. URL http://dx.doi.org/10.1029/2008JC005092.

Jadranka Šepić, Ivica Vilibić, and Nataša Strelec Mahović. Northern adriatic meteorological tsunamis: Observations, link to the atmosphere, and predictability. Journal of Geophysical Research: Oceans, 117 (C2), February 2012. ISSN 0148-0227. doi: 10.1029/2011jc007608. URL http://dx.doi.org/10.1029/2011JC007608.

Jadranka Šepić, Ivica Vilibić, Alexander B. Rabinovich, and Sebastian Monserrat. Widespread tsunami-like waves of 23-27 june in the mediterranean and black seas generated by high-altitude atmospheric forcing. Scientific Reports, 5(1), June 2015. ISSN 2045-2322. doi: 10.1038/srep11682. URL http://dx.doi.org/10.1038/srep11682.

A

Other Amplification Mechanisms for Meteotsunamis

A.1. Greenspan Resonance

Greenspan resonance is an amplification mechanism related to edge waves (Greenspan, 1956). Edge waves are waves that run along the shore. They are formed by the reflection of incoming waves combined with refraction and entrapment within the surf zone. These edge waves have been assumed to cause longshore, rhythmic topography (McLachlan and Defeo, 2018).

Greenspan resonance occurs when trapped edge waves resonate with the atmospheric forcing (Greenspan, 1956). This mechanism overlaps significantly with the theory for Proudman resonance. Only one of these forms of resonance can occur, depending on the classification of the meteotsunami as either a non-trapped long wave or a trapped edge wave (Kim et al., 2021a). The phase speed of the edge waves is defined by c_{edge}, where c_{edge} is dependent on the wave frequency, mode, and sea bed slope, per Equation A.1 (Kim et al., 2021a).

$$c_{edge} = \frac{g T_{\text{wave}}}{2\pi} \tan[\beta(2n+1)] \tag{A.1}$$

Here c_{edge} represents the phase speed of the edge waves, T is the period of the edge waves, n is the mode of the edge wave, and β is the sea bed slope. Greenspan resonance is likely to occur if c_{edge} is close to the alongshore component of the atmospheric forcing speed.

A.2. Shelf Resonance

A third resonance mechanism relevant to the amplification of meteotsunamis is shelf resonance, which occurs at the boundary of a continental shelf (Webb, 1976). At such a shelf, the depth decreases suddenly in the onshore direction, causing reflection from the shelf break. This results in a reflected wave and a transmitted wave, each with its own wave properties. Both the reflection coefficient R and the transmission coefficient T can be calculated following Equation A.2 and Equation A.3 (Levin and Nosov, 2016).

$$R = \frac{\sqrt{H_1/H_2} - 1}{\sqrt{H_1/H_2} + 1} \tag{A.2}$$

$$T = \frac{2\sqrt{H_1/H_2}}{\sqrt{H_1/H_2} + 1} \tag{A.3}$$

Here H_1/H_2 is the ratio of depths before and after the step, due to the shelf. Furthermore, both coefficients are related, following Equation A.4:

$$1 + R = T \tag{A.4}$$

If H_1 is much smaller then H_2 (for example when the depth suddenly increases a lot), the reflectivity coefficient can become negative. In practice, a negative reflection coefficient results in a smaller amplitude of the transmitted wave. In Figure A.1, the development of both coefficients is shown over this ratio.

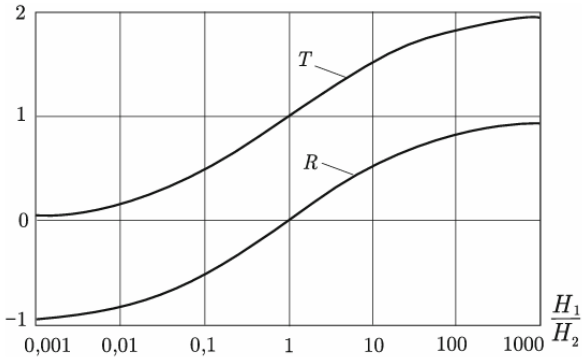

Figure A.1: Reflection coefficients T and R plotted against the depth ratio, in case of a step in the water (Levin and Nosov, 2016). At a very large step ($H_1 >> H_2$), the transmitted wave can become twice as large, whereas at no step ($H_1 = H_2$) there is no reflected wave. A step down ($H_1 << H_2$) results in a negative reflected wave.

The interference between the initial wave and the reflected wave can lead to amplification of the transmitted wave. This can produce large amplitude and phase variations near the coast. The other way around, when moving from shallow to deep water, the transmitted wave amplitude decreases (Levin and Nosov, 2016).

A.3. Seiching

Apart from Proudman Resonance, Seiching is the most relevant amplification mechanism in the growth of meteotsunamis. Without seiching, meteotsunamis will not grow larger than approximately 1 meter. Seiching can cause meteotsunamis to grow to significant heights of 4 to 6 meters (Williams, 2019), increasing the dangers of the incoming tsunami waves. This phenomenon is mostly known from port designs, where it occurs when the eigenfrequency of the wave and harbor match (de Jong and Battjes, 2004). However, seiching can also occur in semi-enclosed basins. This seiching has caused meteotsunami amplification on several occasions, both near the Mediterranean coast (Šepić et al., 2015) and in the Yellow Sea (Choi et al., 2014). The eigenfrequency of a basin is independent of external forcing, and can therefore be calculated independently of the tsunami wave. Since the eigenfrequency of a basin can vary a lot, seiching occurs when it matches the eigenfrequency of the dominant mode of the meteotsunami (Rabinovich, 2009).

The meteotsunami propagates towards the coast, and after arrival, it is reflected by the closed end of the basin. If this reflected wave is in phase with the incoming wave, a standing wave forms, which then superimposes the incoming wave. Repetitive occurrence results in significant growth of the incoming wave. The resonant period of a semi-enclosed basin is calculated via Merian's formula (Equation A.5) (Pugh and Woodworth, 2014).

$$T_n = \frac{2L}{n\sqrt{gH}} \tag{A.5}$$

Here n represents the mode of the resonant wave, L the basin length, g the gravitational constant, and H the water depth. The fundamental mode is calculated at $n = 1$, which relates to the wave that has the maximum period that can occur in the basin. Since real basins are two-dimensional and vary in depth, often Merian's formula has to be adapted (Rabinovich, 2009). As the shape becomes more complicated, so do the seiching patterns. Seiching is generally most common in thin basins with narrow entrances (Williams, 2019).

Near the Dutch coast, several seiching events have been reported as well, for example at the port of IJmuiden and the port of Rotterdam. The seawaves responsible for these seiches had an atmospheric origin (de Jong and Battjes, 2004). It is therefore plausible these events were meteotsunamis.

A.4. Shoaling and Refraction

Additionally, more common mechanisms such as shoaling and refraction are known to have influenced meteotsunami generation on several occasions.

Shoaling is a mechanism that occurs when the water depth gradually changes. Due to the decreasing water depth, the wave speed and wavelength decrease, while the wave height increases. Shoaling can occur with any wave whose behavior is influenced by the sea bed (Jackson and Short, 2020). Consequently, tsunami waves can experience the effects of shoaling. Shoaling effects can be calculated using Green's Law (Equation A.6) (Green, 1838):

$$a_2 = \sqrt{\frac{c_{g,1}}{c_{g,2}}} a_1 \tag{A.6}$$

Here, a_i represents the amplitude of the wave at both locations and $c_{g,i}$ the group velocity. The term under the square root is known as the shoaling coefficient. As the waves approach the coast, c_g decreases, the shoaling coefficient increases, and subsequently the wave amplitude increases. There are records of meteotsunamis of up to 1.4 meters that were amplified by a combination of Proudman resonance and shoaling (Chen and Niu, 2018).

In shoaling it is assumed that the width between wave rays stays constant. However, when waves do not approach the coast perpendicularly, they will slowly change direction due to the depth variation along the crest. These depth variations cause an inhomogeneous propagation speed, as the waves move faster in the deeper part of the water. The difference in propagation speed causes the waves to bend. The angle that the waves make with the coast (θ) can also describe the decrease in width between the waves as they approach the coast. If the depth contours are parallel, the influence of the reduction in width on the wave height can best be described via Snell's Law (Equation A.7) (Holthuijsen, 2007). This law has been used in literature to describe the propagation of meteotsunamis (Latifah et al., 2024).

$$c_1 = \frac{\sin\theta_0}{\sin\theta_1} c_0 \tag{A.7}$$

Here, c_n is the wave speed ant θ_n the angle of incidence at a given location. Refraction can also be included in the formula for shoaling, as is done in Equation A.8.

$$a_2 = \sqrt{\frac{c_{g,1}}{c_{g,2}}} \sqrt{\frac{sin\theta_1}{sin\theta_2}} a_1 \tag{A.8}$$

The refraction coefficient is represented by the square root of the two sine terms. Refraction also occurs when the depth contours are not straight lines. This might result in even further amplification of the waves on foreshore, and dampening of the waves when the distance between wave rays grows. Refraction has been found to be responsible for the amplification of hurricanes and edge waves over the shelf, comparable to meteotsunamis (Pasquet et al., 2013).

B

Namelist WRF

```
&time_control
run_days = 0,
run_hours = 12,
run_minutes = 0,
run_seconds = 0,
start_year = 2017, 2017, 2017,
start_month = 05, 05, 05,
start_day = 29, 29, 29,
start_hour = 00, 00, 00,
end_year = 2017, 2017, 2017,
end_month = 05, 05, 05,
end_day = 29, 29, 29,
end_hour = 12, 12, 12,
interval_seconds = 3600,
input_from_file = .true.,.true.,.true.,
history_interval = 360, 360, 2,
frames_per_outfile = 1, 1, 1,
restart = .true.,
restart_interval = 360,
override_restart_timers = .true.,
io_form_history = 2,
io_form_restart = 2,
io_form_input = 2,
io_form_boundary = 2,
debug_level = 0,
!iofields_filename = "iofield_lists", "iofield_lists", "iofield_lists",
ignore_iofields_warning = .true.,
auxinput4_inname = "wrflowinp_d<domain>"
auxinput4_interval = 60 ,60,60,
io_form_auxinput4 = 2
/

&domains
time_step = 15,
use_adaptive_time_step = .false.,
time_step_fract_num = 0,
time_step_fract_den = 1,
max_dom = 3,
e_we = 220, 346, 331,
e_sn = 270, 409, 454,
e_vert = 80, 80, 80,
```

```
eta_levels = 1.000000, 0.998621, 0.997244, 0.995868, 0.994495,
0.993123, 0.991753, 0.990385, 0.989018, 0.987653,
0.986291, 0.984929, 0.983570, 0.982213, 0.980857,
0.979503, 0.978151, 0.976800, 0.975451, 0.974104,
0.972759, 0.971415, 0.970073, 0.968732, 0.967393,
0.966054, 0.964715, 0.963377, 0.962036, 0.960690,
0.959337, 0.957970, 0.956580, 0.955150, 0.953657,
0.952060, 0.950295, 0.948260, 0.945792, 0.942634,
0.938390, 0.932460, 0.923975, 0.911752, 0.894345,
0.870275, 0.838489, 0.798900, 0.752652, 0.701859,
0.648956, 0.596096, 0.544846, 0.496177, 0.450589,
0.408266, 0.369196, 0.333257, 0.300271, 0.270038,
0.242351, 0.217011, 0.193825, 0.172615, 0.153215,
0.135473, 0.119246, 0.104407, 0.090836, 0.078426,
0.067077, 0.056698, 0.047207, 0.038528, 0.030591,
0.023333, 0.016696, 0.010626, 0.005076, 0.000000,
p_top_requested = 5000,
num_metgrid_levels = 38,
num_metgrid_soil_levels = 4,
dx = 9000, 3000, 1000,
dy = 9000, 3000, 1000,
grid_id = 1, 2, 3,
parent_id = 1, 1, 2,
i_parent_start = 1, 47, 135,
j_parent_start = 1, 90, 105,
parent_grid_ratio = 1, 3, 3,
parent_time_step_ratio = 1, 3, 3,
feedback = 1,
smooth_option = 0
sfcp_to_sfcp = .true.,
/

&physics
mp_physics = 10, 10, 10,
ra_lw_physics = 4, 4, 4,
ra_sw_physics = 4, 4, 4,
radt = 27, 9, 3,
sf_sfclay_physics = 1, 1, 1,
sf_surface_physics = 2, 2, 2,
bl_pbl_physics = 5, 5, 5,
bl_mynn_tkebudget = 1, 1, 1,
bldt = 0, 0, 0,
cu_physics = 1, 0, 0,
cudt = 5, 0, 0,
isfflx = 1,
ifsnow = 0,
icloud = 1,
surface_input_source = 1,
num_land_cat = 21,
maxiens = 1,
maxens = 3,
maxens2 = 3,
maxens3 = 16,
ensdim = 144,
sf_urban_physics = 0, 0, 0,
windfarm_opt = 0, 0, 0,
sst_update = 1,
```

```
/

&fdda
grid_fdda = 0, 0, 0,
gfdda_inname = "wrffdda_d<domain>"
gfdda_interval_m = 360, 360, 360,
gfdda_end_h = 720, 720, 720,
io_form_gfdda = 2,
fgdt = 0, 0, 0,
if_zfac_uv = 1, 1, 1,
if_zfac_t = 1, 1, 1,
if_zfac_q = 1, 1, 1,
k_zfac_uv = 23, 23, 23,
k_zfac_t = 23, 23, 23,
k_zfac_q = 23, 23, 23,
guv = 0.0003, 0.0003, 0.0003,
gt = 0.0003, 0.0003, 0.0003,
gq = 0.0003, 0.0003, 0.0003,
if_ramping = 0,
dtramp_min = 60.0,
/

&dynamics
w_damping = 1,
diff_opt = 1, 1, 1,
km_opt = 4, 4, 4,
diff_6th_opt = 0, 0, 0,
diff_6th_factor = 0.12, 0.12, 0.12,
base_temp = 290.
damp_opt = 0,
zdamp = 5000., 5000., 5000.,
dampcoef = 0.2, 0.2, 0.2,
khdif = 0, 0, 0,
kvdif = 0, 0, 0,
non_hydrostatic = .true., .true., .true.,
moist_adv_opt = 1, 1, 1,
scalar_adv_opt = 1, 1, 1,
/

&bdy_control
spec_bdy_width = 5,
spec_zone = 1,
relax_zone = 4,
specified = .true., .false.,.false.,
nested = .false., .true., .true.,
/

&grib2
/

&namelist_quilt
nio_tasks_per_group = 0,
nio_groups = 1,
/
```

C

Literature on Physical Parameters

	(Heo, 2016)Heo and Ha (2016)	(Ha, 2018) Ha et al. (2018)	(Mourre, 2020)Mourre et al. (2020)	(Denamiel, 2019)Denamiel et al. (2019)	(Horvath, 2014)Horvath and Vilibić (2014)	(Horvath, 2018)Horvath et al. (2018)	(Sepic, 2009)Šepić et al. (2009)
Microphysics	WSM5	WSM5	Thompson	Morrison 2	Morrison 2	Morrison 2	Lin et al.
Longwave radiation	RRTMG	RRTMG	RRTM	RRTM	RRTM	RRTM	
Shortwave radiation	RRTMG	RRTMG	Goddard	Dudhia	Dudhia	Dudhia	
Planetary boundary layer	YSU PBL	YSU PBL	Mellor- Yamada Nakanishi and Nino	MYJ	Mellor-Yamada-Janjic	MYJ	MYJ
Surface layer	Monin-Obukhov	Monin-Obukhov	Monin-Obukhov	Eta		Eta	
Land surface model	Noah LSM	Noah LSM	Noah LSM	Five-layer thermal diffusion scheme	Noah LSM	Five-layer thermal diffusion scheme	
Cumulus	Kain-Fritsch	Kain-Fritsch	Grell-Devenyi	Kain-Fritsch	Grell-Devenyi	Kain-Fritsch	Grell-Devenyi

D

Threshold Selection

D.1. Calculation relative thresholds

As stated, for the calculation of the relative thresholds, the root mean square wave heights are calculated via Equation D.1

$$a_{rms} = \sqrt{\overline{a_i^2}} \tag{D.1}$$

Where a_rms is the root mean squared amplitude and a_i every amplitude in the dataset. The results are shown in Table D.1 and Table D.2

	2010	**2011**	**2012**	**2013**	**2014**	**2015**	**2016**	**2017**	**2018**
A12	0.03	0.08	0.05	0.04	0.12	0.23	0.03	0.04	0.04
D15	0.03	0.03	0.03	0.04	0.03	0.05	0.07	NaN	NaN
F16	0.03	0.03	0.03	0.03	0.03	0.03	0.03	0.03	0.03
J6	0.04	0.04	0.05	0.06	0.06	0.04	0.04	0.08	0.04
H	0.03	0.71	0.03	0.03	0.03	0.03	0.03	0.03	0.03
IJM	0.15	0.04	0.04	0.04	0.03	0.03	0.04	0.03	0.04
EUR	0.04	0.03	0.04	0.11	0.03	0.04	0.07	0.04	0.04
LG	NaN	NaN	NaN	0.03	0.03	0.03	0.03	0.03	0.08

Table D.1: Root mean square wave height for each location for each year, according to the threshold suggested by Monserrat et al.

	2010	**2011**	**2012**	**2013**	**2014**	**2015**	**2016**	**2017**	**2018**
A12	0.05	0.12	0.08	0.06	0.18	0.34	0.05	0.06	0.05
D15	0.05	0.05	0.05	0.05	0.05	0.08	0.11	NaN	NaN
F16	0.05	0.05	0.04	0.05	0.04	0.05	0.04	0.05	0.04
J6	0.06	0.06	0.08	0.10	0.09	0.06	0.05	0.12	0.06
H	0.05	1.06	0.04	0.05	0.05	0.05	0.04	0.05	0.04
IJM	0.23	0.05	0.06	0.07	0.04	0.04	0.06	0.05	0.06
EUR	0.07	0.05	0.06	0.16	0.04	0.05	0.11	0.06	0.06
LG	NaN	NaN	NaN	0.04	0.04	0.04	0.04	0.04	0.11

Table D.2: Root mean square wave height for each location for each year and the mean over the years, according to the threshold suggestion by Williams et al.

The years with NaN values are either missing or unusable. The means of all locations will be used as the relative thresholds.

D.2. Visual Inspection

D.2.1. 0.10-meter threshold

	A12	D15	F16	J6	H	IJM	EUR	LG	Count
8-12-2011	1	0	0	0	0	1	0	-	2
3-1-2012	1	0	0	1	0	1	0	-	3
22-1-2012	1	1	0	0	0	0	0	-	2
15-8-2012	0	0	0	0	1	1	0	-	2
25-1-2014	1	0	0	0	1	0	0	0	2
7-3-2014	1	1	0	0	0	0	0	0	2
18-7-2014	0	0	0	0	0	0	1	1	2
19-7-2014	1	0	1	1	0	1	0	0	4
7-1-2015	1	0	1	0	0	0	0	0	2
10-1-2015	1	0	0	0	0	0	1	0	2
28-1-2015	0	1	0	0	0	0	0	1	2
12-2-2017	1	-	1	0	0	0	0	0	2
29-5-2017	0	-	0	0	1	1	1	1	4
2-3-2018	1	-	1	0	0	0	0	0	2

D.2.2. 0.25-meter threshold

	A12	D15	F16	J6	H	IJM	EUR	LG	Count
29-5-2017	0	-	0	0	0	1	1	1	3

E

Found Meteotsunamis

For each selected event, an overview of the filtered elevation data at each station is plotted, to give insight into the propagation of the meteotsunami between the stations. Furthermore, per station three plots are presented, including the original signal, the filtered signal, and a zoomed version of the original signal. The limits of the zoomed plot are 1.5 hours before and after the maximum amplitude of the filtered signal (also visualized by the black vertical lines in the plots). If the station its data has been filtered out, the zoom limits of the previous station are used for the zoomed plot.

E.1. Winter event of 2012

E.1.1. Overview

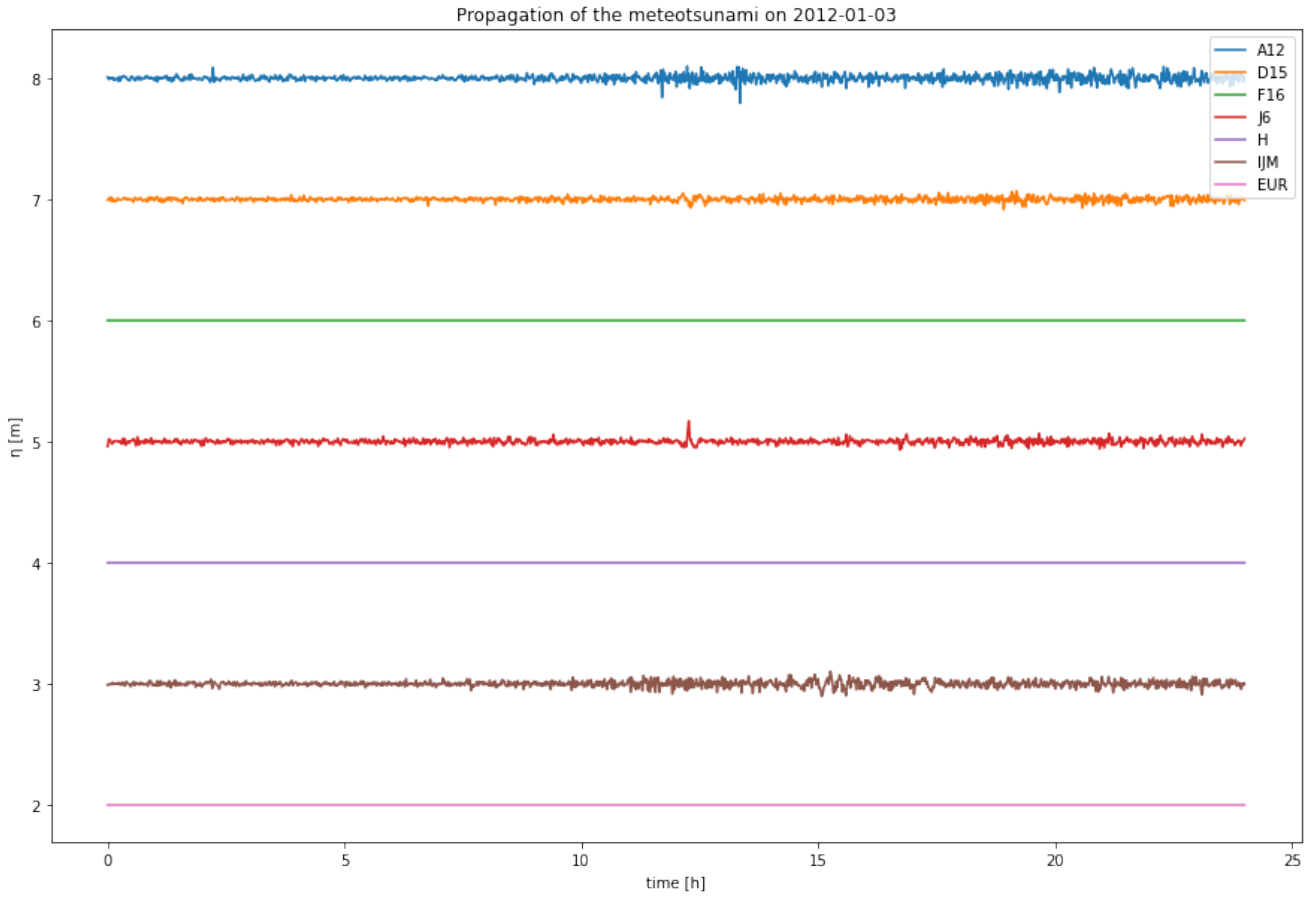

Figure E.1: Overview of band-pass filtered elevation data for the winter event of 2012.

E.1.2. Data per location

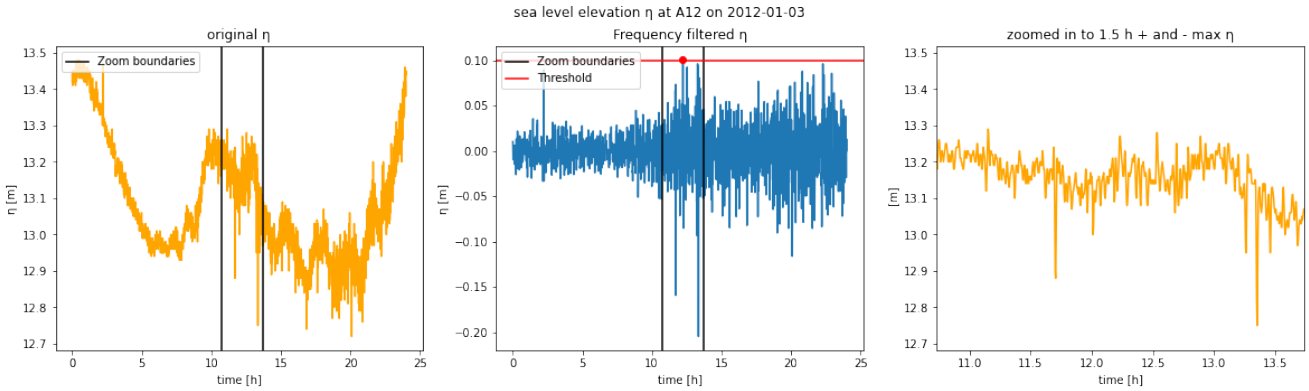

Figure E.2: Original elevation data (left), band-pass filtered elevation data (middle), and zoom of the original elevation data at the max amplitude (right) of station A12, during the winter event of 2012.

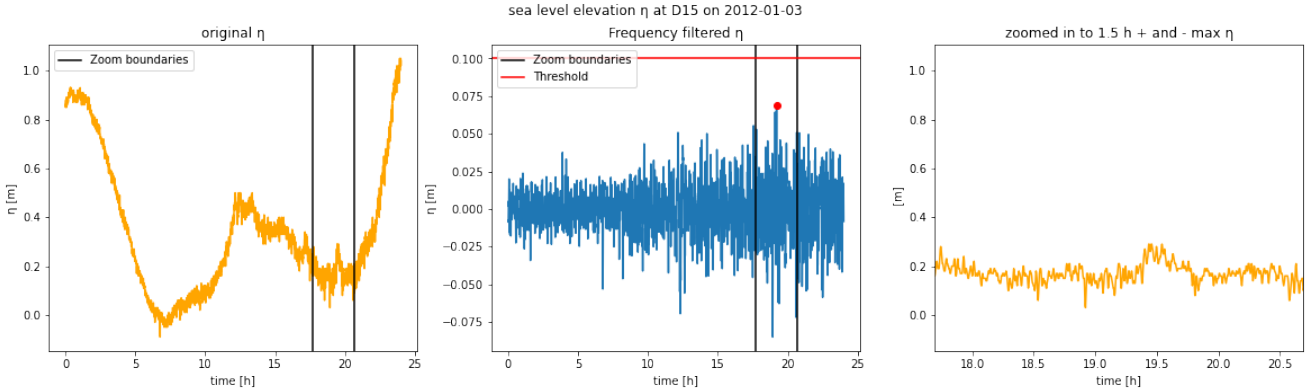

Figure E.3: Original elevation data (left), band-pass filtered elevation data (middle), and zoom of the original elevation data at the max amplitude (right) of station D15, during the winter event of 2012.

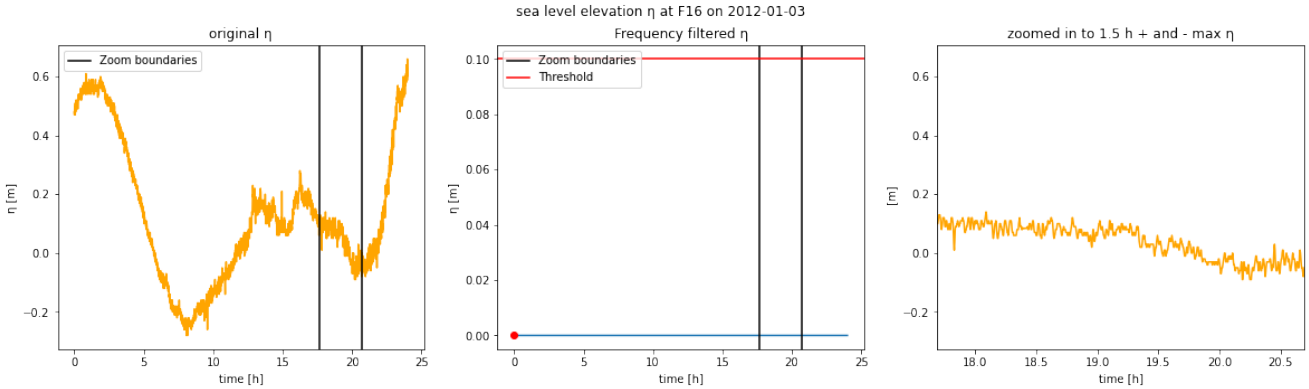

Figure E.4: Original elevation data (left), band-pass filtered elevation data (middle), and zoom of the original elevation data at the max amplitude (right) of station F16, during the winter event of 2012.

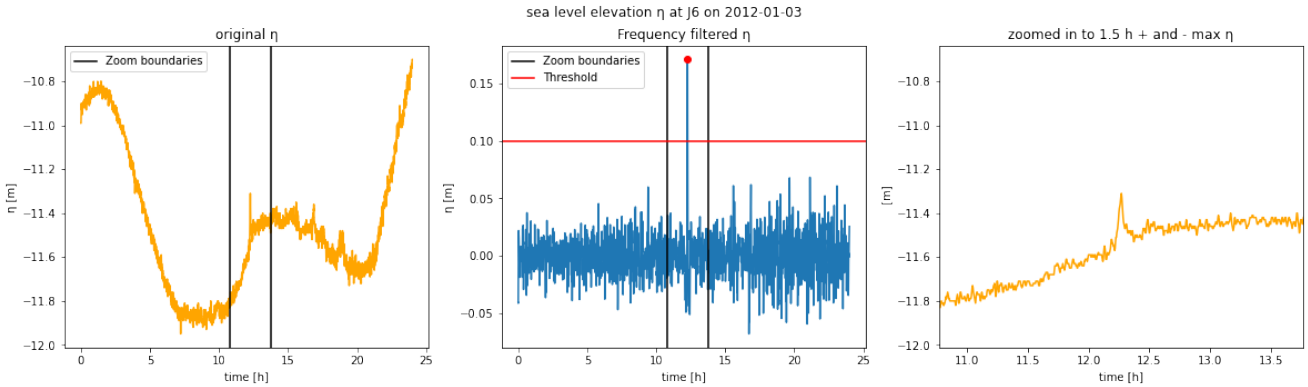

Figure E.5: Original elevation data (left), band-pass filtered elevation data (middle), and zoom of the original elevation data at the max amplitude (right) of station J6, during the winter event of 2012.

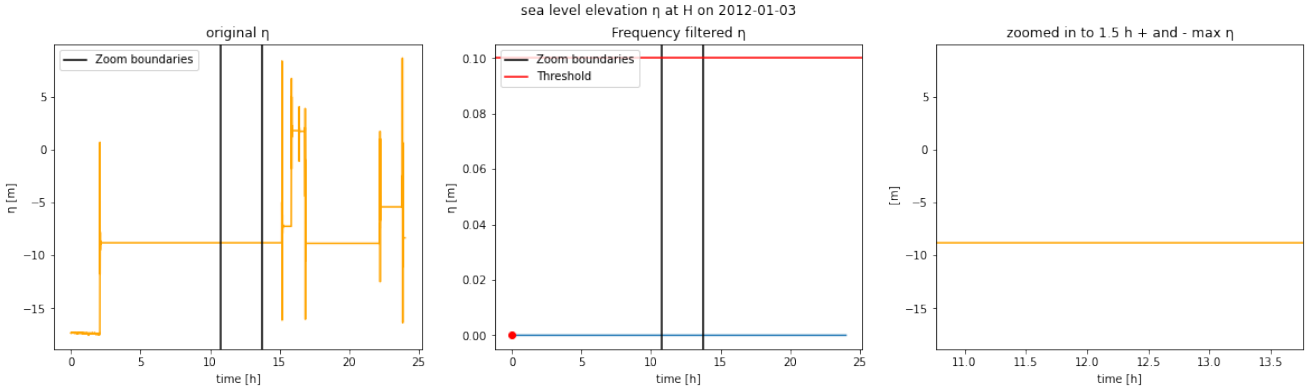

Figure E.6: Original elevation data (left), band-pass filtered elevation data (middle), and zoom of the original elevation data at the max amplitude (right) of station H, during the winter event of 2012.

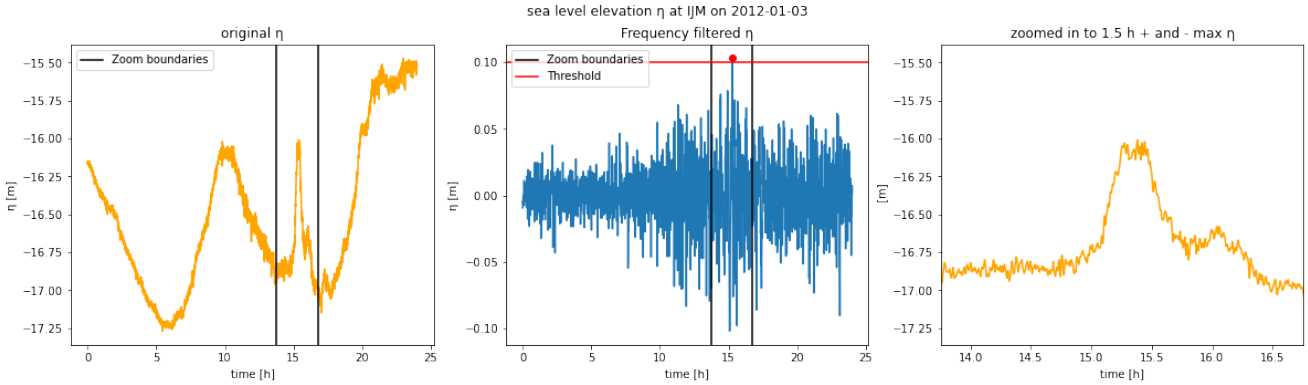

Figure E.7: Original elevation data (left), band-pass filtered elevation data (middle), and zoom of the original elevation data at the max amplitude (right) of station IJM, during the winter event of 2012.

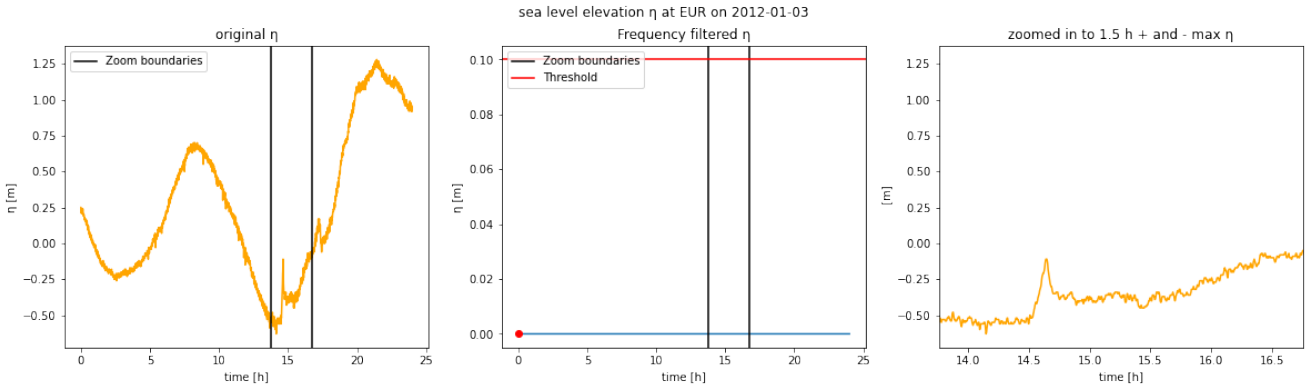

Figure E.8: Original elevation data (left), band-pass filtered elevation data (middle), and zoom of the original elevation data at the max amplitude (right) of station EUR, during the winter event of 2012.

E.2. Summer event of 2012

E.2.1. Overview

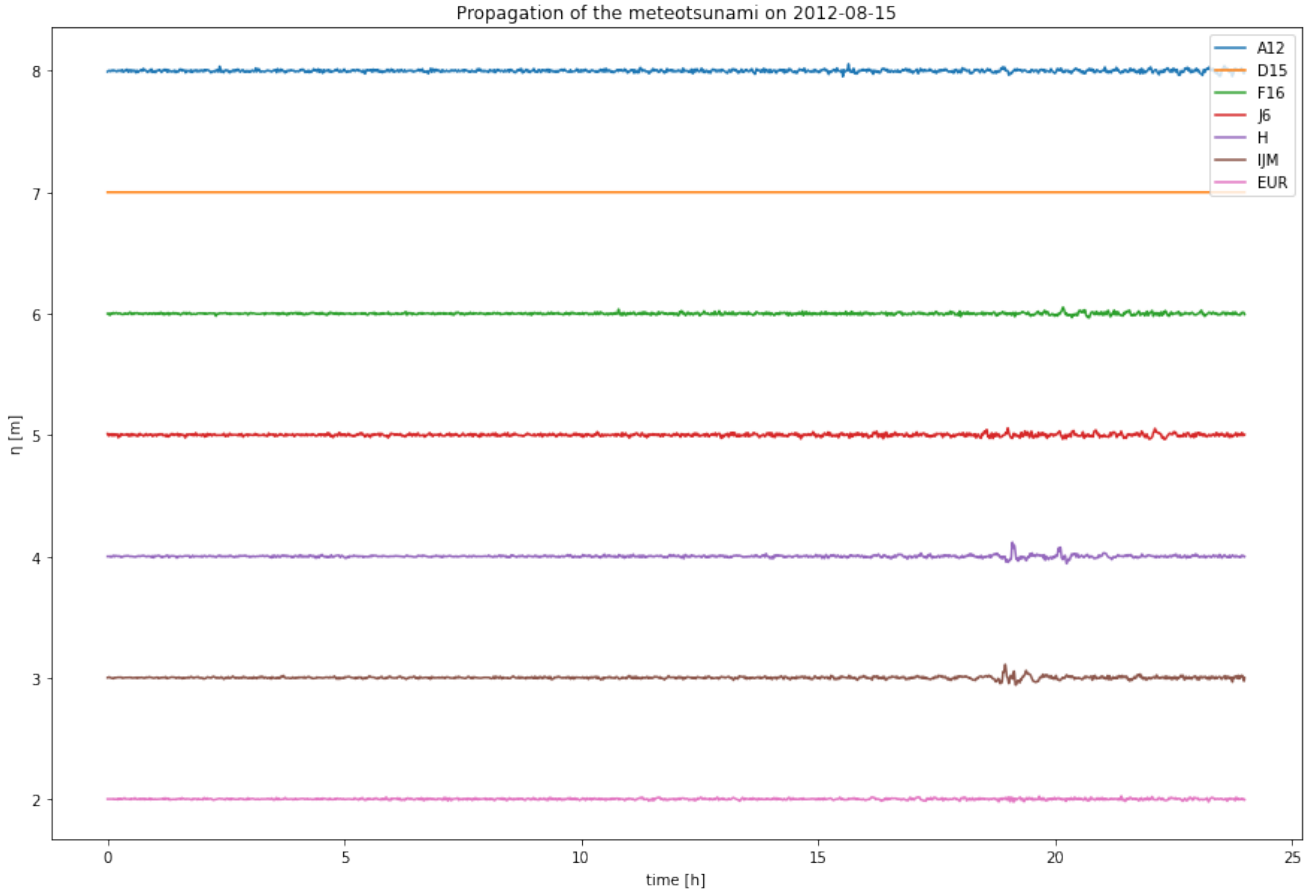

Figure E.9: Overview of band-pass filtered elevation data for the summer event of 2012.

E.2.2. Data per location

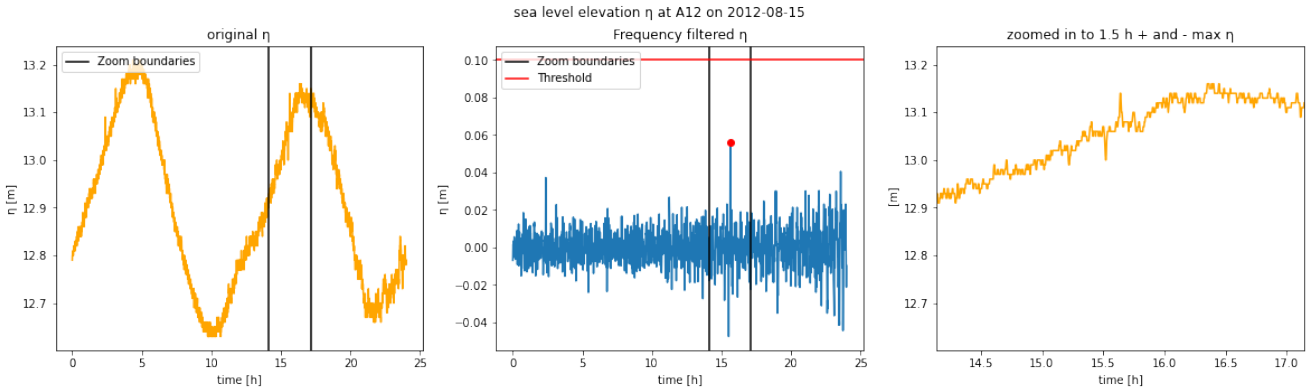

Figure E.10: Original elevation data (left), band-pass filtered elevation data (middle), and zoom of the original elevation data at the max amplitude (right) of station A12, during the summer event of 2012.

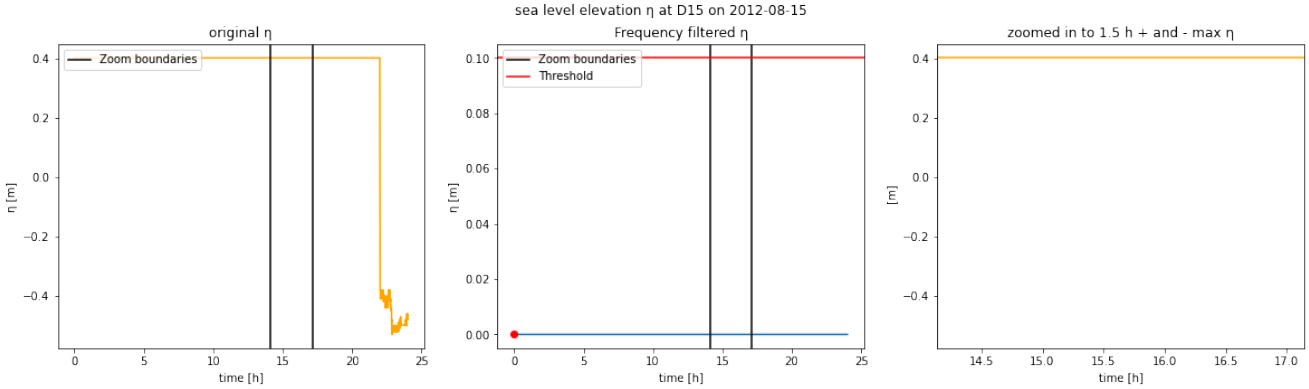

Figure E.11: Original elevation data (left), band-pass filtered elevation data (middle), and zoom of the original elevation data at the max amplitude (right) of station D15, during the summer event of 2012.

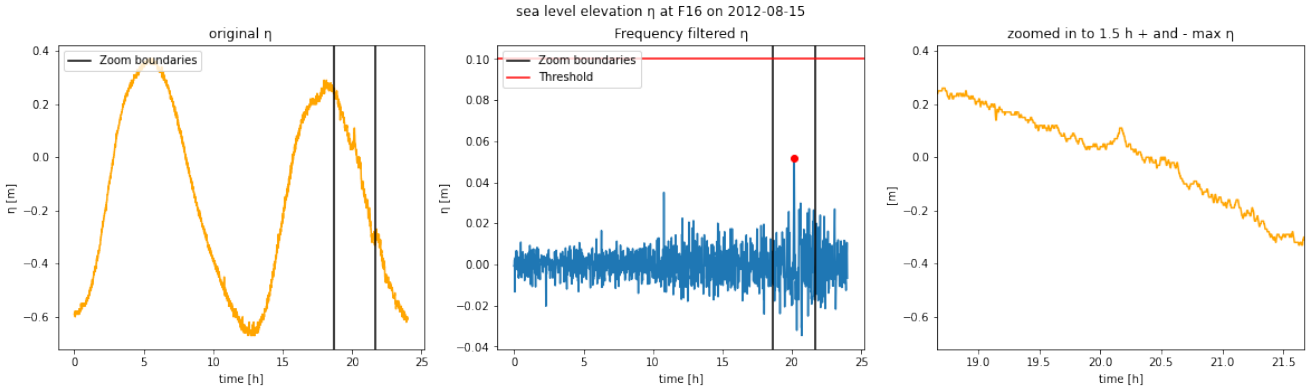

Figure E.12: Original elevation data (left), band-pass filtered elevation data (middle), and zoom of the original elevation data at the max amplitude (right) of station F16, during the summer event of 2012.

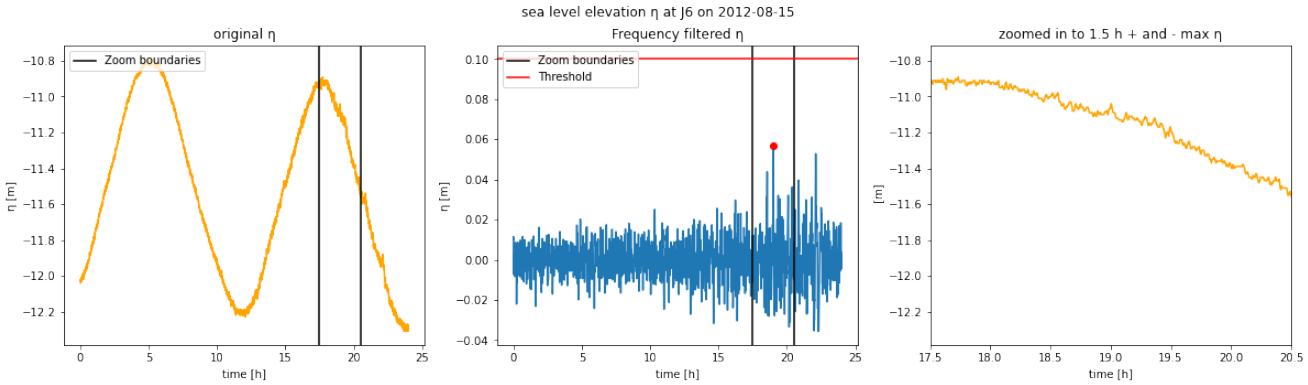

Figure E.13: Original elevation data (left), band-pass filtered elevation data (middle), and zoom of the original elevation data at the max amplitude (right) of station J6, during the summer event of 2012.

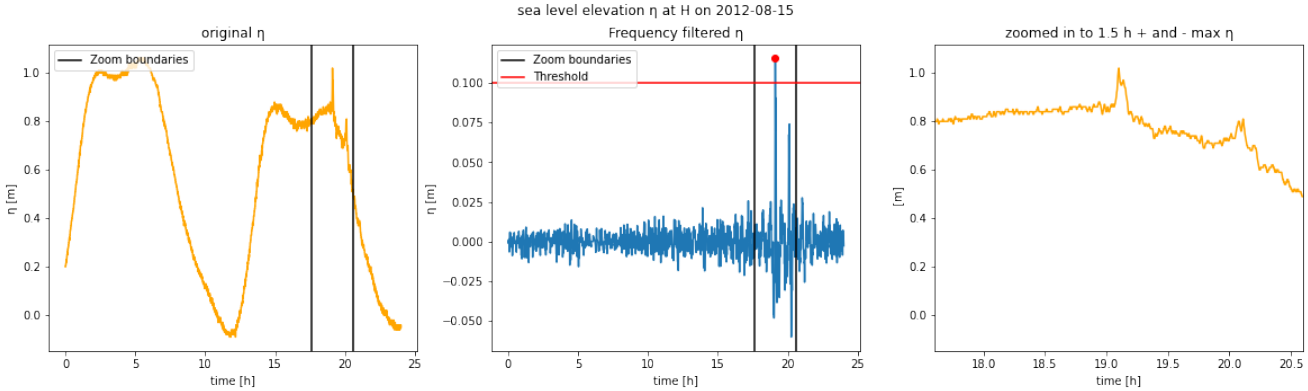

Figure E.14: Original elevation data (left), band-pass filtered elevation data (middle), and zoom of the original elevation data at the max amplitude (right) of station H, during the summer event of 2012.

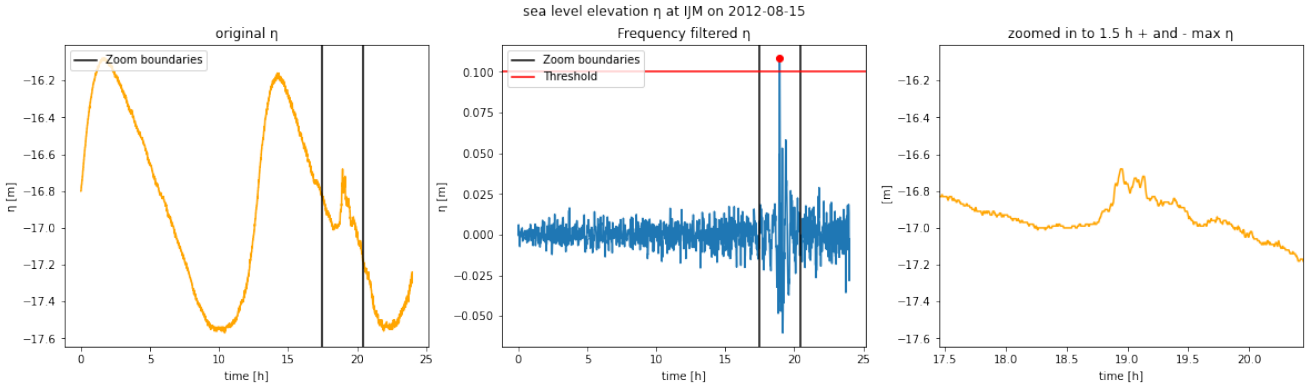

Figure E.15: Original elevation data (left), band-pass filtered elevation data (middle), and zoom of the original elevation data at the max amplitude (right) of station IJM, during the summer event of 2012.

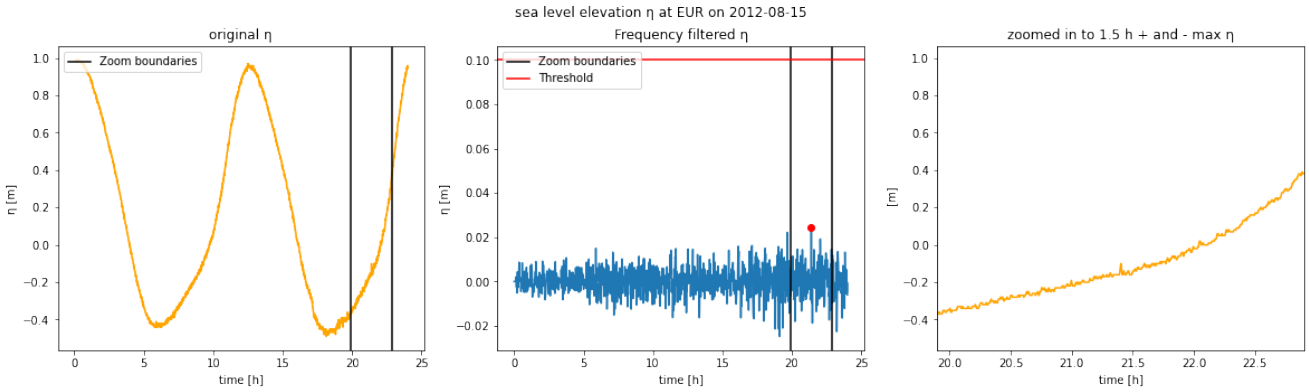

Figure E.16: Original elevation data (left), band-pass filtered elevation data (middle), and zoom of the original elevation data at the max amplitude (right) of station EUR, during the summer event of 2012.

E.3. Summer events of 2014

E.3.1. Overview

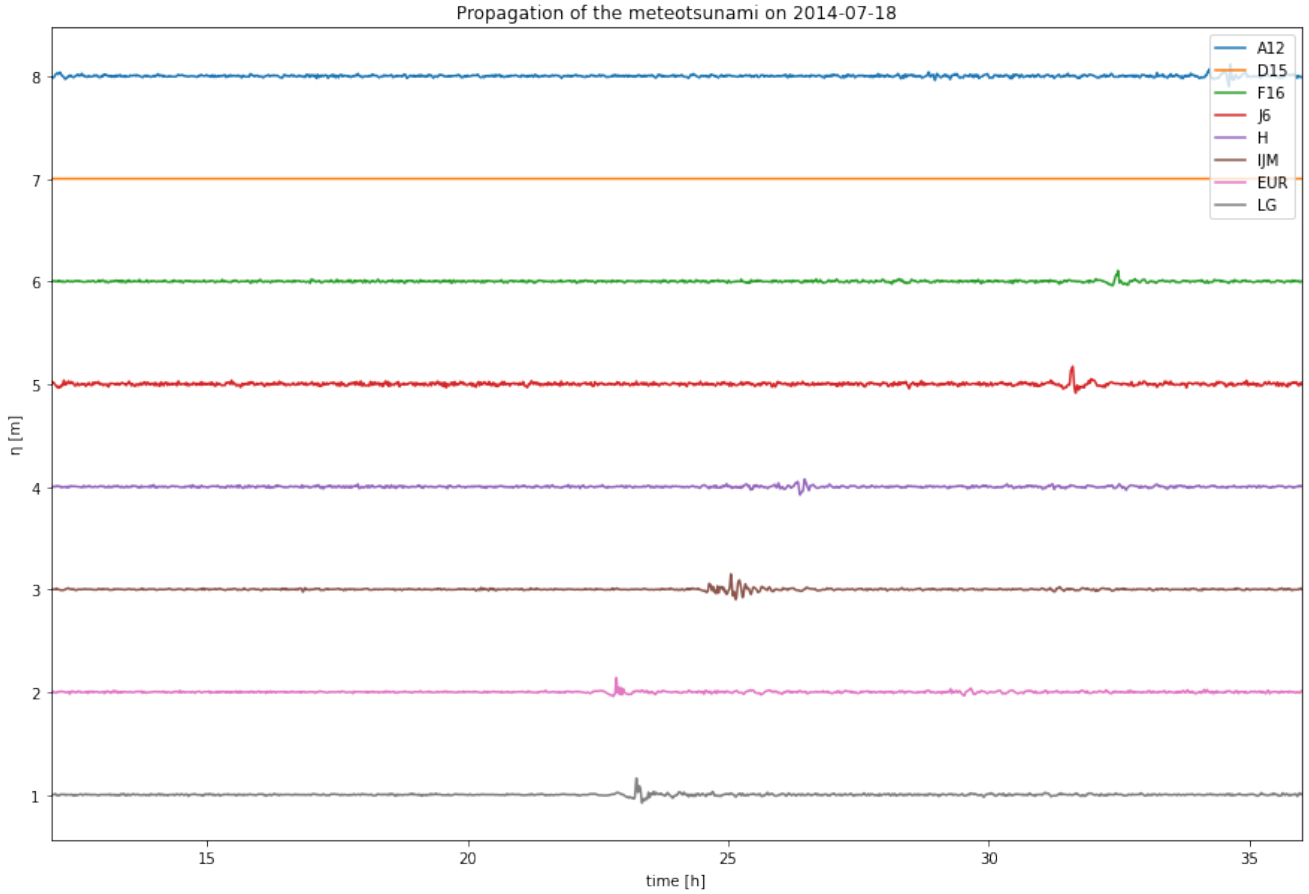

Figure E.17: Overview of band-pass filtered elevation data for the summer events of 2014.

E.3.2. Data per location

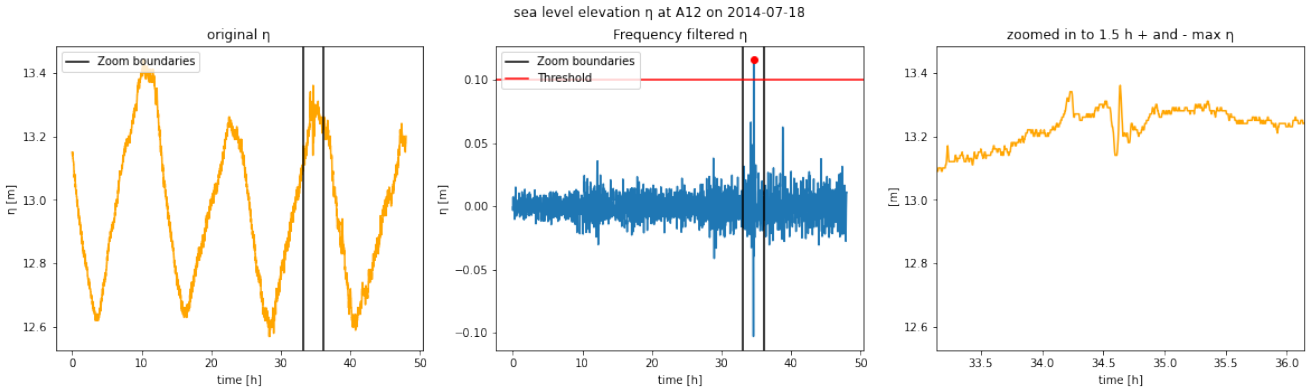

Figure E.18: Original elevation data (left), band-pass filtered elevation data (middle), and zoom of the original elevation data at the max amplitude (right) of station A12, during the summer events of 2014.

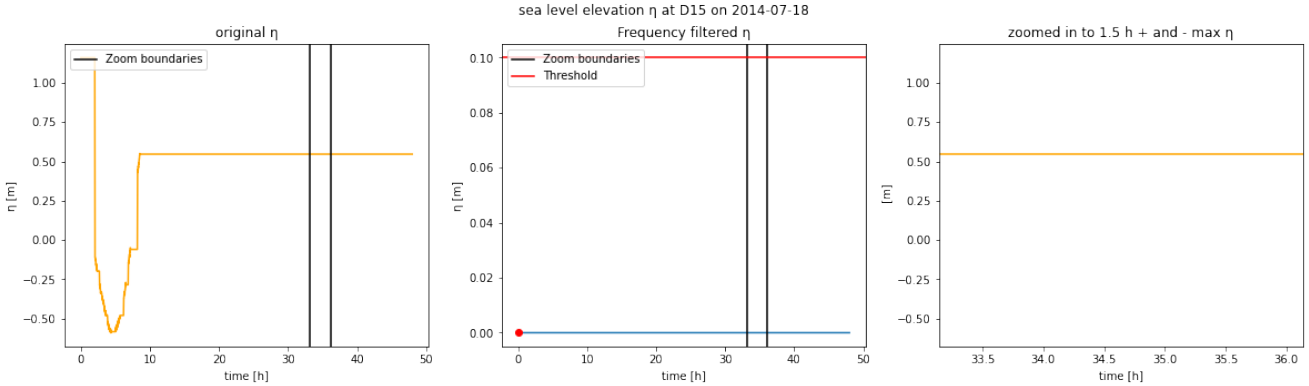

Figure E.19: Original elevation data (left), band-pass filtered elevation data (middle), and zoom of the original elevation data at the max amplitude (right) of station D15, during the summer events of 2014.

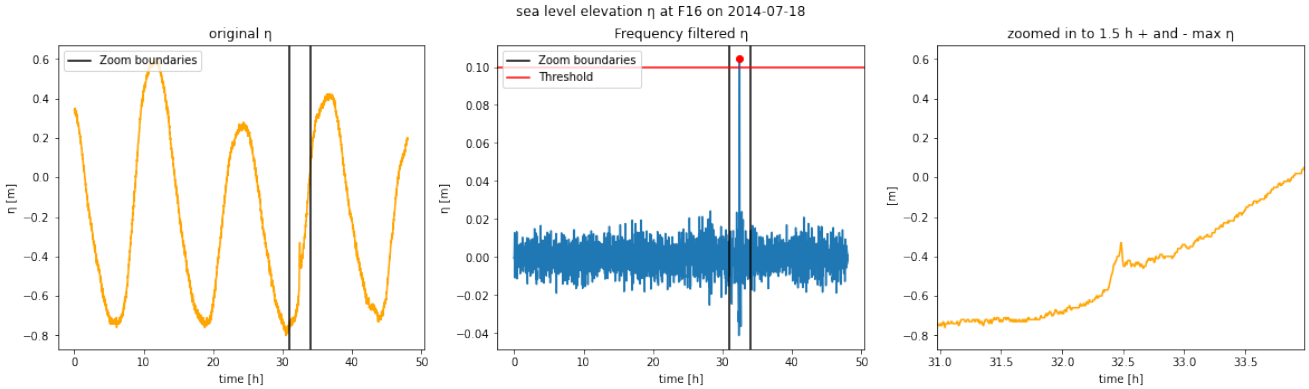

Figure E.20: Original elevation data (left), band-pass filtered elevation data (middle), and zoom of the original elevation data at the max amplitude (right) of station F16, during the summer events of 2014.

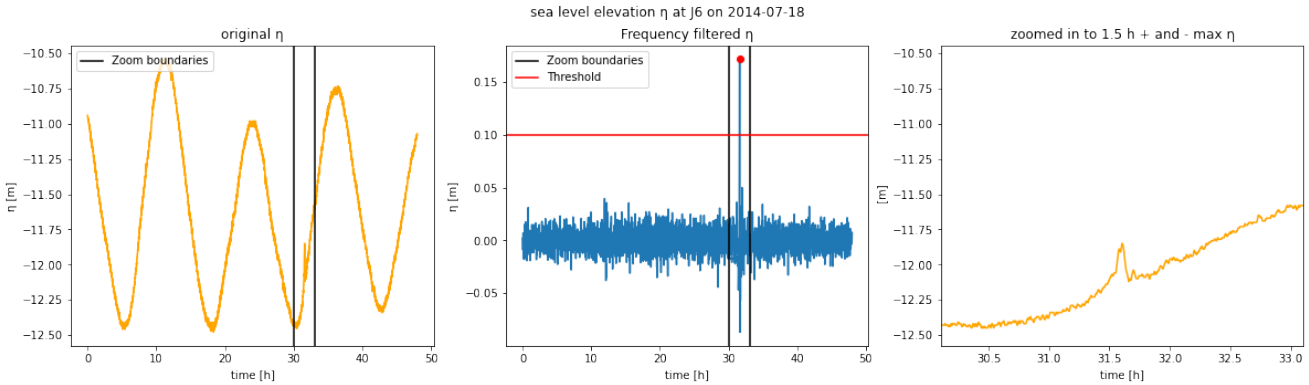

Figure E.21: Original elevation data (left), band-pass filtered elevation data (middle), and zoom of the original elevation data at the max amplitude (right) of station J6, during the summer events of 2014.

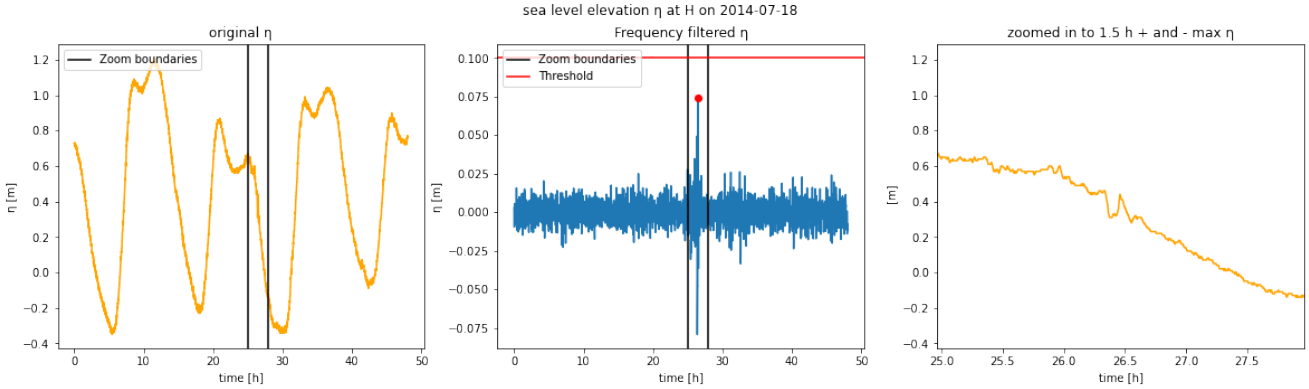

Figure E.22: Original elevation data (left), band-pass filtered elevation data (middle), and zoom of the original elevation data at the max amplitude (right) of station H, during the summer events of 2014.

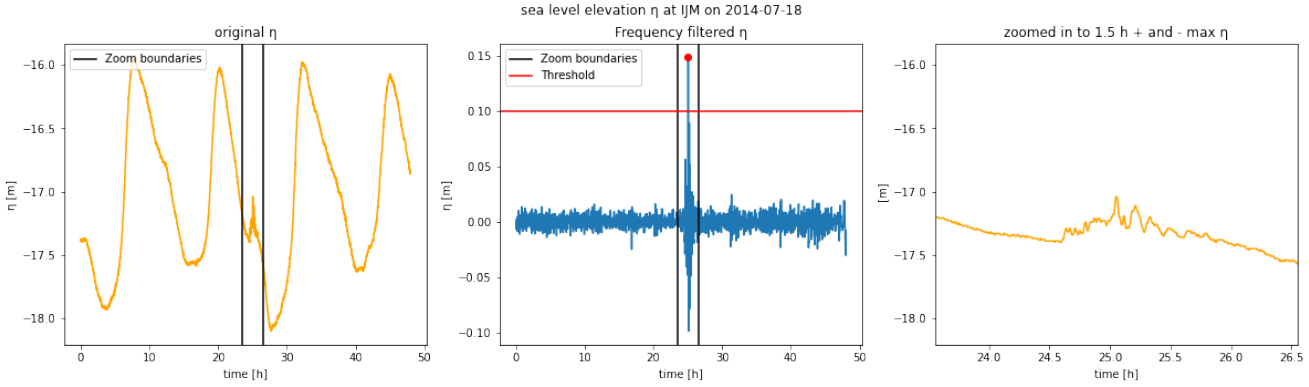

Figure E.23: Original elevation data (left), band-pass filtered elevation data (middle), and zoom of the original elevation data at the max amplitude (right) of station IJM, during the summer events of 2014.

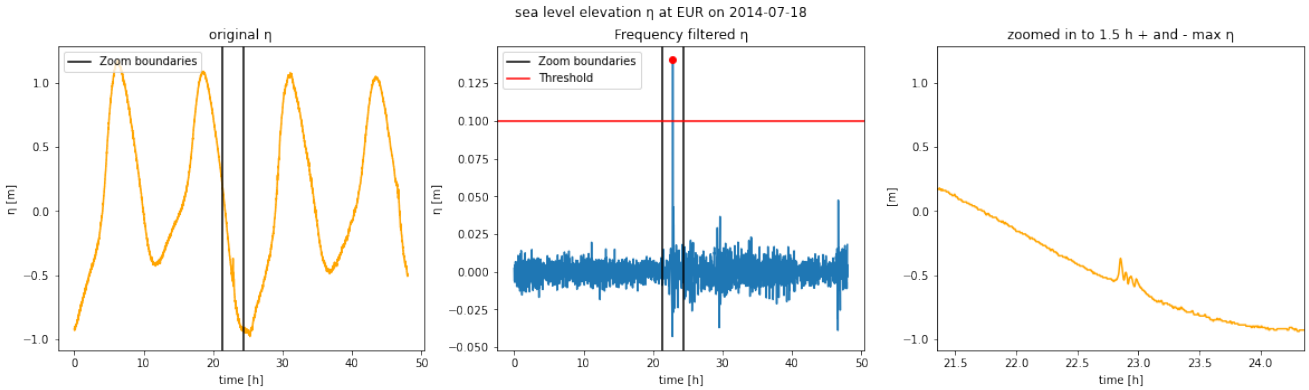

Figure E.24: Original elevation data (left), band-pass filtered elevation data (middle), and zoom of the original elevation data at the max amplitude (right) of station EUR, during the summer events of 2014.

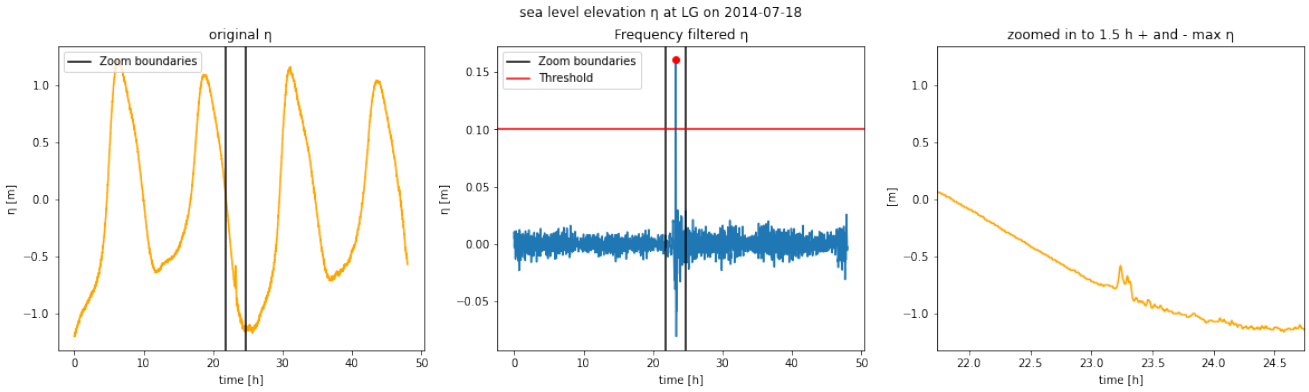

Figure E.25: Original elevation data (left), band-pass filtered elevation data (middle), and zoom of the original elevation data at the max amplitude (right) of station LG, during the summer events of 2014.

E.4. Winter event of 2015

E.4.1. Overview

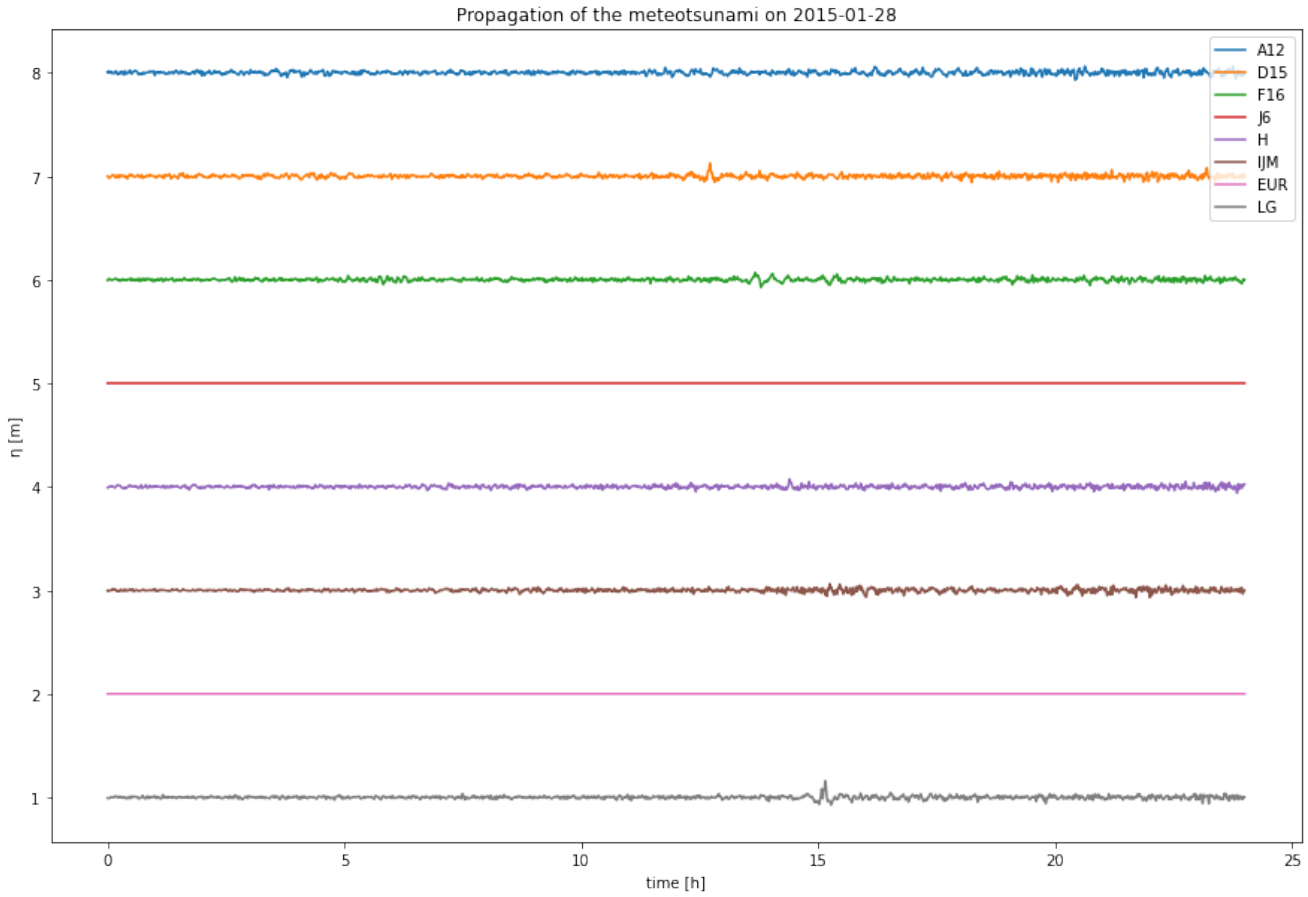

Figure E.26: Overview of band-pass filtered elevation data for the winter event of 2015.

E.4.2. Data per location

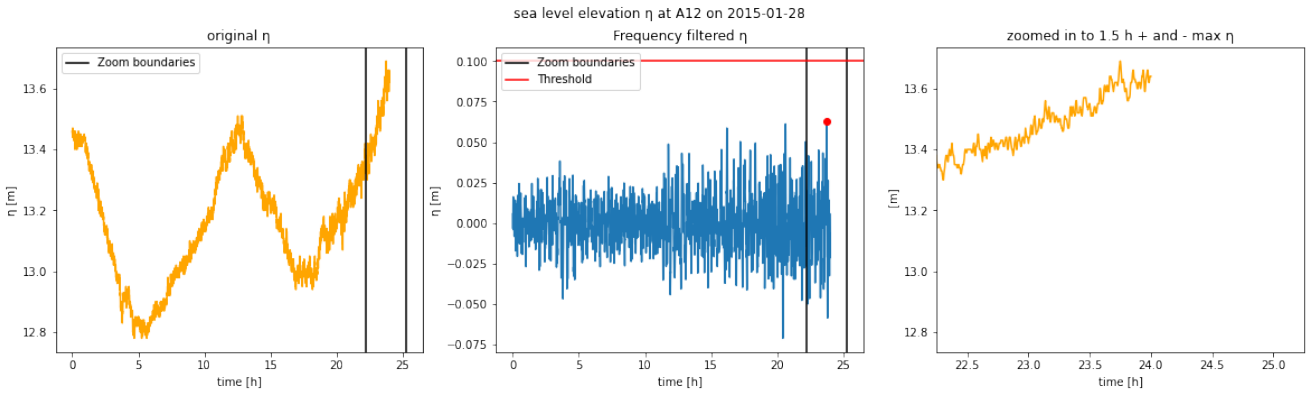

Figure E.27: Original elevation data (left), band-pass filtered elevation data (middle), and zoom of the original elevation data at the max amplitude (right) of station A12, during the winter event of 2015.

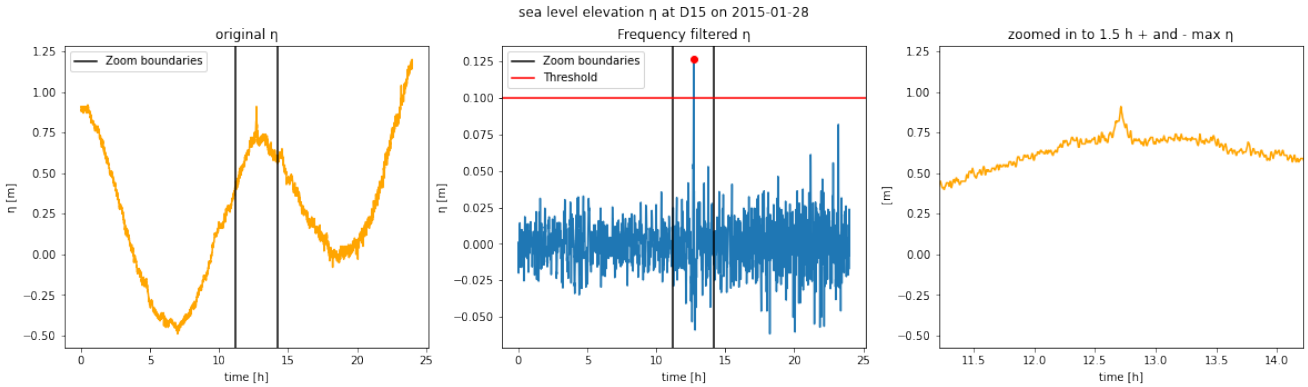

Figure E.28: Original elevation data (left), band-pass filtered elevation data (middle), and zoom of the original elevation data at the max amplitude (right) of station D15, during the winter event of 2015.

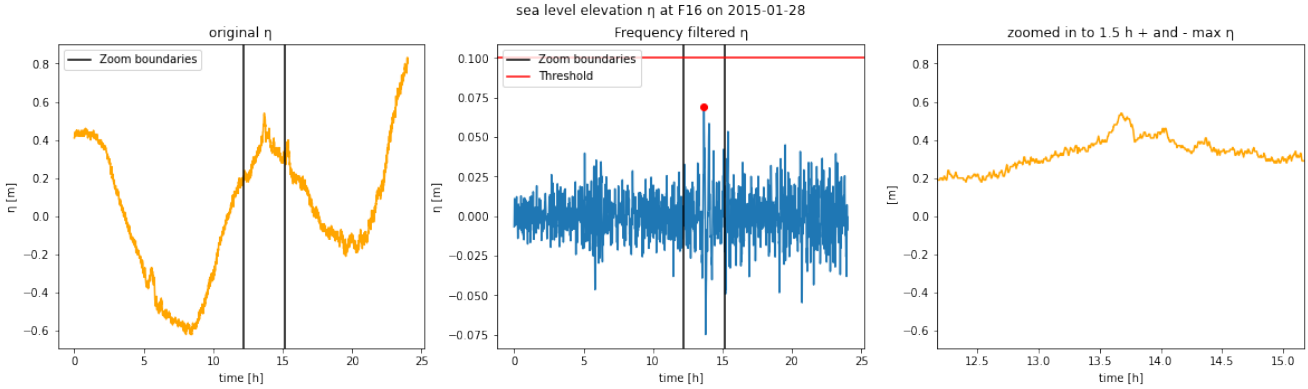

Figure E.29: Original elevation data (left), band-pass filtered elevation data (middle), and zoom of the original elevation data at the max amplitude (right) of station F16, during the winter event of 2015.

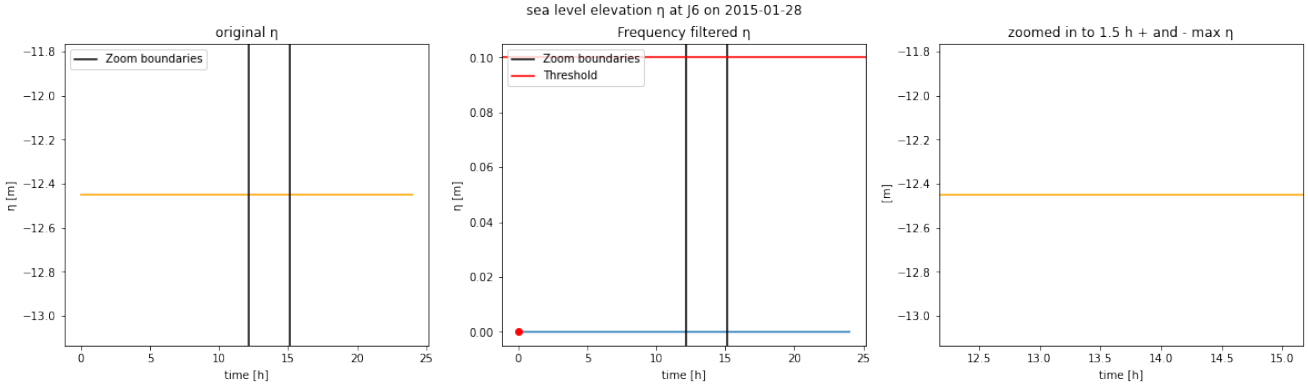

Figure E.30: Original elevation data (left), band-pass filtered elevation data (middle), and zoom of the original elevation data at the max amplitude (right) of station J6, during the winter event of 2015.

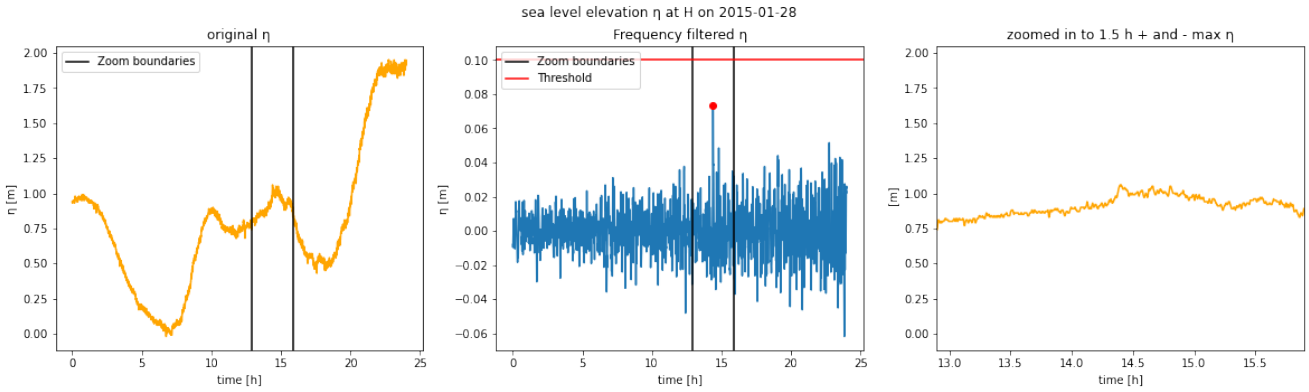

Figure E.31: Original elevation data (left), band-pass filtered elevation data (middle), and zoom of the original elevation data at the max amplitude (right) of station H, during the winter event of 2015.

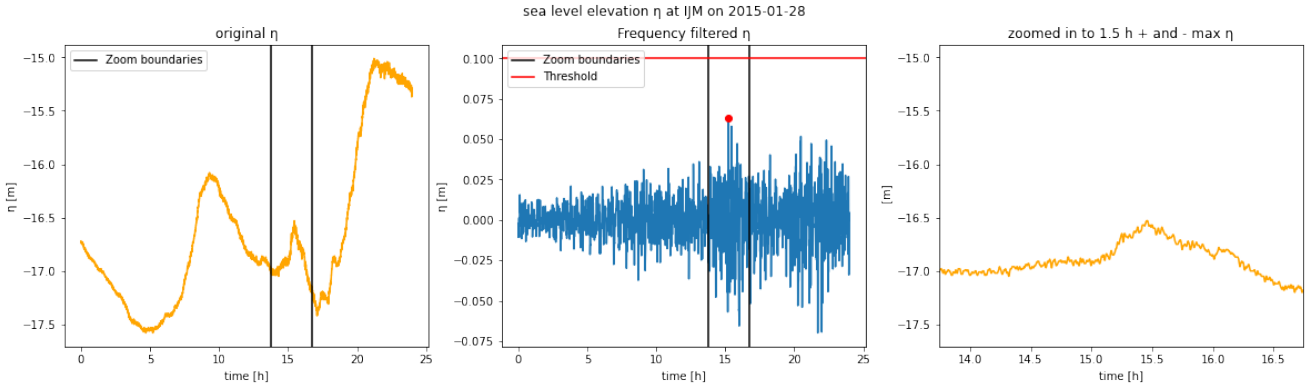

Figure E.32: Original elevation data (left), band-pass filtered elevation data (middle), and zoom of the original elevation data at the max amplitude (right) of station IJM, during the winter event of 2015.

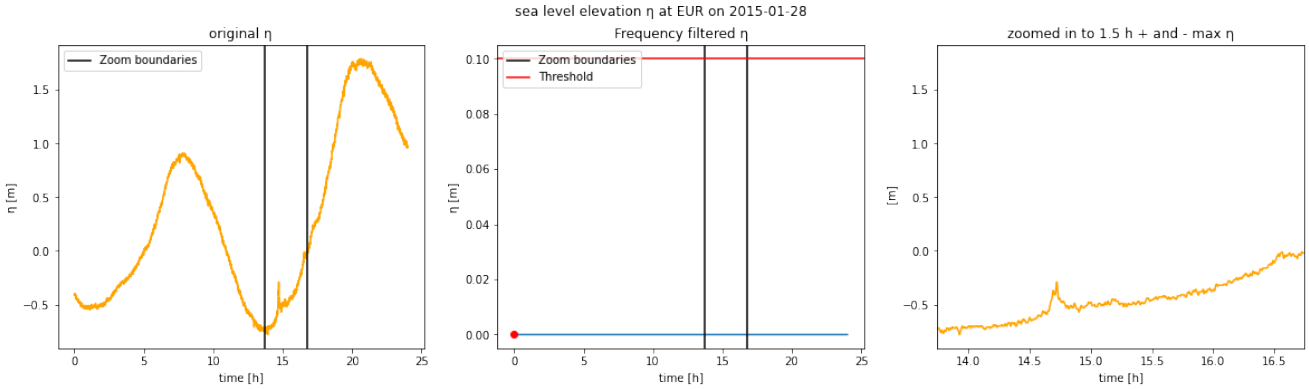

Figure E.33: Original elevation data (left), band-pass filtered elevation data (middle), and zoom of the original elevation data at the max amplitude (right) of station EUR, during the winter event of 2015.

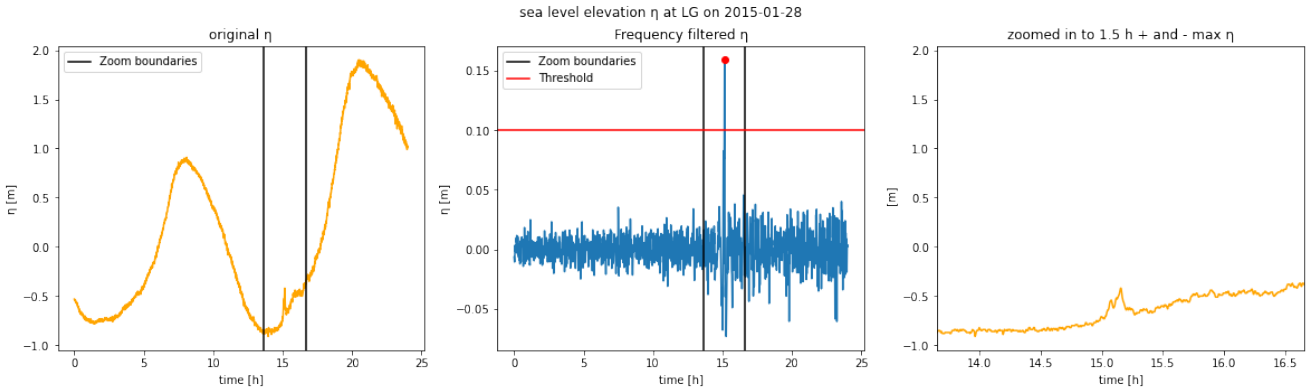

Figure E.34: Original elevation data (left), band-pass filtered elevation data (middle), and zoom of the original elevation data at the max amplitude (right) of station LG, during the winter event of 2015.

E.5. Spring event of 2017

E.5.1. Overview

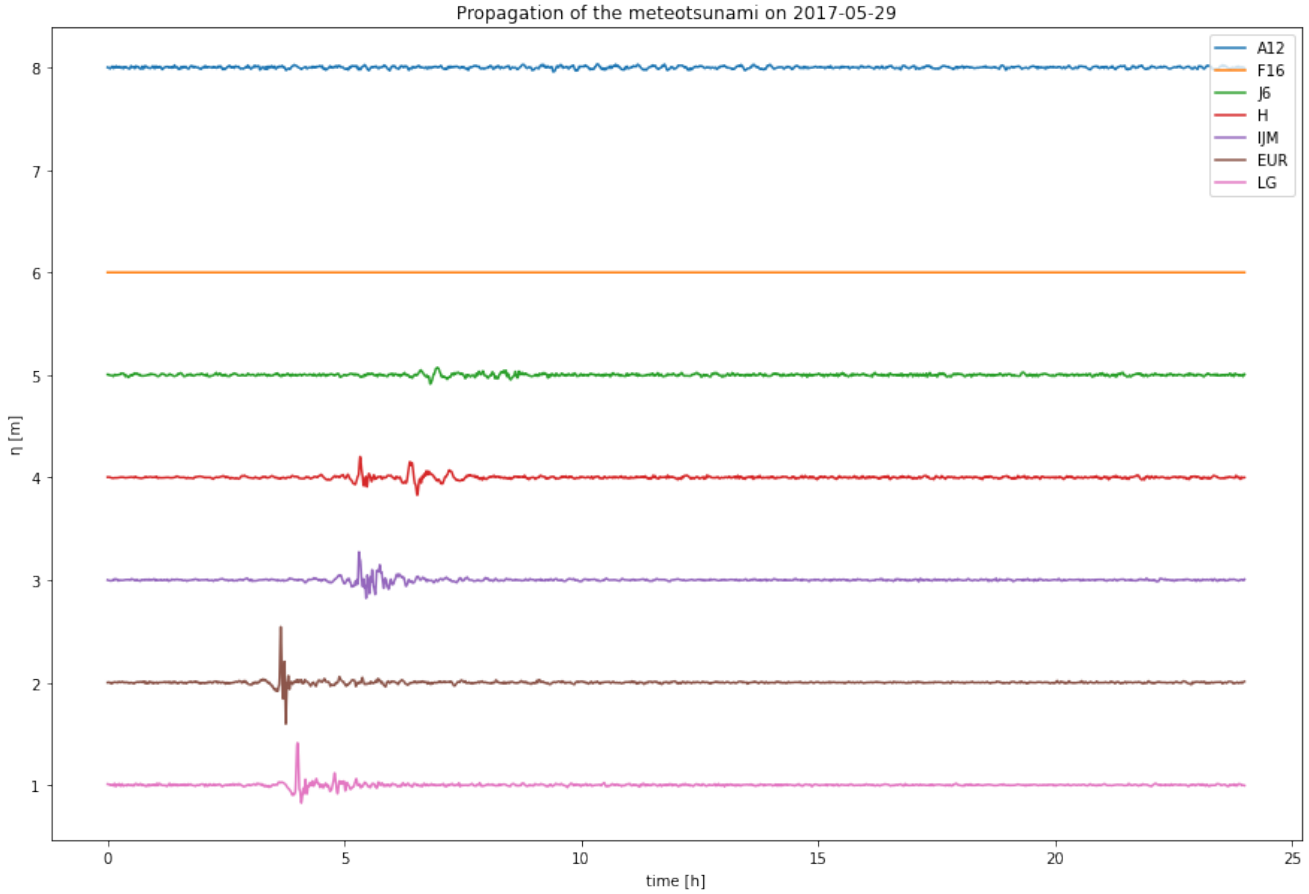

Figure E.35: Overview of band-pass filtered elevation data for the spring event of 2017.

E.5.2. Data per location

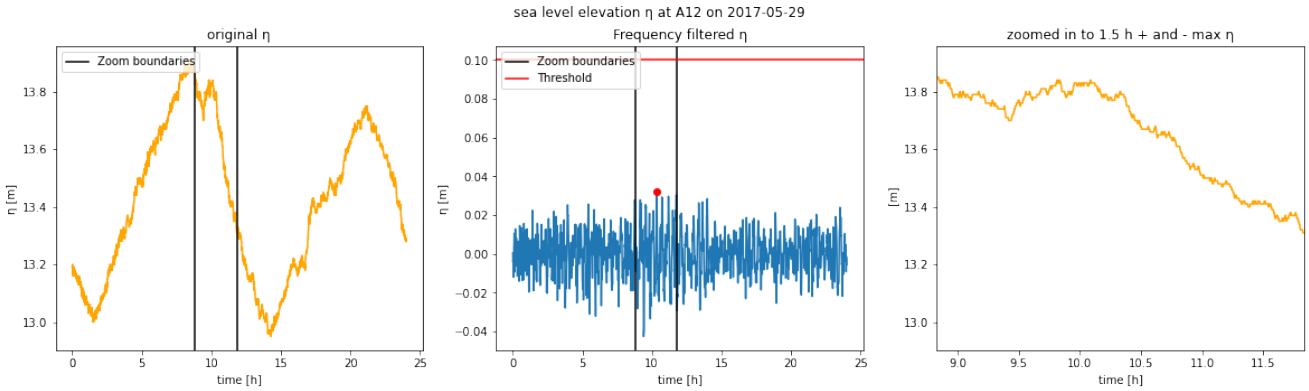

Figure E.36: Original elevation data (left), band-pass filtered elevation data (middle), and zoom of the original elevation data at the max amplitude (right) of station A12, during the spring event of 2017.

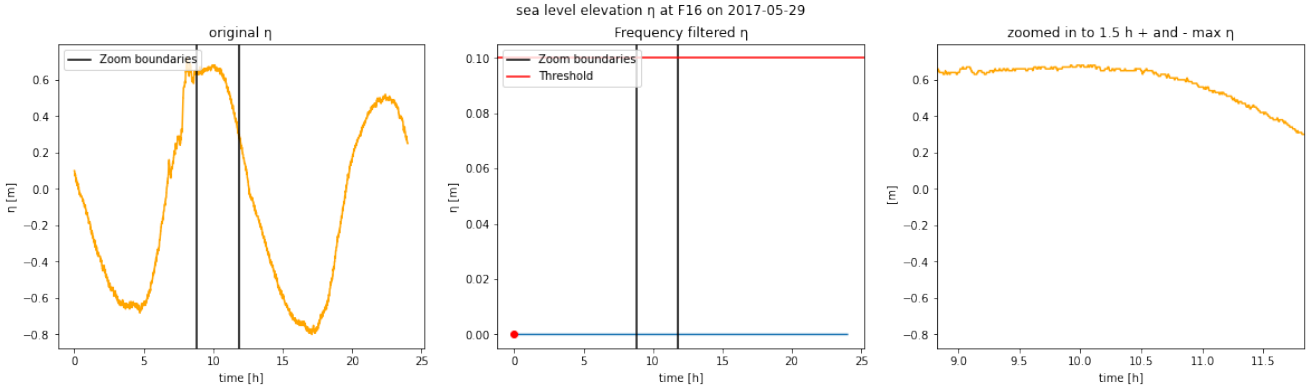

Figure E.37: Original elevation data (left), band-pass filtered elevation data (middle), and zoom of the original elevation data at the max amplitude (right) of station F16, during the spring event of 2017.

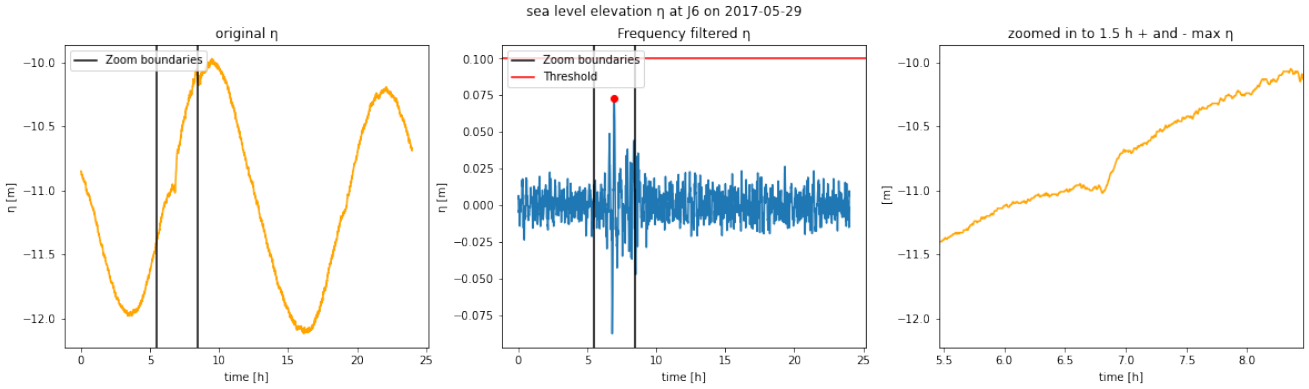

Figure E.38: Original elevation data (left), band-pass filtered elevation data (middle), and zoom of the original elevation data at the max amplitude (right) of station J6, during the spring event of 2017.

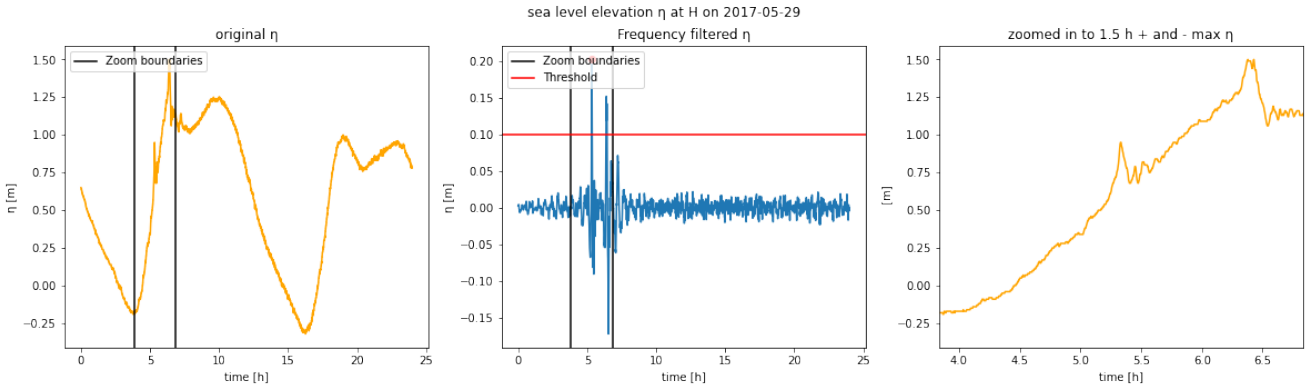

Figure E.39: Original elevation data (left), band-pass filtered elevation data (middle), and zoom of the original elevation data at the max amplitude (right) of station H, during the spring event of 2017.

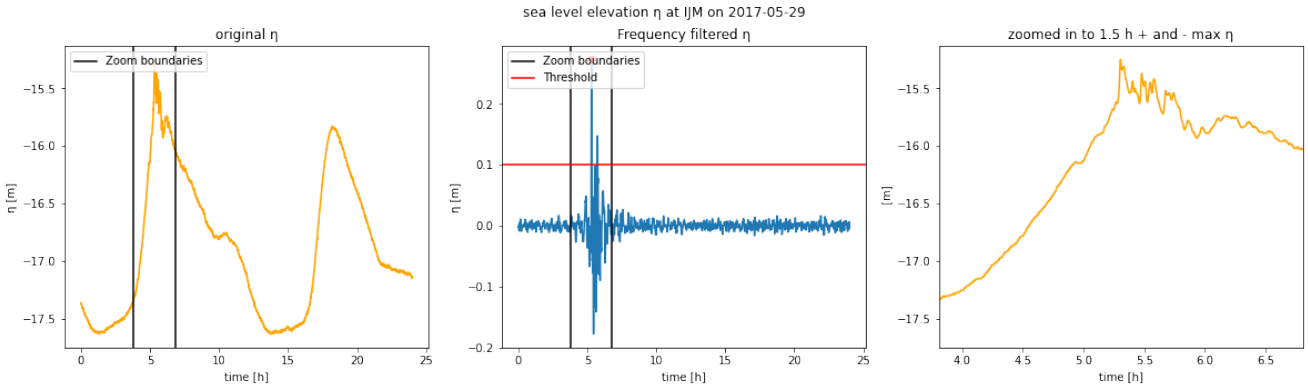

Figure E.40: Original elevation data (left), band-pass filtered elevation data (middle), and zoom of the original elevation data at the max amplitude (right) of station IJM, during the spring event of 2017.

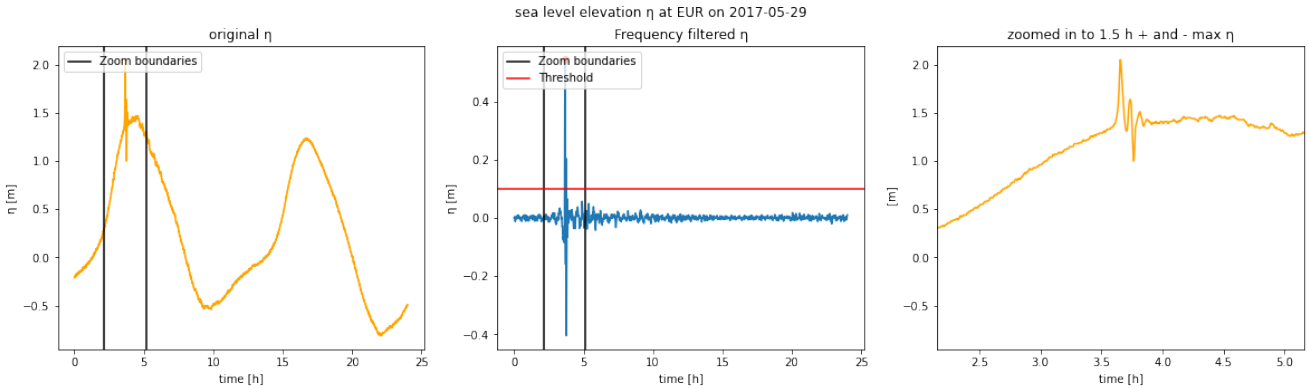

Figure E.41: Original elevation data (left), band-pass filtered elevation data (middle), and zoom of the original elevation data at the max amplitude (right) of station EUR, during the spring event of 2017.

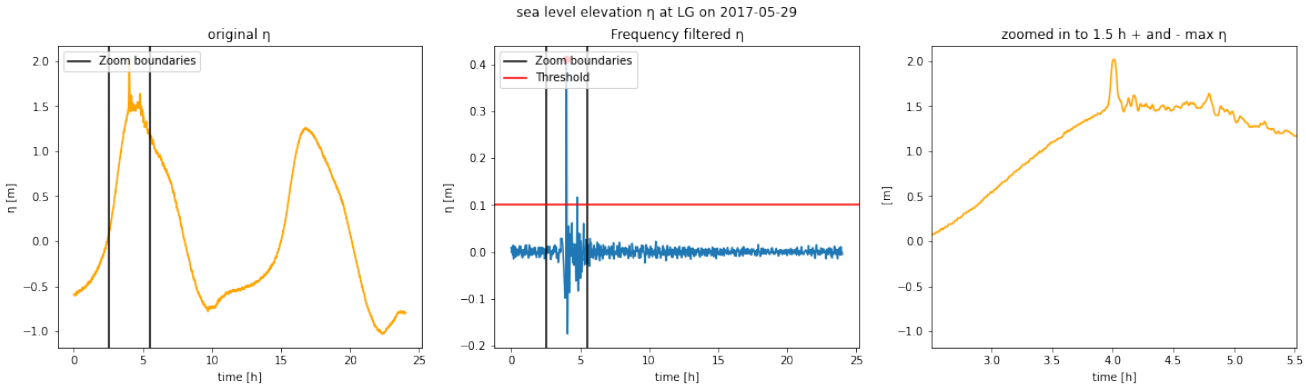

Figure E.42: Original elevation data (left), band-pass filtered elevation data (middle), and zoom of the original elevation data at the max amplitude (right) of station LG, during the spring event of 2017.

F

Scalograms

F.1. Winter event of 2012

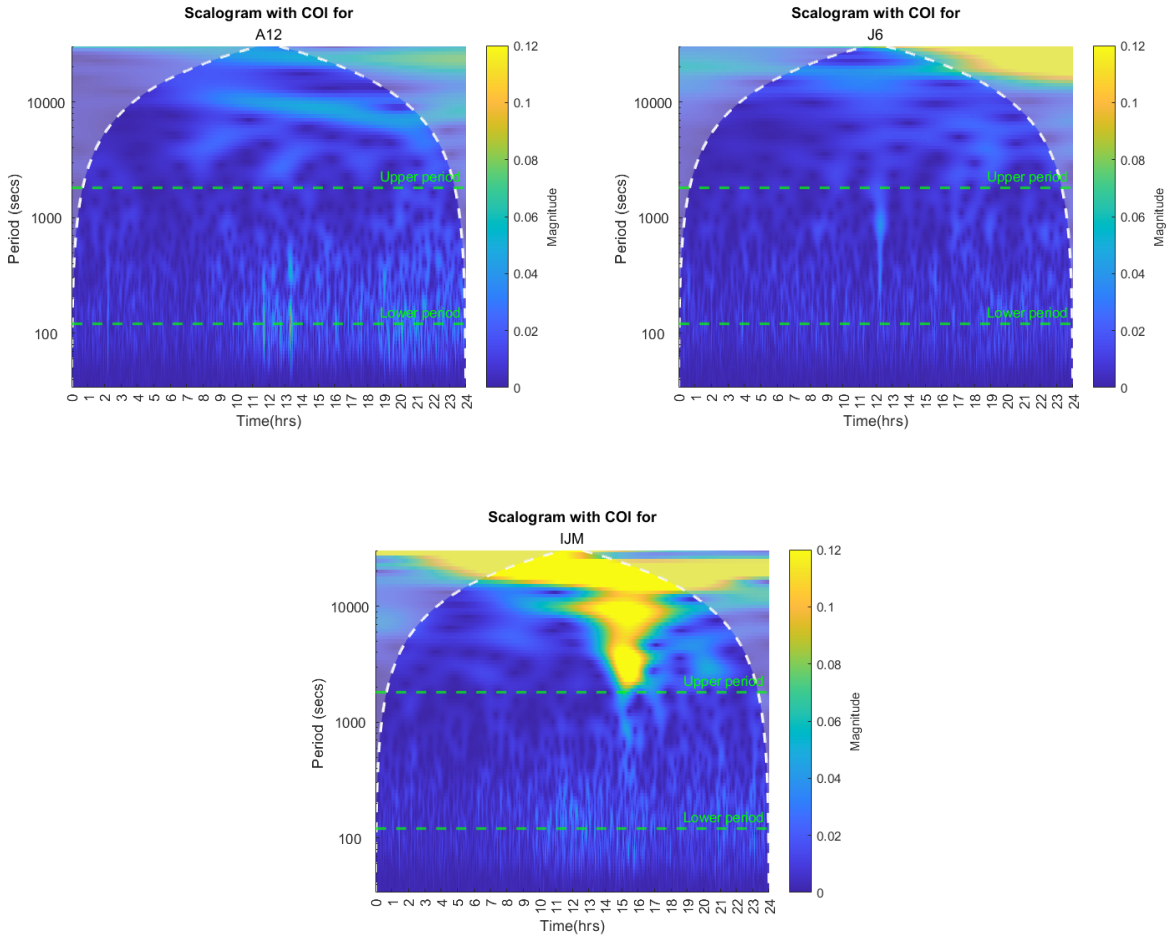

Figure F.2: Scalograms of flagged stations for the winter event of 2012.

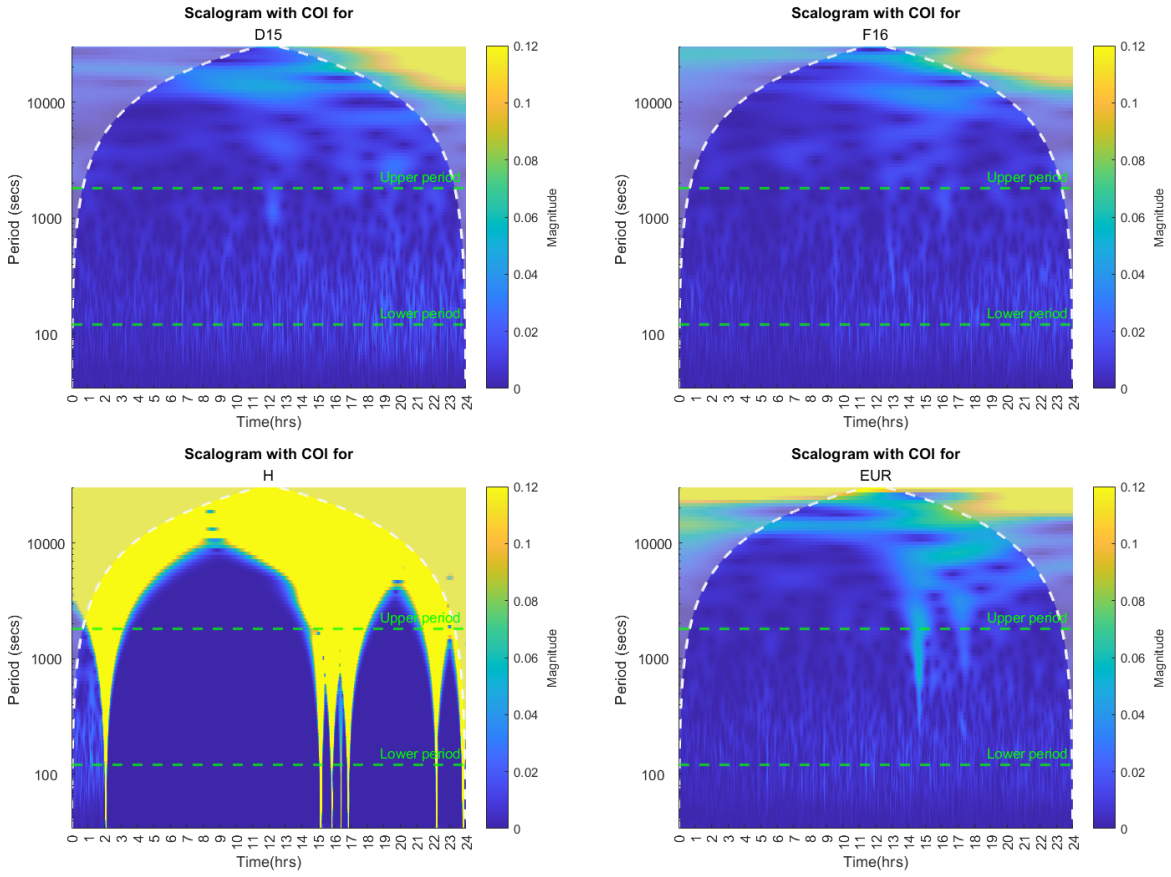

Figure F.3: Scalograms of the other locations for the winter event of 2012.

F.2. Winter event of 2015

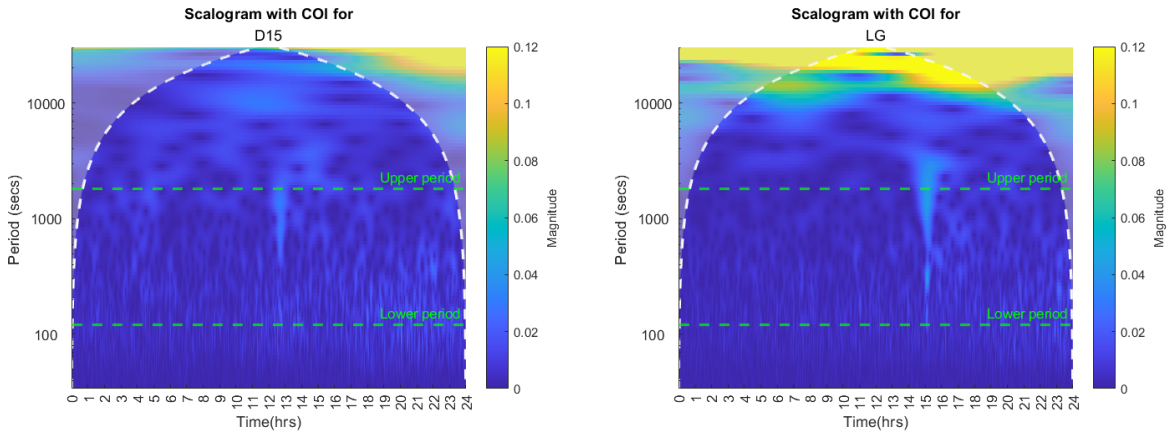

Figure F.4: Scalograms of the flagged locations for the winter event of 2015

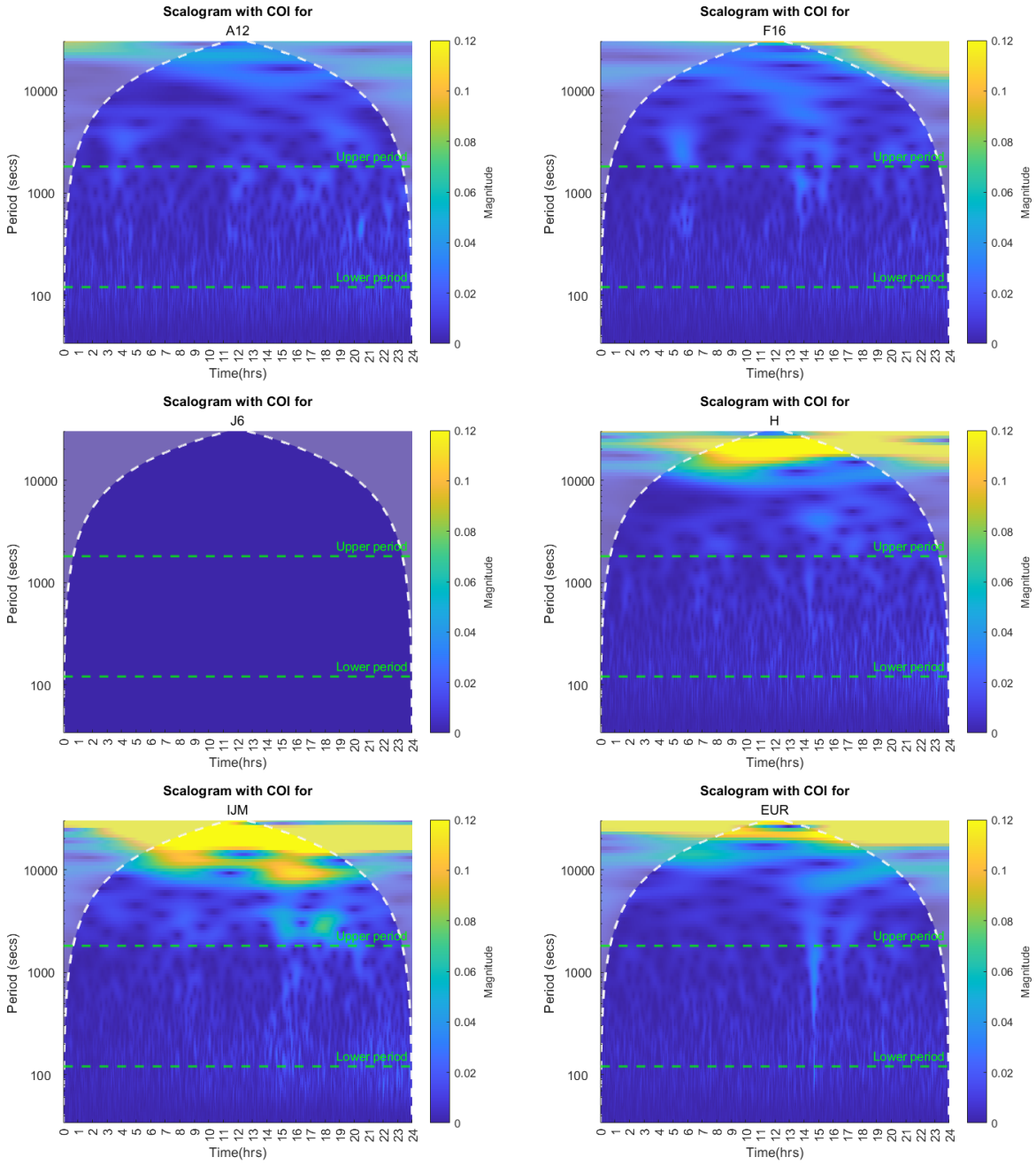

Figure F.5: Scalograms of the other locations for the winter event of 2015

F.3. Summer event of 2012

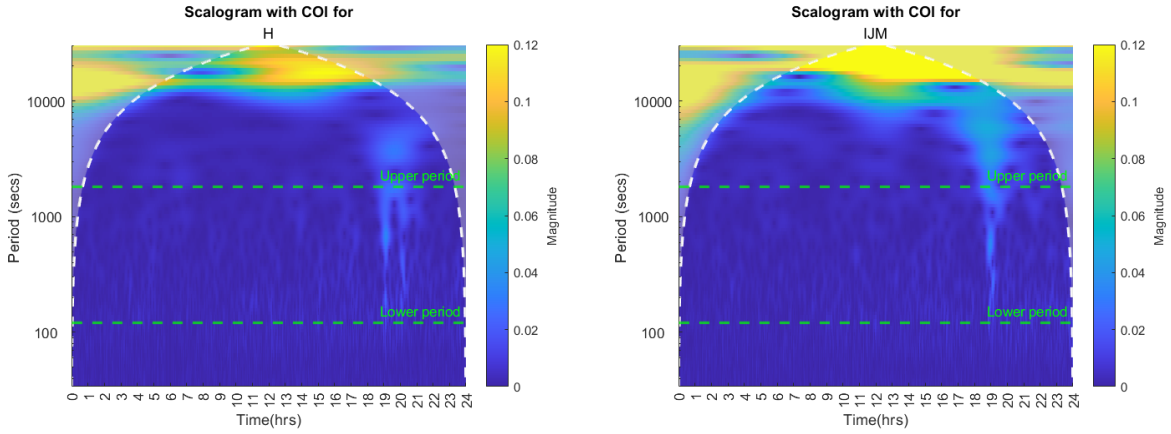

Figure F.6: Scalograms of the flagged locations for the summer event of 2012

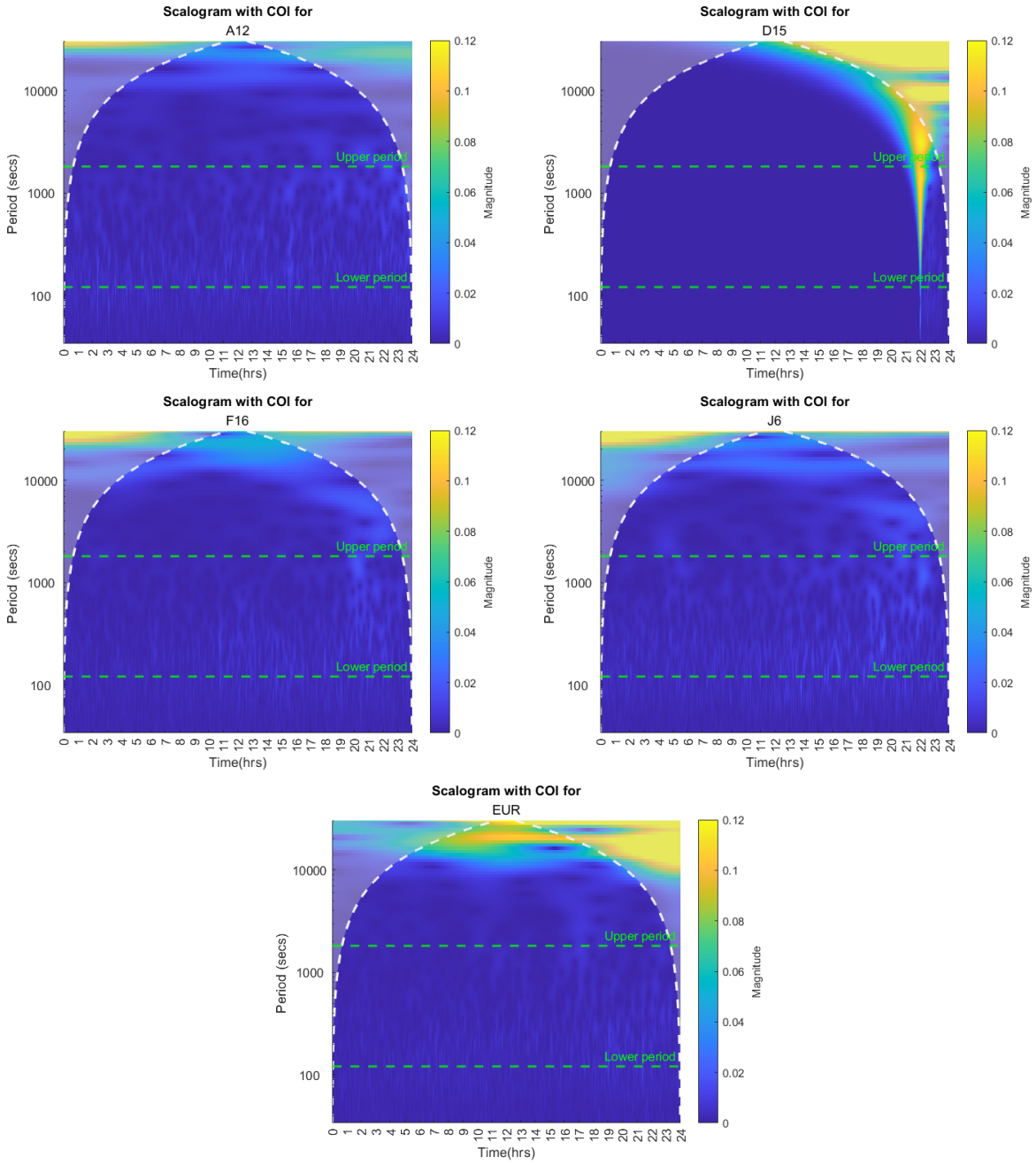

Figure F.7: Scalograms of the other locations for the summer event of 2012

F.4. Summer events of 2014

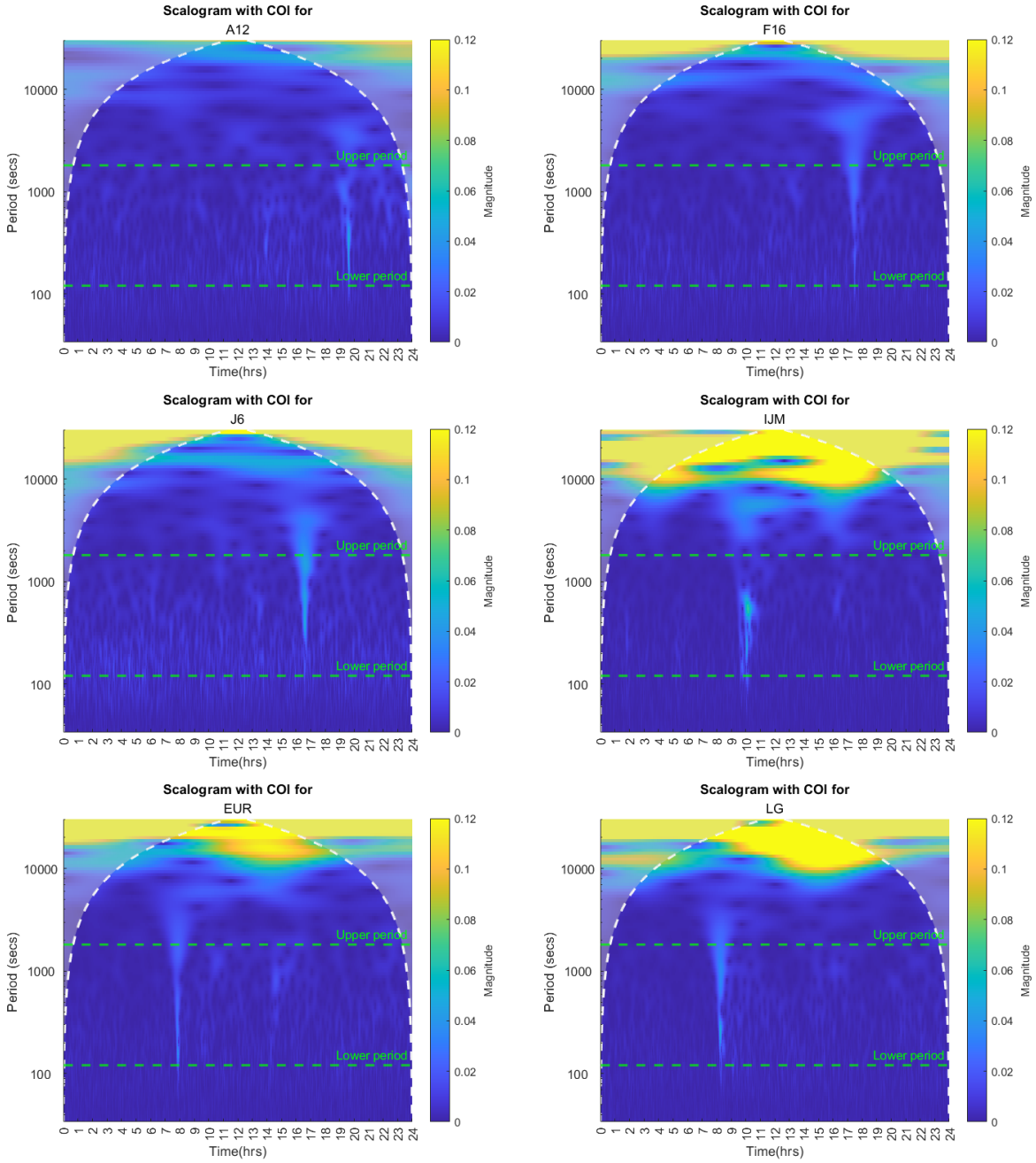

Figure F.8: Scalograms of the flagged locations for the summer events of 2014

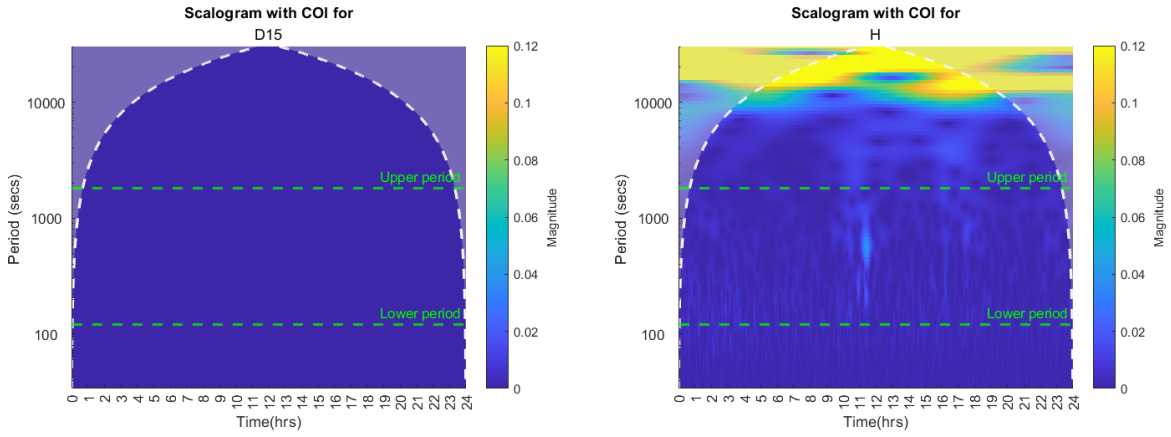

Figure F.9: Scalograms of the other locations for the summer events of 2014

F.5. Spring event of 2017

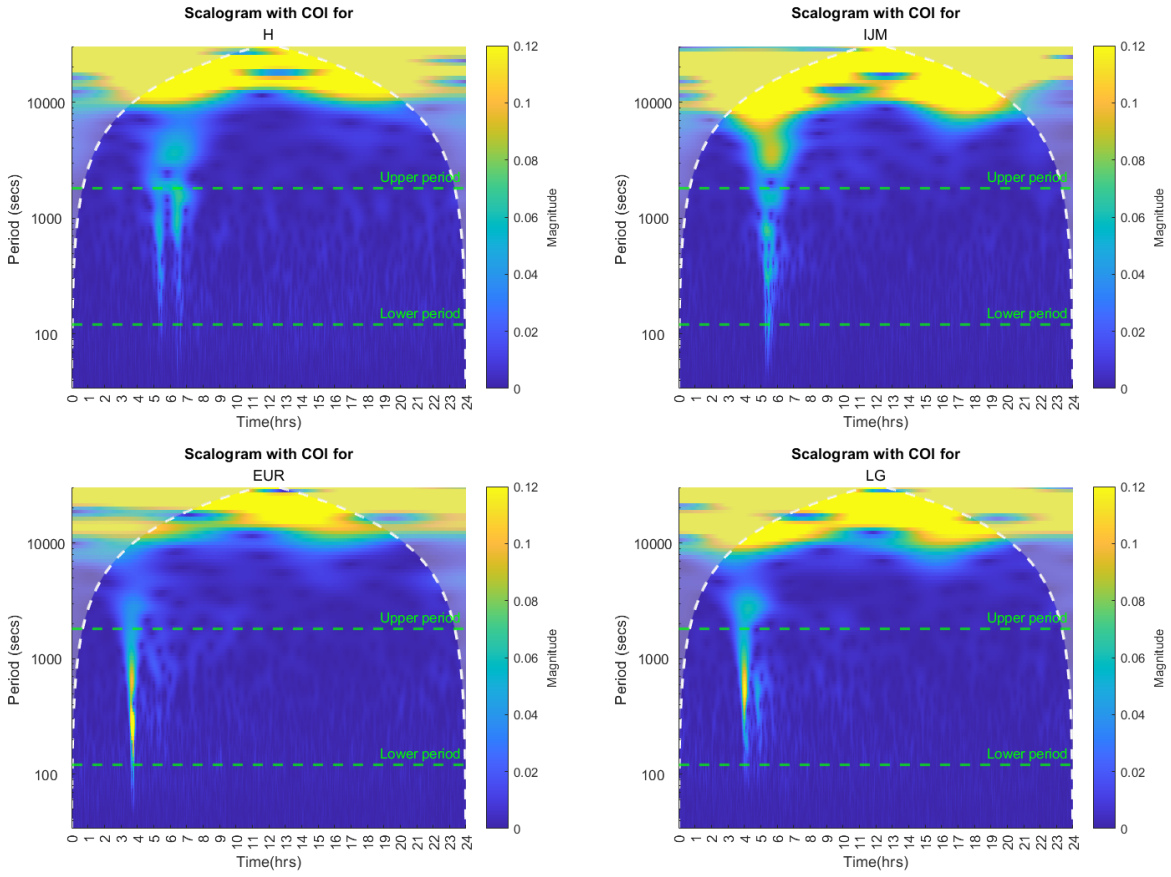

Figure F.10: Scalograms of the flagged locations for the spring event of 2017

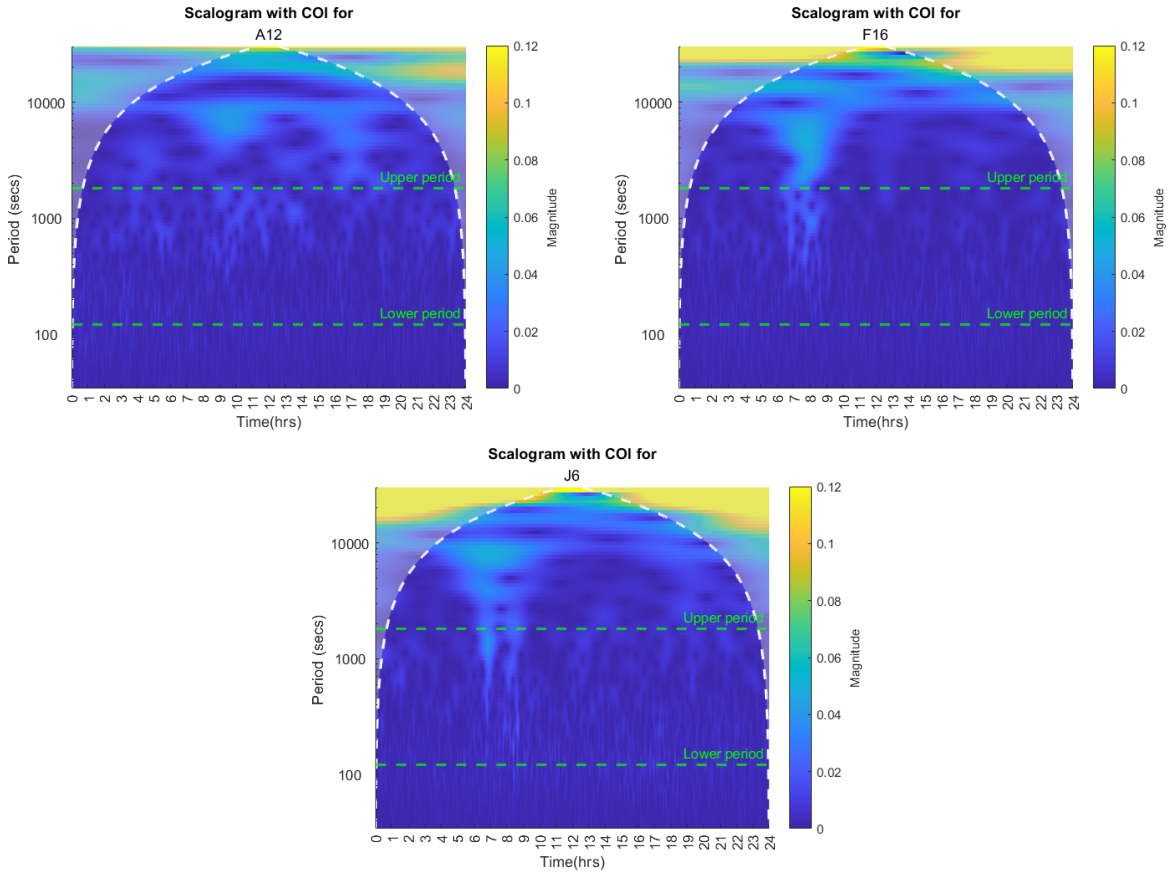

Figure F.11: Scalograms of the other locations for the spring event of 2017

G

Origins

G.1. Winter event of 2012

Figure G.1: Hypothetical origins of the meteotsunami for each relevant wave speed for winter event of 2012

G.2. Winter event of 2015

Figure G.2: Hypothetical origins for each relevant mean wave speed for the winter event of 2015.

G.3. Summer event of 2012

Figure G.3: Hypothetical origins of the meteotsunami for each relevant wave speed for the summer event of 2012.

G.4. First summer event of 2014

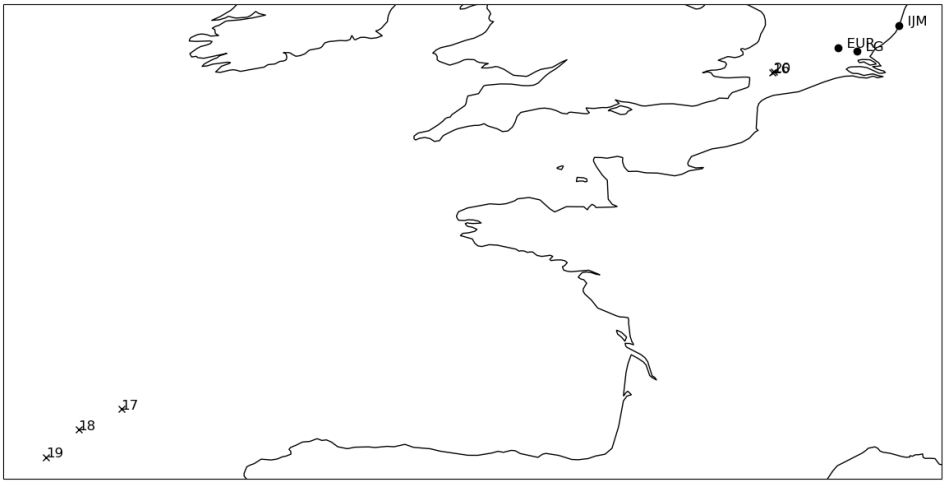

Figure G.4: Hypothetical origins of the meteotsunami for each relevant wave speed for the first summer event of 2014.

G.5. Consecutive summer event of 2014

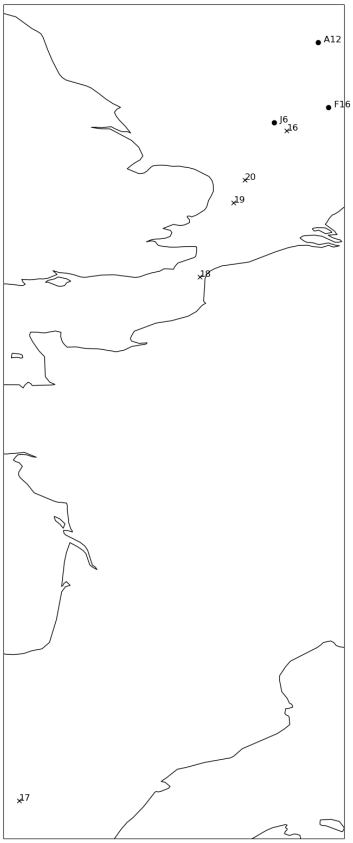

Figure G.5: Hypothetical origins of the meteotsunami for each relevant wave speed for the consecutive summer event of 2014.

G.6. Spring event of 2017

Figure G.6: Hypothetical origin of the meteotsunami for each relevant wave speed for the spring event of 2017.

H

Zero Down Crossing Analysis

H.1. Winter event of 2012

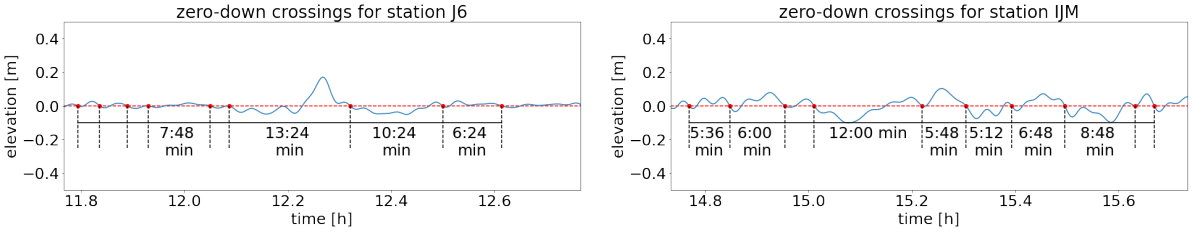

Figure H.1: wave periods around the time of occurrence for the relevant stations for the winter event of 2012.

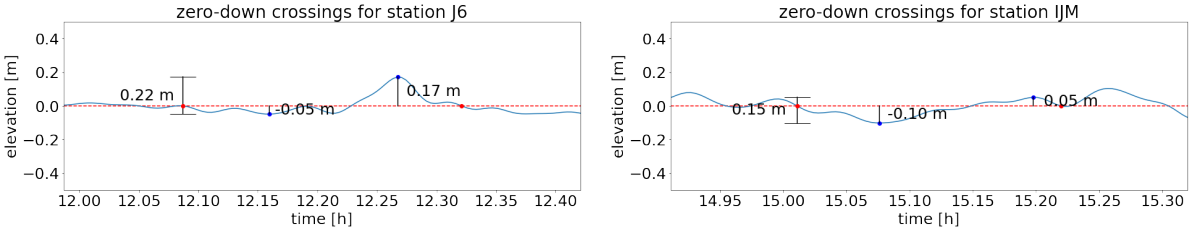

Figure H.2: Wave height of highest wave for the relevant stations for the winter event of 2012.

H.2. Winter event of 2015

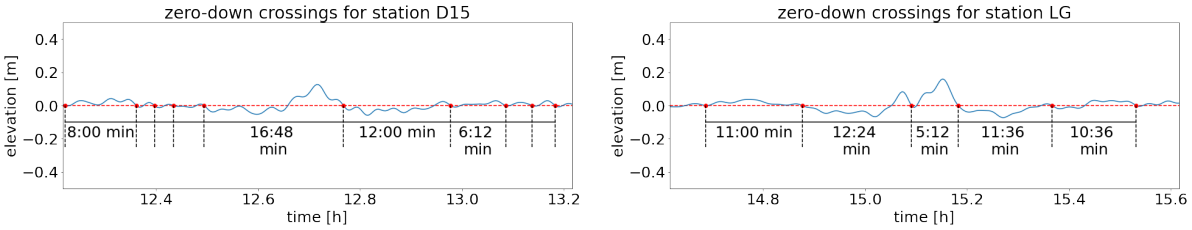

Figure H.3: wave periods around the time of occurrence for the relevant stations for the winter event of 2015.

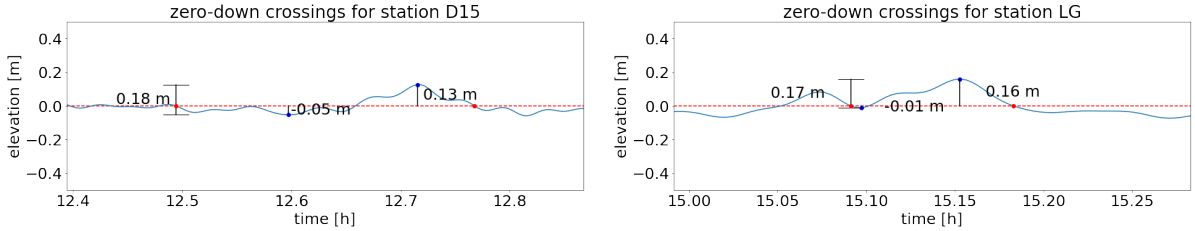

Figure H.4: Wave height of highest wave for the relevant stations for the winter event of 2015.

H.3. Summer event of 2012

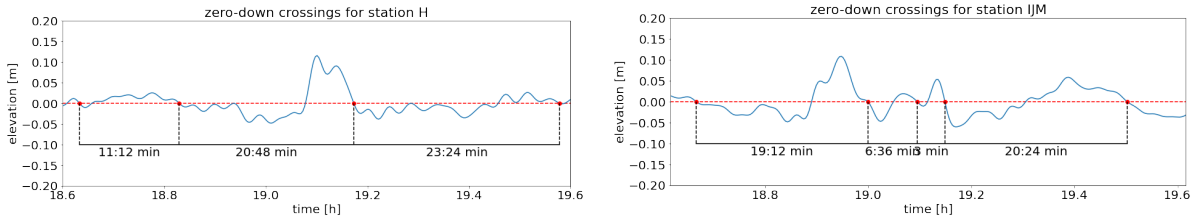

Figure H.5: wave periods around the time of occurrence for the relevant stations for the summer event of 2012.

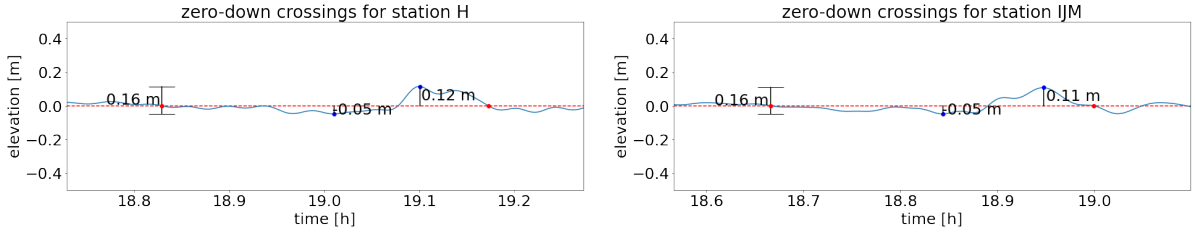

Figure H.6: Wave height of highest wave for the relevant stations for the summer event of 2012.

H.4. First summer event of 2014

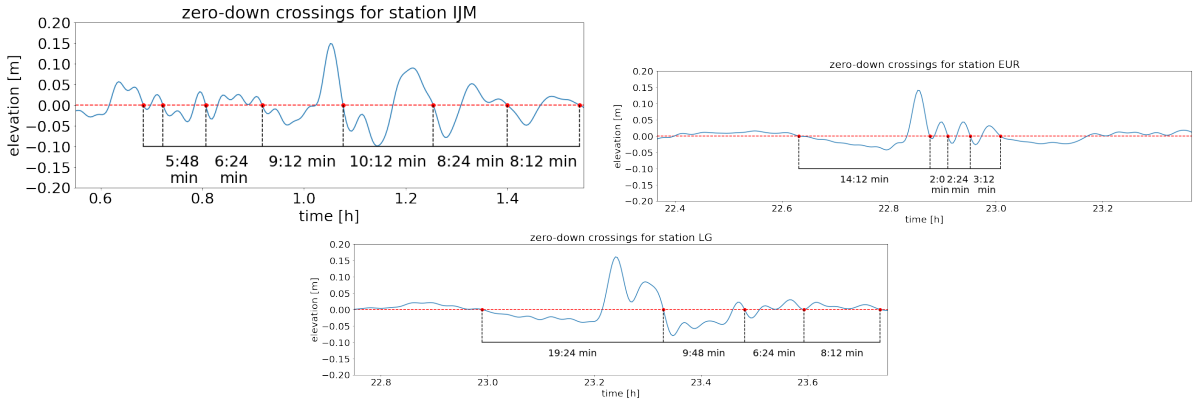

Figure H.7: wave periods around the time of occurrence for the relevant stations for the first summer event of 2014.

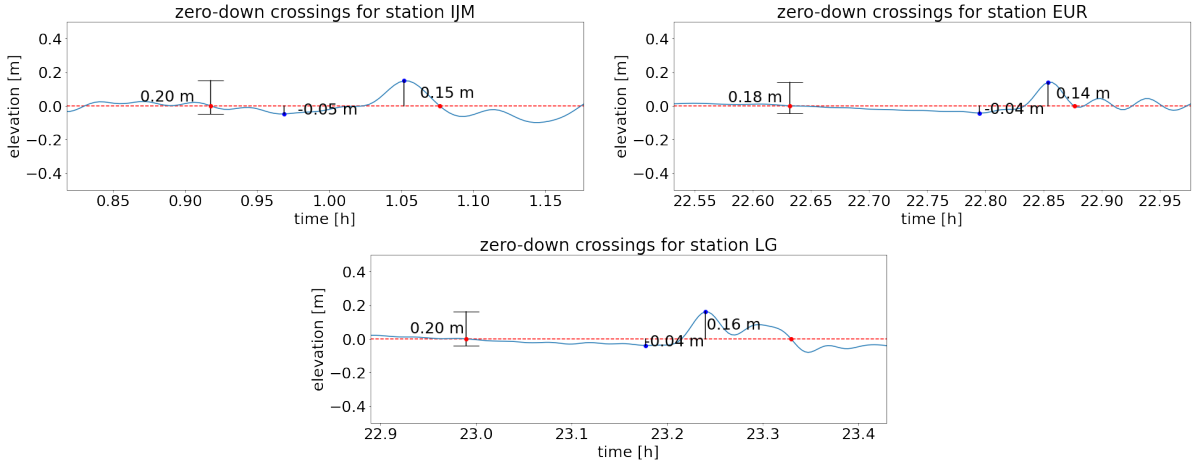

Figure H.8: Wave height of highest wave for the relevant stations for the first summer event of 2014.

H.5. Consecutive summer event of 2014

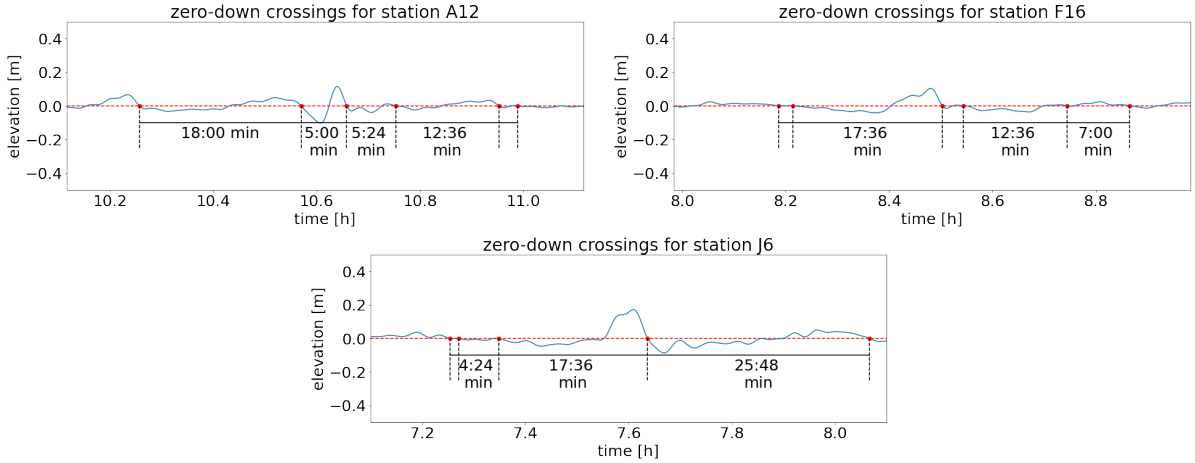

Figure H.9: wave periods around the time of occurrence for the relevant stations for the consecutive summer event of 2014.

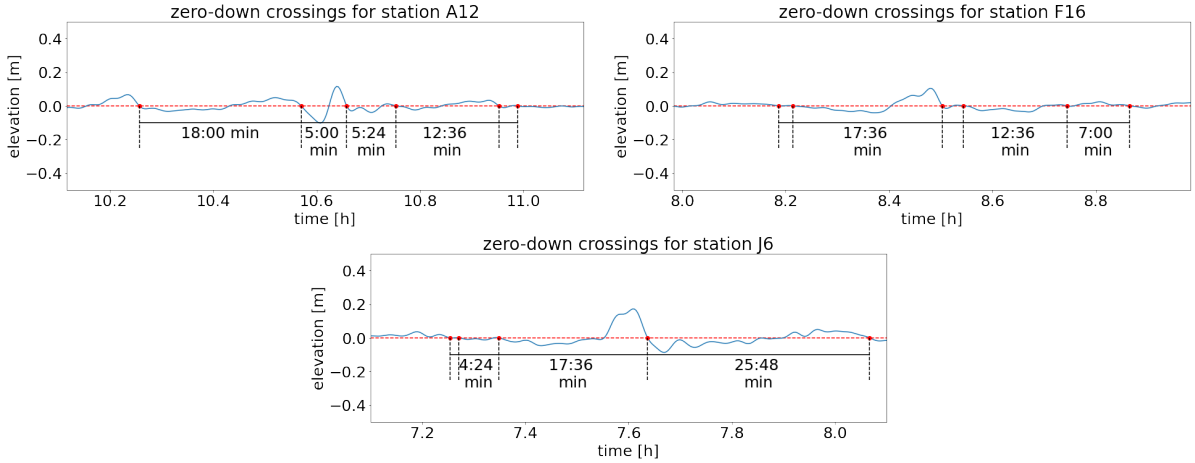

Figure H.10: Wave height of highest wave for the relevant stations for the consecutive summer event of 2014.

H.6. Spring event of 2017

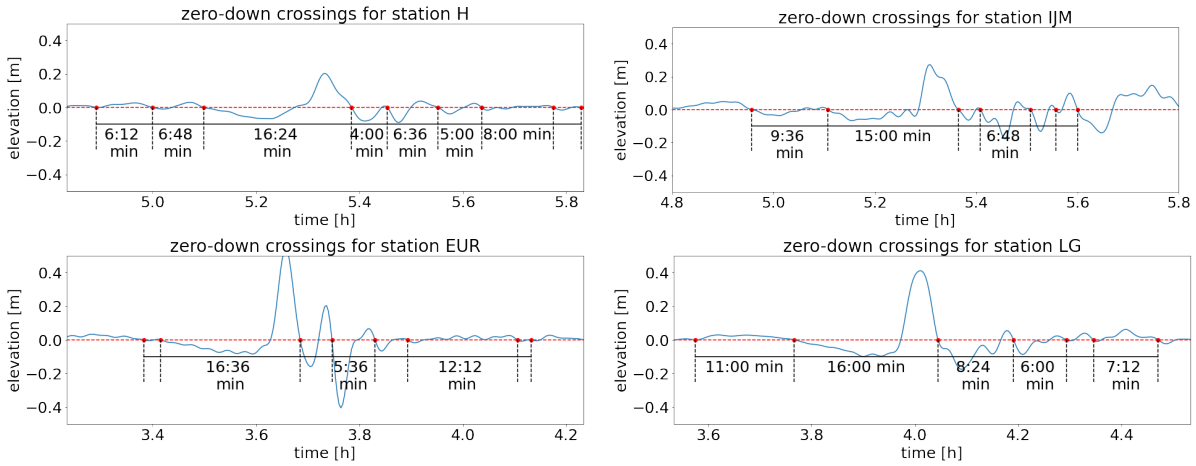

Figure H.11: wave periods around the time of occurrence for the relevant stations for the spring event of 2017.

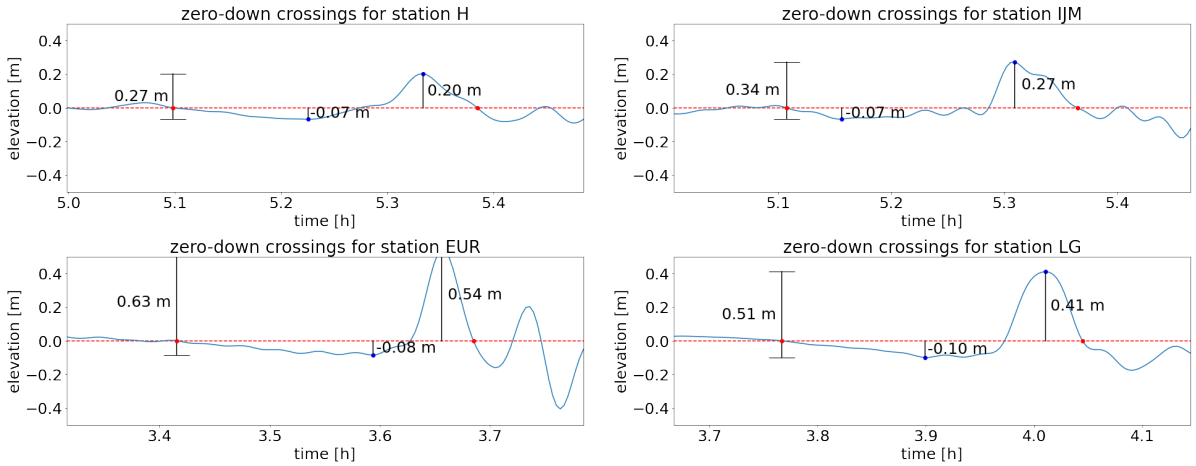

Figure H.12: Wave height of highest wave for the relevant stations for the spring event of 2017.

I

Proudman Resonance Check

I.1. Winter event of 2012

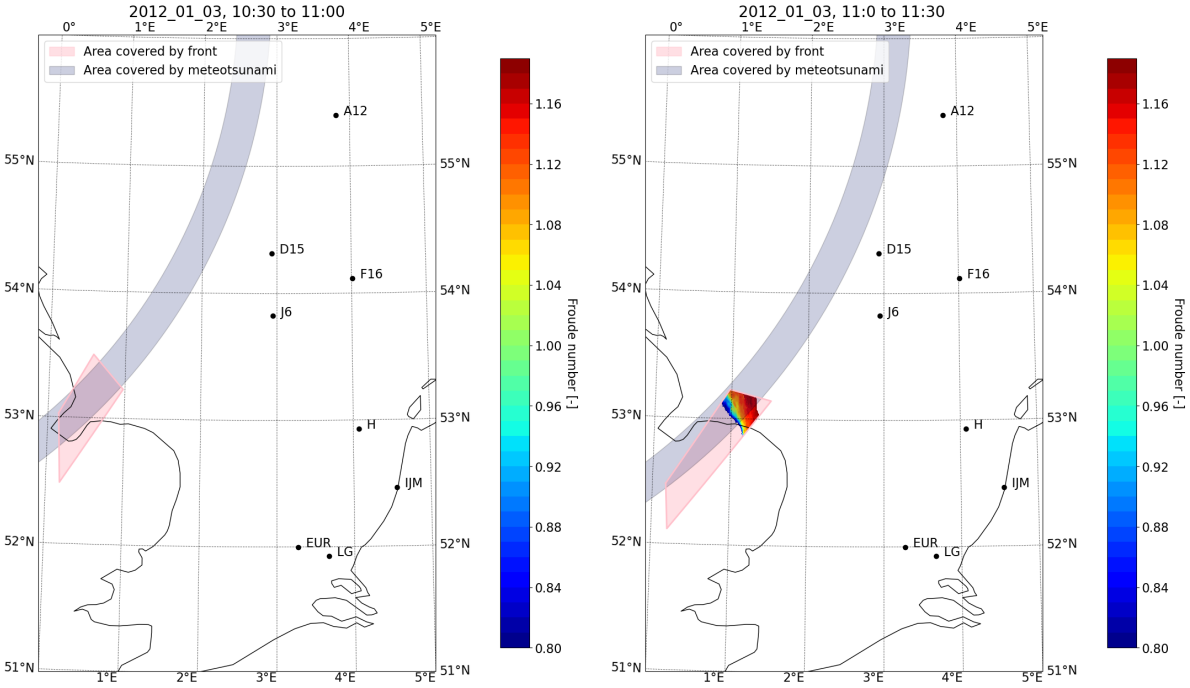

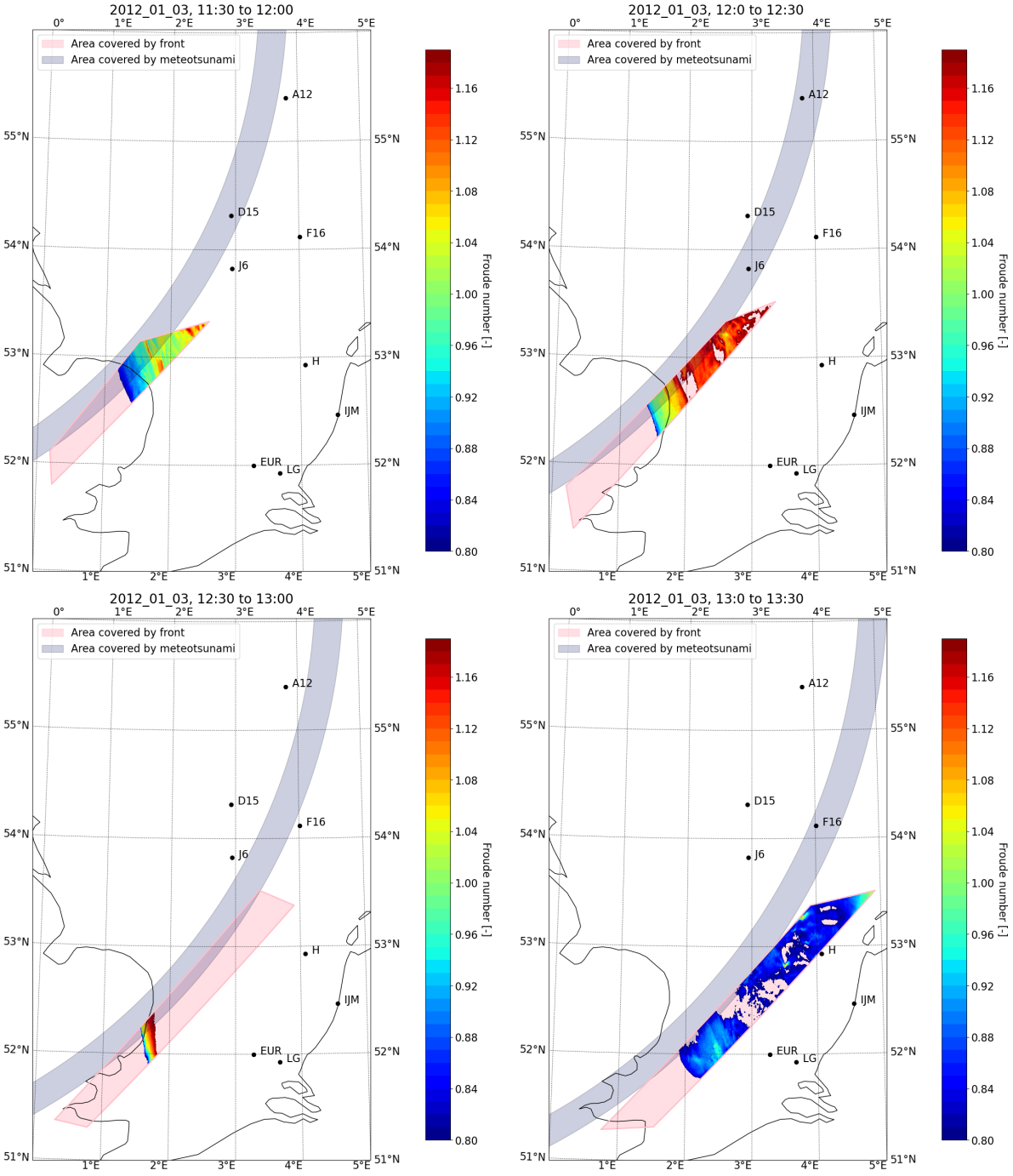
2012_01_03, 11:30 to 12:00
2012_01_03, 12:0 to 12:30
2012_01_03, 12:30 to 13:00
2012_01_03, 13:0 to 13:30
Area covered by front
Area covered by meteotsunami
A12
D15
F16
J6
H
IJM
EUR
LG
Froude number [-]

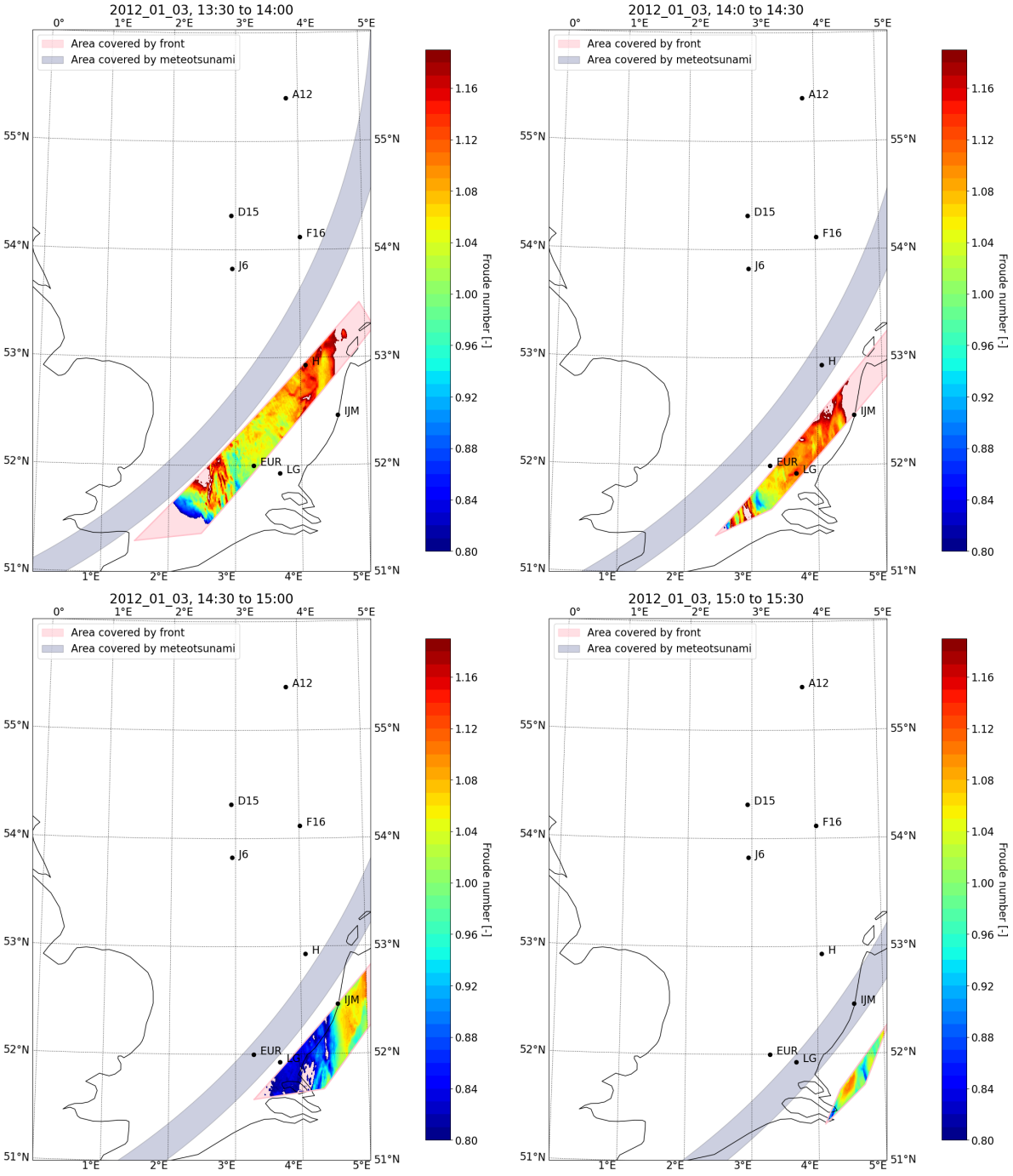
2012_01_03, 13:30 to 14:00
2012_01_03, 14:0 to 14:30
2012_01_03, 14:30 to 15:00
2012_01_03, 15:0 to 15:30
Area covered by front
Area covered by meteotsunami
A12
D15
F16
J6
H
IJM
EUR
LG
Froude number [-]
0.80
0.84
0.88
0.92
0.96
1.00
1.04
1.08
1.12
1.16
0°
1°E
2°E
3°E
4°E
5°E
51°N
52°N
53°N
54°N
55°N

I.2. Winter event of 2015

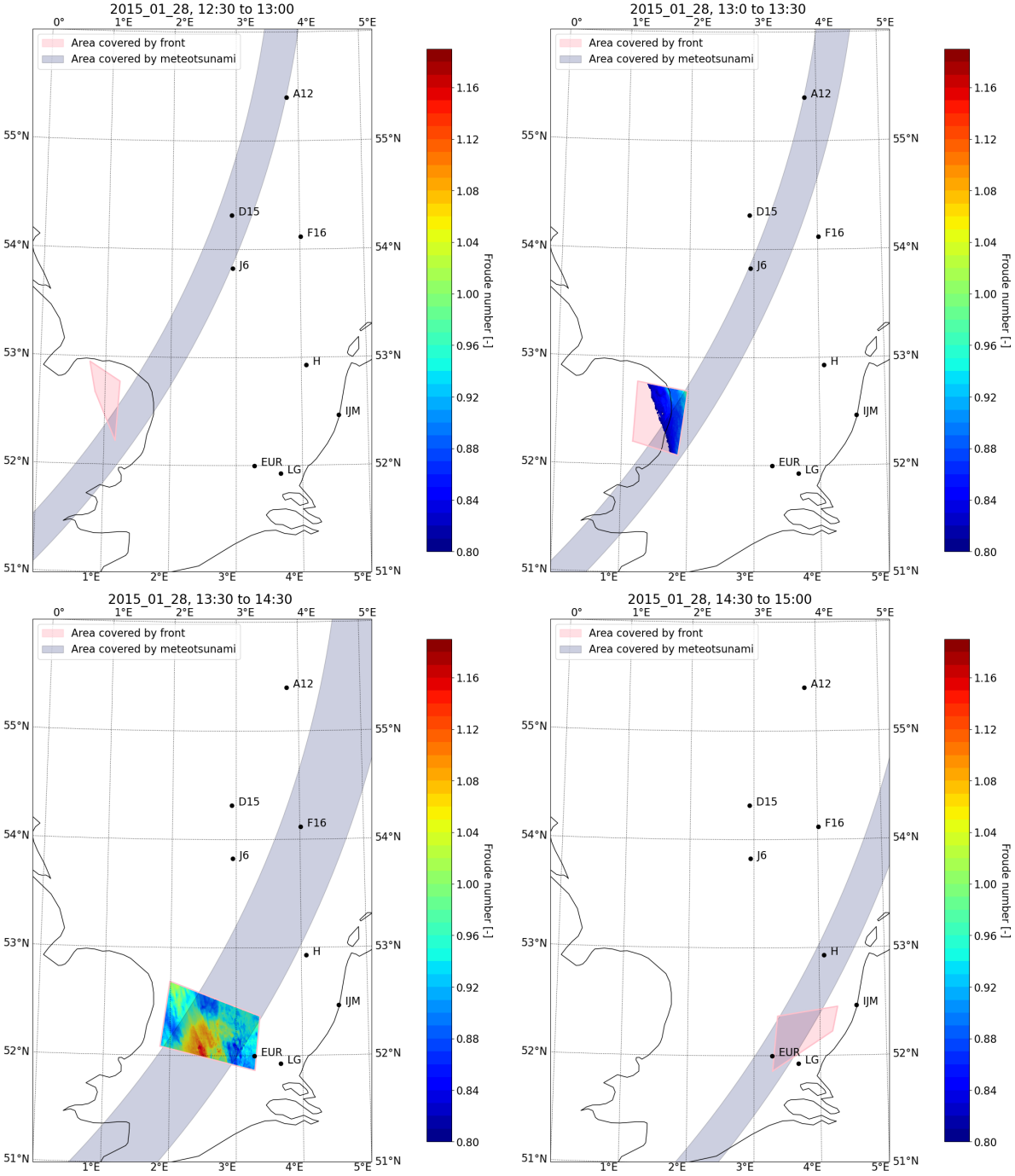

I.3. Spring event of 2017

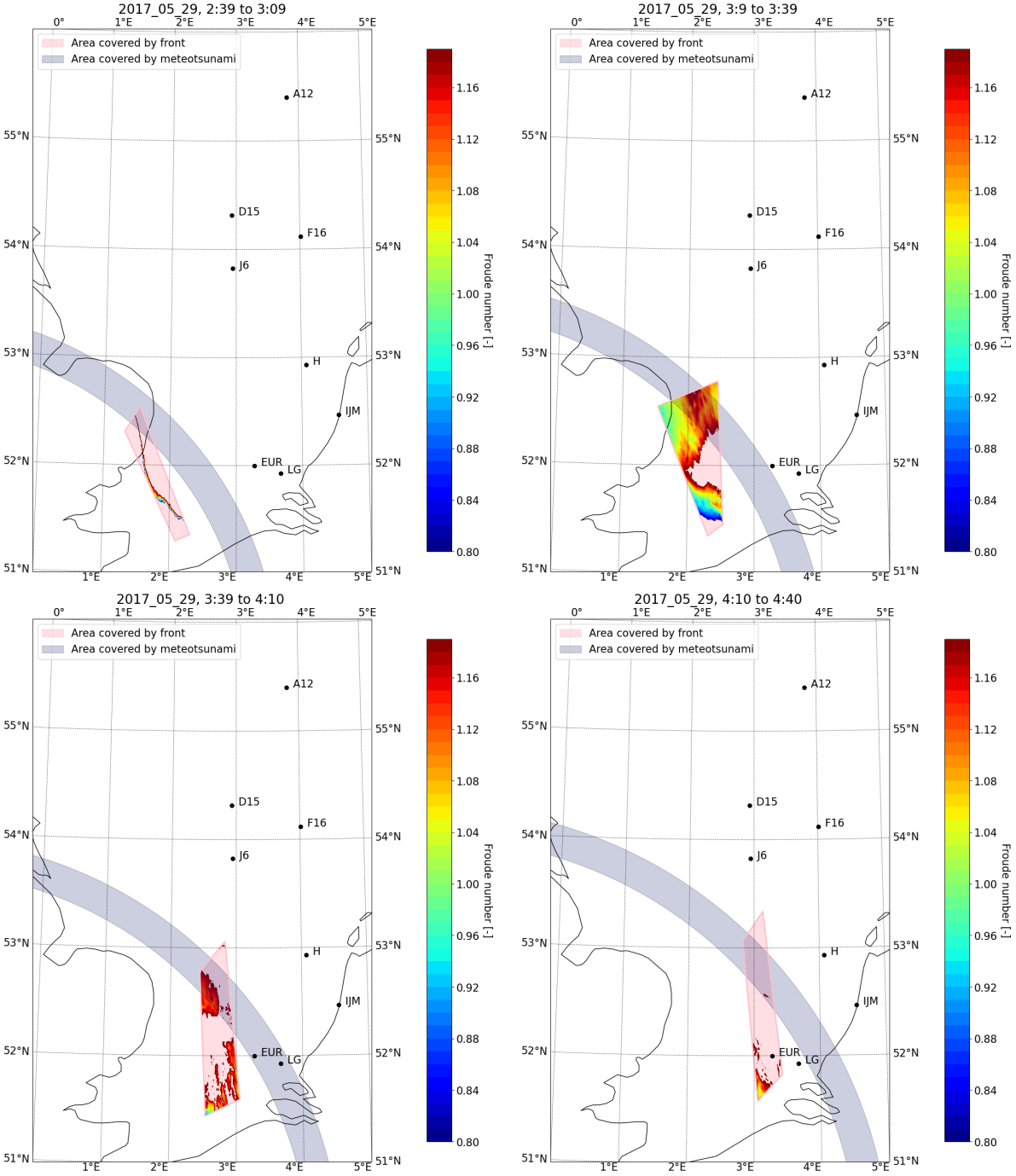

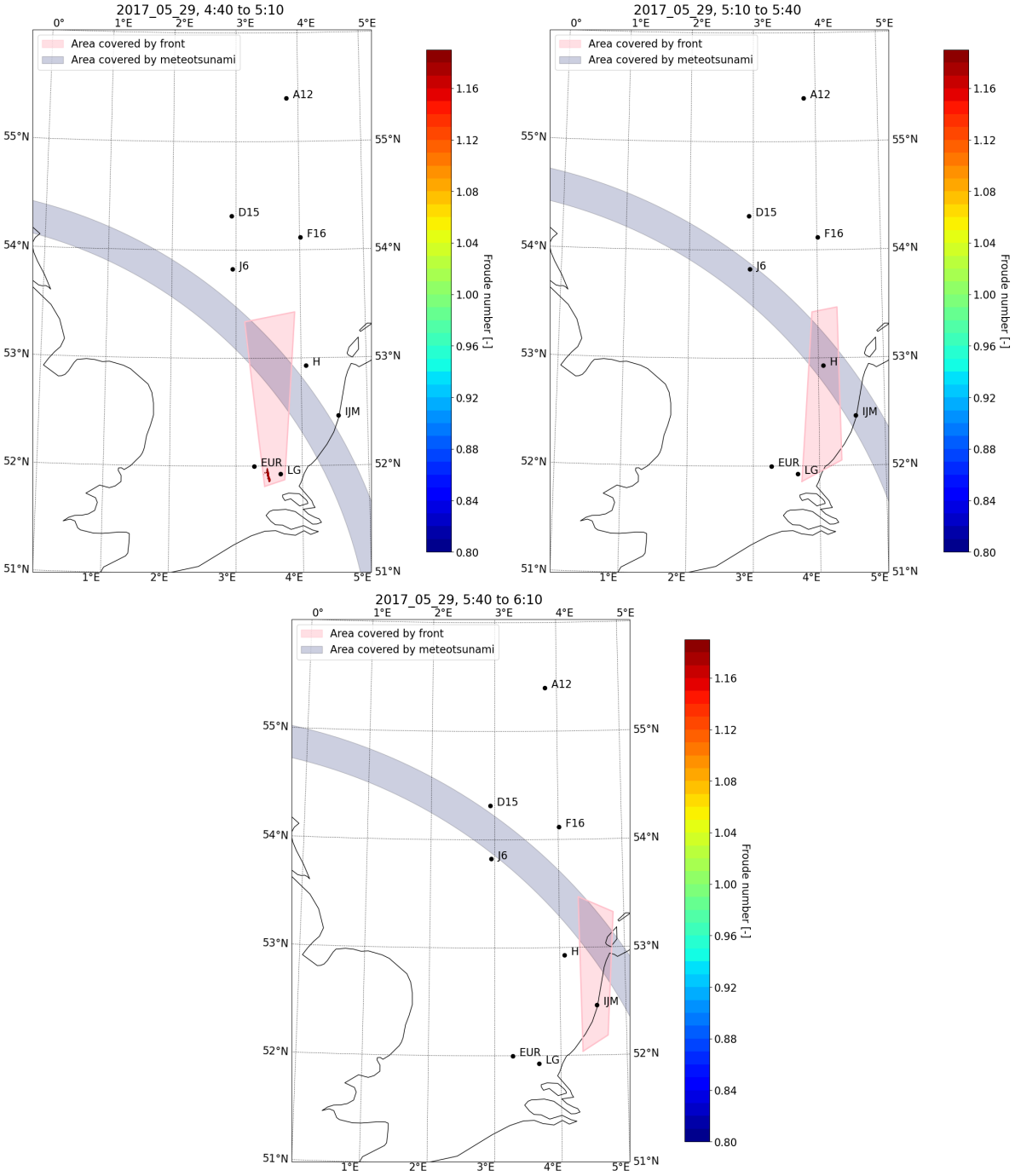
2017_05_29, 4:40 to 5:10
2017_05_29, 5:10 to 5:40
2017_05_29, 5:40 to 6:10
Area covered by front
Area covered by meteotsunami
A12
D15
F16
J6
H
IJM
EUR
LG
Froude number [-]
0.80
0.84
0.88
0.92
0.96
1.00
1.04
1.08
1.12
1.16
0°
1°E
2°E
3°E
4°E
5°E
51°N
52°N
53°N
54°N
55°N